Measuring and Modelling the Earthquake Deformation Cycle at Continental Dip-Slip Faults

Thomas Francis Ingleby

Submitted in accordance with the requirements for the degree of
Doctor of Philosophy

The University of Leeds
School of Earth and Environment

September 2018

The candidate confirms that the work submitted is his own, except where work which has formed part of jointly authored publications has been included. The contribution of the candidate and the other authors to this work has been explicitly indicated below. The candidate confirms that appropriate credit has been given within the thesis where reference has been made to the work of others.

The work in Chapter 2 of the thesis has appeared in publication as follows:
Ingleby, T., and T.J. Wright (2017), *Omori-like decay of postseismic velocities following continental earthquakes*, Geophysical Research Letters, 44, 31193130, doi:10.1002/2017GL072865
The original motivation for the paper was suggested by T.J. Wright and refined by both authors. I performed the data collection, data analysis and modelling and wrote the manuscript. The manuscript was improved by input from T.J. Wright as well as the comments of reviewers, R. Burgmann and S. Barbot.

The work in Chapter 3 is in revision for publication as follows:
Ingleby, T., T.J. Wright, A. Hooper, T.J. Craig and J.R. Elliott (2019), *Constraints on the geometry and frictional properties of the Main Himalayan Thrust using co-, post- and interseismic deformation in Nepal*, Journal of Geophysical Research: Solid Earth
The work originated from the suggestion of T.J. Wright and my co-supervisors, A. Hooper and G. Houseman to study the postseismic deformation following the 2015 Gorkha earthquake in Nepal. The ideas in the paper evolved over time, through discussion between myself, T.J. Wright and A. Hooper with input from J.R Elliott. I processed InSAR and GNSS displacement data, developed the modelling software, analysed the results and wrote the manuscript. T.J. Craig processed GNSS atmospheric delay data, included in the supplementary material of the paper. All authors improved the manuscript through suggested revisions. Editor Paul Tregoning, Associate Editor Emma Hill and two anonymous reviewers have provided helpful comments.

The work in Chapter 4 is a draft manuscript, ready for submission:
Ingleby, T., T.J. Wright, J. Weiss, and V. Butterworth (2019), *Fold and Thrust Belt Growth from over 25 years of InSAR Data*
Near the start of my PhD, I identified a number of potential targets for investigating long lived postseismic deformation following dip-slip earthquakes. The Sibi fold and thrust belt was one of these target areas and I wrote an undergraduate research project proposal to determine whether InSAR could detect any ongoing deformation. V. Butterworth carried out this work for her undergraduate research project. She processed Envisat data to form InSAR time series which revealed ongoing postseismic deformation. I then processed ERS and Sentinel-1 data and combined these with the Envisat data to form the 25 year long InSAR time series and applied various corrections to

reduce noise in the data. Discussions with T.J. Wright and J. Weiss helped to steer the project and J. Weiss suggested the link to critical tapers.

Acknowledgements

The last four years have been a learning experience in a whole host of ways: largely due to the variety of wise, knowledgeable people around me from whom I could learn. With so many helpful people around me, I'm sorry if I miss anybody from these brief thanks!

Firstly, a huge thanks to my supervisors: Tim Wright, Andy Hooper and Greg Houseman. Greg, thank you for the valuable insights you provided near the start of my PhD. Andy, thanks so much for all your technical knowledge which has meant otherwise impossible concepts for me to get my head around became possible. Thanks also for hosting walks/parties and for introducing me to Ferarri pizza ovens! Tim, thank you for being my primary supervisor over the past four years. Thank you for always being approachable and for being my first port of call for questions about pretty much any aspect of my PhD! Thanks for knowing when to push me to keep trying at something, and when to tell me to move on. Thank you also for teaching me how to write scientifically and how to avoid using 'however' inappropriately or speak in the passive voice...

A number of other academic and research staff have been really helpful throughout my PhD. Thanks must go to David and Karsten for being the InSAR gurus when I first arrived, and thank you David for teaching me how to use StAMPS and TRAIN. Karsten, thanks for all your recent help and support as I finish PhD and get involved with SatSense. I'm also thankful for Pablo teaching me how to use LiCSAR and for his ability to write well commented scripts which significantly helped my own script writing. Thanks also to John E for his constant willingness to help and his useful comments on work. Thank you Jonathan W for all your help with my work in Pakistan and your friendly character.

There have also been larger scale structures and bodies which have been really helpful. I'm thankful to NERC for providing the funds for this PhD and to the University of Leeds and IGT for hosting me. The academic environment here has been friendly, approachable and stimulating. I've had the pleasure of co-supervising two undergraduate research projects in my time here. Thank you Vanessa and Alex for being great students and for the interesting results you produced. A huge thanks also to the support staff at Leeds, in particular to Richard Rigby, who was able to combine incredible

ability with patience and friendliness! Thanks also to COMET for providing such a helpful network of experienced researchers and peers to learn from.

My peers have been one of the most significant sources of help, encouragement and laughter over the last few years. Thank you to all my PhD friends, both old and new. Thank you Ekbal for your enthusiasm and happiness to help. Thank you Matt and Jeanne for all the shared InSAR experience and the fun times at various FRINGE and Living Planet conferences. The wider InSAR community in COMET has also been great to be part of. Thank you Eleanor, Ryan, Camilla and Sam W for making conferences not just interesting but fun too.

Office 8.152 has been a wonderful place to be. Thanks to everybody in the office for secret Santas, Bobbie, baking and fun. The one o'clock lunch crowd deserve a special mention for giving us all a space to forget about PhD for an hour in the middle of the day. Thanks go to Ben, George, Gemma, Claire, Huw and Ruth A for being great friends both at work and outside of it. Ruth A has been a fantastic friend to share a PhD with. Thank you Ruth for sharing wisdom, knowledge, experience, tips, jokes, food and fun over the last four years. Your thoughtfulness and friendliness has been a great help, not to mention the amazing baking and the establishment of IGT bakeoff!

Thankfully, there is also life outside of academia. I'm so grateful for my church family at Redeemer, for their support and encouragement throughout my PhD. In particular, a massive thanks to everybody within my city group: for their interest in my work and simultaneously their reminders that there are bigger, more important things than a PhD and that 'God is our refuge and strength'. Thank you Jonny and Sarah for being amazing friends, wise leaders and fantastic examples. Thanks also to the Postgraduate Christian Fellowship and Church Scientific groups for their help in thinking about the interaction between faith and scholarship.

My family have been wonderful throughout my PhD. My parents have been supportive of me throughout the ups and downs of life and have always sought to put my needs before their own - thank you for such kindness. Thank you for the ways you have encouraged me throughout the last four years and helped me to reach the end! Thanks also to Sophie, Nick, Zoe, Liz, Paul and Andrew - you have all helped to keep me sane and been so supportive of me and each other.

Finally, the one person who has made the last four years doable is my amazing wife, Ruth. Thank you for all the ways in which you have encouraged me, provided for me and served me. Thank you for everything you have said and done, for the ways in which you have made your life harder in order to make my life easier. Thank you for making us have fun when I'm tempted to work too much. This thesis is dedicated to you.

Abstract

In order for an earthquake to become a natural disaster, it needs to be significantly large, close to vulnerable populations or both. The largest earthquakes in the world occur in subduction zones, where cool, shallowly dipping fault planes enable brittle failure over a large area. However, these earthquakes often occur far away from major cities, reducing their impact. Similar, low angle fault planes can be found in continental fold and thrust belts, where sub-horizontal decollements offer large potential rupture areas. These seismic sources are often much closer to major urban centres than offshore subduction zone sources. It is therefore essential to understand the processes that control how strain is accommodated and released in such settings.

Much of our current understanding of the earthquake cycle comes from studying strike-slip faults. Can our knowledge of strike-slip faults be transferred over to dip-slip faults, and in particular, fold and thrust belts? Previous work has suggested that there may be significant differences between strike-slip and dip-slip settings, and therefore further study of the earthquake cycle in dip-slip environments is required. The recent launch of Sentinel-1, and the extensive Synthetic Aperture Radar (SAR) archive of the European Space Agency (ESA), offer an opportunity to obtain measurements of strain in dip-slip environments that can contribute to our understanding.

In this thesis, I use geodetic measurements to contribute to our understanding of the earthquake cycle. Enhanced surface deformation rates following earthquakes (so called postseismic deformation) show temporal and spatial variation. Such variation can be used to investigate the material properties of faults and the surrounding medium. I collate measurements of postseismic velocity following contintental earthquakes to examine the temporal evolution of strain following an earthquake over multiple timescales. The compilation show a simple relationship, with velocity inversely proportional to time since the earthquake. This relationship holds for all fault types, with no significant difference between dip-slip and strike-slip environments. Such lack of difference implies that, at least in terms of the temporal evolution of near field postseismic deformation, both environments behave similarly.

I compare these measurements with the predictions of various models that are routinely used to explain postseismic deformation. I find that the results are best explained using either rate-strengthening afterslip or power-law creep in a shear zone

with high stress exponent. Such a relationship indicates that fault zone processes dominate the near-field surface deformation field from hours after an earthquake to decades later. This implies that using such measurements to determine the strength of the bulk lithosphere should only be done with caution.

I then collate geodetic measurements from throughout the earthquake cycle in the Nepal Himalaya to constrain the geometry and frictional properties of the fault system. I use InSAR to measure postseismic deformation following the 2015 M_w 7.8 Gorkha earthquake and combine this with Global Navigation Satellite System (GNSS) displacements to infer the predominance of down-dip afterslip. I then combine these measurements with coseismic and interseismic geodetic data to determine fault geometries which are capable of simultaneously explaining all three data sets. Unfortunately, the geodetic data alone cannot determine the most appropriate geometry. It is therefore necessary to combine such measurements with other relevant data, along with the expertise to understand the uncertainties in each data set.

Such combined measurements ought to be understood using physically consistent models. I developed a mechanically coupled coseismic-postseismic inversion, based on rate and state friction. The model simultaneously inverts the coseismic and postseismic surface deformation field to determine the range of frictional properties and coseismic slip which can explain the data within uncertainties. I applied this model to the geodetic data compilation in Nepal and obtained a range of values for the rate-and-state 'a' parameter between $0.8 - 1.6 \times 10^{-3}$, depending on the geometry used.

Whilst the Nepal Himalaya is well instrumented, many continental collision zones suffer from a severe lack of data. The Sulaiman fold and thrust belt is one such region, with very sparse GNSS data, but significant seismicity. I apply InSAR to part of the Sulaiman fold and thrust belt near Sibi to examine the evolution of strain throughout the seismic cycle. I tie together observations from ERS, Envisat and Sentinel-1 to produce a time series of displacements over 25 years long which covers an earthquake which occurred in 1997. Using this time series, I investigate the contributions of different parts of the earthquake cycle to the development of topography. I find that postseismic deformation plays a clear role in the construction of short wavelength folds, and that the combination of coseismic and postseismic deformation can reproduce the topography over a variety of lengthscales.

The shape of the frontal section of the fold and thrust belt, including the gradient of the topography, is roughly reproduced in a single earthquake cycle. This suggests that fold and thrust belts can maintain their taper in a single earthquake cycle, rather than through earthquakes occurring at different points throughout the belt. I find that approximately 1000 earthquakes like the 1997 event, along with associated postseismic deformation, can reproduce the topography seen today to first order. Such a result may aid our use of topography as a long-term record of earthquake cycle deformation.

I finish by drawing these various findings together and commenting on common

themes. Afterslip plays an important role in the earthquake cycle, contributing to the surface deformation field in multiple locations, over multiple timescales, and generating topography. This afterslip can be explained using a rate-strengthening friction law with $a\sigma$ between 0.2 and 1.54 MPa. Combining this rate dependence with the static coefficient of friction determined from other methods, such as critical taper analysis, would enable a more complete picture of fault friction to be determined. Fault geometry in fold and thrust belts may control the size of potential ruptures, with junctions and changes in dip angle potentially arresting ruptures.

In order to fully determine the role of fault geometry and friction in controlling the earthquake cycle in dip-slip settings, I suggest a more thorough exploitation of the wealth of InSAR data which is now available. These data then need to be combined with measurements from other fields, and models produced which are consistent within the uncertainties of each data set. I suggest that measurements of topography and insights from structural geology may help with understanding the long term and short term processes governing earthquake patterns in an area. As both observations and models are developed, interdisciplinary teams may be able to better constrain the key controls on earthquake hazard in continental dip-slip settings.

Contents

List of Figures

List of Tables

Nomenclature

List of acronyms

ALOS	Advanced Land Observing Satellite
APS	Atmospheric Phase Screen
CMT	Centroid Moment Tensor
COMET	Centre for the Observation and Modelling of Earthquakes, Volcanoes and Tectonics
CS	Coseismic
DEM	Digital Elevation Model
DORIS	Delft Object-oriented Radar Interferometric Software
ECMWF	European Centre for Medium-Range Weather Forecasts
Envisat	Environmental satellite
ERA	ECMWF Re-Analysis
ERS	European Remote-sensing Satellite
ESA	European Space Agency
FRF	Flat Ramp Flat
GDP	Gross Domestic Product
GIA	Glacial Isostatic Adjustment
GIPSY-OASIS	GNSS-Inferred Positioning System and Orbit Analysis Simulation Software
GMT	Generic Mapping Tools
GNSS	Global Navigation Satellite System

GPS	Global Positioning System
GSRM	Global Strain Rate Model
InSAR	Interferometric Synthetic Aperture Radar
IS	Interseismic
JPL	Jet Propulsion Laboratory
LiCS	Looking Inside the Continents from Space
LOS	Line Of Sight
MCMC	Marcov Chain Monte Carlo
MERIS	Medium Resolution Imaging Spectrometer
MFT	Main Frontal Thrust
MHT	Main Himalayan Thrust
MODIS	Moderate Resolution Imaging Spectroradiometer
NERC	Natural Environment Research Council
PDF	Probability Density Function
PS	Persistent Scatterer
PS	Postseismic
PWV	Precipitable Water Vapour
ROI_PAC	Repeat Orbit Interferometry PACkage
SAR	Synthetic Aperture Radar
SBAS	Small Baseline Subset
SLC	Single Look Complex
SRTM	Shuttle Radar Topography Mission (DEM)
StaMPS	Stanford Method of Persistent Scatterers
TRAIN	Toolbox for Reducing Atmospheric InSAR Noise
UNAVCO	University NAVSTAR Consortium
USGS	United States Geological Survey

List of symbols

η	Viscosity	[Pa s]
μ	Shear Modulus	[Pa]
σ	Normal Stress	[Pa]
τ	Relaxation Time	[years]
a	Rate Dependence of Fault Friction	[-]
D	Screw Dislocation Locking Depth	[km]
D_c	Critical Slip Distance	[m]
M_w	Moment Magnitude	[-]
s	Screw Dislocation Slip Rate	[mm/yr]
t	Time	[years]
V	Velocity	[mm/yr]
x	Horizontal Distance	[km]

Chapter 1

Introduction

1.1 Motivation

1.1.1 Seismic Hazard

Earthquakes impact more people now than ever before, primarily due to population growth and urbanisation (*Bilham*, 2004, *Tucker*, 2004, *Jackson*, 2006). Figure 1.1 summarises population density, megacity locations and geodetic strain rates, highlighting the risk posed to people over the Alpine-Himalayan belt. Scientific research into earthquakes can inform civil protection agencies of the risks they need to account for (*Giardini et al.*, 1999) and lead to a greater understanding of how our planet works (*Bürgmann and Dresen*, 2008, *Wright et al.*, 2013, *Watts et al.*, 2013).

Destructive earthquakes occur on all types of fault (strike-slip, normal and thrust) and in a variety of settings. Strike-slip faults are capable of hosting a variety of earthquake sizes, with the largest recorded event being the M_w 8.6 Indian Ocean earthquake, which occurred on 11 April 2012 (*McGuire and Beroza*, 2012, *Pollitz et al.*, 2012). Despite the size of this event, the large distance between the event and the nearest population centres resulted in relatively few casualties. Large strike-slip earthquakes are also seen on the continents, with the 1905, M_w 8.4 Bolnay earthquake in Mongolia representing one of the largest known continental earthquakes (*Schlupp and Cisternas*, 2007). These continental earthquakes pose a potentially larger hazard, due to the much smaller distances between the seismic rupture and the nearest urban centres. Unfortunately, these continental earthquakes do not need to be particularly large to cause significant destruction, with some of the deadliest earthquakes in recent history being much smaller than those discussed above. Normal faults rarely produce earthquakes larger than M_w 7.0 (*Middleton et al.*, 2016). However, when large normal faulting earthquakes strike, they can be deadly. The 1908 M_w 7.1 Messina earthquake in Italy resulted in between 75,000 and 200,000 fatalities, making it the deadliest earthquake in recorded European history.

The largest earthquakes in the world occur in areas of convergence where one tec-

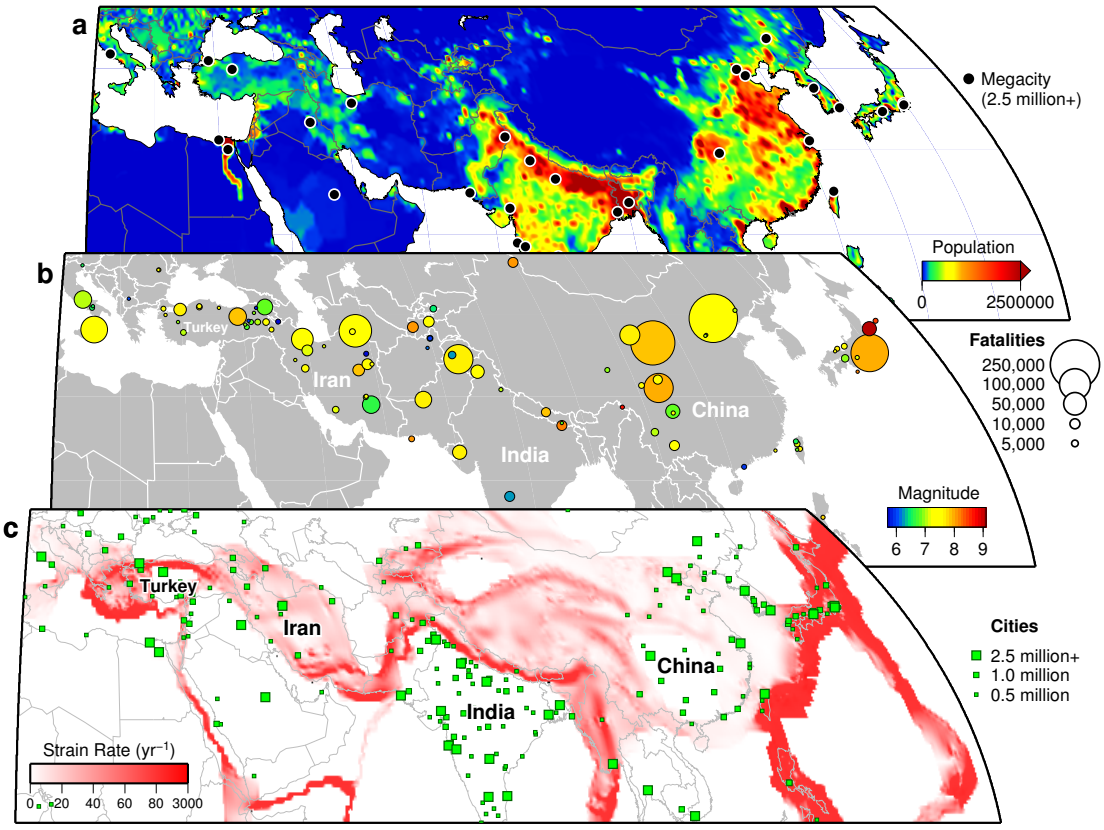

Figure 1.1: Maps of exposure to earthquake hazard across the Alpine-Himalayan belt. Reproduced with permission from *Elliott et al.* (2016a). a) Population count on a half-degree by half-degree grid for 2005. Megacities with populations over 2.5 million are marked by black circles. Data are the UN-adjusted population count from the Center for International Earth Science Information Network (CIESIN), Columbia University, United Nations Food and Agriculture Programme (FAO) and Centro Internacional de Agricultura Tropical (CIAT) (`http://sedac.ciesin.columbia.edu/gpw`). b) Locations of past earthquakes in the period 1900-2015 resulting in more than 1,000 fatalities are denoted by circles coloured by magnitude and scaled in size by the number of fatalities (source: USGS, `http://earthquake.usgs.gov/earthquakes/world/world_deaths.php`). c) Global Strain Rate Model (v2.1) showing the second invariant of the strain rate tensor (*Kreemer et al.*, 2014). Large cities are overlayed (green) and scaled by population size.

tonic plate is thrust beneath another in a subduction zone. Earthquake magnitudes greater than M_w 9.0 are possible in these settings due to the large potential rupture area allowed by the small angle at which these plates dip as they enter the Earths mantle. The low dip angle means that more of the fault plane is in the cooler, brittle regime which is capable of rupturing in earthquakes.

These low angle rupture planes are not only present in underwater subduction zones but are also commonly associated with areas of plate convergence on the continents. These regions are made up of belts of folded rocks and accompanying thrust faults, and as such are known as fold and thrust belts. Low angle faults known as decollements often underlie these fold and thrust belts and research has highlighted their potential to host large earthquakes (*Hubbard et al.*, 2015). The earthquake potential of these large rupture planes poses a significant seismic hazard to communities in the vicinity of these fold and thrust belts. The earthquake hazard is potentially higher than that from subduction zones since urban centres can and do exist closer to the earthquake source than is possible in subduction zone settings. Kathmandu in Nepal is one example of a megacity (more than two million inhabitants) placed directly on top of one of these fold and thrust belts. The fold and thrust belt was struck by a M_w 7.8 earthquake in 2015, resulting in nearly 9000 fatalities and economic damage equivalent to approximately 50% of Nepals GDP. Furthermore, larger earthquakes (M 8+) are known to have occurred here in the past (*Sapkota et al.*, 2013). Given the destructive nature of earthquakes on all three fault types, it is essential to better understand the hazards posed in different tectonic settings.

1.1.2 Fault Zone Characteristics

Strike-slip faults like the Denali fault (*Oglesby*, 2004, *Pollitz*, 2005, *Freed et al.*, 2006, *Biggs et al.*, 2009) and the San Andreas fault (*Barker*, 1976, *Langbein*, 2006, *Freed*, 2007) are the source of some of the largest continental earthquakes and have warranted significant study. Furthermore, modelling strike-slip faults is simpler due to the symmetry of the system, near-vertical fault planes and smaller gravitational effects (*Savage*, 1990, *Hetland*, 2005, *Yamasaki et al.*, 2014, *Caniven et al.*, 2015). Faults like the North Anatolian Fault in Turkey have been observed and modelled in significant detail. These major strike-slip faults accumulate interseismic strain slowly, over long intervals between earthquakes, in a narrow region focussed around the fault (*Wright et al.* (2013), *Vernant* (2015) and references therein). These features suggest a rheology with high viscosity. However immediately following an earthquake, rapid postseismic transients typically occur, which suggests a rheology with a low viscosity (*Barbot et al.*, 2008, *Ergintav et al.*, 2009, *Diao et al.*, 2010, *Cetin et al.*, 2012).

These competing observations require earthquake deformation models with complex single rheologies that have time-dependent (*Ryder et al.*, 2007) or stress-dependent (*Freed and Bürgmann*, 2004) viscosities; or a local weak zone model whereby the fault

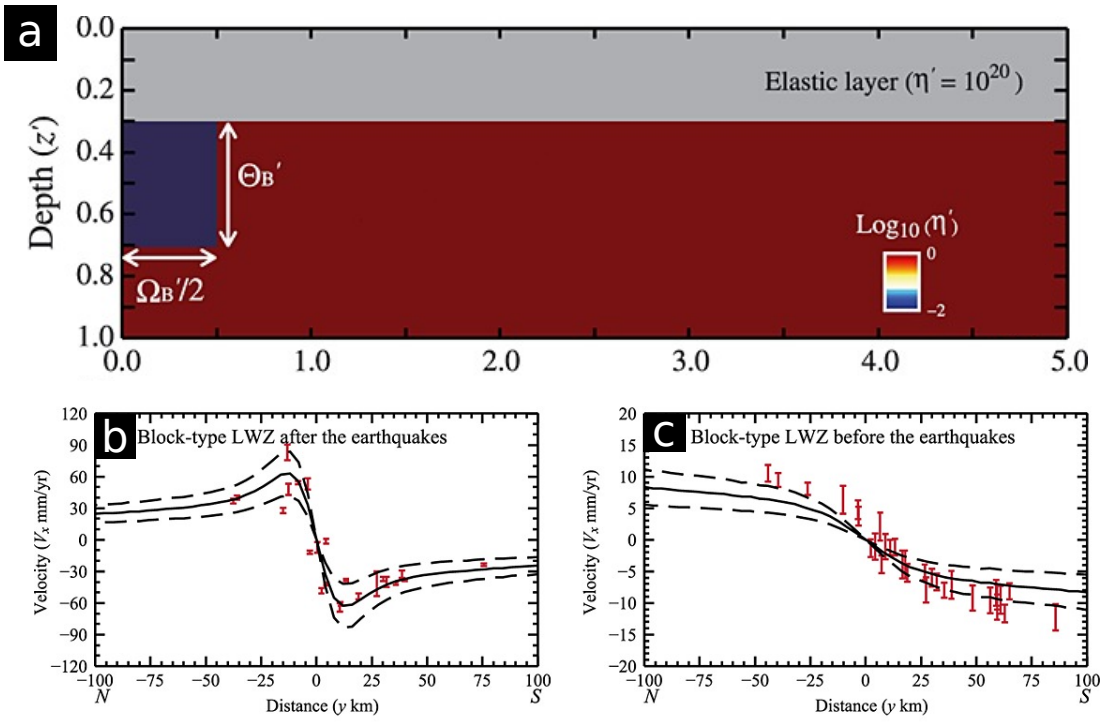

Figure 1.2: Model set-up and results for a weak zone embedded in a strong substrate; modified from *Yamasaki et al.* (2014). a) Model set-up showing a rectangular weak zone in blue (low viscosity) surrounded by a stronger substrate (high viscosity). b) Comparison between model displacements (solid line) and observations from postseismic GNSS data (red errorbars). c) Comparison between model displacements (solid line) and observations from interseismic GNSS data (red errorbars).

is surrounded by weaker material than the rest of the lithosphere (*Le Pourhiet et al.*, 2014). Figure 1.2 shows a weak zone set-up for the North Anatolian Fault, which can explain observations from both interseismic and postseismic GNSS data (*Yamasaki et al.*, 2014). These so called weak zones may be the result of grain size reduction, structural discontinuity or lithological change. Furthermore, observations of earthquake cycle deformation have been used to make inferences about the rheology of the whole lithosphere (*Bürgmann and Dresen*, 2008, *Wright et al.*, 2013, *Watts et al.*, 2013). If weak zones are present beneath major strike-slip faults then these observations only provide information on the rheology of the lithosphere in these laterally discontinuous weak zones.

The development of a weak zone may be related to fault maturity or age. Figure 1.3 shows that as faults accrue more displacement, the damage zone around them tends to increase (*Savage and Brodsky*, 2011, *Faulkner et al.*, 2011). The increasing thickness of such damage zones may in turn lead to the development of weak zones. On average, there are some differences in total fault displacement between the different fault types. Normal faults tend to have total displacements less than one kilometre, thrust faults can reach displacements on the order of tens of kilometres and strike-slip faults can

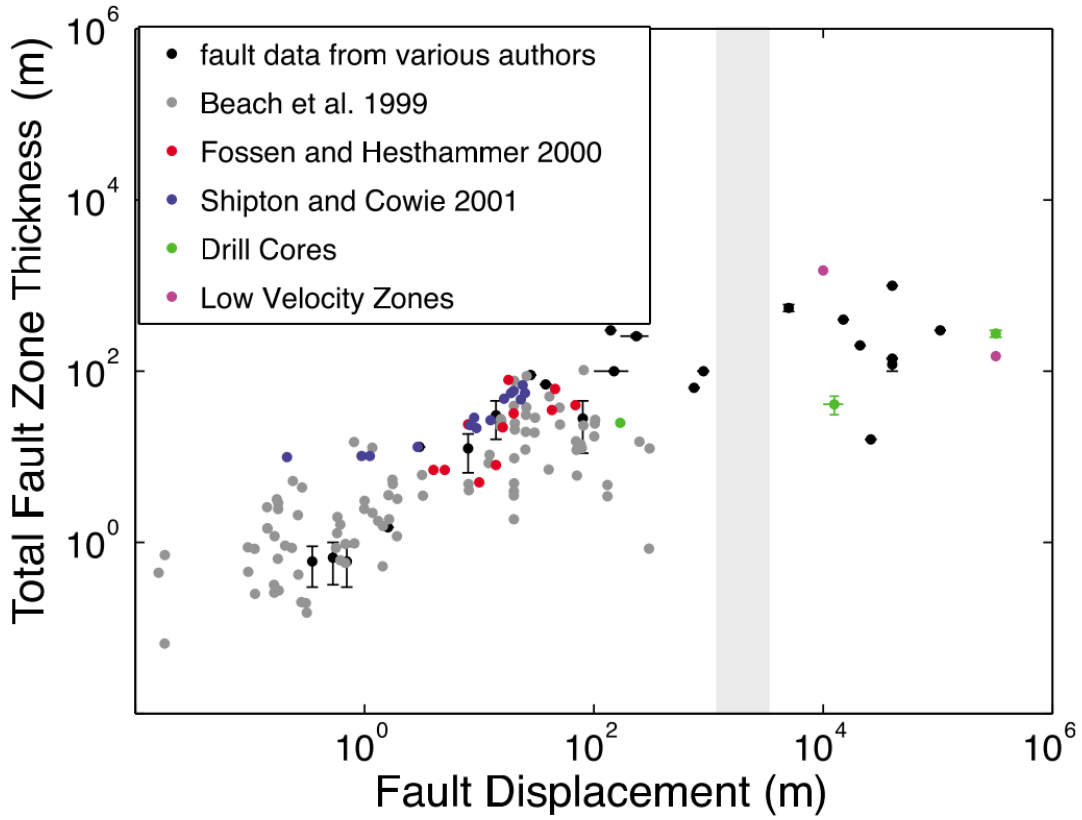

Figure 1.3: Scaling of fault zone thickness with displacement. Reproduced with permission from *Savage and Brodsky* (2011).

reach total displacements of hundreds of kilometres (*Kim and Sanderson*, 2005). This may mean that weak zones, as proposed for the North Anatolian Fault, may not exist in dip-slip settings.

Anderson (1905) recognised the basic mechanical differences between strike-slip, thrust and normal faults. Figure 1.4 shows a simple explanation of Andersonian fault mechanics. The orientation of the maximum and minimum stress directions vary for each kind of fault and suggest that these three kinds of faulting may behave differently. With this in mind, I will now outline some other observations and reasoning which could be used to suggest that fault type plays a significant role in determining how the earthquake cycle functions.

Continental dip-slip faults (i.e. thrust and normal faults) are asymmetrical about dipping fault planes and are more greatly influenced by gravitational effects than strike-slip faults. The geometry and mechanics of dip-slip faults means that, generally speaking, continental dip-slip faults cannot host as large earthquakes as continental strike-slip faults (*Stock and Smith*, 2000). This is because slip in dip-slip earthquakes is usually approximately parallel to the down-dip direction. Whilst dip-slip ruptures can and do propagate along-strike, rupture propagation is enhanced in the slip-parallel direction,

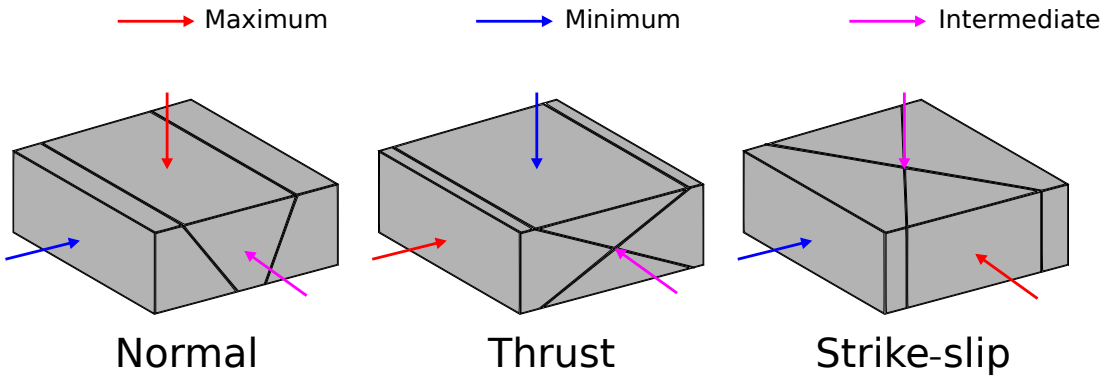

Figure 1.4: Mechanics of faulting based on *Anderson* (1905). Red, blue and magenta arrows correspond to the maximum, minimum and intermediate stress directions respectively.

i.e. down dip. However, the down-dip width of any fault is controlled by the thickness of the seismogenic layer and the dip of the fault. Many normal faults have relatively steep dips, restricting down-dip widths and therefore the size of ruptures (*Jackson and White*, 1989), and leading to segmentation along strike. This control on earthquake size is further supported by the scaling of normal fault scarps with down-dip widths (*Jackson and White*, 1989). However, some low angle dip-slip faults such as sub-horizontal decollements in fold and thrust belts, may enable large potential rupture areas (*Hubbard et al.*, 2015).

Furthermore, research has shown that fault type can play a significant role in controlling a number of earthquake phenomena such as fault friction (*Sibson*, 1974), earthquake stress drop (*Allmann and Shearer*, 2009), earthquake size distributions (*Schorlemmer et al.*, 2005), stress triggering of nearby earthquakes (*Wu et al.*, 2004), and radiated seismic energy (*Pérez-Campos and Beroza*, 2001). These differences suggest that the earthquake cycle at dip-slip faults may be different from that at strike-slip faults, and therefore further work may be required in order to transfer knowledge from strike-slip faults over to the realm of dip-slip faults.

1.1.3 Geodetic Data Availability

Geodetic data allow the study of ground deformation associated with earthquakes and faulting. A variety of techniques have been applied to the earthquake cycle, including triangulation, levelling and space geodetic techniques. Global Navigation Satellite System (GNSS) stations provide measurements of displacement at point localities around fault zones. These can be in the form of temporary stations which are installed during repeated field campaigns or permanent GNSS receivers which provide a time series of displacements. The amount of GNSS data has increased dramatically, as shown by the difference in the number of sites used in versions of the Global Strain Rate Model (GSRM) (*Kreemer et al.*, 2000, 2003, 2014): version 1.2 contained 4,281 sites, whereas version 2 contains 17,491. However, the installation and maintenance of such receivers

is not always possible due to inaccessibility, thus limiting the places which can be studied using GNSS alone. Furthermore, whilst GNSS can provide accurate position time series, it can only do so at point locations.

Remote sensing techniques using satellite imagery have vastly increased the data available to earthquake scientists (*Elliott et al.*, 2016a). A whole suite of satellites over the last 30 years (see Figure 1.5) have provided optical and radar imagery and enabled the production of digital elevation models and surface motion maps. All of this data has revolutionised the way that earthquakes and earthquake cycle deformation have been studied. Synthetic Aperture Radar (SAR) images can be used to produce maps of surface deformation over large areas of ground by interferometry (InSAR). These surface deformation maps (interferograms) have been used to study the sudden displacements in earthquakes (*Massonnet et al.*, 1993), providing powerful constraints on how the earthquake fault slipped at depth. InSAR can be used for studying the small displacements between earthquakes by constructing time series of images in order to reduce the effects of noise (*Hooper et al.*, 2012). The amount of SAR data available for producing surface deformation maps has also significantly increased, with the launch of new missions such as Sentinel-1, which produces over 10 TB of data every day (*Potin et al.*, 2017). Sentinel-1a and b can produce images over hundreds of kilometres wide with pixel resolution of 5 m by 20 m and a revisit time as small as six days in many tectonic regions. These data are open source, allowing anybody to access them and use them for free. These characteristics make Sentinel-1 ideally placed to study remote, inaccessible regions and increase the breadth of environments contributing to our understanding of the earthquake cycle.

1.2 InSAR Methods

Interferometric Synthetic Aperture Radar (InSAR) has now become a routine tool in the study of earth surface deformation. InSAR allows the production of surface deformation maps at centimetre to millimetre levels of accuracy, over regions on the order of hundreds of kilometres. These characteristics make InSAR an excellent tool for studying the different stages of the earthquake deformation cycle. Furthermore, spaceborne SAR enables the study of otherwise inaccessible regions and thus can provide data which would otherwise be impossible to attain with survey based geodesy such as GNSS or levelling. There are many excellent reviews of InSAR methods and applications, and I refer the reader to these for a full treatment (*Massonnet and Feigl*, 1998, *Rosen et al.*, 2000, *Bürgmann et al.*, 2000, *Hooper et al.*, 2012). Here, I will briefly outline the main stages in InSAR processing, the primary error sources and the techniques used in this thesis.

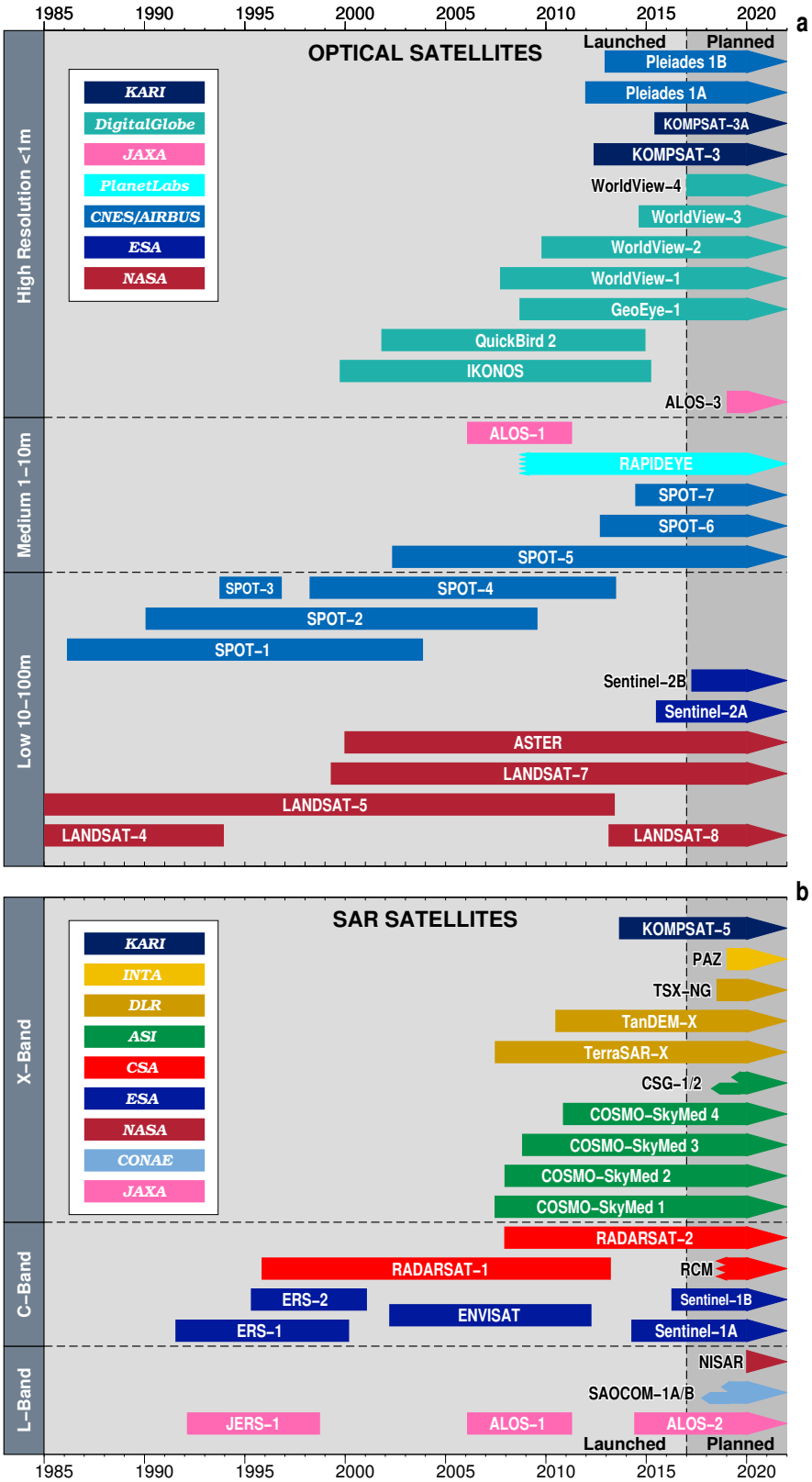

Figure 1.5: Timeline of select optical and SAR satellites used in tectonics research since 1985. Missions planned for the future are also included. Reproduced with permission from *Elliott et al.* (2016a).

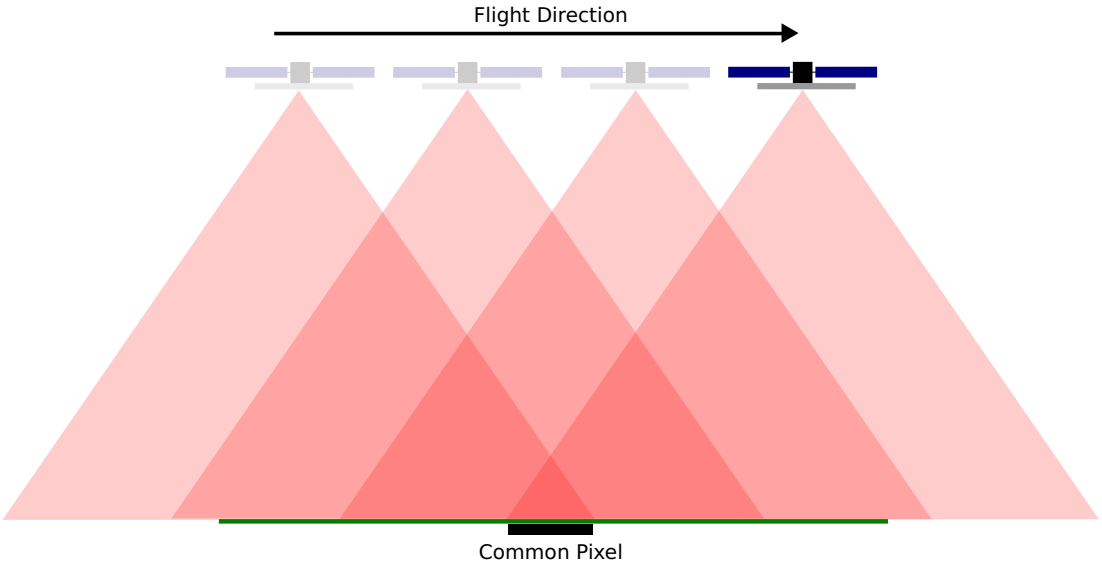

Figure 1.6: Schematic diagram illustrating the construction of a synthetic aperture by combining multiple returns from the same pixel.

1.2.1 Synthetic Aperture Radar (SAR)

The resolution of any radar satellite is inversely proportional to the size of the instrument aperture. Satellites orbiting thousands of kilometres above the Earth have a resolution on the order of tens of kilometres (*Massonnet and Feigl*, 1998). The resolution can be significantly improved by constructing a 'synthetic aperture' by combining multiple returns from the same ground point, in a similar way to common midpoint stacking in reflection seismology (see Figure 1.6). This process is known as focussing, and produces Single Look Complex images, with a complex number for each pixel defining the amplitude and phase of the signal. The amplitude of a pixel is affected by the angle of the reflecting surface, as well as its reflection characteristics. For example, steep slopes oriented perpendicular to the incident radar waves are highly reflective and appear brightly in radar amplitude images (Figure 1.7). In contrast, calm water bodies result in very little energy return to the satellite due to the angle of reflection with the surface (Figure 1.7). The phase of the returned signal depends on a number of factors and appears completely random.

1.2.2 SAR Interferometry (InSAR)

InSAR involves the combination of two SAR images to derive a map of phase differences, known as an interferogram. This can be achieved provided that the two SAR images are carefully coregistered, such that pixels in one image align with the same pixels in the other image. This coregistration is usually achieved through a combination of orbital information and amplitude image cross correlation. Advanced techniques such as spectral diversity are sometimes required in recent satellites such as Sentinel-1, to

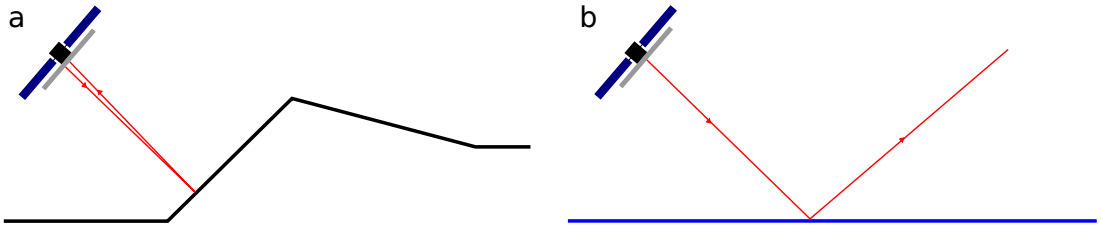

Figure 1.7: Two extreme examples for radar amplitude images. The left-hand image shows an example where the slope of the topography is perpendicular to the incident radar wave, resulting in a strong reflection back to the satellite. The right-hand image shows an example of radar waves incident on a calm water body, resulting in little reflection back to the satellite.

ensure that coregistration is accurate on a sub-pixel level (*Prats-Iraola et al.*, 2012, *Yague-Martinez et al.*, 2016). Whilst the phase in a single SAR image is random, the interference pattern produced by the difference between two phase images is not. Inteferograms consist of phase measurements between $-\pi$ and π. The total phase change between two images is the result of a number of processes:

$$\delta\phi_{total} = \delta\phi_{orbit} + \delta\phi_{topo} + \delta\phi_{atmo} + \delta\phi_{defo} + \delta\phi_{noise} \tag{1.1}$$

In order to apply InSAR to the study of earthquake cycle deformation, the $\delta\phi_{defo}$ term needs to be isolated, and all other terms removed, such that the total phase change is only the result of surface deformation. The first term to be removed is the phase change due to the different acquisition geometries. InSAR relies on satellites flying in reasonably consistent orbits, but unless these orbits are precisely the same, then a phase change is introduced between two images due to the different position of the satellite at each acquisition. The difference in position is related to the perpendicular baseline between the satellite acquisitions. This phase change can be very large, producing many cycles of phase change ('fringes') and masking all other signals. Fortunately, the majority of this signal can be removed using the orbital information of the satellite, firstly by assuming a flat earth with no topography. This process, known as 'flattening', handles the majority of the phase change due to differences in orbital geometry, although residual orbital errors sometimes remain.

Figure 1.8 shows the result of the flattening procedure in the top panel. The remaining fringes are associated with topography, which is ignored in the flattening correction. In order to remove these topography related fringes, two approaches can be used. Firstly, a second interferogram with a different perpendicular baseline can be used to estimate the topographic contribution (*Gabriel et al.*, 1989). A second alternative is to use a Digital Elevation Model (DEM) to estimate the topographic phase and remove it from the interferogram. This second approach is now commonly used due to global DEM datasets such as the Shuttle Radar Topographic Mission (SRTM) (*Farr et al.*, 2007), and this is used in the example in Figure 1.8.

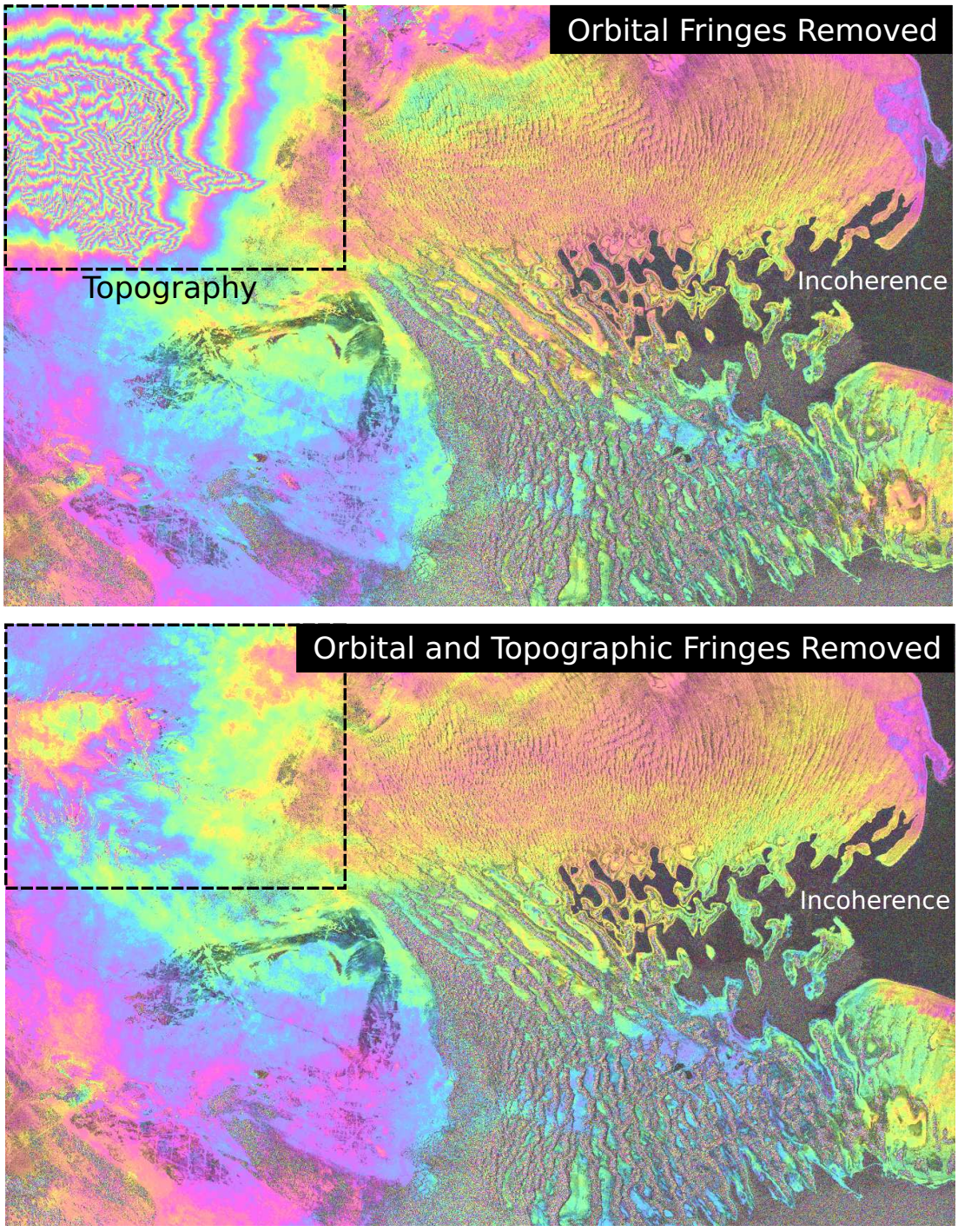

Figure 1.8: Examples of an interferogram with various features discussed in the main text. Note that these images are in radar coordinates, not geographical coordinates. Top image has been flattened, but fringes due to unaccounted topography still remain. Bottom image has had these fringes removed using a DEM.

Once the topographic fringes have been removed, the interferogram still contains a number of signals we need to remove or minimise. Decorrelation noise ($\delta\phi_{noise}$) is random noise introduced to an interferogram due to the scattering properties of a pixel changing through time. The phase of any pixel in a SAR image is the sum of the phase returned by all scatterers within that pixel on the ground. If the nature of the scatterers within a pixel remains relatively stable through time, then the returned phase values remain consistent through time and small differences due to signals of interest can be observed. However, if the scattering properties of a pixel, or the viewing geometry of the satellite change, then the returned phase is meaningless compared to the phase of the previous SAR image. For example, it is impossible to use InSAR over the oceans because the scattering properties of the ocean surface change randomly all the time, meaning that the returned phase values also randomly change. In contrast, InSAR is well suited to studying arid environments where the surface scattering properties change very little between satellite acquisitions. Figure 1.8 shows the difference in the signal returned in these two environments. The smoothly varying, bright colours over land on the left of the images show a consistent phase return over arid western Turkmenistan. The noisy, darker pixels to the right of the images show the random phase return over the Caspian Sea.

A number of approaches can be taken to reduce the impact of decorrelation noise. Firstly, noisy pixels can be masked out by calculating the 'coherence' of an interferogram. Coherence is a measure of how similar the phase of a pixel is to other pixels nearby and ranges between 0 (completely incoherent) and 1 (perfect coherence). The coherence for any pixel can be calculated using a boxcar approach, using all pixels within a certain window around the pixel of interest (*Touzi et al.*, 1999). Alternatively, the coherence can be calculated using more sophisticated methods which only compare the phase of a pixel with those of nearby pixels with similar scattering properties, known as siblings (*Spaans and Hooper*, 2016). Whichever approach is used, a coherence threshold can then be applied where pixels with a coherence below such a threshold are ignored in subsequent processing and analysis.

In addition to simple masking approaches, time series methods have been developed for InSAR which help to minimise the impact of decorrelation noise. Two broad categories of time series algorithms have been developed: **S**mall **BA**seline **S**ubset (SBAS) and **P**ersistent **S**catterer (PS). SBAS techniques construct a network of connected interferograms with small temporal and perpendicular baselines (*Berardino et al.*, 2002, *Hooper*, 2008). Smaller temporal baselines (times between satellite acquisitions) reduce the likelihood of significant change in scatter properties on the ground. Smaller perpendicular baselines reduce the differences in viewing geometry between the two acquisitions. Selecting interferograms with small baselines therefore selects only those interferograms that are likely to have maximum coherence. Persistent scatterer techniques identify pixels that show phase stability through time (*Ferretti et al.*, 2001,

Hooper et al., 2004). These pixels are often dominated by a particular stable, strong scatterer, such as the corner of a building and therefore suffer from very little noise due to surface properties changing over time. These time series approaches are time consuming and therefore inappropriate for providing rapid results following an event such as an earthquake. However, the methods outlined above are useful for studying the long term activity over fault zones and at volcanoes, where signals are typically much smaller than those seen in volcanic crises and earthquakes.

1.2.3 Atmospheric Noise

Time series methods can be used to not only reduce the impact of random, decorrelation noise, but also to reduce the impact of atmospheric noise. SAR signals propagate through the atmosphere and are delayed by varying degrees depending on the properties of the atmosphere at the time of acquisition. When two SAR images (delayed by different amounts) are combined to form an interferogram, the delay difference is manifest as atmospheric noise in the interferogram. Figure 1.9 shows an example InSAR time series produced using the time series software package StaMPS (Stanford Method for Persistent Scatterers, *Hooper* (2008)). The top row shows the raw phase values for persistent scatterers identified by the algorithm, referenced to the first image acquisition. The raw phase on certain dates shows very strong long wavelength signals (e.g. 20031025), which could be long wavelength atmosphere or due to orbital errors. These signals can be effectively removed by fitting a bilinear phase ramp to the image (deramping), as shown in the second row of Figure 1.9.

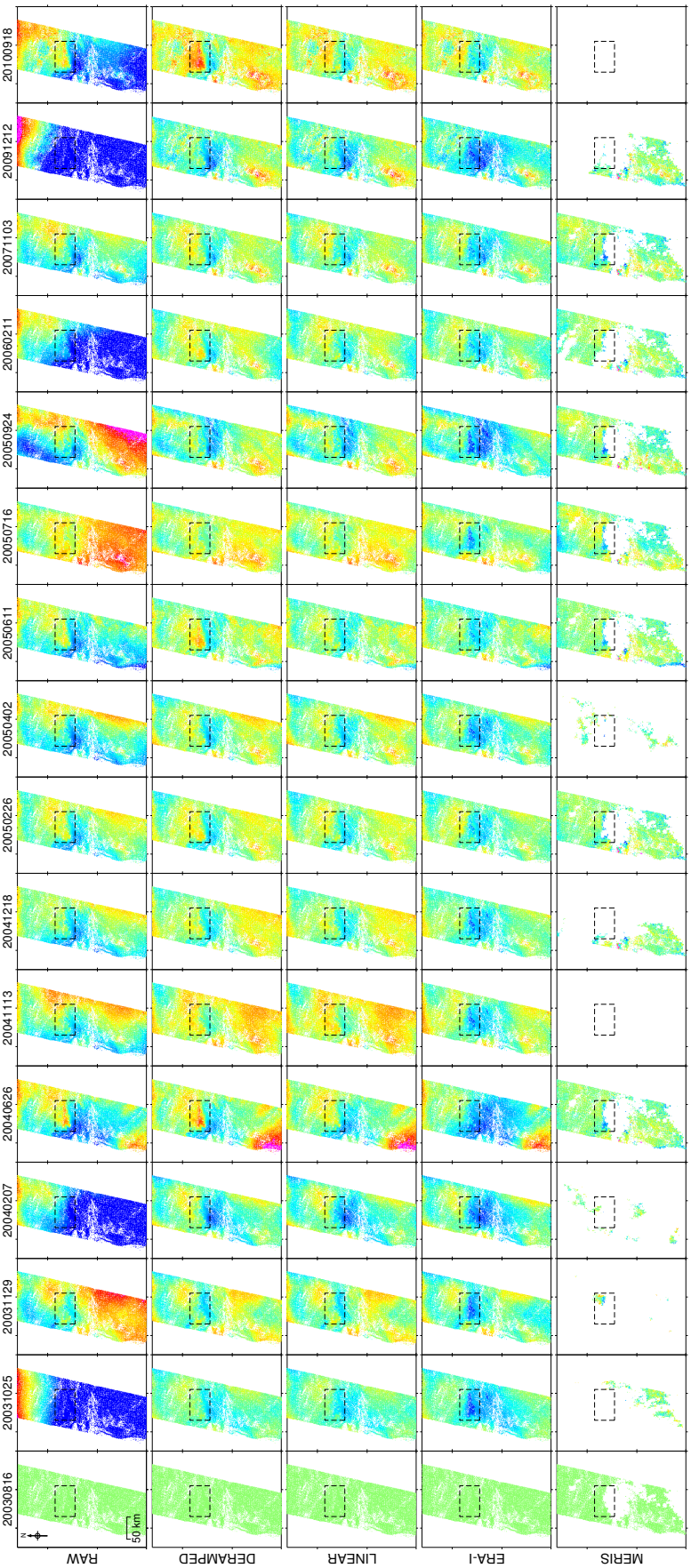

Figure 1.9: Example of an InSAR time series with various atmospheric corrections applied. Acquisition dates are along the top of the figure for each column of images. Each row corresponds to a different set of applied corrections.

The remaining signals seen in the deramped data are either deformation signals or shorter wavelength atmospheric signals. The region around the Caspian sea is known to have significant spatial and temporal variation in tropospheric delays (*Walters et al.*, 2013). The bottom three rows of Figure 1.9 show different methods for mitigating these tropospheric delays, implemented within the Toolbox for Reducing Atmospheric InSAR Noise (TRAIN, *Bekaert et al.* (2015a)). The first approach is to estimate the correlation between height and phase delay. SAR signals have to traverse more of the stratified atmosphere when reflecting from points at lower elevation, thus producing a relationship between atmospheric delay and scatterer height. This relationship is often seen to be approximately linear and can therefore be estimated and removed from each interferogram (*Elliott et al.*, 2008). This technique cannot remove atmospheric variation that is not associated with changes in topography (e.g. turbulent atmospheric delays) and must be used with caution in regions where deformation is also expected to be correlated with topography (e.g. many actively deforming mountain belts or volcanoes (*Hamlyn et al.*, 2018)). Despite these limitations, the method is easy to implement and can effectively remove significant delays in some regions. The third row on Figure 1.9 shows the results of removing both a ramp and an estimate of the topographically correlated atmosphere. The differences between these results and those in row two are relatively small, but can be seen in areas of high topography (dashed box). Other empirical methods can be used to estimate the atmosphere, such as the spatially variable power-law approach (*Bekaert et al.*, 2015b).

An alternative approach is to bring in auxiliary data to estimate the atmospheric delay. Weather models can be used to extract meteorological parameters for each image acquisition time and derive an atmospheric delay map for each interferogram (*Jolivet et al.*, 2011). One such model which is routinely used is the ERA-Interim reanalysis product, which is supplied on a global grid at 0.75 degree spacing. Row four in Figure 1.9 shows interferograms deramped and corrected using the results of these weather models. The results appear similar to the linear correction, largely because the ERA-Interim model is particularly effective at correcting topographically-correlated atmosphere. However, using weather models also allows for the correction of long wavelength (on the order of the grid spacing i.e. 0.75 degrees or approximately 80 km) atmospheric signals which are not correlated with topography (e.g. 20041113). The method cannot account for shorter wavelength signals though and can sometimes increase the atmospheric noise in places if the weather model (or the interpolation) is incorrect. For example, the high topography in the dashed box appears to have been over corrected in many interferograms.

Spatial interpolation can be avoided by using high resolution spectrometer data to obtain the water content of the atmosphere. Spectrometers such as the Moderate Resolution Imaging Spectroradiometer (MODIS) on board the Terra and Aqua satellites and the Medium Resolution Imaging Spectrometer (MERIS) on board Envisat provide

measurements of precipitable water vapour (PWV) at a similar resolution to InSAR, thereby avoiding many of the problems associated with spatial interpolation. MERIS offers the additional benefit of acquiring data at the same time as SAR acquisitions for day-time SAR acquisitions by Envisat (*Li et al.*, 2006, *Walters et al.*, 2013), thereby avoiding interpolation in time as well as space. The bottom row in Figure 1.9 shows deramped interferograms corrected using MERIS to remove the wet/turbulent component of the atmosphere and ERA-Interim to remove the dry/hydrostatic component. The first thing to note are the significant data gaps due to cloud cover. Some dates have no cloud-free MERIS data, whilst others have only a tiny fraction of the image cloud-free. This limitation is the primary disadvantage of spectrometer based methods and significantly limits their global use. In cloud-free areas, the spectrometer is able to remove the vast majority of the atmospheric signal, and is generally considered to give the best representation of the atmosphere in cloud-free areas (*Bekaert et al.*, 2015a). The largest signals remaining in the interferograms are those on the edges of areas of missing data, and are likely due to an inadequate cloud mask supplied by the MERIS product.

Other auxiliary data can be used to correct interferograms, such as GNSS data and meteorological radar data. GNSS relies on the transmission of radio waves through the atmosphere in an analogous way to InSAR. As such, these transmissions are delayed by the atmosphere in a similar way and can be used to estimate these delays at specific locations in an interferogram (*Li et al.*, 2003, *Yu et al.*, 2017). These point delay measurements can then be interpolated to provide an estimate of atmospheric delay over the entire interferogram. GNSS based methods are unaffected by cloud cover and offer measurements of the actual state of their immediate, local atmosphere, but are only applicable in regions with a reasonable density of continuous GNSS stations. Meteorological radars are used to determine the location of precipitation by measuring reflections from droplets in the atmosphere. These measurements are obtained on a continuous basis over a large area surrounding each radar station and therefore offer an interesting alternative to GNSS measurements. *Hanssen et al.* (1999) showed a reasonable correlation between the locations of rainfall events over the Netherlands and the locations of large delays in interferograms covering the same period. *Kinoshita et al.* (2013) observed a similar correlation for a heavy rainfall event over Japan in 2008. Preliminary investigations of the potential for using weather radar to correct interferograms has shown some potential (*Jackson*, 2017), but significant limitations remain. Meteorological radar measure the location of precipitation but offer no information on the precipitable water vapour in the atmosphere, which is the most significant component of the wet delay in an interferogram. Furthermore, these methods would only be applicable in locations within range of a meteorological radar.

An alternative approach to those outlined above is to use the properties of the InSAR time series itself to estimate the atmospheric contribution to each interferogram.

The atmosphere is expected to be largely uncorrelated in time but highly correlated in space (*Ferretti et al.*, 2000, 2001), allowing us to construct a combination of temporal and spatial filters to isolate an estimate of the atmosphere. The combination of a high-pass filter in time and a low-pass filter in space can provide an estimate of the atmospheric phase screen (APS) and is commonly referred to as an APS filter. These filters rely on certain assumptions about the time series which are likely to be invalid in certain circumstances. For example, an earthquake in the time series would produce a spatially correlated jump in the displacement time series and thus be partly interpreted as atmosphere. On the other hand, seasonal variations in atmosphere are not accounted for by the high-pass temporal filter and could introduce errors in deformation estimates.

Various noise terms can also be reduced by inverting the time series for a linear surface deformation rate. This process is analogous to stacking a number of interferograms and is expected to reinforce consistent signals and reduce random noise. Linear velocity maps are shown for each of the InSAR time series discussed above in Figure 1.10. The errors on these velocity maps can be obtained via bootstrapping, where a random selection of images are used in each bootstrap realisation and the best linear velocity obtained for that set of images. Similar features can be seen in the lower three velocity maps, derived from atmospherically corrected InSAR data. In particular, a region of subsidence is seen in the south of the velocity maps and is likely the result of oil field exploitation or deformation associated with mud volcanoes visible in satellite imagery.

1.3 The Earthquake Cycle

InSAR, along with other geodetic techniques, enables us to measure surface deformation associated with the earthquake cycle. *Reid* (1910) first suggested that an earthquake can be considered as a release of stored elastic energy after studying deformation data from the 1906 San Francisco earthquake. In the elastic rebound model, faults are locked between earthquakes, accumulating elastic energy, which is then released suddenly in an earthquake. These different periods of strain accumulation and release have been termed the interseismic and coseismic stages of the earthquake cycle respectively. The simple picture of strain accumulation between earthquakes and release in earthquakes is complicated by other forms of fault motion identified over the last century. Enhanced strain rates following earthquakes were identified from the 1960s onwards using geodetic surveys (*Smith and Wyss*, 1968, *Kanamori*, 1973, *Savage and Church*, 1974, *Thatcher*, 1975, *Reilinger*, 1984). Since then, observations of so-called postseismic deformation have become commonplace, with most moderate to large earthquakes being followed by a period of enhanced strain (*Wright et al.*, 2013). Furthermore, aseismic slip on faults has been observed as near-continuous creep (*Titus et al.*, 2006), distinct creep events (*Bilham et al.*, 2016) and slow-slip events (*Beroza and Ide*, 2011). The earthquake

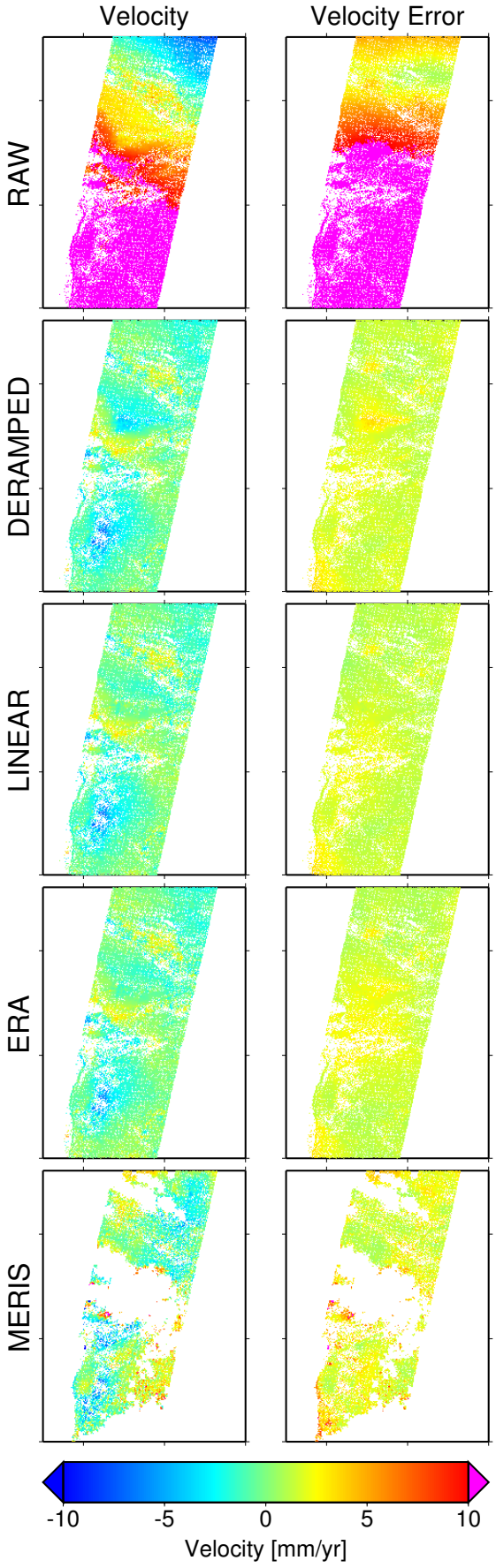

Figure 1.10: Examples of the velocity maps produced by time series inversion of each of the data sets shown in Figure 1.9. Note that the MERIS velocity map does not include data from dates mostly covered by cloud.

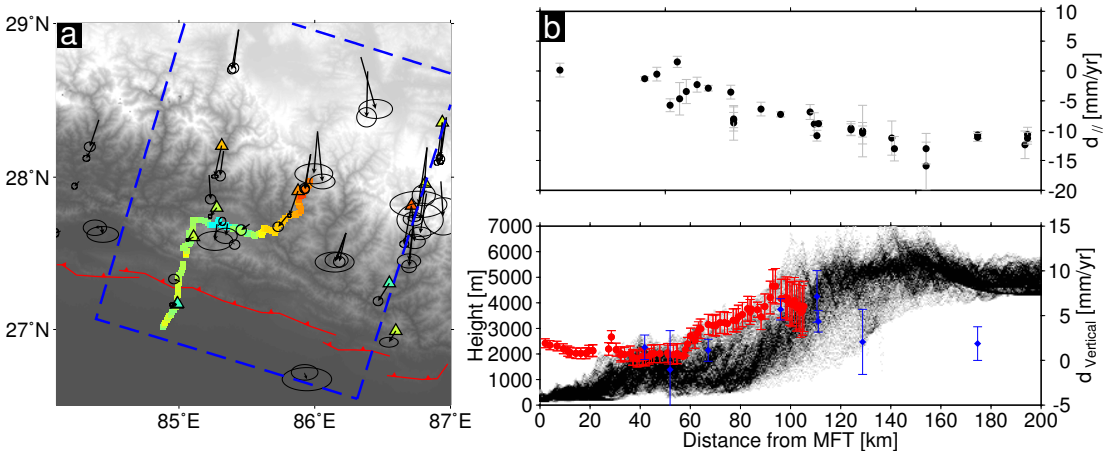

Figure 1.11: Example of interseismic deformation observed in the Nepalese Himalaya a) Map view. Red saw-tooth line is the Main Frontal Thrust (MFT) surface outcrop. Arrows are GNSS velocities from the Global Strain Rate Model (*Kreemer et al.*, 2014). Coloured triangles show vertical GNSS velocities from *Ader et al.* (2012). Coloured squares are levelling data from (*Jackson and Bilham*, 1994). Blue rectangle shows extent of swath profile. b) Comparison between horizontal and vertical deformation rates and topography. Top panel shows profile parallel GNSS velocities. Lower panel shows vertical velocities from levelling (red) and GNSS (blue), compared with topography (black).

cycle therefore consists of a number of different phenomena and varies in both space and time. Despite these complications, it is possible to make some generalisations about the three main stages of the earthquake cycle. In this section, I will discuss the general features of interseismic, coseismic and postseismic deformation with particular reference to dip-slip faulting examples.

1.3.1 Interseismic Deformation

Measurements

Continental thrust faults exhibit a range of styles. They can be large, laterally continuous faults (e.g. Main Himalayan Thrust; Longitudinal Valley Fault, Taiwan) where a large portion of the regional convergence is accommodated on a single fault. These large single megathrusts tend to have high slip rates and can be identified using geodesy (*Peyret et al.*, 2011, *Ader et al.*, 2012, *Cheloni et al.*, 2014). Alternatively, thrust faults can be small faults within fold-and-thrust belts (e.g. Zagros, Iran) where convergence is more distributed and is measured over the compressional region (*Tatar et al.*, 2002). Normal faulting tends to occur within systems of graben where deformation is spread over a number of smaller faults (e.g. Gulf of Corinth, Greece; Basin and Range, USA). Extension rates over these fault systems have been measured using geodesy (*Briole et al.*, 2000, *Thatcher*, 1999). However, there are some examples of measured extension rates being assigned to an individual, large normal fault in the region (*Chang et al.*, 2006, *Hreinsdottir and Bennett*, 2009).

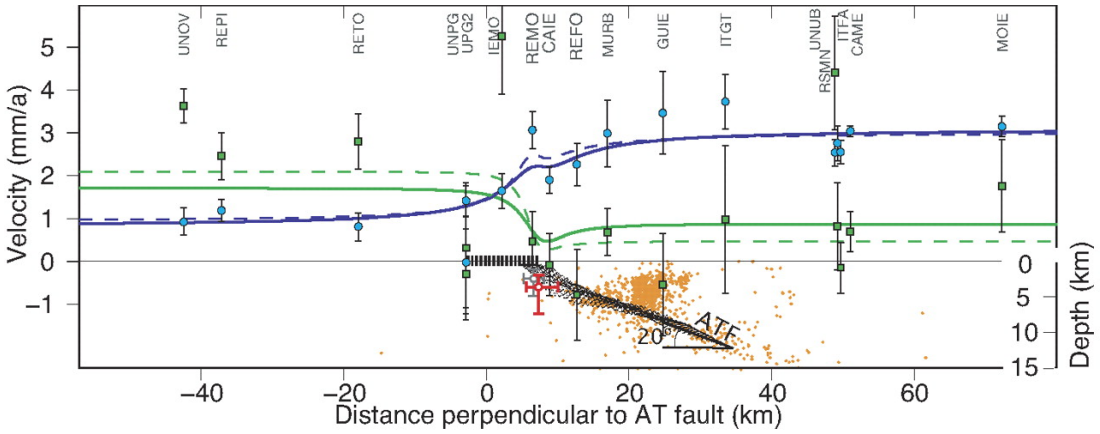

Figure 1.12: Example of interseismic deformation from the Alto Tiberina normal fault (ATF), Italy. Reproduced with permission from *Hreinsdottir and Bennett* (2009). Horizontal velocities perpendicular to the strike of the ATF are shown as blue dots, whilst vertical velocities are green squares (both with error bars corresponding to 95% confidence intervals). Solid and dashed blue and green lines are model fits to the data using an elastic dislocation model.

Two examples of interseismic deformation are shown in Figures 1.11 and 1.12. The first example is from the Nepalese Himalaya and shows the convergence between India and Eurasia. All geodetic measurements are with respect to stable India and have been collated from *Jackson and Bilham* (1994), *Ader et al.* (2012) and *Kreemer et al.* (2014). Several key features of interseismic deformation over a major continental thrust fault can be seen. Firstly, the orogen perpendicular horizontal velocities gradually increase, from approximately 0 near the Main Frontal Thrust (MFT) to almost 15 mm/yr on the Tibetan plateau, 160 km away from the MFT surface outcrop. Secondly, interseismic vertical velocities reach their maximum at almost 10 mm/yr approximately 100 km away from the MFT. This distance coincides with the inflection point in the interseismic horizontal velocities. These features, combined with estimates of geological shortening rates (*Stevens and Avouac*, 2015), indicate that elastic energy is being stored. In other words, the faults in the region are locked and the interseismic deformation observed is mostly recoverable rather than permanent. Full details of these data and the tectonics of the region are described in chapter 3. The second example shows interseismic deformation associated with the Alto Tiberina normal fault (ATF) in Italy (*Hreinsdottir and Bennett*, 2009). As in Nepal, both the horizontal and vertical velocity field recorded by GNSS are affected by elastic strain accumulation on the ATF. However, the vertical velocities are in the opposite sense of motion to those seen in a thrust faulting setting and the wavelength and amplitude of the deformation is smaller, due to the lower slip rates and shallower locking depth.

Models

For strike-slip faults, interseismic deformation is usually modelled using a screw-dislocation in an elastic half space (*Savage and Burford*, 1973, *Vernant*, 2015). This simple model, using an infinitely long fault (dislocation), predicts that fault parallel surface velocities should be a function of perpendicular distance (x) from the fault given by:

$$v = \frac{s}{\pi} \arctan \frac{x}{D} \tag{1.2}$$

where s is the slip rate on the fault at depths below the locking depth, D. Dip-slip faults are more complicated in terms of their geometry and cannot be modelled as vertical, infinitely long faults. Dislocation models are still used to estimate fault slip rates at thrust faults (*Shui-Beih et al.*, 1990, *Vergne et al.*, 2001, *Hsu et al.*, 2003, *Elliott et al.*, 2016b), in which case, the dislocation extends over a great distance in the fault-perpendicular direction, away from the fault locking line. Dip-slip faults are sometimes modelled in the interseismic period using backslip calculations (*Savage*, 1983). In these models, the surface deformation field is explained by the combination of two processes. Firstly, the surface deformation produced by the whole fault freely sliding at the overall convergence rate is calculated. Secondly, the deformation expected from motion in the opposite sense to the convergence direction is calculated for the locked portion of the fault. The summation of these two deformation fields results in the deformation field expected from free sliding at depth but not in the locked region. This approach allows for the degree of locking to vary spatially over the fault, and therefore enable variable interseismic strain accumulation (e.g *Perfettini et al.*, 2010, *Ader et al.*, 2012, *Stevens and Avouac*, 2015).

1.3.2 Coseismic Deformation

Measurements

Strain accumulated in the interseismic period needs to be released, either seismically or aseismically. Seismic release of strain in earthquakes is often investigated for moderate/large ($M_w > 6$) dip-slip earthquakes. The potential size of a dip-slip faulting earthquake depends on the available rupture area. Generally speaking, earthquakes are restricted to cool, brittle crust since other deformation mechanisms dominate at higher temperatures (*Bürgmann and Dresen*, 2008). Where normal faulting occurs in regions of extended, thinned crust, the seismogenic thickness is smaller, leading to generally smaller earthquakes. The thickness of the seismogenic layer appears to not only control the depth extent of faulting, but also along strike segmentation (*Jackson and White*, 1989). Conversely, where the crust is thicker, such as at the southern end of the East African Rift, larger normal faulting earthquakes are possible (*Ambraseys*, 1991, *Hayward and Ebinger*, 1996). Shallowly dipping faults such as fold and thrust

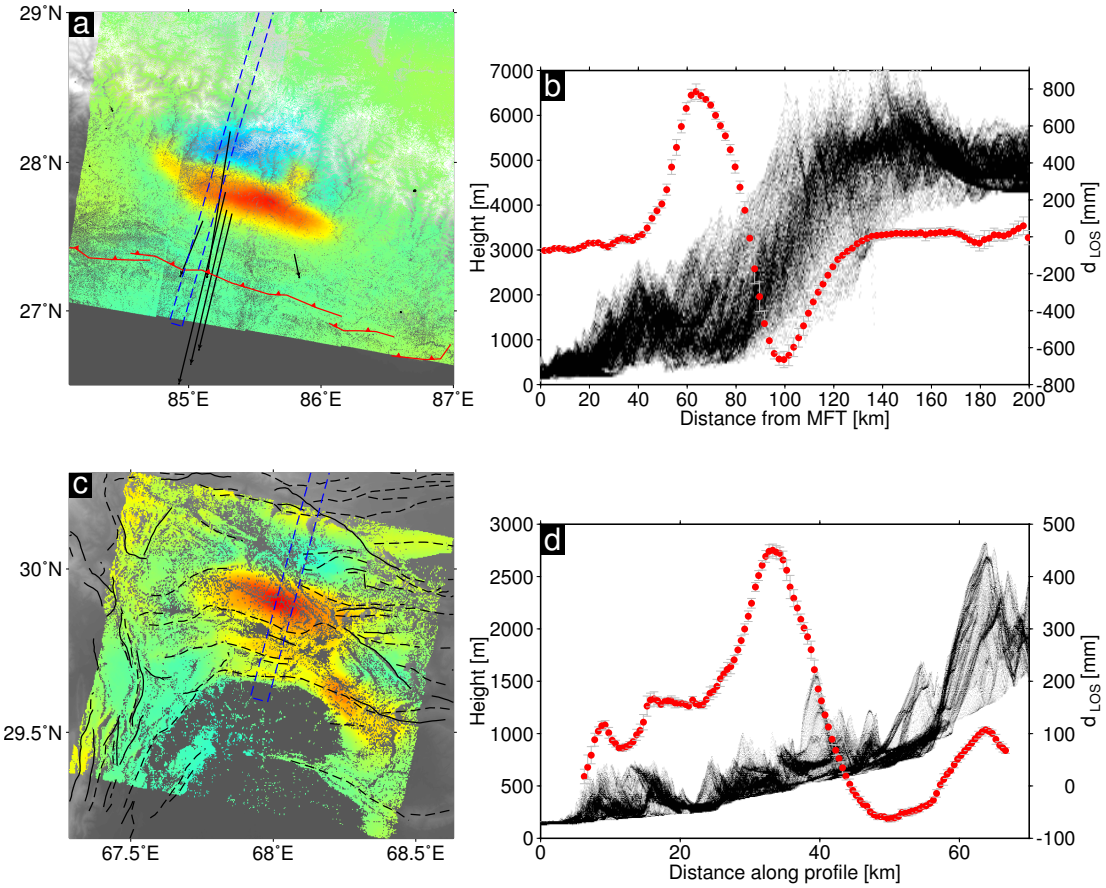

Figure 1.13: Examples of coseismic deformation observed in two regions of thrust faulting. a) Map of the Nepalese Himalaya overlaid with deformation measurements from the 2015 M_w7.8 Gorkha earthquake. Arrows are GNSS displacements from the earthquake (*Galetzka et al.*, 2015). InSAR data are one of many ALOS interferograms available for the earthquake (*Lindsey et al.*, 2015). Blue rectangle shows extent of swath profile. b) Comparison between coseismic deformation and topography. c) Map of a part of the Sulaiman fold and thrust belt near Sibi, Pakistan with an ERS interferogram spanning the 1997 M_w7.1 Sibi earthquake overlaid. Black solid lines are faults and black dashed lines are anticline fold axes (*Nissen et al.*, 2016). Blue dashed box shows location of swath profile. d) LOS displacements compared with topography.

belt decollements allow a much larger rupture area to exist over the seismogenic depth range (*Hubbard et al.*, 2015). Furthermore, large earthquakes are possible through multiple fault segments rupturing at once (*Biasi and Wesnousky*, 2016, *Nissen et al.*, 2016).

Examples of coseismic deformation for two regions are shown in Figure 1.13. The first example comes from the 2015 M_w 7.8 Gorkha earthquake in the Nepal Himalaya, allowing comparison with the interseismic data in 1.11. The size of the deformation signal in this earthquake is orders of magnitude greater than those seen in the interseismic deformation example. This observation, along with the fact that the peak coseismic uplift signal is south of the peak interseismic uplift signal suggests the earthquake represents the release of accumulated elastic strain energy. The Gorkha earthquake shows

a subsidence signal of similar magnitude to the uplift signal, indicative of a shallowly dipping fault. The second example is from the 1997 M_w 7.1 Sibi (Pakistan) earthquake. In contrast with the Gorkha example, the subsidence signal in the Sibi earthquake is much smaller than the main uplift signal, suggesting a more steeply dipping fault plane. The earthquakes differ in the magnitude and extent of deformation as well, with the larger Gorkha event causing a higher amplitude, longer wavelength and greater along-strike surface deformation signal. Finally, the Sibi interferogram shows secondary peaks in surface deformation south of the main uplift signal. These peaks are likely to be caused by postseismic deformation contaminating the ERS interferogram (see chapter 4).

Models

Coseismic deformation is usually modelled as an elastic dislocation (*Okada*, 1985). Determining the best-fit fault geometry is a non-linear problem and is usually found by using uniform slip over a rectangular fault plane. Once the fault plane is determined, it can be split in to many smaller patches and the distribution of slip solved for (*Wald et al.*, 1996, *Koketsu et al.*, 2004, *Elliott et al.*, 2010, *Walker et al.*, 2013). When splitting the fault plane in to many smaller patches, the problem is usually under determined and certain assumptions are required to provide extra constraints. These assumptions include that slip is smooth in space (usually implemented via Laplacian smoothing) or that slip is self-similar in an analogous way to fault surfaces (*Amey et al.*, 2018). Solutions for triangular dislocations have enabled the construction of more complicated fault geometries (*Meade*, 2007, *Nikkhoo and Walter*, 2015) in slip inversions and the use of Bayesian methods have allowed for the generation of the probability distributions for slip on each sub-fault (*Fukuda and Johnson*, 2008, *Amey et al.*, 2018).

1.3.3 Postseismic Deformation

Measurements

Accelerated surface deformation rates have been observed following a number of earthquakes (*Wright et al.*, 2013). GNSS stations are routinely used to study these enhanced deformation rates, and are particularly effective at examining the temporal evolution of the displacements. The displacement time series often show a logarithmic displacement history where the rate of surface deformation decreases over time (*Ingleby and Wright*, 2017). However, the shape of the postseismic time series varies spatially: some GNSS time series are better fit using logarithmic functions whereas others are better fit using exponential decay functions (*Rollins et al.*, 2015). The timescale of this transient deformation appears to vary, but postseismic deformation has been observed over decades (*Gourmelen and Amelung*, 2005, *Copley*, 2014, *Huang et al.*, 2016, *Zhou et al.*, 2018) and possibly centuries (*Calais et al.*, 2002).

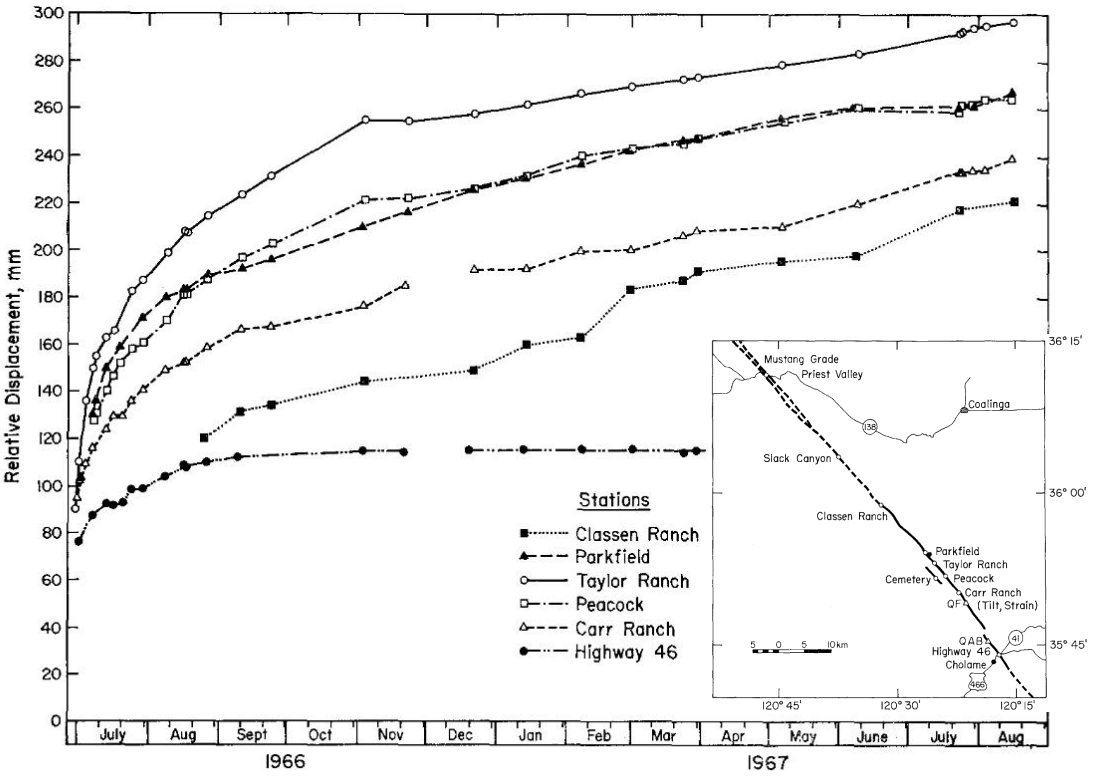

Figure 1.14: Temporal evolution of fault displacement following the 1966 Parkfield earthquake, reproduced with permission from *Smith and Wyss* (1968). Each line corresponds to a different geodetic station, measuring the temporal evolution of displacements across the fault. Inset map shows the locations of the geodetic stations from *Smith and Wyss* (1968). Solid black line shows earthquake rupture trace in 1966, and dashed line is the San Andreas fault trace.

Postseismic deformation is also seen over a number of spatial scales. Short wavelength features in the vicinity of faults are often seen following earthquakes (*Freed*, 2007, *Floyd et al.*, 2016, *Wimpenny et al.*, 2017, *Zhou et al.*, 2018). Fold and thrust belts often display such short wavelength deformation, particularly associated with folds (*Nishimura et al.*, 2008, *Copley and Reynolds*, 2014, *Zhou et al.*, 2018). Broader deformation signals are also seen in the postseismic period. These signals are clearly the result of some deeper process, but it is not always simple to determine the cause (*Savage*, 1990, *Wright et al.*, 2013).

Examples of postseismic deformation are shown in Figures 1.14 and 1.15. Figure 1.14 shows the temporal evolution of near-field relative displacements across the San Andreas fault following the 1966 Parkfield earthquake (*Smith and Wyss*, 1968). Multiple geodetic stations display a logarithmic displacement evolution over a number of months, typical of near-field postseismic deformation. Figure 1.15 shows a very different postseismic deformation signal. These signals are broad, low amplitude and visible over 50 years after the causative earthquakes (*Ryder et al.*, 2014). The signals near Bam Co and east of the Gulu Fault are thought to be produced by lower-crustal flow

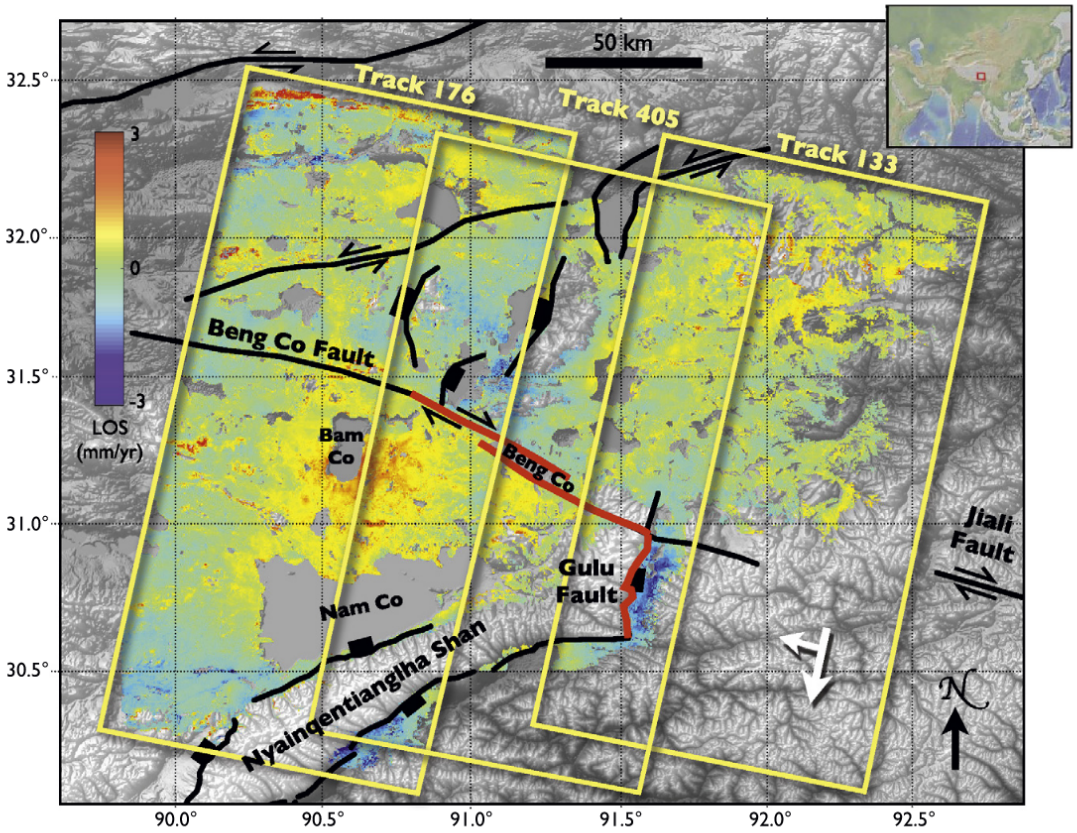

Figure 1.15: InSAR rate maps showing late stage postseismic deformation in Tibet, reproduced with permission from *Ryder et al.* (2014). Colours indicate LOS velocities measured between 1992 and 2010 using ERS and Envisat. The large uplift signal around Bam Co and the subsidence signal east of the Gulu Fault are thought to result from lower-crustal flow in Tibet following earthquakes in 1951 and 1952 (*Ryder et al.*, 2014).

in the thickened, hot Tibetan crust (*Ryder et al.*, 2014).

Models

Postseismic deformation is modelled using a wide variety of models which have their basis in viscoelasticity, friction laws and fluid flow. There is still a large degree of ambiguity as to which processes are more important over different lengthscales and timescales (see chapter 2). Short wavelength, short timescale features have been explained by the movement of pore fluids induced by pore pressure changes following earthquakes (*Peltzer et al.*, 1998, *Jónsson et al.*, 2003, *Fialko*, 2004). Surface deformation produced by poroelastic rebound can be calculated using the difference between elastic dislocation models in drained crust and undrained crust simulated using different values of Poisson's ratio (*Peltzer et al.*, 1998, *Fialko*, 2004). The temporal evolution of such displacements depends on the overall permeability of the porous medium. *Jónsson et al.* (2003) was able to correlate, both spatially and temporally, changing water levels in wells with changing pore pressures during and after earthquakes in southern Iceland. This correlation strongly suggests that poroelastic rebound played a significant role in producing the postseismic surface deformation observed in this example.

Postseismic deformation closely associated with faults is often thought to result from ongoing fault slip (afterslip). This slip can be shallow, resulting in very short wavelength deformation features, or deep, producing longer wavelength deformation. Afterslip is often modeled using the rate-and-state friction laws (*Dieterich*, 1972, 1979, *Ruina*, 1983, *Marone*, 1998). These friction laws are empirical fits to data obtained from laboratory experiments on small samples of various materials including rocks and simulated fault gouge. These experiments found that the frictional strength of a fault depends on the sliding rate of the fault and the contact time (or state) of the fault.

Friction can either increase (velocity strengthening) or decrease (velocity weakening) with an increase in the fault sliding rate. For example, localised slip on bare rock surfaces tend to show velocity weakening behaviour, whilst distributed shear within fault gouge tends to show velocity strengthening behaviour (*Marone*, 1998). Velocity weakening materials are capable of nucleating earthquake ruptures, since friction drops as slip rate increases, leading to slip instability and seismic rupture (*Ruina*, 1983, *Dieterich*, 1992). In contrast, velocity strengthening materials prevent a run-away slip instability from nucleating within them due to friction increasing with sliding rate (*Ruina*, 1983, *Dieterich*, 1992).

In addition to this rate dependence, experiments have revealed an increase in frictional strength with the total time that surfaces are held in contact (*Dieterich*, 1972). This behaviour is explained by 'state' variation in the rate-and-state friction laws.

These laws usually take the form of equation 1.3:

$$\mu = \mu_0 + a \ln \left(\frac{V}{V_0} \right) + b \ln \left(\frac{V_0 \theta}{D_c} \right) \tag{1.3}$$

where μ is the coefficient of friction at velocity V and μ_0 is the coefficient of friction at a reference sliding velocity V_0. a and b are constants determined from experiments, D_c is the critical slip distance and θ is the state evolution variable. The evolution of the state variable is defined using either the slip law (equation 1.4) or the aging law (equation 1.5), both of which can reproduce many features of the laboratory experiments:

$$\frac{d\theta}{dt} = -\frac{V\theta}{D_c} \ln \left(\frac{V\theta}{D_c} \right) \tag{1.4}$$

$$\frac{d\theta}{dt} = 1 - \frac{V\theta}{D_c} \tag{1.5}$$

where the symbols are as explained above. Whilst these laws have proven successful in reproducing the laboratory data, questions remain as to their usefulness in geological settings. These laws are fundamentally an empirical fit to experimental data, and are not derived from our knowledge of rock mechanics. Using such an experimentally derived law in conditions which differ by orders of magnitude from those in the original experiments is a significant assumption (*Marone*, 1998, *van den Ende et al.*, 2018). Nevertheless, these rate-and-state friction laws have been widely used to explain a large number of fault and earthquake phenomena. Using these laws, it is possible to obtain relationships between the coseismic stress change, the frictional properties of a fault and its resulting afterslip (*Helmstetter and Shaw*, 2009, *Barbot et al.*, 2009, *Rousset et al.*, 2012, *Feng et al.*, 2016). Fault slip evolves logarithmically in time in a rate-and-state afterslip model.

Alternatively, postseismic fault creep may be the result of other processes such as pressure solution creep. Pressure solution creep is a low temperature ductile deformation mechanism where minerals are dissolved in regions of high pressure and precipitated in regions of low pressure. This mechanism has been proposed to explain aseismic creep on part of the San Andreas fault (*Gratier et al.*, 2011) as well as postseismic creep (*Gratier et al.*, 2014). Pressure solution creep experiments which mimic a response to a coseismic stress change produce displacements which follow a power-law relationship in time (*Gratier et al.*, 2014).

All of the above proposed mechanisms are relatively localised, producing deformation near the coseismic fault zone. However, broad viscous deformation has also been suggested as a way to explain postseismic deformation. Over long timescales, the lower crust and/or the upper mantle may behave like a fluid and be capable of flow (*Watts et al.*, 2013). At depth, various deformation mechanisms can operate, depending on the stresses, grain size, temperature and composition of the deforming rocks. Experiments

on a wide range of materials suggest a general relationship between strain rate, $\dot{\varepsilon}$, and stress, σ of the form:

$$\dot{\varepsilon} = A\sigma^n d^{-m} f_{H_2O}\, e^{-\frac{Q+pV}{RT}} \tag{1.6}$$

where A is a material constant, n is the stress exponent (often referred to as the power-law exponent), d is the grain size, m is the grain size exponent, f_{H_2O} is the water fugacity, Q is the activation energy, p is the pressure, V is the volume, R is the molar gas constant and T is the temperature (*Kohlstedt et al.*, 1995, *Hirth and Kohlstedt*, 2003, *Bürgmann and Dresen*, 2008). If the stress exponent, n, is equal to 1, then the material shows a linear relationship between stress and strain rate, and is controlled by diffusion creep processes. Stress exponents greater than 1 imply a power-law rheology, where the effective viscosity of the rheology decreases as stress increases, and are controlled by dislocation creep processes with typical values for n in the range 2 - 6. The dominant creep behaviour of a particular rock depends on a wide variety of parameters, making extrapolation from laboratory samples to the real world challenging (*Bürgmann and Dresen*, 2008).

These various flow mechanisms form the basis for modelling broad postseismic deformation signals. These models can take the form of a simpler analogue, such as various arrangements of springs and viscous dashpots (*Reilinger*, 1986, *Pollitz*, 1997, *Jónsson*, 2008), or be based on the actual flow laws themselves (*Freed and Bürgmann*, 2004, *Freed et al.*, 2010). Unfortunately, it is not always easy to distinguish between viscoelastic relaxation and deep fault slip (*Savage*, 1990). At significantly large distances however, it is possible to distinguish the role and importance of viscoelastic relaxation in explaining the observed deformation (*Pollitz et al.*, 2000, *Gourmelen and Amelung*, 2005, *Bürgmann and Dresen*, 2008, *Zhao et al.*, 2017).

1.4 The Bigger Picture

A full understanding of the earthquake cycle requires the tying together of observations and models from all of the individual stages of the earthquake cycle. The uncertainties of various observations and models should be accounted for in order to obtain a range of possible parameters rather than a single best-fit value. Furthermore, relatively short term observations, made over periods from seconds to centuries need to be combined with longer term measurements of the earthquake cycle.

1.4.1 Earthquake Cycle Models

The models discussed in section 1.3 are used to investigate individual stages of the earthquake cycle. Another class of models seek to model the key features of the whole earthquake cycle. One set of models has arisen out of laboratory experiments on fault

rocks (*Dieterich*, 1972, 1979, *Marone*, 1998). These observations have come to be explained by the rate-and-state friction laws which have now been widely applied to various aspects of the earthquake cycle (*Marone*, 1998, *Liu and Rice*, 2005, *Helmstetter and Shaw*, 2009). Faults with spatially variable rate-and-state friction parameters allow a number of different phenomena occurring on the same fault (*Barbot et al.*, 2009, *Avouac*, 2014).

The laboratory can also be used to develop physical, analogue models of the earthquake cycle. Stick-slip models involving spring-slider combinations were some of earliest developments of analog earthquake cycle models (*Byerlee*, 1970, *Carlson and Langer*, 1989). Springs and sliders have been replaced by more complex analog materials (e.g. foams, plastics and gels) and observing these models has been greatly helped by the development of high-speed cameras (*Rosenau et al.*, 2009, *Corbi et al.*, 2013, *Caniven et al.*, 2015). These more complicated models can be 2D or 3D and incorporate rate-and-state friction laws as well as viscoelastic materials which are important when investigating postseismic deformation. Such models tend to focus on subduction megathrusts and strike-slip faults.

The increase in computational power has allowed the development of more realistic numerical models of the earthquake cycle. The purely elastic model of *Reid* (1910) has since been improved with the addition of viscoelasticity (*Savage and Prescott*, 1978, *Rundle*, 1982), allowing for time-dependent behaviour such as postseismic deformation. Additional complexity has been added to these models, allowing the modelling of multiple deformation mechanisms (e.g. *Barbot and Fialko*, 2010); incorporation of depth-dependent viscosity structures (e.g. *Hetland and Hager*, 2006, *Riva and Govers*, 2009); and the incorporation of non-linear rheologies (e.g. *Yamasaki et al.*, 2010). Many of these models have been developed using strike-slip faults and often have prescribed earthquake slip repeated at set intervals.

Hampel and Hetzel (2015) developed a linear, 3D finite element model with a continental dip-slip fault. Their model includes rheological layering, gravity, isostasy and far-field tectonic loading forces (extension or compression across the model box). Earthquakes are then a function of the loading rate, rather than an imposed, defined parameter. Their results are in broad agreement with observations from the L'Aquila and Chi-Chi earthquakes, although there is some discrepancy in the postseismic results.

In all of the above cases, the earthquake cycle models are developed to match key features of earthquake cycle deformation. An alternative approach would be to develop a model which can be used in an inverse sense, whereby the best-fit model parameters are found using real data. I have developed one such model in chapter 3, where the frictional properties of a fault are solved for using real coseismic and postseismic deformation data.

1.4.2 Accounting for Uncertainty using Bayesian Inversions

Many geophysical problems are under-determined, meaning that many different solutions could equally well explain the data we have. For example, when solving for the distribution of fault slip in an earthquake, often many different solutions can fit the geodetic, geological and seismological data equally well. The range of solutions which fit the data can be represented using probability density functions (PDF) which show the probability that a particular parameter is a certain value.

Bayesian methods can provide these PDFs for a wide range of problems. Bayes' rule states that the probability a parameter takes a certain value depends on constraints provided by the data being modelled, and prior information about the parameter. Mathematically this is represented as:

$$p(m|d) \propto p(d|m) \times p(m) \tag{1.7}$$

where the posterior PDF, $p(m|d)$, is the probability that model parameter m takes a particular value given the data, d that we observe. $p(d|m)$ is the likelihood of the model with parameter m, in other words, how well it matches the data and $p(m)$ is the prior probability of the parameter m. The prior probability is defined using a PDF, with common forms being Gaussian and uniform prior PDFs. These prior PDFs are defined explicitly before hand and are generally based on our current understanding of a given parameter. For example, in the earthquake slip example, we may define a prior PDF using a uniform distribution which only allows slip between 0 and 10 m for an earthquake of M_W 6. By doing this, we are stating that we know slip cannot be negative (e.g. left lateral in a right lateral earthquake) or be larger than 10 m for a moderate sized earthquake.

Throughout this thesis, I use Monte Carlo Markov Chain methods to obtain estimates of the posterior PDF. Samples are obtained as follows, starting from the current model, m_i:

1. Move to new trial model, m_{i+1} with probability given by the prior PDF
2. Calculate the data likelihood of the model m_{i+1} and compare it with the data likelihood of the previous model m_i
3. Accept the new trial model as the current model if is more likely than the current model ($p(d|m_{i+1}) > p(d|m_i)$) or if the ratio of the likelihoods is greater than a number drawn from a uniform distribution between 0 and 1 ($p(d|m_{i+1})/p(d|m_i) > U(0,1)$)
4. Repeat

This algorithm is known as the Metropolis-Hastings algorithm and allows a search of

parameter space which correctly samples the posterior PDF (*Mosegaard and Tarantola*, 1995).

1.4.3 Longer Term Measurements

Whereas we have so far considered measurements and models for single earthquake cycles, it is important to consider longer term earthquake cycle deformation. Accessing information about deformation from multiple earthquake cycles is challenging due to the long time spans between earthquakes and the relatively short time span covered by modern seismological and geodetic measurements. Alternative approaches are therefore required to study earthquakes that occurred centuries or millennia ago.

In the recent past, the approximate locations and magnitudes of earthquakes can be determined by historical records. These historical catalogs are constructed using written records of shaking, damage or ground rupture. Where multiple records exists for the same earthquake, approximate intensity maps can be produced and the epicentre of the earthquake estimated. In other cases, only the fact that an earthquake of significant magnitude occurred can be determined. This approach is limited to inhabited regions with a long history of written records such as the near and middle-east (*Ambraseys and Melville*, 1982) and throughout the Mediterranean (*Poirier and Taher*, 1980, *Boschi*, 2000). These written records can be supplemented by archaeological studies using the destruction or displacement of ancient structures (*Noller and Lightfoot*, 1997, *Jones and Stiros*, 2000, *Meghraoui et al.*, 2003, *Galli and Naso*, 2009).

Alternatively, the effects of earthquakes on the landscape can be used to obtain historical or pre-historical data. In coastal regions, the uplift and subsidence associated with dip-slip faulting earthquakes can result in relative sea-level changes recorded in rocks and fossils (*Stiros et al.*, 1992, *Kershaw and Guo*, 2001). Tropical regions such as Indonesia enable the use of corals as palaeo-geodetic markers, indicating histories of relative sea-level rise and fall associated with the subduction megathrust (*Meltzner et al.*, 2010, *Gagan et al.*, 2015). A different set of tools are available for terrestrial settings. Fault scarps from surface ruptures are preserved in the landscape to varying degrees depending on local conditions. These scarps are often measured in height and length to estimate earthquake magnitudes for relatively recent earthquakes (*Middleton et al.*, 2016). As fault scarps become eroded over time, it is often necessary to dig trenches or use road/river cuttings to examine older events. These trenches can be used to study multiple previous earthquakes and potentially estimate dates for these events using radiogenic dating techniques (*Daeron et al.*, 2007). Slip rates for strike-slip faults can be determined by measuring offsets between geomorphic markers such as streams and dating such offsets (*Walker et al.*, 2010). In some locations, such as the Italian Apennines, normal faults progressively reveal fault planes which offer the opportunity to probe temporal and spatial variations in fault slip rate since the last glacial maximum (*Cowie et al.*, 2017). The exhumation of these fault planes points

to the interaction between tectonics and topography. The shape of the topography in actively deforming zones therefore offers another way by which longer term deformation measurements can be obtained.

1.4.4 Tectonics and Topography

The topography in tectonically active regions such as mountain belts and rift zones is at least partially controlled by the earthquake cycle. The formation of topography and geological structures through many earthquake cycles has been long recognised as a concept (*King et al.*, 1988, *Stein et al.*, 1988, *Ainscoe et al.*, 2017). However, the means by which such structures develop remains unclear since some earthquakes actually result in the net destruction of topography (*Parker et al.*, 2011) or the lowering of the highest peaks (*Elliott et al.*, 2016b, *Melnick*, 2016). Other mechanisms are therefore sometimes required to generate topography, such as isostatic rebound (*Molnar*, 2012), or deformation during other parts of the earthquake cycle. *Nishimura et al.* (2008) observed fold growth using InSAR which was likely related to a nearby M_w 6.8 earthquake and *Copley and Reynolds* (2014) found folds growing due to afterslip over 16 years after the Sefidabeh earthquakes. *Stevens and Avouac* (2015) argue for the role of interseismc deformation in building the Himalayas because of the similarity between uplift patterns produced by their interseismic slip model and the topography along the Himalayan arc. (*Bufe et al.*, 2017) use InSAR to study deformation along fold axes in the Tien Shan and Pamir which does not appear to be associated with any particular earthquake but instead represents interseismic deformation. *Melnick* (2016) suggest that the large number of deep, moderate earthquakes along the Andean subduction zone are responsible for the rise of the Andean coastline. These earthquakes counteract the subsidence caused by the larger megathrust events.

Models of topographic growth associated with tectonics vary. Deformation associated with short wavelength folds is often modelled using elastic dislocation models (*Okada*, 1985, *Ellis and Densmore*, 2006, *Copley and Reynolds*, 2014, *Ainscoe et al.*, 2017). The short wavelength of the deformation and resulting topography means that deeper mechanisms such as viscous flow and isostasy can be ignored in these cases. Alternatively, kinematic models exist which link the shape of a fold with the shape of an underlying fault by maintaining layer thicknesses (*Suppe*, 1983).

Over longer wavelengths, different models can be used which link topography and tectonics. Fold-and-thrust belts are often modelled using critical taper wedge mechanics, which considers the belt to be similar to a pile of sand being pushed up a shallow incline (*Davis et al.*, 1983, *Dahlen et al.*, 1984, *Dahlen*, 1990). In this model, the overall topographic slope of the wedge is a function of the strength of the basal detachment and the internal strength of the wedge material (*Suppe*, 2007). These critical wedges maintain the overall angle between the basal decollement and the topographic slope (their taper) by faulting and erosion. Faulting near the toe of the wedge and propaga-

tion of the fold and thrust belt into the foreland reduces taper, whilst internal, out of sequence thrusting increases taper. These models have been widely applied in a variety of settings (*Davis et al.*, 1983, *Hubbard et al.*, 2010, *von Hagke et al.*, 2014, *Cubas et al.*, 2013), but rest on significant assumptions about the rheology of the belt. Critical taper models require that the whole wedge be on the verge of failure and consist of uniform strength material controlled by brittle deformation. These conditions are clearly not appropriate in all circumstances, particularly in areas where viscous effects are known to be important.

Thin viscous sheet models treat the lithosphere as a fluid and are appropriate for modelling long wavelength deformation patterns and topography (*England and McKenzie*, 1982, *Walters et al.*, 2017). Similar models can be used to model mountain ranges produced by convergence, taking into account the rigid base they are often riding over (*Copley*, 2012). These models can reproduce the shape of the topography and patterns of deformation to first order in a number of locations (*Copley and McKenzie*, 2007, *Reynolds et al.*, 2015). However, these models cannot match short wavelength deformation due to individual faults.

1.5 Thesis Outline

1.5.1 Aims and Objectives

I aim to investigate continental dip-slip faults and build on the previous work discussed above. I will make geodetic measurements of the earthquake cycle using InSAR and combine these with other observations. These observations will then be used to develop models of the seismic cycle and link earthquake cycle deformation to topography. This overall aim will be pursued through a number of objectives:

1. Collate geodetic measurements of the seismic cycle from a number of previously studied dip-slip earthquakes.

2. Use InSAR to produce new surface deformation measurements around dip-slip faults.

3. Combine all of these geodetic data from multiple stages of the earthquake cycle to build up a full picture of deformation around dip-slip faults.

4. Determine an appropriate model to explain observations from throughout the seismic cycle. Develop additional models as required to explain the observations.

5. Examine the relationship between earthquake cycle deformation and topography in a dip-slip fault setting to see how topography is grown in these regions.

1.5.2 Outline of Work

In the subsequent chapters, I seek to achieve the objectives stated above. In chapter 2, I collate near-field geodetic measurements of postseismic deformation from a large number of dip-slip and strike-slip earthquakes. I examine the evolution of postseismic velocity with time since an earthquake and find a remarkably simple pattern. Postseismic velocities are seen to decay as $1/t$ where t is the time since the earthquake. This temporal pattern is consistent with fault-zone based processes such as frictional afterslip or power-law creep in a shear zone, and suggests these processes dominate near-field deformation for decades. I also found that dip-slip and strike-slip faults were indistinguishable in the temporal evolution of their postseismic velocities. This chapter appears in publication as *Ingleby and Wright* (2017), and contributes to objectives 1,3 and 4.

In chapter 3, I construct an InSAR time series to study postseismic deformation following the 2015 M_w 7.8 Gorkha earthquake in Nepal. I combine these measurements with GNSS data to build a picture of the postseismic deformation field in space and time. I then combine these measurements with interseismic and coseismic geodetic data from other studies to determine fault geometries which satisfy surface deformation data from throughout the earthquake cycle. I develop a mechanically coupled model based on rate-and-state friction which inverts coseismic and postseismic data simultaneously. I find that a large number of different fault geometries produce acceptable fits to the available geodetic data, even when using the extra constraint of mechanical coupling between coseismic and postseismic slip. This chapter has been through peer review and is in revision for resubmission to the Journal of Geophysical Research. This work contributes to objectives 2,3 and 4.

In chapter 4, I combine SAR data from three generations of ESA satellites to study deformation in a fold-and-thrust belt in Pakistan. I build an InSAR time series over 25 years long by tying each of the individual SAR data sets together. This time series reveals the deformation associated with each stage of the seismic cycle as an earthquake occurred here in 1997. I separate out the deformation from each stage of the earthquake cycle and examine their contributions to the topographic growth in the fold-and-thrust belt. I find that coseismic and postseismic deformation combined are capable of explaining multiple lengthscales of topography. These findings also have implications for critical taper wedge mechanics as they show that it is possible to maintain taper in a single earthquake cycle. This work is presented as a draft paper and contributes to objectives 2,3 and 5.

In chapter 5, I draw together the findings of the previous three papers and comment on some common themes. I evaluate my findings in light of the objectives listed above and consider future directions for research.

References

Ader, T., J.-P. Avouac, J. Liu-Zeng, H. Lyon-Caen, L. Bollinger, J. Galetzka, J. Genrich, M. Thomas, K. Chanard, S. N. Sapkota, S. Rajaure, P. Shrestha, L. Ding, and M. Flouzat (2012), Convergence rate across the Nepal Himalaya and interseismic coupling on the Main Himalayan Thrust: Implications for seismic hazard, *Journal of Geophysical Research*, *117*(B4), B04,403, doi:10.1029/2011JB009071. 1.11, 1.3.1, 1.3.1, 1.3.1

Ainscoe, E. A., J. R. Elliott, A. Copley, T. J. Craig, T. Li, B. E. Parsons, and R. T. Walker (2017), Blind Thrusting, Surface Folding, and the Development of Geological Structure in the M_w 6.3 2015 Pishan (China) Earthquake, *Journal of Geophysical Research: Solid Earth*, *122*(11), 9359–9382, doi:10.1002/2017JB014268. 1.4.4

Allmann, B. P., and P. M. Shearer (2009), Global variations of stress drop for moderate to large earthquakes, *Journal of Geophysical Research*, *114*(B1), B01,310, doi:10.1029/2008JB005821. 1.1.2

Ambraseys, N. N. (1991), Earthquake hazard in the Kenya Rift: the Subukia earthquake 1928, *Geophysical Journal International*, *105*(1), 253–269, doi:10.1111/j.1365-246X.1991.tb03460.x. 1.3.2

Ambraseys, N. N., and C. P. Melville (1982), *A history of Persian earthquakes*, Cambridge University Press. 1.4.3

Amey, R. M. J., A. Hooper, and R. J. Walters (2018), A Bayesian Method for Incorporating Self-Similarity Into Earthquake Slip Inversions, *Journal of Geophysical Research: Solid Earth*, doi:10.1029/2017JB015316. 1.3.2

Anderson, E. M. (1905), The dynamics of faulting, *Transactions of the Edinburgh Geological Society*, *8*(3), 387–402, doi:10.1144/transed.8.3.387. 1.1.2, 1.4

Avouac, J.-P. (2014), From Geodetic Imaging of Seismic and Aseismic Fault Slip to Dynamic Modeling of the Seismic Cycle, *Annual Review of Earth and Planetary Sciences*, *43*(1), 150223150959,000, doi:10.1146/annurev-earth-060614-105302. 1.4.1

Barbot, S., and Y. Fialko (2010), A unified continuum representation of post-seismic relaxation mechanisms: semi-analytic models of afterslip, poroelastic rebound and viscoelastic flow, *Geophysical Journal International*, *182*(3), 1124–1140, doi:10.1111/j.1365-246X.2010.04678.x. 1.4.1

Barbot, S., Y. Hamiel, and Y. Fialko (2008), Space geodetic investigation of the coseismic and postseismic deformation due to the 2003 M w 7.2 Altai earthquake: Implications for the local lithospheric rheology, *Journal of Geophysical Research*, *113*(B3), B03,403, doi:10.1029/2007JB005063. 1.1.2

Barbot, S., Y. Fialko, and Y. Bock (2009), Postseismic deformation due to the M w 6.0 2004 Parkfield earthquake: Stress-driven creep on a fault with spatially variable rate-and-state friction parameters, *Journal of Geophysical Research*, *114*(B7), B07,405, doi:10.1029/2008JB005748. 1.3.3, 1.4.1

Barker, T. G. (1976), Quasi-static Motions near the San Andreas Fault Zone, *Geophysical Journal International*, *45*(3), 689–705, doi:10.1111/j.1365-246X.1976.tb06918.x. 1.1.2

Bekaert, D., R. Walters, T. Wright, A. Hooper, and D. Parker (2015a), Statistical comparison of InSAR tropospheric correction techniques, *Remote Sensing of Environment*, *170*, 40–47, doi:10.1016/j.rse.2015.08.035. 1.2.3

Bekaert, D. P. S., A. Hooper, and T. J. Wright (2015b), A spatially-variable power-law tropospheric correction technique for InSAR data, *Journal of Geophysical Research: Solid Earth*, pp. n/a–n/a, doi:10.1002/2014JB011558. 1.2.3

Berardino, P., G. Fornaro, R. Lanari, and E. Sansosti (2002), A new algorithm for surface deformation monitoring based on small baseline differential SAR interferograms, *IEEE Transactions on Geoscience and Remote Sensing*, *40*(11), 2375–2383, doi:10.1109/TGRS.2002.803792. 1.2.2

Beroza, G. C., and S. Ide (2011), Slow Earthquakes and Nonvolcanic Tremor, *Annual Review of Earth and Planetary Sciences*, *39*(1), 271–296, doi:10.1146/annurev-earth-040809-152531. 1.3

Biasi, G. P., and S. G. Wesnousky (2016), Steps and Gaps in Ground Ruptures: Empirical Bounds on Rupture Propagation, *Bulletin of the Seismological Society of America*, *106*(3), 1110–1124, doi:10.1785/0120150175. 1.3.2

Biggs, J., R. Burgmann, J. T. Freymueller, Z. Lu, B. Parsons, I. Ryder, G. Schmalzle, and T. Wright (2009), The postseismic response to the 2002 M 7.9 Denali Fault earthquake: constraints from InSAR 2003-2005, *Geophysical Journal International*, *176*(2), 353–367, doi:10.1111/j.1365-246X.2008.03932.x. 1.1.2

Bilham, R. (2004), Urban Earthquake Fatalities: A Safer World, or Worse to Come?, *Seismological Research Letters*, *75*(6), 706–712, doi:10.1785/gssrl.75.6.706. 1.1.1

Bilham, R., H. Ozener, D. Mencin, A. Dogru, S. Ergintav, Z. Cakir, A. Aytun, B. Aktug, O. Yilmaz, W. Johnson, and G. Mattioli (2016), Surface creep on the North Anatolian Fault at Ismetpasa, Turkey, 1944-2016, *Journal of Geophysical Research: Solid Earth*, *121*(10), 7409–7431, doi:10.1002/2016JB013394. 1.3

Boschi, E. (2000), A 'new generation' earthquake catalogue, *Annals of Geophysics*, *43*(4), doi:10.4401/ag-3660. 1.4.3

Briole, P., A. Rigo, H. Lyon-Caen, J. C. Ruegg, K. Papazissi, C. Mitsakaki, A. Balodimou, G. Veis, D. Hatzfeld, and A. Deschamps (2000), Active deformation of the Corinth rift, Greece: Results from repeated Global Positioning System surveys between 1990 and 1995, *Journal of Geophysical Research*, *105*(B11), 25,605, doi:10.1029/2000JB900148. 1.3.1

Bufe, A., D. P. S. Bekaert, E. Hussain, B. Bookhagen, D. W. Burbank, J. A. Thompson Jobe, J. Chen, T. Li, L. Liu, and W. Gan (2017), Temporal changes in rock uplift rates of folds in the foreland of the Tian Shan and the Pamir from geodetic and geologic data, *Geophysical Research Letters*, *44*(21), 10,977–10,987, doi:10.1002/2017GL073627. 1.4.4

Bürgmann, R., and G. Dresen (2008), Rheology of the Lower Crust and Upper Mantle: Evidence from Rock Mechanics, Geodesy, and Field Observations, *Annual Review of Earth and Planetary Sciences*, *36*, 531–567. 1.1.1, 1.1.2, 1.3.2, 1.3.3

Bürgmann, R., P. A. Rosen, and E. J. Fielding (2000), Synthetic Aperture Radar Interferometry to Measure Earth's Surface Topography and Its Deformation, *Annual Review of Earth and Planetary Sciences*, *28*(1), 169–209, doi:10.1146/annurev.earth.28.1.169. 1.2

Byerlee, J. (1970), The mechanics of stick-slip, *Tectonophysics*, *9*(5), 475–486, doi:10.1016/0040-1951(70)90059-4. 1.4.1

Calais, E., M. Vergnolle, J. Déverchère, V. San'kov, A. Lukhnev, and S. Amarjargal (2002), Are post-seismic effects of the M = 8.4 Bolnay earthquake (1905 July 23) still influencing GPS velocities in the Mongolia-Baikal area?, *Geophysical Journal International*, *149*(1), 157–168, doi:10.1046/j.1365-246X.2002.01624.x. 1.3.3

Caniven, Y., S. Dominguez, R. Soliva, R. Cattin, M. Peyret, M. Marchandon, C. Romano, and V. Strak (2015), A new multilayered visco-elasto-plastic experimental model to study strike-slip fault seismic cycle, *Tectonics*, pp. n/a–n/a, doi:10.1002/2014TC003701. 1.1.2, 1.4.1

Carlson, J. M., and J. S. Langer (1989), Mechanical model of an earthquake fault, *Physical Review A*, *40*(11), 6470–6484, doi:10.1103/PhysRevA.40.6470. 1.4.1

Cetin, E., M. Meghraoui, Z. Cakir, A. M. Akoglu, O. Mimouni, and M. Chebbah (2012), Seven years of postseismic deformation following the 2003 Mw=6.8 Zemmouri earthquake (Algeria) from InSAR time series, *Geophysical Research Letters*, *39*(10), n/a–n/a, doi:10.1029/2012GL051344. 1.1.2

Chang, W.-L., R. B. Smith, C. M. Meertens, and R. A. Harris (2006), Contemporary deformation of the Wasatch Fault, Utah, from GPS measurements with implications for interseismic fault behavior and earthquake hazard: Observations and kinematic analysis, *Journal of Geophysical Research*, *111*(B11), B11,405, doi:10.1029/2006JB004326. 1.3.1

Cheloni, D., N. D'Agostino, and G. Selvaggi (2014), Interseismic coupling, seismic potential, and earthquake recurrence on the southern front of the Eastern Alps (NE Italy), *Journal of Geophysical Research: Solid Earth*, *119*(5), 4448–4468, doi:10.1002/2014JB010954. 1.3.1

Copley, A. (2012), The formation of mountain range curvature by gravitational spreading, *Earth and Planetary Science Letters*, *351-352*, 208–214, doi:10.1016/J.EPSL.2012.07.036. 1.4.4

Copley, A. (2014), Postseismic afterslip 30 years after the 1978 Tabas-e-Golshan (Iran) earthquake: observations and implications for the geological evolution of thrust belts, *Geophysical Journal International*, *197*(2), 665–679, doi:10.1093/gji/ggu023. 1.3.3

Copley, A., and D. McKenzie (2007), Models of crustal flow in the India-Asia collision zone, *Geophysical Journal International*, *169*(2), 683–698, doi:10.1111/j.1365-246X.2007.03343.x. 1.4.4

Copley, A., and K. Reynolds (2014), Imaging topographic growth by long-lived postseismic afterslip at Sefidabeh, east Iran, *Tectonics*, *33*(3), 330–345, doi:10.1002/2013TC003462. 1.3.3, 1.4.4

Corbi, F., F. Funiciello, M. Moroni, Y. van Dinther, P. M. Mai, L. A. Dalguer, and C. Faccenna (2013), The seismic cycle at subduction thrusts: 1. Insights from laboratory models, *Journal of Geophysical Research: Solid Earth*, *118*(4), 1483–1501, doi:10.1029/2012JB009481. 1.4.1

Cowie, P. A., R. J. Phillips, G. P. Roberts, K. McCaffrey, L. J. J. Zijerveld, L. C. Gregory, J. Faure Walker, L. N. J. Wedmore, T. J. Dunai, S. A. Binnie, S. P. H. T. Freeman, K. Wilcken, R. P. Shanks, R. S. Huismans, I. Papanikolaou, A. M. Michetti, and M. Wilkinson (2017), Orogen-scale uplift in the central Italian Apennines drives episodic behaviour of earthquake faults, *Scientific Reports*, *7*(1), 44,858, doi:10.1038/srep44858. 1.4.3

Cubas, N., J.-P. Avouac, P. Souloumiac, and Y. Leroy (2013), Megathrust friction determined from mechanical analysis of the forearc in the Maule earthquake area, *Earth and Planetary Science Letters*, *381*, 92–103, doi:10.1016/J.EPSL.2013.07.037. 1.4.4

Daeron, M., Y. Klinger, P. Tapponnier, A. Elias, E. Jacques, and A. Sursock (2007), 12,000-Year-Long Record of 10 to 13 Paleoearthquakes on the Yammouneh Fault, Levant Fault System, Lebanon, *Bulletin of the Seismological Society of America*, *97*(3), 749–771, doi:10.1785/0120060106. 1.4.3

Dahlen, F. A. (1990), Critical Taper Model of Fold-And-Thrust Belts and Accretionary Wedges, *Annual Review of Earth and Planetary Sciences*, *18*(1), 55–99, doi:10.1146/annurev.ea.18.050190.000415. 1.4.4

Dahlen, F. A., J. Suppe, and D. Davis (1984), Mechanics of fold-and-thrust belts and accretionary wedges: Cohesive Coulomb Theory, *Journal of Geophysical Research: Solid Earth*, *89*(B12), 10,087–10,101, doi:10.1029/JB089iB12p10087. 1.4.4

Davis, D., J. Suppe, and F. A. Dahlen (1983), Mechanics of fold-and-thrust belts and accretionary wedges, *Journal of Geophysical Research*, *88*(B2), 1153, doi:10.1029/JB088iB02p01153. 1.4.4

Diao, F., X. Xiong, and R. Wang (2010), Mechanisms of Transient Postseismic Deformation Following the 2001 Mw 7.8 Kunlun (China) Earthquake, *Pure and Applied Geophysics*, *168*(5), 767–779, doi:10.1007/s00024-010-0154-5. 1.1.2

Dieterich, J. H. (1972), Time-dependent friction in rocks, *Journal of Geophysical Research*, *77*(20), 3690–3697, doi:10.1029/JB077i020p03690. 1.3.3, 1.4.1

Dieterich, J. H. (1979), Modeling of rock friction: 1. Experimental results and constitutive equations, *Journal of Geophysical Research*, *84*(B5), 2161, doi:10.1029/JB084iB05p02161. 1.3.3, 1.4.1

Dieterich, J. H. (1992), Earthquake nucleation on faults with rate-and state-dependent strength, *Tectonophysics*, *211*(1-4), 115–134, doi:10.1016/0040-1951(92)90055-B. 1.3.3

Elliott, J., R. Walters, and T. Wright (2016a), The role of space-based observation in understanding and responding to active tectonics and earthquakes, *Nature Communications*, *7*, 13,844, doi:10.1038/ncomms13844. 1.1, 1.1.3, 1.5

Elliott, J., R. Jolivet, P. J. González, J.-P. Avouac, J. Hollingsworth, M. P. Searle, and V. Stevens (2016b), Himalayan megathrust geometry and relation to topography revealed by the Gorkha earthquake, *Nature Geoscience*, *9*(2), 174–180, doi:10.1038/ngeo2623. 1.3.1, 1.4.4

Elliott, J. R., J. Biggs, B. Parsons, and T. J. Wright (2008), InSAR slip rate determination on the Altyn Tagh Fault, northern Tibet, in the presence of topographically correlated atmospheric delays, *Geophysical Research Letters*, *35*(12), n/a–n/a, doi:10.1029/2008GL033659. 1.2.3

Elliott, J. R., R. J. Walters, P. C. England, J. A. Jackson, Z. Li, and B. Parsons (2010), Extension on the Tibetan plateau: recent normal faulting measured by InSAR and body wave seismology, *Geophysical Journal International*, *183*(2), 503–535, doi:10.1111/j.1365-246X.2010.04754.x. 1.3.2

Ellis, M. A., and A. L. Densmore (2006), First-order topography over blind thrusts, in *Tectonics, Climate and Landscape Evolution*, vol. 398, edited by S. D. Willets, N. Hovius, M. T. Brandon, and D. M. Fisher, p. 447, Geological Society of America. 1.4.4

England, P., and D. McKenzie (1982), A thin viscous sheet model for continental deformation, *Geophysical Journal International*, *70*(2), 295–321, doi:10.1111/j.1365-246X.1982.tb04969.x. 1.4.4

Ergintav, S., S. McClusky, E. Hearn, R. Reilinger, R. Cakmak, T. Herring, H. Ozener, O. Lenk, and E. Tari (2009), Seven years of postseismic deformation following the 1999, M = 7.4 and M = 7.2, Izmit-Düzce, Turkey earthquake sequence, *Journal of Geophysical Research*, *114*(B7), B07,403, doi:10.1029/2008JB006021. 1.1.2

Farr, T. G., P. A. Rosen, E. Caro, R. Crippen, R. Duren, S. Hensley, M. Kobrick, M. Paller, E. Rodriguez, L. Roth, D. Seal, S. Shaffer, J. Shimada, J. Umland, M. Werner, M. Oskin, D. Burbank, and D. Alsdorf (2007), The Shuttle Radar Topography Mission, *Reviews of Geophysics*, *45*(2), RG2004, doi:10.1029/2005RG000183. 1.2.2

Faulkner, D. R., T. M. Mitchell, E. Jensen, and J. Cembrano (2011), Scaling of fault damage zones with displacement and the implications for fault growth processes, *Journal of Geophysical Research*, *116*(B5), B05,403, doi:10.1029/2010JB007788. 1.1.2

Feng, L., S. Barbot, E. M. Hill, I. Hermawan, P. Banerjee, and D. H. Natawidjaja (2016), Footprints of past earthquakes revealed in the afterslip of the 2010 M_w 7.8 Mentawai tsunami earthquake, *Geophysical Research Letters*, *43*(18), 9518–9526, doi:10.1002/2016GL069870. 1.3.3

Ferretti, A., C. Prati, and F. Rocca (2000), Nonlinear subsidence rate estimation using permanent scatterers in differential SAR interferometry, *IEEE Transactions on Geoscience and Remote Sensing*, *38*(5), 2202–2212, doi:10.1109/36.868878. 1.2.3

Ferretti, A., C. Prati, and F. Rocca (2001), Permanent scatterers in SAR interferometry, *IEEE Transactions on Geoscience and Remote Sensing*, *39*(1), 8–20, doi:10.1109/36.898661. 1.2.2, 1.2.3

Fialko, Y. (2004), Evidence of fluid-filled upper crust from observations of postseismic deformation due to the 1992 M w 7.3 Landers earthquake, *Journal of Geophysical Research: Solid Earth*, *109*(B8), n/a–n/a, doi:10.1029/2004JB002985. 1.3.3

Floyd, M. A., R. J. Walters, J. R. Elliott, G. J. Funning, J. L. Svarc, J. R. Murray, A. J. Hooper, Y. Larsen, P. Marinkovic, R. Bürgmann, I. A. Johanson, and T. J. Wright (2016), Spatial variations in fault friction related to lithology from rupture and afterslip of the 2014 South Napa, California, earthquake, *Geophysical Research Letters*, *43*(13), 6808–6816, doi:10.1002/2016GL069428. 1.3.3

Freed, A. M. (2007), Afterslip (and only afterslip) following the 2004 Parkfield, California, earthquake, *Geophysical Research Letters*, *34*(6), L06,312, doi:10.1029/2006GL029155. 1.1.2, 1.3.3

Freed, A. M., and R. Bürgmann (2004), Evidence of power-law flow in the Mojave desert mantle., *Nature*, *430*(6999), 548–51, doi:10.1038/nature02784. 1.1.2, 1.3.3

Freed, A. M., R. Bürgmann, E. Calais, J. Freymueller, and S. Hreinsdóttir (2006), Implications of deformation following the 2002 Denali, Alaska, earthquake for postseismic relaxation processes and lithospheric rheology, *Journal of Geophysical Research*, *111*(B1), B01,401, doi:10.1029/2005JB003894. 1.1.2

Freed, A. M., T. Herring, and R. Bürgmann (2010), Steady-state laboratory flow laws alone fail to explain postseismic observations, *Earth and Planetary Science Letters*, *300*(1-2), 1–10, doi:10.1016/j.epsl.2010.10.005. 1.3.3

Fukuda, J., and K. M. Johnson (2008), A Fully Bayesian Inversion for Spatial Distribution of Fault Slip with Objective Smoothing, *Bulletin of the Seismological Society of America*, *98*(3), 1128–1146, doi:10.1785/0120070194. 1.3.2

Gabriel, A. K., R. M. Goldstein, and H. A. Zebker (1989), Mapping small elevation changes over large areas: Differential radar interferometry, *Journal of Geophysical Research*, *94*(B7), 9183, doi:10.1029/JB094iB07p09183. 1.2.2

Gagan, M. K., S. M. Sosdian, H. Scott-Gagan, K. Sieh, W. S. Hantoro, D. H. Natawidjaja, R. W. Briggs, B. W. Suwargadi, and H. Rifai (2015), Coral 13C/12C records of vertical seafloor displacement during megathrust earthquakes west of Sumatra, *Earth and Planetary Science Letters*, *432*, 461–471, doi:10.1016/J.EPSL.2015.10.002. 1.4.3

Galetzka, J., D. Melgar, J. F. Genrich, J. Geng, S. Owen, E. O. Lindsey, X. Xu, Y. Bock, J.-P. Avouac, L. B. Adhikari, B. N. Upreti, B. Pratt-Sitaula, T. N. Bhattarai, B. P. Sitaula, A. Moore, K. W. Hudnut, W. Szeliga, J. Normandeau, M. Fend, M. Flouzat, L. Bollinger, P. Shrestha, B. Koirala, U. Gautam, M. Bhatterai, R. Gupta, T. Kandel, C. Timsina, S. N. Sapkota, S. Rajaure, and N. Maharjan (2015), Slip pulse and resonance of the Kathmandu basin during the 2015 Gorkha earthquake, Nepal, *Science*, *349*(6252). 1.13

Galli, P. A. C., and J. A. Naso (2009), Unmasking the 1349 earthquake source (southern Italy): paleoseismological and archaeoseismological indications from the Aquae Iuliae fault, *Journal of Structural Geology*, *31*(2), 128–149, doi:10.1016/J.JSG.2008.09.007. 1.4.3

Giardini, D., G. Grünthal, K. M. Shedlock, and P. Zhang (1999), The GSHAP Global Seismic Hazard Map, doi:10.4401/ag-3784. 1.1.1

Gourmelen, N., and F. Amelung (2005), Postseismic mantle relaxation in the Central Nevada Seismic Belt., *Science (New York, N.Y.)*, *310*(5753), 1473–6, doi:10.1126/science.1119798. 1.3.3, 1.3.3

Gratier, J.-P., J. Richard, F. Renard, S. Mittempergher, M.-L. Doan, G. Di Toro, J. Hadizadeh, and A.-M. Boullier (2011), Aseismic sliding of active faults by pressure solution creep: Evidence from the San Andreas Fault Observatory at Depth, *Geology*, *39*(12), 1131–1134, doi:10.1130/G32073.1. 1.3.3

Gratier, J. P., F. Renard, and B. Vial (2014), Postseismic pressure solution creep: Evidence and time-dependent change from dynamic indenting experiments, *Journal of Geophysical Research: Solid Earth*, *119*(4), 2764–2779, doi:10.1002/2013JB010768. 1.3.3

Hamlyn, J., T. Wright, R. Walters, C. Pagli, E. Sansosti, F. Casu, S. Pepe, M. Edmonds, B. McCormick Kilbride, D. Keir, J. Neuberg, and C. Oppenheimer (2018), What causes subsidence following the 2011 eruption at Nabro (Eritrea)?, *Progress in Earth and Planetary Science*, *5*(1), 31, doi:10.1186/s40645-018-0186-5. 1.2.3

Hampel, A., and R. Hetzel (2015), Horizontal surface velocity and strain patterns near thrust and normal faults during the earthquake cycle: The importance of viscoelastic relaxation in the lower crust and implications for interpreting geodetic data, *Tectonics*, *34*(4), 731–752, doi:10.1002/2014TC003605. 1.4.1

Hanssen, R. F., T. M. Weckwerth, H. A. Zebker, and R. Klees (1999), High-Resolution Water Vapor Mapping from Interferometric Radar Measurements., *Science (New York, N.Y.)*, *283*(5406), 1297–1299, doi:10.1126/SCIENCE.283.5406.1297. 1.2.3

Hayward, N. J., and C. J. Ebinger (1996), Variations in the along-axis segmentation of the Afar Rift system, *Tectonics*, *15*(2), 244–257, doi:10.1029/95TC02292. 1.3.2

Helmstetter, A., and B. E. Shaw (2009), Afterslip and aftershocks in the rate-and-state friction law, *Journal of Geophysical Research*, *114*(B1), B01,308, doi:10.1029/2007JB005077. 1.3.3, 1.4.1

Hetland, E. A. (2005), Postseismic and interseismic displacements near a strike-slip fault: A two-dimensional theory for general linear viscoelastic rheologies, *Journal of Geophysical Research*, *110*(B10), B10,401, doi:10.1029/2005JB003689. 1.1.2

Hetland, E. A., and B. H. Hager (2006), The effects of rheological layering on post-seismic deformation, *Geophysical Journal International*, *166*(1), 277–292, doi:10.1111/j.1365-246X.2006.02974.x. 1.4.1

Hirth, G., and D. Kohlstedt (2003), Rheology of the upper mantle and the mantle wedge: A view from the experimentalists, pp. 83–105, American Geophysical Union, doi:10.1029/138GM06. 1.3.3

Hooper, A. (2008), A multi-temporal InSAR method incorporating both persistent scatterer and small baseline approaches, *Geophysical Research Letters*, *35*(16), L16,302, doi:10.1029/2008GL034654. 1.2.2, 1.2.3

Hooper, A., H. Zebker, P. Segall, and B. Kampes (2004), A new method for measuring deformation on volcanoes and other natural terrains using InSAR persistent scatterers, *Geophysical Research Letters*, *31*(23), n/a–n/a, doi:10.1029/2004GL021737. 1.2.2

Hooper, A., D. Bekaert, K. Spaans, and M. Arkan (2012), Recent advances in SAR interferometry time series analysis for measuring crustal deformation, *Tectonophysics*, *514-517*, 1–13, doi:10.1016/j.tecto.2011.10.013. 1.1.3, 1.2

Hreinsdottir, S., and R. A. Bennett (2009), Active aseismic creep on the Alto Tiberina low-angle normal fault, Italy, *Geology*, *37*(8), 683–686, doi:10.1130/G30194A.1. 1.3.1, 1.12, 1.3.1

Hsu, Y.-J., M. Simons, S.-B. Yu, L.-C. Kuo, and H.-Y. Chen (2003), A two-dimensional dislocation model for interseismic deformation of the Taiwan mountain belt, *Earth and Planetary Science Letters*, *211*(3-4), 287–294, doi:10.1016/S0012-821X(03)00203-6. 1.3.1

Huang, M.-H., R. Bürgmann, and F. Pollitz (2016), Lithospheric rheology constrained from twenty-five years of postseismic deformation following the 1989 Mw 6.9 Loma Prieta earthquake, doi:10.1016/j.epsl.2015.12.018. 1.3.3

Hubbard, J., J. H. Shaw, and Y. Klinger (2010), Structural Setting of the 2008 Mw 7.9 Wenchuan, China, Earthquake, *Bulletin of the Seismological Society of America*, *100*(5B), 2713–2735, doi:10.1785/0120090341. 1.4.4

Hubbard, J., S. Barbot, E. M. Hill, and P. Tapponnier (2015), Coseismic slip on shallow décollement megathrusts: implications for seismic and tsunami hazard, *Earth-Science Reviews*, *141*, 45–55, doi:10.1016/J.EARSCIREV.2014.11.003. 1.1.1, 1.1.2, 1.3.2

Ingleby, T., and T. J. Wright (2017), Omori-like decay of postseismic velocities following continental earthquakes, *Geophysical Research Letters*, *44*(7), 3119–3130, doi:10.1002/2017GL072865. 1.3.3, 1.5.2

Jackson, A. P. (2017), The Application of Weather Radar for InSAR Atmospheric Corrections, Masters thesis, University of Leeds. 1.2.3

Jackson, J. (2006), Fatal attraction: living with earthquakes, the growth of villages into megacities, and earthquake vulnerability in the modern world., *Philosophical transactions. Series A, Mathematical, physical, and engineering sciences*, *364*(1845), 1911–25, doi:10.1098/rsta.2006.1805. 1.1.1

Jackson, J., and N. White (1989), Normal faulting in the upper continental crust: observations from regions of active extension, *Journal of Structural Geology*, *11*(1-2), 15–36, doi:10.1016/0191-8141(89)90033-3. 1.1.2, 1.3.2

Jackson, M., and R. Bilham (1994), Constraints on Himalayan deformation inferred from vertical velocity fields in Nepal and Tibet, *Journal of Geophysical Research: Solid Earth*, *99*(B7), 13,897–13,912, doi:10.1029/94JB00714. 1.11, 1.3.1

Jolivet, R., R. Grandin, C. Lasserre, M.-P. Doin, and G. Peltzer (2011), Systematic InSAR tropospheric phase delay corrections from global meteorological reanalysis data, *Geophysical Research Letters*, *38*(17), n/a–n/a, doi:10.1029/2011GL048757. 1.2.3

Jones, R. E., and S. C. Stiros (2000), The advent of archaeoseismology in the Mediterranean, *Geological Society, London, Special Publications*, *171*(1), 25–32, doi:10.1144/GSL.SP.2000.171.01.04. 1.4.3

Jónsson, S. (2008), Importance of post-seismic viscous relaxation in southern Iceland, *Nature Geoscience*, *1*(2), 136–139, doi:10.1038/ngeo105. 1.3.3

Jónsson, S., P. Segall, R. Pedersen, and G. Björnsson (2003), Post-earthquake ground movements correlated to pore-pressure transients, *Nature*, *424*(6945), 179–183, doi:10.1038/nature01776. 1.3.3

Kanamori, H. (1973), Mode of Strain Release Associated with Major Earthquakes in Japan, *Annual Review of Earth and Planetary Sciences*, *1*(1), 213–239, doi:10.1146/annurev.ea.01.050173.001241. 1.3

Kershaw, S., and L. Guo (2001), Marine notches in coastal cliffs: indicators of relative sea-level change, Perachora Peninsula, central Greece, *Marine Geology*, *179*(3-4), 213–228, doi:10.1016/S0025-3227(01)00218-3. 1.4.3

Kim, Y.-S., and D. J. Sanderson (2005), The relationship between displacement and length of faults: a review, *Earth-Science Reviews*, *68*(3-4), 317–334, doi:10.1016/J.EARSCIREV.2004.06.003. 1.1.2

King, G. C. P., R. S. Stein, and J. B. Rundle (1988), The Growth of Geological Structures by Repeated Earthquakes 1. Conceptual Framework, *Journal of Geophysical Research: Solid Earth*, *93*(B11), 13,307–13,318, doi:10.1029/JB093iB11p13307. 1.4.4

Kinoshita, Y., M. Shimada, and M. Furuya (2013), InSAR observation and numerical modeling of the water vapor signal during a heavy rain: A case study of the 2008 Seino event, central Japan, *Geophysical Research Letters*, *40*(17), 4740–4744, doi:10.1002/grl.50891. 1.2.3

Kohlstedt, D. L., B. Evans, and S. J. Mackwell (1995), Strength of the lithosphere: Constraints imposed by laboratory experiments, *Journal of Geophysical Research*, *100*(B9), 17,587, doi:10.1029/95JB01460. 1.3.3

Koketsu, K., K. Hikima, S. Miyazaki, and S. Ide (2004), Joint inversion of strong motion and geodetic data for the source process of the 2003 Tokachi-oki, Hokkaido, earthquake, *Earth, Planets, and Space*, *56*, 329–334. 1.3.2

Kreemer, C., J. Haines, W. E. Holt, G. Blewitt, and D. Lavallee (2000), On the determination of a global strain rate model, *Earth, Planets and Space*, *52*(10), 765–770, doi:10.1186/BF03352279. 1.1.3

Kreemer, C., W. E. Holt, and A. J. Haines (2003), An integrated global model of present-day plate motions and plate boundary deformation, *Geophysical Journal International*, *154*(1), 8–34, doi:10.1046/j.1365-246X.2003.01917.x. 1.1.3

Kreemer, C., G. Blewitt, and E. C. Klein (2014), A geodetic plate motion and Global Strain Rate Model, *Geochemistry, Geophysics, Geosystems*, *15*(10), 3849–3889, doi:10.1002/2014GC005407. 1.1, 1.1.3, 1.11, 1.3.1

Langbein, J. (2006), Coseismic and Initial Postseismic Deformation from the 2004 Parkfield, California, Earthquake, Observed by Global Positioning System, Electronic Distance Meter, Creepmeters, and Borehole Strainmeters, *Bulletin of the Seismological Society of America*, *96*(4B), S304–S320, doi:10.1785/0120050823. 1.1.2

Le Pourhiet, L., B. Huet, and N. Traoré (2014), Links between long-term and short-term rheology of the lithosphere: Insights from strike-slip fault modelling, *Tectonophysics*, *631*, 146–159, doi:10.1016/j.tecto.2014.06.034. 1.1.2

Li, Z., J.-P. Muller, and P. Cross (2003), Comparison of precipitable water vapor derived from radiosonde, GPS, and Moderate-Resolution Imaging Spectroradiometer measurements, *Journal of Geophysical Research*, *108*(D20), 4651, doi:10.1029/2003JD003372. 1.2.3

Li, Z., E. J. Fielding, P. Cross, and J.-P. Muller (2006), Interferometric synthetic aperture radar atmospheric correction: Medium Resolution Imaging Spectrometer and Advanced Synthetic Aperture Radar integration, *Geophysical Research Letters*, *33*(6), L06,816, doi:10.1029/2005GL025299. 1.2.3

Lindsey, E. O., R. Natsuaki, X. Xu, M. Shimada, M. Hashimoto, D. Melgar, and D. T. Sandwell (2015), Line-of-sight displacement from ALOS-2 interferometry: M w 7.8 Gorkha Earthquake and M w 7.3 aftershock, *Geophysical Research Letters*, *42*(16), 6655–6661, doi:10.1002/2015GL065385. 1.13

Liu, Y., and J. R. Rice (2005), Aseismic slip transients emerge spontaneously in three-dimensional rate and state modeling of subduction earthquake sequences, *Journal of Geophysical Research*, *110*(B8), B08,307, doi:10.1029/2004JB003424. 1.4.1

Marone, C. (1998), Laboratory-derived friction laws and their application to seismic faulting, *Annual Review of Earth and Planetary Sciences*, *26*, 643–696. 1.3.3, 1.3.3, 1.4.1

Massonnet, D., and K. L. Feigl (1998), Radar interferometry and its application to changes in the Earth's surface, *Reviews of Geophysics*, *36*(4), 441–500, doi:10.1029/97RG03139. 1.2, 1.2.1

Massonnet, D., M. Rossi, C. Carmona, F. Adragna, G. Peltzer, K. Feigl, and T. Rabaute (1993), The displacement field of the Landers earthquake mapped by radar interferometry, *Nature*, *364*(6433), 138–142, doi:10.1038/364138a0. 1.1.3

McGuire, J. J., and G. C. Beroza (2012), Geophysics. A rogue earthquake off Sumatra., *Science (New York, N.Y.)*, *336*(6085), 1118–9, doi:10.1126/science.1223983. 1.1.1

Meade, B. J. (2007), Algorithms for the calculation of exact displacements, strains, and stresses for triangular dislocation elements in a uniform elastic half space, *Computers & Geosciences*, *33*(8), 1064–1075, doi:10.1016/J.CAGEO.2006.12.003. 1.3.2

Meghraoui, M., F. Gomez, R. Sbeinati, J. Van der Woerd, M. Mouty, A. N. Darkal, Y. Radwan, I. Layyous, H. Al Najjar, R. Darawcheh, F. Hijazi, R. Al-Ghazzi, and M. Barazangi (2003), Evidence for 830 years of seismic quiescence from palaeoseismology, archaeoseismology and historical seismicity along the Dead Sea fault in Syria, *Earth and Planetary Science Letters*, *210*(1-2), 35–52, doi:10.1016/S0012-821X(03)00144-4. 1.4.3

Melnick, D. (2016), Rise of the central Andean coast by earthquakes straddling the Moho, *Nature Geoscience*, *9*(5), 401–407, doi:10.1038/ngeo2683. 1.4.4

Meltzner, A. J., K. Sieh, H.-W. Chiang, C.-C. Shen, B. W. Suwargadi, D. H. Natawidjaja, B. E. Philibosian, R. W. Briggs, and J. Galetzka (2010), Coral evidence for earthquake recurrence and an A.D. 13901455 cluster at the south end of the 2004 AcehAndaman rupture, *Journal of Geophysical Research*, *115*(B10), B10,402, doi:10.1029/2010JB007499. 1.4.3

Middleton, T. A., R. T. Walker, B. Parsons, Q. Lei, Y. Zhou, and Z. Ren (2016), A major, intraplate, normal-faulting earthquake: The 1739 Yinchuan event in northern China, *Journal of Geophysical Research: Solid Earth*, *121*(1), 293–320, doi:10.1002/2015JB012355. 1.1.1, 1.4.3

Molnar, P. (2012), Isostasy can't be ignored, *Nature Geoscience*, *5*(2), 83–83, doi:10.1038/ngeo1383. 1.4.4

Mosegaard, K., and A. Tarantola (1995), Monte Carlo sampling of solutions to inverse problems, *Journal of Geophysical Research: Solid Earth*, *100*(B7), 12,431–12,447, doi:10.1029/94JB03097. 1.4.2

Nikkhoo, M., and T. R. Walter (2015), Triangular dislocation: an analytical, artefact-free solution, *Geophysical Journal International*, *201*(2), 1119–1141, doi:10.1093/gji/ggv035. 1.3.2

Nishimura, T., M. Tobita, H. Yarai, T. Amagai, M. Fujiwara, H. Une, and M. Koarai (2008), Episodic growth of fault-related fold in northern Japan observed by SAR interferometry, *Geophysical Research Letters*, *35*(13), L13,301, doi:10.1029/2008GL034337. 1.3.3, 1.4.4

Nissen, E., J. R. Elliott, R. A. Sloan, T. J. Craig, G. J. Funning, A. Hutko, B. E. Parsons, and T. J. Wright (2016), Limitations of rupture forecasting exposed by instantaneously triggered earthquake doublet, *Nature Geoscience 2016 9:4*, *9*(4), 330, doi:10.1038/ngeo2653. 1.13, 1.3.2

Noller, J. S., and K. G. Lightfoot (1997), An archaeoseismic approach and method for the study of active strike-slip faults, *Geoarchaeology*, *12*(2), 117–135, doi:10.1002/(SICI)1520-6548(199703)12:2¡117::AID-GEA2¿3.0.CO;2-7. 1.4.3

Oglesby, D. D. (2004), Inverse Kinematic and Forward Dynamic Models of the 2002 Denali Fault Earthquake, Alaska, *Bulletin of the Seismological Society of America*, *94*(6B), S214–S233, doi:10.1785/0120040620. 1.1.2

Okada, Y. (1985), Surface deformation due to shear and tensile faults in a half-space, *Bulletin of the Seismological Society of America*, *75*(4), 1135–1154. 1.3.2, 1.4.4

Parker, R. N., A. L. Densmore, N. J. Rosser, M. de Michele, Y. Li, R. Huang, S. Whadcoat, and D. N. Petley (2011), Mass wasting triggered by the 2008 Wenchuan earthquake is greater than orogenic growth, *Nature Geoscience*, *4*(7), 449–452, doi:10.1038/ngeo1154. 1.4.4

Peltzer, G., P. Rosen, F. Rogez, and K. Hudnut (1998), Poroelastic rebound along the Landers 1992 earthquake surface rupture, *Journal of Geophysical Research: Solid Earth*, *103*(B12), 30,131–30,145, doi:10.1029/98JB02302. 1.3.3

Pérez-Campos, X., and G. C. Beroza (2001), An apparent mechanism dependence of radiated seismic energy, *Journal of Geophysical Research*, *106*(B6), 11,127, doi:10.1029/2000JB900455. 1.1.2

Perfettini, H., J.-P. Avouac, H. Tavera, A. Kositsky, J.-M. Nocquet, F. Bondoux, M. Chlieh, A. Sladen, L. Audin, D. L. Farber, and P. Soler (2010), Seismic and aseismic slip on the Central Peru megathrust, *Nature*, *465*(7294), 78–81, doi:10.1038/nature09062. 1.3.1

Peyret, M., S. Dominguez, R. Cattin, J. Champenois, M. Leroy, and A. Zajac (2011), Present-day interseismic surface deformation along the Longitudinal Valley, eastern Taiwan, from a PS-InSAR analysis of the ERS satellite archives, *Journal of Geophysical Research*, *116*(B3), B03,402, doi:10.1029/2010JB007898. 1.3.1

Poirier, J. P., and M. A. Taher (1980), Historical seismicity in the near and Middle East, North Africa, and Spain from Arabic documents (VIIth-XVIIIth century), *Bulletin of the Seismological Society of America*, *70*(6), 2185–2201. 1.4.3

Pollitz, F. F. (1997), Gravitational viscoelastic postseismic relaxation on a layered spherical Earth, *Journal of Geophysical Research: Solid Earth*, *102*(B8), 17,921–17,941, doi:10.1029/97JB01277. 1.3.3

Pollitz, F. F. (2005), Transient rheology of the upper mantle beneath central Alaska inferred from the crustal velocity field following the 2002 Denali earthquake, *Journal of Geophysical Research*, *110*(B8), B08,407, doi:10.1029/2005JB003672. 1.1.2

Pollitz, F. F., G. Peltzer, and R. Bürgmann (2000), Mobility of continental mantle: Evidence from postseismic geodetic observations following the 1992 Landers earthquake, *Journal of Geophysical Research: Solid Earth*, *105*(B4), 8035–8054, doi:10.1029/1999JB900380. 1.3.3

Pollitz, F. F., R. S. Stein, V. Sevilgen, and R. Bürgmann (2012), The 11 April 2012 east Indian Ocean earthquake triggered large aftershocks worldwide, *Nature*, *490*(7419), 250–253, doi:10.1038/nature11504. 1.1.1

Potin, P., B. Rosich, N. Miranda, and P. Grimont (2017), Sentinel-1 Mission Status, in *ESA Fringe Meeting 2017, abstract #115*. 1.1.3

Prats-Iraola, P., R. Scheiber, L. Marotti, S. Wollstadt, and A. Reigber (2012), TOPS Interferometry With TerraSAR-X, *IEEE Transactions on Geoscience and Remote Sensing*, *50*(8), 3179–3188, doi:10.1109/TGRS.2011.2178247. 1.2.2

Reid, H. (1910), The mechanics of the earthquake. 1.3, 1.4.1

Reilinger, R. (1984), Coseismic and postseismic vertical movements associated with the 1940 M 7.1 Imperial Valley, California, earthquake, *Journal of Geophysical Research*, *89*(B6), 4531, doi:10.1029/JB089iB06p04531. 1.3

Reilinger, R. (1986), Evidence for postseismic viscoelastic relaxation following the 1959 M = 7.5 Hebgen Lake, Montana, Earthquake, *Journal of Geophysical Research*, *91*(B9), 9488, doi:10.1029/JB091iB09p09488. 1.3.3

Reynolds, K., A. Copley, and E. Hussain (2015), Evolution and dynamics of a fold-thrust belt: the Sulaiman Range of Pakistan, *Geophysical Journal International*, *201*(2), 683–710, doi:10.1093/gji/ggv005. 1.4.4

Riva, R. E. M., and R. Govers (2009), Relating viscosities from postseismic relaxation to a realistic viscosity structure for the lithosphere, *Geophysical Journal International*, *176*(2), 614–624, doi:10.1111/j.1365-246X.2008.04004.x. 1.4.1

Rollins, C., S. Barbot, and J.-P. Avouac (2015), Postseismic Deformation Following the 2010 M = 7.2 El Mayor-Cucapah Earthquake: Observations, Kinematic Inversions, and Dynamic Models, *Pure and Applied Geophysics*, doi:10.1007/s00024-014-1005-6. 1.3.3

Rosen, P., S. Hensley, I. Joughin, F. Li, S. Madsen, E. Rodriguez, and R. Goldstein (2000), Synthetic aperture radar interferometry, *Proceedings of the IEEE*, *88*(3), 333–382, doi:10.1109/5.838084. 1.2

Rosenau, M., J. Lohrmann, and O. Oncken (2009), Shocks in a box: An analogue model of subduction earthquake cycles with application to seismotectonic forearc evolution, *Journal of Geophysical Research*, *114*(B1), B01,409, doi:10.1029/2008JB005665. 1.4.1

Rousset, B., S. Barbot, J.-P. Avouac, and Y.-J. Hsu (2012), Postseismic deformation following the 1999 Chi-Chi earthquake, Taiwan: Implication for lower-crust rheology, *Journal of Geophysical Research: Solid Earth*, *117*(B12), n/a–n/a, doi:10.1029/2012JB009571. 1.3.3

Ruina, A. (1983), Slip instability and state variable friction laws, *Journal of Geophysical Research*, *88*(B12), 10,359, doi:10.1029/JB088iB12p10359. 1.3.3

Rundle, J. B. (1982), Viscoelastic-gravitational deformation by a rectangular thrust fault in a layered Earth, *Journal of Geophysical Research*, *87*(B9), 7787, doi:10.1029/JB087iB09p07787. 1.4.1

Ryder, I., B. Parsons, T. J. Wright, and G. J. Funning (2007), Post-seismic motion following the 1997 Manyi (Tibet) earthquake: InSAR observations and modelling, *Geophysical Journal International*, *169*(3), 1009–1027, doi:10.1111/j.1365-246X.2006.03312.x. 1.1.2

Ryder, I., H. Wang, L. Bie, and A. Rietbrock (2014), Geodetic imaging of late postseismic lower crustal flow in Tibet, *Earth and Planetary Science Letters*, *404*, 136–143, doi:10.1016/j.epsl.2014.07.026. 1.3.3, 1.15

Sapkota, S. N., L. Bollinger, Y. Klinger, P. Tapponnier, Y. Gaudemer, and D. Tiwari (2013), Primary surface ruptures of the great Himalayan earthquakes in 1934 and 1255, *Nature Geoscience*, *6*, 71–76. 1.1.1

Savage, H. M., and E. E. Brodsky (2011), Collateral damage: Evolution with displacement of fracture distribution and secondary fault strands in fault damage zones, *Journal of Geophysical Research*, *116*(B3), B03,405, doi:10.1029/2010JB007665. 1.1.2, 1.3

Savage, J. C. (1983), A dislocation model of strain accumulation and release at a subduction zone, *Journal of Geophysical Research: Solid Earth*, *88*(B6), 4984–4996, doi:10.1029/JB088iB06p04984. 1.3.1

Savage, J. C. (1990), Equivalent strike-slip earthquake cycles in half-space and lithosphere-asthenosphere earth models, *Journal of Geophysical Research*, *95*(B4), 4873, doi:10.1029/JB095iB04p04873. 1.1.2, 1.3.3, 1.3.3

Savage, J. C., and R. O. Burford (1973), Geodetic determination of relative plate motion in central California, *Journal of Geophysical Research*, *78*(5), 832–845, doi:10.1029/JB078i005p00832. 1.3.1

Savage, J. C., and J. P. Church (1974), Evidence for postearthquake slip in the Fairview Peak, Dixie Valley, and Rainbow Mountain fault areas of Nevada, *Bulletin of the Seismological Society of America*, *64*(3-1), 687–698. 1.3

Savage, J. C., and W. H. Prescott (1978), Asthenosphere readjustment and the earthquake cycle, *Journal of Geophysical Research*, *83*(B7), 3369, doi:10.1029/JB083iB07p03369. 1.4.1

Schlupp, A., and A. Cisternas (2007), Source history of the 1905 great Mongolian earthquakes (Tsetserleg, Bolnay), *Geophysical Journal International*, *169*(3), 1115–1131, doi:10.1111/j.1365-246X.2007.03323.x. 1.1.1

Schorlemmer, D., S. Wiemer, and M. Wyss (2005), Variations in earthquake-size distribution across different stress regimes., *Nature*, *437*(7058), 539–42, doi:10.1038/nature04094. 1.1.2

Shui-Beih, Y., D. D. Jackson, Y. Guey-Kuen, and L. Chi-Ching (1990), Dislocation model for crustal deformation in the Longitudinal Valley area, Eastern Taiwan, *Tectonophysics*, *183*(1-4), 97–109, doi:10.1016/0040-1951(90)90190-J. 1.3.1

Sibson, R. H. (1974), Frictional constraints on thrust, wrench and normal faults, *Nature*, *249*(5457), 542–544, doi:10.1038/249542a0. 1.1.2

Smith, S. W., and M. Wyss (1968), Displacement on the San Andreas fault subsequent to the 1966 Parkfield earthquake, *Bulletin of the Seismological Society of America*, *58*(6), 1955–1973. 1.3, 1.14, 1.3.3

Spaans, K., and A. Hooper (2016), InSAR processing for volcano monitoring and other near-real time applications, *Journal of Geophysical Research: Solid Earth*, *121*(4), 2947–2960, doi:10.1002/2015JB012752. 1.2.2

Stein, R. S., G. C. P. King, and J. B. Rundle (1988), The Growth of Geological Structures by Repeated Earthquakes 2. Field Examples of Continental Dip-Slip Faults, *Journal of Geophysical Research: Solid Earth*, *93*(B11), 13,319–13,331, doi:10.1029/JB093iB11p13319. 1.4.4

Stevens, V. L., and J. P. Avouac (2015), Interseismic coupling on the main Himalayan thrust, *Geophysical Research Letters*, *42*(14), 5828–5837, doi:10.1002/2015GL064845. 1.3.1, 1.3.1, 1.4.4

Stiros, S., M. Arnold, P. Pirazzoli, J. Laborel, F. Laborel, and S. Papageorgiou (1992), Historical coseismic uplift on Euboea Island, Greece, *Earth and Planetary Science Letters*, *108*(1-3), 109–117, doi:10.1016/0012-821X(92)90063-2. 1.4.3

Stock, C., and E. G. C. Smith (2000), Evidence for different scaling of earthquake source parameters for large earthquakes depending on faulting mechanism, *Geophysical Journal International*, *143*(1), 157–162, doi:10.1046/j.1365-246x.2000.00225.x. 1.1.2

Suppe, J. (1983), Geometry and kinematics of fault-bend folding, *American Journal of Science*, *283*(7), 684–721, doi:10.2475/ajs.283.7.684. 1.4.4

Suppe, J. (2007), Absolute fault and crustal strength from wedge tapers, *Geology*, *35*(12), 1127, doi:10.1130/G24053A.1. 1.4.4

Tatar, M., D. Hatzfield, J. Martinod, A. Walpersdorf, M. Ghafori-Ashtiany, and J. Chéry (2002), The present-day deformation of the central Zagros from GPS measurements, *Geophysical Research Letters*, *29*(19), 1927, doi:10.1029/2002GL015427. 1.3.1

Thatcher, W. (1975), Strain accumulation on the northern San Andreas Fault Zone since 1906, *Journal of Geophysical Research*, *80*(35), 4873–4880, doi:10.1029/JB080i035p04873. 1.3

Thatcher, W. (1999), Present-Day Deformation Across the Basin and Range Province, Western United States, *Science*, *283*(5408), 1714–1718, doi:10.1126/science.283.5408.1714. 1.3.1

Titus, S. J., C. DeMets, and B. Tikoff (2006), Thirty-Five-Year Creep Rates for the Creeping Segment of the San Andreas Fault and the Effects of the 2004 Parkfield Earthquake: Constraints from Alignment Arrays, Continuous Global Positioning System, and Creepmeters, *Bulletin of the Seismological Society of America*, *96*(4B), S250–S268, doi:10.1785/0120050811. 1.3

Touzi, R., A. Lopes, J. Bruniquel, and P. Vachon (1999), Coherence estimation for SAR imagery, *IEEE Transactions on Geoscience and Remote Sensing*, *37*(1), 135–149, doi:10.1109/36.739146. 1.2.2

Tucker, B. E. (2004), Trends in Global Urban Earthquake Risk: A Call to the International Earth Science and Earthquake Engineering Communities, *Seismological Research Letters*, *75*(6), 695–700, doi:10.1785/gssrl.75.6.695. 1.1.1

van den Ende, M., J. Chen, J.-P. Ampuero, and A. Niemeijer (2018), A comparison between rate-and-state friction and microphysical models, based on numerical simulations of fault slip, *Tectonophysics*, *733*, 273–295, doi:10.1016/J.TECTO.2017.11.040. 1.3.3

Vergne, J., R. Cattin, and J. P. Avouac (2001), On the use of dislocations to model interseismic strain and stress build-up at intracontinental thrust faults, *Geophysical Journal International*, *147*(1), 155–162, doi:10.1046/j.1365-246X.2001.00524.x. 1.3.1

Vernant, P. (2015), What can we learn from 20 years of interseismic GPS measurements across strike-slip faults?, *Tectonophysics*, *644-645*, 22–39, doi:10.1016/j.tecto.2015.01.013. 1.1.2, 1.3.1

von Hagke, C., O. Oncken, and S. Evseev (2014), Critical taper analysis reveals lithological control of variations in detachment strength: An analysis of the Alpine basal detachment (Swiss Alps), *Geochemistry, Geophysics, Geosystems*, *15*(1), 176–191, doi:10.1002/2013GC005018. 1.4.4

Wald, D. J., T. H. Heaton, and K. W. Hudnut (1996), The slip history of the 1994 Northridge, California, earthquake determined from strong-motion, teleseismic, GPS, and leveling data, *Bulletin of the Seismological Society of America*, *86*(1B), S49–S70. 1.3.2

Walker, R. T., M. Talebian, R. A. Sloan, A. Rasheedi, M. Fattahi, and C. Bryant (2010), Holocene slip-rate on the Gowk strike-slip fault and implications for the distribution of tectonic strain in eastern Iran, *Geophysical Journal International*, *181*(1), 221–228, doi:10.1111/j.1365-246X.2010.04538.x. 1.4.3

Walker, R. T., E. A. Bergman, J. R. Elliott, E. J. Fielding, A.-R. Ghods, M. Ghoraishi, J. Jackson, H. Nazari, M. Nemati, B. Oveisi, M. Talebian, and R. J. Walters (2013), The 2010-2011 South Rigan (Baluchestan) earthquake sequence and its implications for distributed deformation and earthquake hazard in southeast Iran, *Geophysical Journal International*, *193*(1), 349–374, doi:10.1093/gji/ggs109. 1.3.2

Walters, R. J., J. R. Elliott, Z. Li, and B. Parsons (2013), Rapid strain accumulation on the Ashkabad fault (Turkmenistan) from atmosphere-corrected InSAR, *Journal of Geophysical Research: Solid Earth*, *118*(7), 3674–3690, doi:10.1002/jgrb.50236. 1.2.3

Walters, R. J., P. C. England, and G. A. Houseman (2017), Constraints from GPS measurements on the dynamics of the zone of convergence between Arabia and Eurasia, *Journal of Geophysical Research: Solid Earth*, *122*(2), 1470–1495, doi:10.1002/2016JB013370. 1.4.4

Watts, A., S. Zhong, and J. Hunter (2013), The Behavior of the Lithosphere on Seismic to Geologic Timescales, *Annual Review of Earth and Planetary Sciences*, *41*(1), 443–468, doi:10.1146/annurev-earth-042711-105457. 1.1.1, 1.1.2, 1.3.3

Wimpenny, S., A. Copley, and T. Ingleby (2017), Fault mechanics and post-seismic deformation at Bam, SE Iran, *Geophysical Journal International*, *209*(2), 1018–1035, doi:10.1093/gji/ggx065. 1.3.3

Wright, T. J., J. R. Elliott, H. Wang, and I. Ryder (2013), Earthquake cycle deformation and the Moho: Implications for the rheology of continental lithosphere, *Tectonophysics*, *609*, 504–523. 1.1.1, 1.1.2, 1.3, 1.3.3

Wu, Z. L., Y. G. Wan, and G. W. Zhou (2004), Focal Mechanism Dependence of a Few Seismic Phenomena and its Implications for the Physics of Earthquakes, *Pure and Applied Geophysics*, *161*(9-10), doi:10.1007/s00024-004-2543-0. 1.1.2

Yague-Martinez, N., P. Prats-Iraola, F. Rodriguez Gonzalez, R. Brcic, R. Shau, D. Geudtner, M. Eineder, and R. Bamler (2016), Interferometric Processing of Sentinel-1 TOPS Data, *IEEE Transactions on Geoscience and Remote Sensing*, *54*(4), 2220–2234, doi:10.1109/TGRS.2015.2497902. 1.2.2

Yamasaki, T., G. Houseman, I. Hamling, and E. Postek (2010), OREGANO_VE: a new parallelised 3D solver for the general (non-)linear Maxwell visco-elastic problem: validation and application to the calculation of surface deformation in the earthquake cycle, *EGU General Assembly 2010*. 1.4.1

Yamasaki, T., T. J. Wright, and G. A. Houseman (2014), Weak ductile shear zone beneath a major strike-slip fault: Inferences from earthquake cycle model constrained by geodetic observations of the western North Anatolian Fault Zone, *Journal of Geophysical Research: Solid Earth*, *119*(4), 3678–3699, doi:10.1002/2013JB010347. 1.1.2, 1.2

Yu, C., N. T. Penna, and Z. Li (2017), Generation of real-time mode high-resolution water vapor fields from GPS observations, *Journal of Geophysical Research: Atmospheres*, *122*(3), 2008–2025, doi:10.1002/2016JD025753. 1.2.3

Zhao, B., R. Bürgmann, D. Wang, K. Tan, R. Du, and R. Zhang (2017), Dominant Controls of Downdip Afterslip and Viscous Relaxation on the Postseismic Displacements Following the M_w 7.9 Gorkha, Nepal, Earthquake, *Journal of Geophysical Research: Solid Earth*, *122*(10), 8376–8401, doi:10.1002/2017JB014366. 1.3.3

Zhou, Y., M. Y. Thomas, B. Parsons, and R. T. Walker (2018), Time-dependent post-seismic slip following the 1978 Mw 7.3 Tabas-e-Golshan, Iran earthquake revealed by over 20 years of ESA InSAR observations, *Earth and Planetary Science Letters*, *483*, 64–75, doi:10.1016/J.EPSL.2017.12.005. 1.3.3

Chapter 2

Omori-like decay of postseismic velocities following continental earthquakes

T. Ingleby[1], and T.J. Wright[1]

[1] *COMET, School of Earth and Environment, University of Leeds, United Kingdom*

Citation: Ingleby, T., and T. J. Wright (2017), Omori–like decay of postseismic velocities following continental earthquakes, *Geophys. Res. Lett.*, 44, 31193130, doi:10.1002/2017GL072865

Abstract

Various mechanisms have been proposed to explain the transient, enhanced surface deformation rates following earthquakes. Unfortunately, these different mechanisms can produce very similar surface deformation patterns leading to difficulty in distinguishing between them. Here, we return to the observations themselves and compile near-field postseismic velocity measurements following moderate to large continental earthquakes. We find that these velocities have a remarkably consistent pattern, with velocity inversely proportional to time since the earthquake. This suggests that postseismic velocities show an Omori-like decay and that postseismic displacements increase logarithmically over time. These observations are inconsistent with simple, linear Maxwell or Burgers body viscoelastic relaxation mechanisms but are consistent with rate-and-state frictional afterslip models and power-law shear zone models. The results imply that postseismic surface deformation measurements are primarily the result of fault zone

processes, and therefore, that the inference of lower crustal viscosities from near-field postseismic deformation requires care.

2.1 Introduction

The rheology of the continental lithosphere remains poorly understood, with a number of different disciplines contributing sometimes conflicting observations. Glacial Isostatic Adjustment (GIA) studies in continental cratons suggest that the lithosphere has very high viscosities ($> 10^{22}$ Pa s) or behaves elastically (e.g. *Peltier and Drummond*, 2008, *Zhao et al.*, 2012) and generally resolve deep, mantle relaxation with viscosities on the order of 10^{20}-10^{21} Pa s. GIA studies examining plate boundary zones find much thinner elastic lithospheric thicknesses and mantle viscosities in the range 10^{18}-10^{19} Pa s (*James et al.*, 2000, *Ivins et al.*, 2011). On shorter timescales, surface deformation following the draining of lakes (e.g. *England et al.*, 2013) and strain concentration associated with interseismic deformation (e.g. *Johnson et al.*, 2007) also suggest relatively high lithospheric viscosities in the range 10^{19}-10^{22} Pa s.

Viscosity estimates obtained from early postseismic deformation are typically several orders of magnitude lower than those obtained from other disciplines ($\lesssim 10^{18}$ Pa s) (*Watts et al.*, 2013). Apparent viscosities are often seen to increase with time since the earthquake leading to inferences of various transient rheologies (e.g. *Pollitz*, 2003, *Ryder et al.*, 2007, *Freed et al.*, 2010). Whether these inferred viscosities apply to the lower crust, upper mantle or simply the fault zone itself is not always clear (*Bürgmann and Dresen*, 2008, *Wright et al.*, 2013). Furthermore, the observed surface deformation can also be explained by ongoing fault slip (afterslip) and it is often challenging to distinguish between these competing hypotheses (e.g. *Savage*, 1990, *Perfettini and Avouac*, 2004, *Ryder et al.*, 2007, *Hao et al.*, 2012, *Wright et al.*, 2013). Despite these common challenges, it has been possible to determine the predominant postseismic deformation mechanism in a selection of cases (e.g. *Jónsson et al.*, 2003, *Freed*, 2007, *Freed et al.*, 2007, *Jónsson*, 2008).

Many studies do not test multiple models against their postseismic data and so evaluating the relative importance of different deformation mechanisms is challenging. Different authors often reach very different conclusions about the lithosphere using similar observations from the same earthquake (*Wright et al.*, 2013). For example, postseismic deformation following the 1992 Landers earthquake has been attributed to deep afterslip (*Savage and Svarc*, 1997), poroelastic rebound and deep afterslip (*Fialko*, 2004), afterslip and fault zone contraction (*Massonnet et al.*, 1996), lower crustal relaxation (*Deng et al.*, 1998) and power-law mantle flow (*Freed and Bürgmann*, 2004).

Here, we compile postseismic observations from 34 moderate to large, continental, intra-crustal earthquakes/earthquake sequences. The majority of these observations

come from data sources within 25 km of the coseismic fault. We show that the temporal behaviour over timescales from hours to tens of years is remarkably consistent. The results support models in which rate-and-state frictional afterslip and/or viscoelastic relaxation of a power-law shear zone are the primary causes of postseismic deformation. We discuss the implications for the rheology of the continental lithosphere.

2.2 Data Collection

We compiled 151 postseismic velocity data points from 45 publications. These studies cover 34 continental earthquakes/earthquake sequences. The use of the full 3D deformation field through time provides the most information about postseismic processes and rheology. However, trying to combine this information from multiple earthquakes is challenging. Instead, we combine information about the temporal variation of velocities from multiple earthquakes. In order to collect a consistent data set across different earthquakes and time intervals, we extracted the maximum surface velocities observed in the studied time interval (see Tables A.1-A.4 in the supplementary material). If displacements are given at different time intervals for the same earthquake, we use the same observation point (where possible), and this criterion supersedes the criterion of picking the maximum amplitude signal. In other words, if the location of maximal displacement moves with time, we do not follow this and instead extract measurements from the same location through time.

We performed some basic quality control on each measurement by ensuring that the measurements were part of a spatially consistent deformation field. For example, an isolated large displacement or velocity measurement surrounded by much much smaller measurements was ignored. This helped to prevent anomalous, local site effects or erroneous processing from biasing our data. We do not report error bars on our measurements due to the variability in how errors are reported in the various studies used in the compilation.

The distance of the maximum deforming surface location from the coseismic fault is a reasonable proxy for the depth range of maximum deformation. Most of the maximum surface velocities come from points in the near-field (Figure 2.2), which will primarily be affected by near-field, shallow deformation. However, there are some points are at slightly larger distances, which may suggest deeper deformation (e.g. in the lower crust) is dominant. Whilst this focus on near-field measurements will produce an observational bias in our results, it makes a comparison between different earthquakes much more appropriate. Our results come from earthquakes which span a range of focal mechanisms, depths and magnitudes, and occurred in a variety of tectonic settings. This spread of data should reduce any observational bias from other factors and give us a somewhat representative sample of near-field postseismic deformation on the continents.

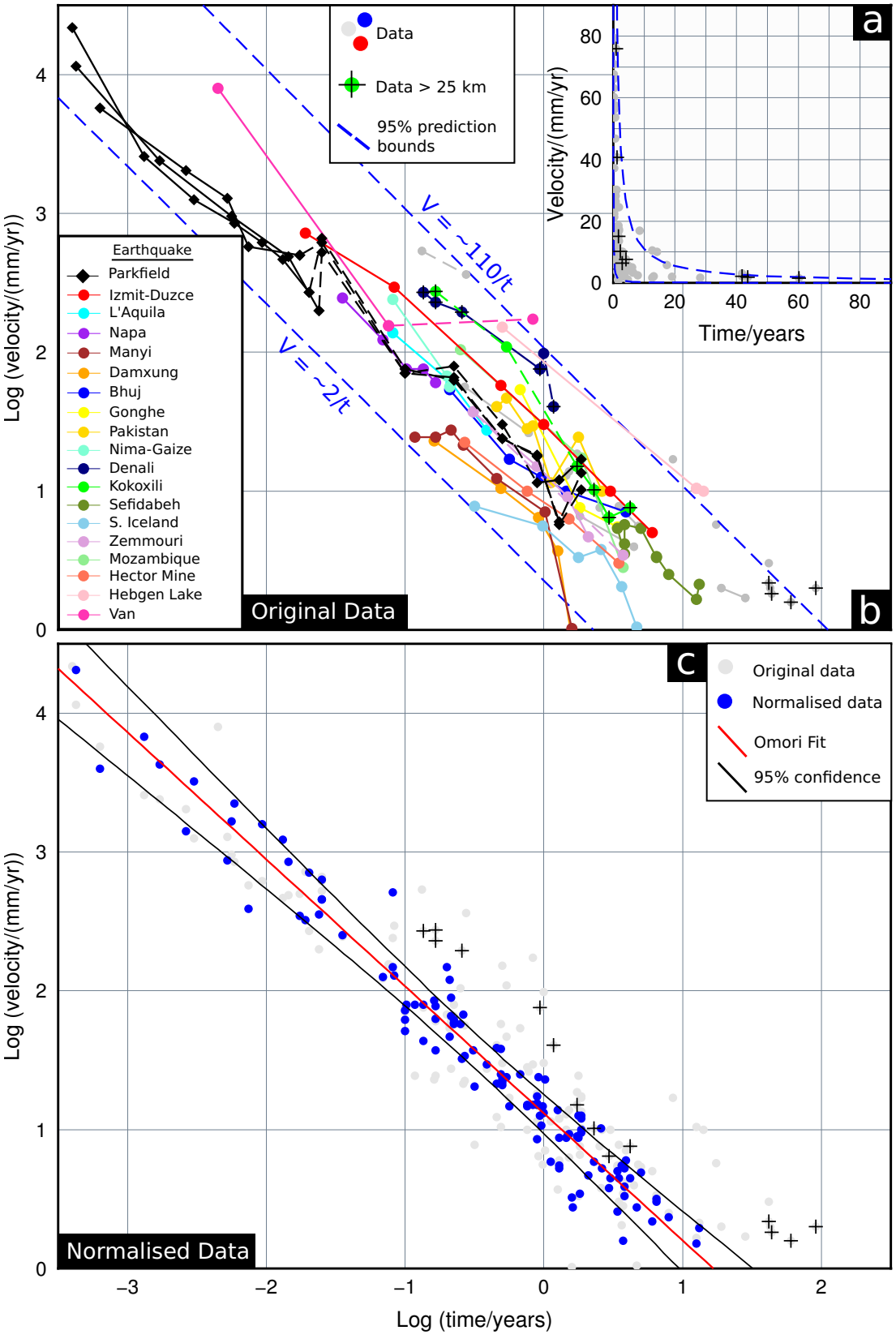
a
Data
Data > 25 km
95% prediction bounds
V = ~1/t
V = ~2/t
Velocity/(mm/yr)
Time/years
Earthquake
Parkfield
Izmit-Duzce
L'Aquila
Napa
Manyi
Damxung
Bhuj
Gonghe
Pakistan
Nima-Gaize
Denali
Kokoxili
Sefidabeh
S. Iceland
Zemmouri
Mozambique
Hector Mine
Hebgen Lake
Van
Original Data
b
c
Original data
Normalised data
Omori Fit
95% confidence
Normalised Data
Log (velocity/(mm/yr))
Log (time/years)

Furthermore, a variety of measurement techniques were used in the original studies, primarily GNSS (e.g. GPS), InSAR and levelling. GNSS is routinely used to study postseismic deformation; GNSS measurements account for 86 of our 151 data points. In general, horizontal displacements/velocities are reported and we extracted the maximum values, excluding any clear outliers. Interferometric Synthetic Aperture Radar (InSAR) has provided 55 of our 151 data points. InSAR measures the change in distance (range) between the satellite and the ground, equivalent to the projection of the 3D displacement vector in the satellite line-of-sight (LOS) direction. We chose to extract the maximum postseismic LOS displacement change for each earthquake. This approach may underestimate postseismic deformation if the predominant deformation direction is at a large angle to the satellite look direction. In practice, InSAR is most sensitive to vertical and east-west displacements. Levelling data records changes in height at particular points along transects and is the source of 10 data points in our compilation. The method allows dense spatial coverage along transects, but generally has sparse temporal coverage. Nevertheless, it allows us to study postseismic deformation from old earthquakes, for example from the 1940 Imperial Valley earthquake (*Reilinger*, 1984). This method is insensitive to horizontal motions, which is problematic for predominantly strike-slip earthquakes.

Isolating a postseismic signal in actively deforming regions of the earth requires the removal of other signals (e.g. interseismic deformation). Most of the studies in our compilation achieve this using data prior to the earthquake or well-established models of other deformation sources. We note those studies where this signal separation is not

Figure 2.1 ***(preceding page)*:** Variation of postseismic surface velocities through time. a: Zoom showing postseismic velocities over the first 90 years. Rapid, early postseismic velocities are cut off. Grey dots show data, black crosses are data points $\geqslant$ 25 km from the fault. Blue dashes show 95% prediction bounds. b: Coloured lines show time series of postseismic surface velocities from a number of continental earthquakes display a linear trend in log-log space. Grey data points show data from earthquakes with less than three postseismic observation times. Grey points joined by lines represent earthquakes where only 2 time series points have been acquired - dashed lines mean those two points came from different studies. Blue dashed lines as in a. c: Normalised results. Light grey circles represent the original data. Blue circles represent the data normalised using intercepts of linear trends through each earthquake time series (see text). Red line shows the best-fitting Omori model and black solid lines show the region where 95% of Omori models plot. Data sources: *Barbot et al.* (2008), *Atzori et al.* (2008), *Reddy et al.* (2012), *Calais et al.* (2002), *Hsu et al.* (2002), *Perfettini and Avouac* (2004), *Gourmelen and Amelung* (2005), *Hammond et al.* (2009), *Hetland and Hager* (2003), *Bie et al.* (2013), *Biggs et al.* (2009), *Freed et al.* (2006a), *Pollitz* (2005), *Lammali et al.* (1997), *Pollitz et al.* (2012), *Amoruso et al.* (2005), *Hao et al.* (2012), *Nishimura and Thatcher* (2003), *Reilinger* (1986), *Pollitz and Thatcher* (2010), *Reilinger* (1984), *Dalla Via* (2005), *Ergintav et al.* (2009), *Diao et al.* (2010), *Ryder et al.* (2011), *Deng et al.* (1998), *D'Agostino et al.* (2012), *Ryder et al.* (2007), *Vergnolle* (2003), *Copley et al.* (2012), *Floyd et al.* (2016), *Ryder et al.* (2010), *Deng et al.* (1999), *Jouanne et al.* (2011), *Barbot et al.* (2009), *Langbein* (2006), *Podgorski et al.* (2007), *Jónsson* (2008), *Copley and Reynolds* (2014), *Copley* (2014), *Riva et al.* (2007), *Dogan et al.* (2014), *Feng et al.* (2014), *Cetin et al.* (2012), *Mahsas et al.* (2008)

possible in Table S1 in the online supplement (e.g. *Calais et al.*, 2002, *Vergnolle*, 2003). The earliest velocity observations included in our compilation are 3.5 hours after an earthquake and the latest are 91.5 years after. Postseismic velocities range from over 10,000 mm/yr immediately following an earthquake to less than 1 mm/yr decades later. Using a log-log plot allows us to show the data clearly from all time scales (Figure 2.1). We connect data points from earthquakes where multiple postseismic deformation rates from different times after the earthquake were available.

In order to examine postseismic velocities at very early times we use data from GPS stations POMM, LAND and HUNT following the 2004 Parkfield earthquake (*Langbein*, 2006). We use the 30 minute solutions provided by *Langbein* (2006) to examine postseismic velocities very shortly after an earthquake. There is significant scatter in the individual 30 minute solutions but a clear trend is visible in the displacement time series. We perform a piece-wise linear fit to the data and extract the postseismic surface velocity over different intervals following the earthquake.

Approximately one hundred years after an earthquake, the postseismic signal is only just detectable with current measurement techniques. The latest postseismic velocity estimates we have are those from earthquakes in Mongolia, including the M 8.4 Bolnay earthquake (*Calais et al.*, 2002, *Vergnolle*, 2003). These estimates are dependent on models to deconvolve secular, long-lived deformation and transient, postseismic velocities and as such do not represent 'raw' observations. Despite this difficulty, the postseismic deformation estimates from these points agree with data from earlier in the postseismic phase.

The data show a remarkably simple trend in log-log space, with a gradient of approximately -1. Postseismic surface velocity (V) is inversely proportional to the time since the earthquake (t). This trend is evident in individual earthquakes as well as for the whole data set. With these results, we can estimate the range of possible postseismic surface velocities at a given time after an earthquake, assuming a $1/t$ relationship. Ninety-five percent of our postseismic velocities lie between the blue dashed lines on Figure 2.1, with a factor of approximately 55 separating the lower velocities and higher velocities at any time. This information may be particularly useful for targeting future studies of long-lived postseismic deformation, or deploying GNSS stations.

2.3 Data Analysis

2.3.1 Normalised Results

There is some scatter in the data which can be attributed to a number of factors. These earthquakes have different magnitudes, depths and mechanisms, have occurred in different parts of the world, and have been observed using different techniques at different distances from the coseismic fault. However, given the large number of variables which

could control postseismic surface velocities, it is surprising how little scatter there is in the data.

A linear regression on each of the individual earthquakes where three or more postseismic velocity measurements were available gave gradients with a mean of -0.96 and a standard deviation of 0.24. Coefficient of determination (R^2) values for these fits were generally high, with most (16 out of 22) higher than 0.9. The slope of the relationship is remarkably similar for all earthquakes, but there is a scale factor that affects the magnitude of postseismic velocities. To remove this effect we normalised each individual earthquake time series. The normalisation was based on the linear regression such that the linear fit for each earthquake had a value of 12.16 mm/yr ($\log V = 1.09$) at a time of 1 year ($\log t = 0$); this normalised the results to the mean linear fit to all the data. The normalised results show significant reduction in scatter and have a gradient of -0.92 ± 0.13 (95% confidence interval from Bayesian inversion) close to the average gradient of the individual earthquakes (Figure 2.1).

2.3.2 Scaling Factors

We investigate whether these postseismic velocities are dependent on a number of physical properties of the earthquake (moment, depth, focal mechanism) or are measuring artifacts (distance of the observation from the fault, measuring technique) (Figure 2.2). Earthquake stress drop is expected to play a significant role in determining the magnitude of any postseismic response. Larger stress drops result in greater stress transfer to neighbouring regions of the fault/lithosphere. However, the surface deformation resulting from regions releasing stress depends on how large these regions are (determined by magnitude), and where they are in the lithosphere (determined by depth and focal mechanism). Stress drops are not easily accessible or generally well resolved for all earthquakes in our compilation, and so we do not include this parameter in our analysis. We performed a Bayesian inversion to determine the linear regression coefficients and their errors for magnitude, distance from fault, CMT depth and time since the earthquake. Time exerted the strongest control, with magnitude and distance from fault playing secondary roles. We found that larger earthquakes generally produced greater postseismic velocities, and that velocities increased with distance from the fault (for distances up to 35 km). CMT depth appeared to play no significant role, but this may be due to large errors in the reported CMT depths.

On a larger scale, there may be scatter due to lateral rheological heterogeneity over the Earth's surface. To test this, we plot each earthquake's power-law decay coefficient at the location of the earthquake (see Figure A.1). We find no clear patterns, although higher decay coefficients are seen in the Tibetan plateau, suggesting that postseismic relaxation may occur more rapidly there. We also examined whether the best-fit velocity gradient or intercept varies with time after an earthquake by using the fits to individual earthquakes (see Figure A.2). There was no clear pattern, with both

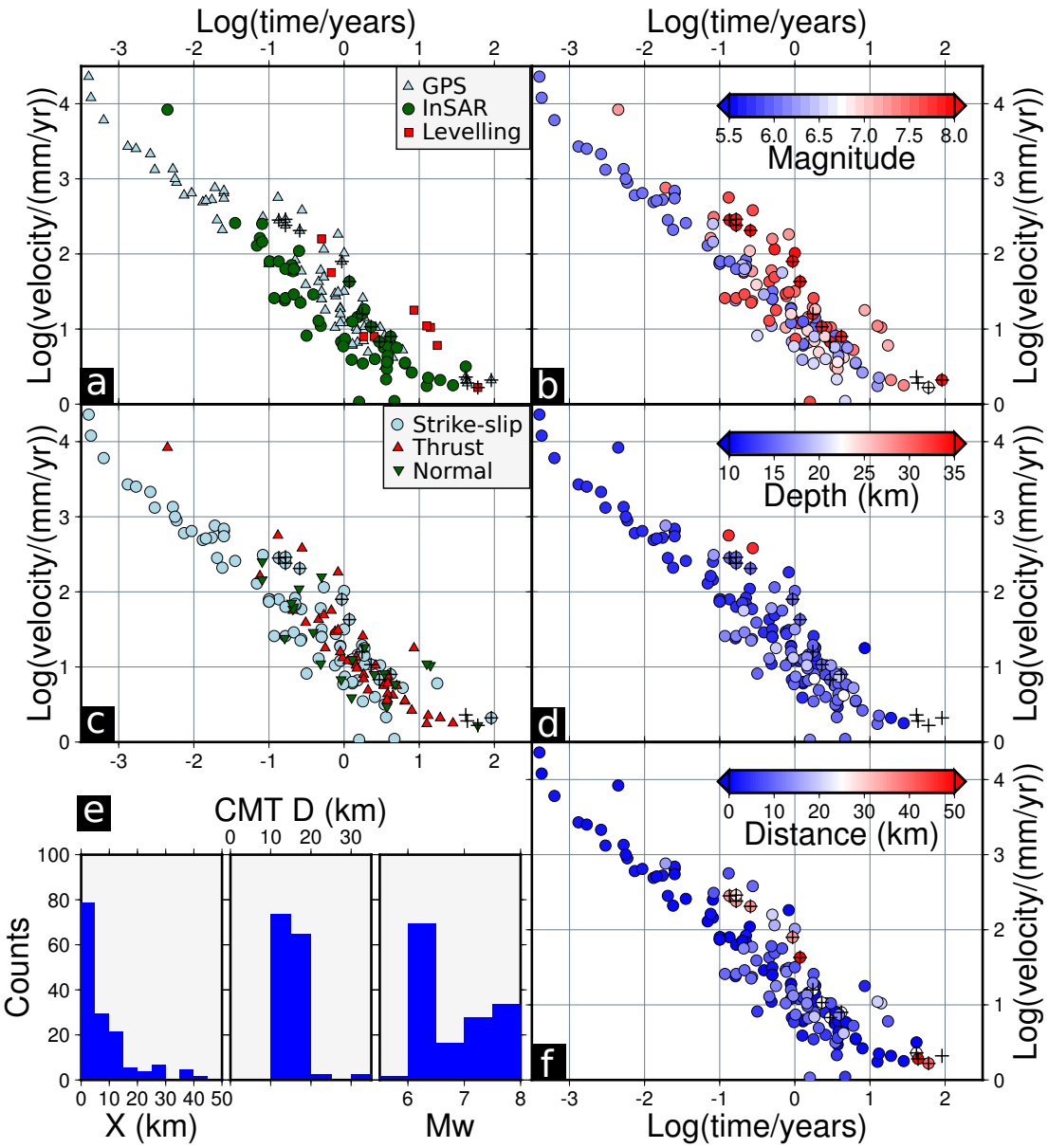

Figure 2.2: Variation of postseismic deformation results with other possible controls. a: variation with observation technique. b: variation with moment magnitude of the earthquake. c: variation with predominant focal mechanism. d: variation with CMT depth. e: histograms showing distribution of samples in terms of distance from fault (X), CMT depth and moment magnitude. f: variation with perpendicular distance between the measurement point and the fault.

velocity gradients and intercepts seemingly independent of time since the earthquake.

2.3.3 Consistency with Omori's Law

Our data compilation suggests that postseismic velocities can be fit using a version of Omori's law. *Utsu* (1957) developed the modified Omori's law which describes the number of aftershocks, n, expected at any time, t, after an earthquake:

$$n(t) = \frac{K}{(t+c)^p} \tag{2.1}$$

Our postseismic velocity compilation can be fit using an equation of the same form, where $n(t)$ is replaced with $V(t)$. We find that p values range between 0.80 and 1.04 (at 95% confidence).

2.4 Modelling

We use the temporal constraints provided by these observations to test postseismic relaxation models for the crust/upper mantle and fault zones. These models are all based on viscoelastic relaxation or afterslip. We do not consider poroelastic rebound here since this effect is only expected to last a short time following an earthquake (*Jónsson et al.*, 2003, *Fialko*, 2004, *Wright et al.*, 2013).

2.4.1 Linear Maxwell Models

The simplest rheological model usually invoked to explain postseismic deformation is the linear Maxwell model. A Maxwell material can be conceptualised as an elastic spring and viscous dash pot in series. In an earthquake there is an instantaneous elastic response followed by a decaying response through time as the material relaxes. Postseismic velocity in a Maxwell material will decay exponentially as:

$$V(t) = V_0 e^{\frac{-t}{\tau}} \tag{2.2}$$

where V_0 and τ are constants (e.g. *Montési*, 2004). The Maxwell relaxation time of the material (τ) is equal to the ratio of viscosity (η) to shear modulus (μ), and the instantaneous velocity (V_0) is inversely proportional to the relaxation time. Although instantaneous postseismic velocities at any time can be matched by this linear Maxwell model, it cannot explain the temporal decay. Low viscosities are required to explain rapid early motions whilst higher viscosities would be required to explain sustained slow motion (Figure 2.3).

A slightly more complicated linear rheology is a Burgers body. The Burgers body has a Maxwell material in series with a Kelvin (Voigt) material and shows two relaxation times (τ) (e.g. *Pollitz*, 2003, 2005). A transient phase of deformation is observed as

the Kelvin material relaxes which is superimposed on the longer timescale Maxwell relaxation. Postseismic motion in a Burgers rheology can be described using:

$$V(t) = V_0 \left[e^{-\frac{t}{\tau_1}} + K e^{-\frac{t}{\tau_2}} \right] \tag{2.3}$$

where $\tau_i = \frac{\eta_i}{\mu_i}$, V_0 is a constant initial velocity and K is a scalar (*Malkin and Isayev*, 2012). The curves produced by these analytical expressions have the same form as those produced using VISCO1D (*Pollitz*, 1992), suggesting the use of these expressions is valid. We perform a Bayesian inversion to obtain the maximum likelihood solution for a Burgers body (Figure 2.3). We find that a 1D Burgers body model can produce results within the scatter of the data. The acceptable ratios of relaxation times are shown in a histogram in Figure 2.3. If both relaxing elements have a similar shear modulus, then the ratio in relaxation times can be seen as a ratio in viscosities. We find viscosity ratios of approximately 100 best fit the data. This is larger than the typical ratios found in previous studies (*Ryder et al.*, 2011; and references therein), and is likely due to the need to explain a greater time range of observations simultaneously. Overall though, the model prediction is inconsistent with the linear log-log trends observed in both the overall data compilation and in individual earthquakes.

Linear Maxwell models and Burgers body models cannot adequately reproduce the temporal evolution observed for postseismic velocities over extended time periods. The addition of more viscoelastic relaxation elements (e.g. a continuum of viscosity values) is able to better reproduce the observed trends (*Hetland and Hager*, 2006). This viscosity variation may also be in space, for example with depth (*Riva and Govers*, 2009, *Yamasaki and Houseman*, 2012), or distance from the fault zone (e.g. *Yamasaki et al.*, 2014). Viscosity has an exponential dependence on depth leading to viscosity varying over orders of magnitude in the lithosphere (*Riva and Govers*, 2009, *Yamasaki and Houseman*, 2012). The sum of these various relaxing elements is capable of reproducing the linear trends seen in the data when viscosity varies over similar ranges found in nature (e.g. 10^{17} - 10^{21} Pa s).

2.4.2 Afterslip Models

The rate-and-state friction law (*Dieterich*, 1979) has been widely used to explain a number of fault-related phenomena including earthquakes, slow slip events, steady creep and afterslip. A number of authors have applied the rate-and-state friction law to postseismic afterslip (*Marone*, 1998, *Hearn*, 2002, *Barbot et al.*, 2009). Rate-and-state friction is often simplified by assuming the fault is close to the steady-state regime. Close to the steady-state regime the state variable is constant in time ($\dot{\theta} = 0$) and there is no loading stress rate. Under these conditions *Marone* (1998) showed that

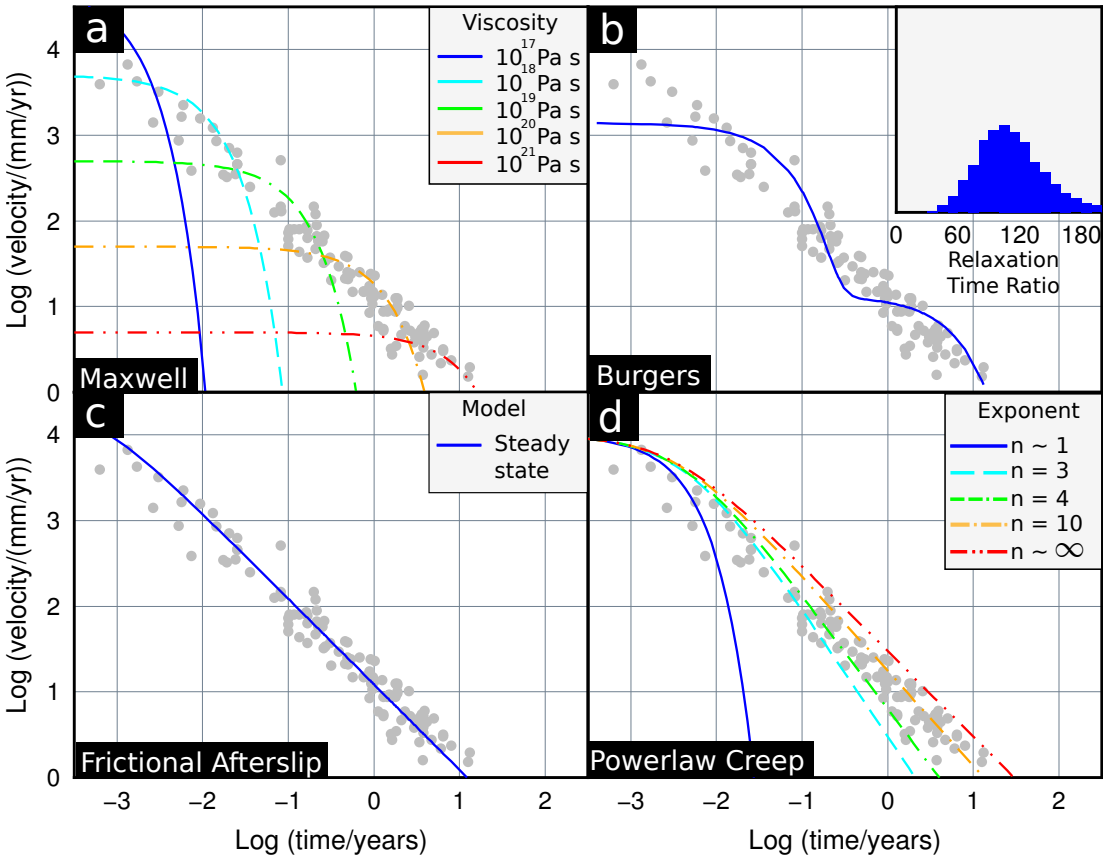

Figure 2.3: Modelling results. a: model runs for Maxwell elements with different viscosities. b: maximum likelihood model for a Burgers rheology with two relaxation times. Histogram shows acceptable relaxation time ratios. c: maximum likelihood model for a steady state afterslip model. d: model runs for power-law rheologies with different stress exponents.

postseismic velocities are:

$$V(t) = \frac{V_0}{1 + \frac{t}{\tau}} \tag{2.4}$$

where τ is a characteristic decay time. In this regime velocity is seen to decay with time following a $1/t$ relationship from an initial value V_0 (Figure 2.3). This is identical to the modified Omori's law formulation (equation 2.1) if $c = \tau$, $K = V_0\tau$ and $p = 1$. The model reproduces the overall temporal decay well.

2.4.3 Shear Zone Models

Montési (2004) investigated postseismic deformation in a power-law shear zone and derived a general relaxation law describing postseismic relaxation:

$$V_s(t) = V_0 \left[1 + \left(1 - \frac{1}{n}\right) \frac{t}{\tau}\right]^{\frac{-1}{\left(1-\frac{1}{n}\right)}} \tag{2.5}$$

where n is the power-law exponent. Non-linear rheologies are those where strain rate is proportional to stress raised to the value of the power-law exponent.

This relaxation law allows us to test various shear zone rheologies since the surface velocity is simply expected to be directly proportional to the shear zone velocity. The law simplifies to two end members. When $1/n \to 1$, the general law tends towards the following:

$$V_s(t) = V_0 e^{\frac{-t}{\tau}} \tag{2.6}$$

This equation defines Newtonian viscous flow in a shear zone and is identical to the linear Maxwell result (equation 2.2). This is shown as the blue line in Figure 2.3d. When $n \gg 1$ and therefore $1/n \to 0$ we obtain the equation for rate-and-state afterslip (equation 2.4) (*Montési*, 2004). From postseismic deformation alone, it is impossible to distinguish between postseismic relaxation of a shear zone with high n and frictional afterslip (see red line in Figure 2.3d). These models are also capable of explaining the overall pattern seen in our postseismic deformation data, provided the power-law exponent is greater than the usual range of experimentally determined values.

2.5 Discussion

2.5.1 Agreement with Common Postseismic Observations

Our compilation of observations is in agreement with a number of common postseismic observations which we outline below. Firstly, postseismic surface displacement time-series are commonly fit using logarithmic equations (e.g. *Donnellan and Lyzenga*, 1998,

Freed et al., 2006a, *Mahsas et al.*, 2008, *Dogan et al.*, 2014). These equations take the general form:

$$x(t) = C \ln(1 + \frac{t}{\tau}) \tag{2.7}$$

where C is a constant and τ is a time constant. If this equation is differentiated then we obtain the equation predicted by rate-and-state afterslip and/or relaxation of a high-n shear zone (i.e. $V \propto 1/t$ for high t). Our data also show that postseismic deformation takes an identical functional form to Omori's law describing the decay of aftershocks (equation 2.1). Typical p values lie in the range 0.6 – 2.5 with a median of about 1.1 (*Utsu et al.*, 1995). Our value for the decay of postseismic surface deformation through time has a p value of about 1 which shows that both post-earthquake processes decay at similar rates. Aftershock sequences for continental earthquakes can last for decades to centuries (e.g. *Ryall*, 1977, *Utsu et al.*, 1995, *Ebel et al.*, 2000, *Stein and Liu*, 2009) which is in agreement with the long postseismic deformation timescales included here. Many have noted the similar decay rates of aftershocks and afterslip velocity, leading to the proposition that aftershocks are primarily controlled by frictional afterslip (e.g. *Perfettini and Avouac*, 2004, *Savage et al.*, 2007, *Helmstetter and Shaw*, 2009).

When postseismic relaxation is explained using a viscoelastic material, many authors have noted an apparent increase in crustal/mantle viscosity through time following earthquakes (e.g. *Pollitz*, 2003, *Freed et al.*, 2006a, *Ryder et al.*, 2007). Our results support this observation and show that this trend continues over a period of 100 years (Figure 2.3). Maxwell viscoelastic models require an increase in effective viscosity through time in order to match the decreasing postseismic velocities. This changing effective viscosity is sometimes modeled using multiple layers with different viscosity (e.g. *Jónsson*, 2008, *Hetland and Hager*, 2006); a transient rheology like a Burgers body or standard linear solid (e.g. *Pollitz*, 2003, 2005, *Ryder et al.*, 2007, 2011); power-law rheologies (e.g. *Freed and Bürgmann*, 2004, *Freed et al.*, 2006b) or a combination of the above. Our compilation shows that any successful model must have a continuously changing viscosity, e.g. power-law models with high n or linear models with a large number of relaxation times.

2.5.2 Temporal Variation and Model Characteristics

We have sampled postseismic deformation over a long time period: from a number of hours after an earthquake up to almost one hundred years later. All these data define a linear trend in log-log space with a gradient close to minus one. This observation suggests that all continental earthquakes exhibit similar temporal postseismic deformation patterns and allows us to give bounds for expected postseismic velocities at any given time after an earthquake.

Univiscous linear Maxwell materials and Burgers bodies with just two relaxation

times cannot reproduce the linear trends seen in our compilation. Viscoelastic models need to be more complex with variations of viscosity in time, space or both. In sufficiently complex rheologies, the surface displacements can be described by a logarithmic function, which when differentiated will produce a $1/t$ relationship (*Hetland and Hager*, 2006). If viscosity varies sufficiently with depth, then the sum of the different relaxing layers can reproduce the linear trends seen in the data. The range of viscosities required to fit the data is similar to that proposed by (*Yamasaki and Houseman*, 2012).

Power-law creep can reproduce linear trends in log-log space as required by our data. This model is also supported by rock experimental results but the exponents found in these studies are usually between 2 and 5 (*Carter and Tsenn*, 1987, *Hirth and Kohlstedt*, 2003, *Freed and Bürgmann*, 2004). Our compilation requires higher power-law exponents: matching the gradient of the data to the same degree as the afterslip model requires an value for n of infinity. Such high values of n suggest brittle, rather than ductile deformation and suggest that either the experimental results cannot be scaled up to tectonic conditions or more likely, that afterslip is the dominant mechanism recorded by our data.

2.5.3 Localised Deformation

We find that the temporal variation of our near-field compilation is best explained by afterslip or power-law creep at high n. Afterslip is a very localised deformation mechanism, involving continued slip on the fault plane. *Moore and Parsons* (2015) found that a power-law rheology contributed to the narrowing of viscous shear zones. They found that narrow shear zones would develop in viscous materials where viscosity varies with depth, with shear-stress heating further narrowing the shear zone. Our data is consistent with a localisation of postseismic deformation as aseismic afterslip in the upper crust and in deep shear zones in the mid-lower crust.

Fault zone related processes best explaining our compilation is perhaps not surprising, since our surface velocity measurements are mostly from within a few km of the fault zone (Figure 2.2). These lengthscales are certainly small enough to be affected by processes centred on the fault zone (e.g. *Freed*, 2007) and may be dominated by fault zone processes rather than lithospheric relaxation. Furthermore, other strands of evidence support localised deformation in fault zones. Geodesy reveals that the majority of continental fault zones show significant strain localisation between earthquakes (*Wright et al.*, 2013, *Vernant*, 2015). Geological evidence from exhumed roots of faults shows that motion at depth is likely localised into shear zones up to a few kilometres wide (*Hanmer*, 1988, *Norris and Cooper*, 2003, *Vauchez and Tommasi*, 2003, *Frost et al.*, 2011). Seismic experiments have also shown deep narrow structures along the North Anatolian Fault in Turkey (*Fichtner et al.*, 2013, *Kahraman et al.*, 2015, *Taylor et al.*, 2016), the San Andreas (*Zhu*, 2000) and dip-slip faults in Tibet (*Zhang et al.*, 2014).

Both afterslip models and power-law creep models find support from other observations. Afterslip models can explain the temporal decay in aftershock frequency (*Helmstetter and Shaw*, 2009). The rate-and-state friction laws which form the basis for the afterslip models used here can also explain a large number of other aspects of the seismic cycle (*Dieterich*, 1994, *Marone*, 1998, *Liu and Rice*, 2005, *Helmstetter and Shaw*, 2009). At high temperatures and stresses, rocks deform by power-law creep in laboratory experiments (*Wilks and Carter*, 1990, *Kohlstedt et al.*, 1995, *Montési and Hirth*, 2003, *Bürgmann and Dresen*, 2008). These conditions may be prevalent in the deeper portions of fault zones.

Fault zone relaxation processes are usually considered to be relatively short-lived, but our data spans decades of the postseismic period. Afterslip has been observed in a few examples decades after earthquakes (*Reilinger*, 1984, *Kaneko et al.*, 2013, *Copley and Reynolds*, 2014, *Copley*, 2014) and often is not tested for on these long timescales. Studies examining postseismic deformation decades after an earthquake should consider the role of continued afterslip, especially for explaining near-fault observations.

Whilst afterslip/power-law creep can explain the temporal variation seen in our data, it is unclear whether it can explain the time varying spatial patterns of postseismic deformation. For example, immediately after an earthquake, poroelastic rebound may play a significant role in determining the spatial pattern of postseismic deformation (*Jónsson et al.*, 2003, *Fialko*, 2004) in the near field. Other studies have suggested that broad viscoelastic relaxation of the mantle is required to match far field observations, for example after the 2002 Denali (Alaska) earthquake (*Freed et al.*, 2006a) or the Landers and Hector Mine earthquakes in California (*Freed et al.*, 2007). In our study, measurements greater than 25 km away from the fault (marked with crosses on Figure 2.1c) are slightly separate from the main trend, suggesting a different mechanism may be operating here. While we argue that the temporal decay of postseismic deformation is a powerful discriminant between competing mechanisms, the spatial patterns of postseismic deformation have been enough to constrain the most important deformation mechanism in a selection of cases (e.g. *Jónsson et al.*, 2003, *Freed et al.*, 2006a, *Freed*, 2007, *Copley et al.*, 2012).

2.5.4 Implications

Despite these caveats, our findings have some important implications. Our compilation suggests that fault zone processes (afterslip or high n shear zones) generate the largest near-field postseismic signals. These signals may dominate postseismic deformation fields for decades, particularly at near-field sites. As such, caution should be exercised when interpreting lower-crustal viscosities derived from postseismic studies using predominantly near-field data.

Acknowledgments

T.I is funded by the UK Natural Environment Research Council (NERC) through the Leeds-York NERC Doctoral Training Program (NE/L002574/1). This work was supported by NERC through the Centre for the Observation and Modelling of Earthquakes, Volcanoes and Tectonics (COMET, http://comet.nerc.ac.uk). Figures were made using the Generic Mapping Tools (GMT) (*Wessel and Smith*, 1991). We thank Andy Hooper and Gregory Houseman for useful discussions. We thank the editor, Andrew Newman, and Roland Burgmann and Sylvain Barbot for thoughtful reviews which significantly improved the manuscript. A table with the compilation of postseismic velocities can be found in the supplementary material.

References

Amoruso, A., L. Crescentini, E. D'Anastasio, and P. M. De Martini (2005), Clues of postseismic relaxation for the 1915 Fucino earthquake (central Italy) from modeling of leveling data, *Geophysical Research Letters*, *32*(22), L22,307, doi:10.1029/2005GL024139. 2.1

Atzori, S., M. Manunta, G. Fornaro, A. Ganas, and S. Salvi (2008), Postseismic displacement of the 1999 Athens earthquake retrieved by the Differential Interferometry by Synthetic Aperture Radar time series, *Journal of Geophysical Research*, *113*(B9), B09,309, doi:10.1029/2007JB005504. 2.1

Barbot, S., Y. Hamiel, and Y. Fialko (2008), Space geodetic investigation of the coseismic and postseismic deformation due to the 2003 M w 7.2 Altai earthquake: Implications for the local lithospheric rheology, *Journal of Geophysical Research*, *113*(B3), B03,403, doi:10.1029/2007JB005063. 2.1

Barbot, S., Y. Fialko, and Y. Bock (2009), Postseismic deformation due to the M w 6.0 2004 Parkfield earthquake: Stress-driven creep on a fault with spatially variable rate-and-state friction parameters, *Journal of Geophysical Research*, *114*(B7), B07,405, doi:10.1029/2008JB005748. 2.1, 2.4.2

Bie, L., I. Ryder, S. E. J. Nippress, and R. Burgmann (2013), Coseismic and post-seismic activity associated with the 2008 Mw 6.3 Damxung earthquake, Tibet, constrained by InSAR, *Geophysical Journal International*, *196*(2), 788–803, doi:10.1093/gji/ggt444. 2.1

Biggs, J., R. Burgmann, J. T. Freymueller, Z. Lu, B. Parsons, I. Ryder, G. Schmalzle, and T. Wright (2009), The postseismic response to the 2002 M 7.9 Denali Fault earthquake: constraints from InSAR 2003-2005, *Geophysical Journal International*, *176*(2), 353–367, doi:10.1111/j.1365-246X.2008.03932.x. 2.1

Bürgmann, R., and G. Dresen (2008), Rheology of the Lower Crust and Upper Mantle: Evidence from Rock Mechanics, Geodesy, and Field Observations, *Annual Review of Earth and Planetary Sciences*, *36*, 531–567. 2.1, 2.5.3

Calais, E., M. Vergnolle, J. Déverchère, V. San'kov, A. Lukhnev, and S. Amarjargal (2002), Are post-seismic effects of the M = 8.4 Bolnay earthquake (1905 July 23) still influencing GPS velocities in the Mongolia-Baikal area?, *Geophysical Journal International*, *149*(1), 157–168, doi:10.1046/j.1365-246X.2002.01624.x. 2.1, 2.2

Carter, N. L., and M. C. Tsenn (1987), Flow properties of continental lithosphere, *Tectonophysics*, *136*(1-2), 27–63, doi:10.1016/0040-1951(87)90333-7. 2.5.2

Cetin, E., M. Meghraoui, Z. Cakir, A. M. Akoglu, O. Mimouni, and M. Chebbah (2012), Seven years of postseismic deformation following the 2003 Mw=6.8 Zemmouri earthquake (Algeria) from InSAR time series, *Geophysical Research Letters*, *39*(10), n/a–n/a, doi:10.1029/2012GL051344. 2.1

Copley, A. (2014), Postseismic afterslip 30 years after the 1978 Tabas-e-Golshan (Iran) earthquake: observations and implications for the geological evolution of thrust belts,

Geophysical Journal International, *197*(2), 665–679, doi:10.1093/gji/ggu023. 2.1, 2.5.3

Copley, A., and K. Reynolds (2014), Imaging topographic growth by long-lived postseismic afterslip at Sefidabeh, east Iran, *Tectonics*, *33*(3), 330–345, doi:10.1002/2013TC003462. 2.1, 2.5.3

Copley, A., J. Hollingsworth, and E. Bergman (2012), Constraints on fault and lithosphere rheology from the coseismic slip and postseismic afterslip of the 2006 M w 7.0 Mozambique earthquake, *Journal of Geophysical Research*, *117*(B3), B03,404, doi:10.1029/2011JB008580. 2.1, 2.5.3

D'Agostino, N., D. Cheloni, G. Fornaro, R. Giuliani, and D. Reale (2012), Space-time distribution of afterslip following the 2009 L'Aquila earthquake, *Journal of Geophysical Research*, *117*(B2), B02,402, doi:10.1029/2011JB008523. 2.1

Dalla Via, G. (2005), Lithospheric rheology in southern Italy inferred from postseismic viscoelastic relaxation following the 1980 Irpinia earthquake, *Journal of Geophysical Research*, *110*(B6), B06,311, doi:10.1029/2004JB003539. 2.1

Deng, J., M. Gurnis, H. Kanamori, and E. Hauksson (1998), Viscoelastic Flow in the Lower Crust after the 1992 Landers, California, Earthquake, *Science*, *282*(5394). 2.1, 2.1

Deng, J., K. Hudnut, M. Gurnis, and E. Hauksson (1999), Stress loading from viscous flow in the lower crust and triggering of aftershocks following the 1994 Northridge, California, Earthquake, *Geophysical Research Letters*, *26*(21), 3209–3212, doi:10.1029/1999GL010496. 2.1

Diao, F., X. Xiong, and R. Wang (2010), Mechanisms of Transient Postseismic Deformation Following the 2001 Mw 7.8 Kunlun (China) Earthquake, *Pure and Applied Geophysics*, *168*(5), 767–779, doi:10.1007/s00024-010-0154-5. 2.1

Dieterich, J. (1994), A constitutive law for rate of earthquake production and its application to earthquake clustering, *Journal of Geophysical Research*, *99*(B2), 2601, doi:10.1029/93JB02581. 2.5.3

Dieterich, J. H. (1979), Modeling of rock friction: 1. Experimental results and constitutive equations, *Journal of Geophysical Research*, *84*(B5), 2161, doi:10.1029/JB084iB05p02161. 2.4.2

Dogan, U., D. Ö. Demir, Z. Çakir, S. Ergintav, H. Ozener, A. M. Akoglu, S. S. Nalbant, and R. Reilinger (2014), Postseismic deformation following the M w 7.2, 23 October 2011 Van earthquake (Turkey): Evidence for aseismic fault reactivation, *Geophysical Research Letters*, *41*(7), 2334–2341, doi:10.1002/2014GL059291. 2.1, 2.5.1

Donnellan, A., and G. A. Lyzenga (1998), GPS observations of fault afterslip and upper crustal deformation following the Northridge earthquake, *Journal of Geophysical Research*, *103*(B9), 21,285, doi:10.1029/98JB01487. 2.5.1

Ebel, J. E., K.-P. Bonjer, and M. C. Oncescu (2000), Paleoseismicity: Seismicity Evidence for Past Large Earthquakes, *Seismological Research Letters*, *71*(2), 283–294, doi:10.1785/gssrl.71.2.283. 2.5.1

England, P. C., R. T. Walker, B. Fu, and M. A. Floyd (2013), A bound on the viscosity of the Tibetan crust from the horizontality of palaeolake shorelines, *Earth and Planetary Science Letters*, *375*, 44–56, doi:10.1016/j.epsl.2013.05.001. 2.1

Ergintav, S., S. McClusky, E. Hearn, R. Reilinger, R. Cakmak, T. Herring, H. Ozener, O. Lenk, and E. Tari (2009), Seven years of postseismic deformation following the 1999, M = 7.4 and M = 7.2, Izmit-Düzce, Turkey earthquake sequence, *Journal of Geophysical Research*, *114*(B7), B07,403, doi:10.1029/2008JB006021. 2.1

Feng, W., Z. Li, T. Hoey, Y. Zhang, R. Wang, S. Samsonov, Y. Li, and Z. Xu (2014), Patterns and mechanisms of coseismic and postseismic slips of the 2011 MW 7.1 Van (Turkey) earthquake revealed by multi-platform synthetic aperture radar interferometry, *Tectonophysics*, *632*, 188–198, doi:10.1016/j.tecto.2014.06.011. 2.1

Fialko, Y. (2004), Evidence of fluid-filled upper crust from observations of postseismic deformation due to the 1992 M w 7.3 Landers earthquake, *Journal of Geophysical Research: Solid Earth*, *109*(B8), n/a–n/a, doi:10.1029/2004JB002985. 2.1, 2.4, 2.5.3

Fichtner, A., E. Saygin, T. Taymaz, P. Cupillard, Y. Capdeville, and J. Trampert (2013), The deep structure of the North Anatolian Fault Zone, *Earth and Planetary Science Letters*, *373*, 109–117, doi:10.1016/j.epsl.2013.04.027. 2.5.3

Floyd, M. A., R. J. Walters, J. R. Elliott, G. J. Funning, J. L. Svarc, J. R. Murray, A. J. Hooper, Y. Larsen, P. Marinkovic, R. Bürgmann, I. A. Johanson, and T. J. Wright (2016), Spatial variations in fault friction related to lithology from rupture and afterslip of the 2014 South Napa, California, earthquake, *Geophysical Research Letters*, *43*(13), 6808–6816, doi:10.1002/2016GL069428. 2.1

Freed, A. M. (2007), Afterslip (and only afterslip) following the 2004 Parkfield, California, earthquake, *Geophysical Research Letters*, *34*(6), L06,312, doi:10.1029/2006GL029155. 2.1, 2.5.3

Freed, A. M., and R. Bürgmann (2004), Evidence of power-law flow in the Mojave desert mantle., *Nature*, *430*(6999), 548–51, doi:10.1038/nature02784. 2.1, 2.5.1, 2.5.2

Freed, A. M., R. Bürgmann, E. Calais, J. Freymueller, and S. Hreinsdóttir (2006a), Implications of deformation following the 2002 Denali, Alaska, earthquake for postseismic relaxation processes and lithospheric rheology, *Journal of Geophysical Research*, *111*(B1), B01,401, doi:10.1029/2005JB003894. 2.1, 2.5.1, 2.5.1, 2.5.3

Freed, A. M., R. Bürgmann, E. Calais, and J. Freymueller (2006b), Stress-dependent power-law flow in the upper mantle following the 2002 Denali, Alaska, earthquake, *Earth and Planetary Science Letters*, *252*(3-4), 481–489, doi:10.1016/j.epsl.2006.10.011. 2.5.1

Freed, A. M., R. Bürgmann, and T. Herring (2007), Far-reaching transient motions after Mojave earthquakes require broad mantle flow beneath a strong crust, *Geophysical Research Letters*, *34*(19), L19,302, doi:10.1029/2007GL030959. 2.1, 2.5.3

Freed, A. M., T. Herring, and R. Bürgmann (2010), Steady-state laboratory flow laws alone fail to explain postseismic observations, *Earth and Planetary Science Letters*, *300*(1-2), 1–10, doi:10.1016/j.epsl.2010.10.005. 2.1

Frost, E., J. Dolan, L. Ratschbacher, B. Hacker, and G. Seward (2011), Direct observation of fault zone structure at the brittle-ductile transition along the Salzach-Ennstal-Mariazell-Puchberg fault system, Austrian Alps, *Journal of Geophysical Research*, *116*(B2), B02,411, doi:10.1029/2010JB007719. 2.5.3

Gourmelen, N., and F. Amelung (2005), Postseismic mantle relaxation in the Central Nevada Seismic Belt., *Science (New York, N.Y.)*, *310*(5753), 1473–6, doi:10.1126/science.1119798. 2.1

Hammond, W. C., C. Kreemer, and G. Blewitt (2009), Geodetic constraints on contemporary deformation in the northern Walker Lane: 3. Central Nevada seismic belt postseismic relaxation, *Geological Society of America Special Papers*, *447*, 33–54, doi:10.1130/2009.2447(03). 2.1

Hanmer, S. (1988), Great Slave Lake Shear Zone, Canadian Shield: reconstructed vertical profile of a crustal-scale fault zone, *Tectonophysics*, *149*(3-4), 245–264, doi:10.1016/0040-1951(88)90176-X. 2.5.3

Hao, M., Z.-K. Shen, Q. Wang, and D. Cui (2012), Postseismic deformation mechanisms of the 1990 Mw 6.4 Gonghe, China earthquake constrained using leveling measurements, *Tectonophysics*, *532-535*, 205–214, doi:10.1016/j.tecto.2012.02.005. 2.1, 2.1

Hearn, E. H. (2002), Dynamics of Izmit Earthquake Postseismic Deformation and Loading of the Duzce Earthquake Hypocenter, *Bulletin of the Seismological Society of America*, *92*(1), 172–193, doi:10.1785/0120000832. 2.4.2

Helmstetter, A., and B. E. Shaw (2009), Afterslip and aftershocks in the rate-and-state friction law, *Journal of Geophysical Research*, *114*(B1), B01,308, doi:10.1029/2007JB005077. 2.5.1, 2.5.3

Hetland, E. A., and B. H. Hager (2003), Postseismic relaxation across the Central Nevada Seismic Belt, *Journal of Geophysical Research*, *108*(B8), 2394, doi:10.1029/2002JB002257. 2.1

Hetland, E. A., and B. H. Hager (2006), The effects of rheological layering on post-seismic deformation, *Geophysical Journal International*, *166*(1), 277–292, doi:10.1111/j.1365-246X.2006.02974.x. 2.4.1, 2.5.1, 2.5.2

Hirth, G., and D. Kohlstedt (2003), Rheology of the upper mantle and the mantle wedge: A view from the experimentalists, pp. 83–105, American Geophysical Union, doi:10.1029/138GM06. 2.5.2

Hsu, Y.-J., N. Bechor, P. Segall, S.-B. Yu, L.-C. Kuo, and K.-F. Ma (2002), Rapid afterslip following the 1999 Chi-Chi, Taiwan Earthquake, *Geophysical Research Letters*, *29*(16), 1–4–1–4, doi:10.1029/2002GL014967. 2.1

Ivins, E. R., M. M. Watkins, D.-N. Yuan, R. Dietrich, G. Casassa, and A. Rülke (2011), On-land ice loss and glacial isostatic adjustment at the Drake Passage: 20032009, *Journal of Geophysical Research*, *116*(B2), B02,403, doi:10.1029/2010JB007607. 2.1

James, T. S., J. J. Clague, K. Wang, and I. Hutchinson (2000), Postglacial rebound at the northern Cascadia subduction zone, *Quaternary Science Reviews*, *19*(14-15), 1527–1541, doi:10.1016/S0277-3791(00)00076-7. 2.1

Johnson, K. M., G. E. Hilley, and R. Bürgmann (2007), Influence of lithosphere viscosity structure on estimates of fault slip rate in the Mojave region of the San Andreas fault system, *Journal of Geophysical Research*, *112*(B7), B07,408, doi:10.1029/2006JB004842. 2.1

Jónsson, S. (2008), Importance of post-seismic viscous relaxation in southern Iceland, *Nature Geoscience*, *1*(2), 136–139, doi:10.1038/ngeo105. 2.1, 2.1, 2.5.1

Jónsson, S., P. Segall, R. Pedersen, and G. Björnsson (2003), Post-earthquake ground movements correlated to pore-pressure transients, *Nature*, *424*(6945), 179–183, doi:10.1038/nature01776. 2.1, 2.4, 2.5.3

Jouanne, F., A. Awan, A. Madji, A. Pêcher, M. Latif, A. Kausar, J. L. Mugnier, I. Khan, and N. A. Khan (2011), Postseismic deformation in Pakistan after the 8 October 2005 earthquake: Evidence of afterslip along a flat north of the Balakot-Bagh thrust, *Journal of Geophysical Research*, *116*(B7), B07,401, doi:10.1029/2010JB007903. 2.1

Kahraman, M., D. G. Cornwell, D. A. Thompson, S. Rost, G. A. Houseman, N. Türkelli, U. Teoman, S. Altuncu Poyraz, M. Utkucu, and L. Gülen (2015), Crustal-scale shear zones and heterogeneous structure beneath the North Anatolian Fault Zone, Turkey, revealed by a high-density seismometer array, *Earth and Planetary Science Letters*, *430*, 129–139, doi:10.1016/j.epsl.2015.08.014. 2.5.3

Kaneko, Y., Y. Fialko, D. T. Sandwell, X. Tong, and M. Furuya (2013), Interseismic deformation and creep along the central section of the North Anatolian Fault (Turkey): InSAR observations and implications for rate-and-state friction properties, *Journal of Geophysical Research: Solid Earth*, *118*(1), 316–331, doi:10.1029/2012JB009661. 2.5.3

Kohlstedt, D. L., B. Evans, and S. J. Mackwell (1995), Strength of the lithosphere: Constraints imposed by laboratory experiments, *Journal of Geophysical Research*, *100*(B9), 17,587, doi:10.1029/95JB01460. 2.5.3

Lammali, K., M. Bezzeghoud, F. Oussadou, D. Dimitrov, and H. Benhallou (1997), Postseismic deformation at El Asnam (Algeria) in the seismotectonic context of northwestern Algeria, *Geophysical Journal International*, *129*(3), 597–612, doi:10.1111/j.1365-246X.1997.tb04496.x. 2.1

Langbein, J. (2006), Coseismic and Initial Postseismic Deformation from the 2004 Parkfield, California, Earthquake, Observed by Global Positioning System, Electronic Distance Meter, Creepmeters, and Borehole Strainmeters, *Bulletin of the Seismological Society of America*, *96*(4B), S304–S320, doi:10.1785/0120050823. 2.1, 2.2

Liu, Y., and J. R. Rice (2005), Aseismic slip transients emerge spontaneously in three-dimensional rate and state modeling of subduction earthquake sequences, *Journal of Geophysical Research*, *110*(B8), B08,307, doi:10.1029/2004JB003424. 2.5.3

Mahsas, A., K. Lammali, K. Yelles, E. Calais, A. M. Freed, and P. Briole (2008), Shallow afterslip following the 2003 May 21, M w = 6.9 Boumerdes earthquake, Algeria, *Geophysical Journal International*, *172*(1), 155–166, doi:10.1111/j.1365-246X.2007.03594.x. 2.1, 2.5.1

Malkin, A. I., and A. I. Isayev (2012), *Rheology : concepts, methods, and applications*, 474 pp., ChemTec Pub. 2.4.1

Marone, C. (1998), Laboratory-derived friction laws and their application to seismic faulting, *Annual Review of Earth and Planetary Sciences*, *26*, 643–696. 2.4.2, 2.5.3

Massonnet, D., W. Thatcher, and H. Vadon (1996), Detection of postseismic fault-zone collapse following the Landers earthquake, *Nature*, *382*(6592), 612–616, doi:10.1038/382612a0. 2.1

Montési, L. G., and G. Hirth (2003), Grain size evolution and the rheology of ductile shear zones: from laboratory experiments to postseismic creep, *Earth and Planetary Science Letters*, *211*(1-2), 97–110, doi:10.1016/S0012-821X(03)00196-1. 2.5.3

Montési, L. G. J. (2004), Controls of shear zone rheology and tectonic loading on postseismic creep, *Journal of Geophysical Research*, *109*(B10), B10,404, doi:10.1029/2003JB002925. 2.4.1, 2.4.3, 2.4.3

Moore, J. D. P., and B. Parsons (2015), Scaling of viscous shear zones with depth-dependent viscosity and power-law stress-strain-rate dependence, *Geophysical Journal International*, *202*(1), 242–260, doi:10.1093/gji/ggv143. 2.5.3

Nishimura, T., and W. Thatcher (2003), Rheology of the lithosphere inferred from postseismic uplift following the 1959 Hebgen Lake earthquake, *Journal of Geophysical Research*, *108*(B8), 2389, doi:10.1029/2002JB002191. 2.1

Norris, R. J., and A. F. Cooper (2003), Very high strains recorded in mylonites along the Alpine Fault, New Zealand: implications for the deep structure of plate boundary faults, *Journal of Structural Geology*, *25*(12), 2141–2157, doi:10.1016/S0191-8141(03)00045-2. 2.5.3

Peltier, W. R., and R. Drummond (2008), Rheological stratification of the lithosphere: A direct inference based upon the geodetically observed pattern of the glacial isostatic adjustment of the North American continent, *Geophysical Research Letters*, *35*(16), L16,314, doi:10.1029/2008GL034586. 2.1

Perfettini, H., and J.-P. Avouac (2004), Postseismic relaxation driven by brittle creep: A possible mechanism to reconcile geodetic measurements and the decay rate of aftershocks, application to the Chi-Chi earthquake, Taiwan, *Journal of Geophysical Research*, *109*(B2), B02,304, doi:10.1029/2003JB002488. 2.1, 2.1, 2.5.1

Podgorski, J., E. H. Hearn, S. McClusky, R. Reilinger, T. Taymaz, O. Tan, M. Prilepin, T. Guseva, and M. Nadariya (2007), Postseismic deformation following the 1991 Racha, Georgia, earthquake, *Geophysical Research Letters*, *34*(4), L04,310, doi:10.1029/2006GL028477. 2.1

Pollitz, F. F. (1992), Postseismic relaxation theory on the spherical earth, *Bulletin of the Seismological Society of America*, *82*(1), 422–453. 2.4.1

Pollitz, F. F. (2003), Transient rheology of the uppermost mantle beneath the Mojave Desert, California, *Earth and Planetary Science Letters*, *215*(1-2), 89–104, doi:10.1016/S0012-821X(03)00432-1. 2.1, 2.4.1, 2.5.1

Pollitz, F. F. (2005), Transient rheology of the upper mantle beneath central Alaska inferred from the crustal velocity field following the 2002 Denali earthquake, *Journal of Geophysical Research*, *110*(B8), B08,407, doi:10.1029/2005JB003672. 2.1, 2.4.1, 2.5.1

Pollitz, F. F., and W. Thatcher (2010), On the resolution of shallow mantle viscosity structure using postearthquake relaxation data: Application to the 1999 Hector Mine, California, earthquake, *Journal of Geophysical Research*, *115*(B10), B10,412, doi:10.1029/2010JB007405. 2.1

Pollitz, F. F., R. Bürgmann, and W. Thatcher (2012), Illumination of rheological mantle heterogeneity by the M7.2 2010 El Mayor-Cucapah earthquake, *Geochemistry, Geophysics, Geosystems*, *13*(6), n/a–n/a, doi:10.1029/2012GC004139. 2.1

Reddy, C. D., P. S. Sunil, R. Bürgmann, D. V. Chandrasekhar, and T. Kato (2012), Postseismic relaxation due to Bhuj earthquake on January 26, 2001: possible mechanisms and processes, *Natural Hazards*, *65*(2), 1119–1134, doi:10.1007/s11069-012-0184-7. 2.1

Reilinger, R. (1984), Coseismic and postseismic vertical movements associated with the 1940 M 7.1 Imperial Valley, California, earthquake, *Journal of Geophysical Research*, *89*(B6), 4531, doi:10.1029/JB089iB06p04531. 2.2, 2.1, 2.5.3

Reilinger, R. (1986), Evidence for postseismic viscoelastic relaxation following the 1959 M = 7.5 Hebgen Lake, Montana, Earthquake, *Journal of Geophysical Research*, *91*(B9), 9488, doi:10.1029/JB091iB09p09488. 2.1

Riva, R. E. M., and R. Govers (2009), Relating viscosities from postseismic relaxation to a realistic viscosity structure for the lithosphere, *Geophysical Journal International*, *176*(2), 614–624, doi:10.1111/j.1365-246X.2008.04004.x. 2.4.1

Riva, R. E. M., A. Borghi, A. Aoudia, R. Barzaghi, R. Sabadini, and G. F. Panza (2007), Viscoelastic relaxation and long-lasting after-slip following the 1997 Umbria-Marche (Central Italy) earthquakes, *Geophysical Journal International*, *169*(2), 534–546, doi:10.1111/j.1365-246X.2007.03315.x. 2.1

Ryall, A. (1977), Earthquake hazard in the Nevada region, *Bulletin of the Seismological Society of America*, *67*(2), 517–532. 2.5.1

Ryder, I., B. Parsons, T. J. Wright, and G. J. Funning (2007), Post-seismic motion following the 1997 Manyi (Tibet) earthquake: InSAR observations and modelling, *Geophysical Journal International*, *169*(3), 1009–1027, doi:10.1111/j.1365-246X.2006.03312.x. 2.1, 2.1, 2.5.1

Ryder, I., R. Bürgmann, and J. Sun (2010), Tandem afterslip on connected fault planes following the 2008 Nima-Gaize (Tibet) earthquake, *Journal of Geophysical Research*, *115*(B3), B03,404, doi:10.1029/2009JB006423. 2.1

Ryder, I., R. Bürgmann, and F. Pollitz (2011), Lower crustal relaxation beneath the Tibetan Plateau and Qaidam Basin following the 2001 Kokoxili earthquake, *Geophysical Journal International*, *187*(2), 613–630, doi:10.1111/j.1365-246X.2011.05179.x. 2.1, 2.4.1, 2.5.1

Savage, J. C. (1990), Equivalent strike-slip earthquake cycles in half-space and lithosphere-asthenosphere earth models, *Journal of Geophysical Research*, *95*(B4), 4873, doi:10.1029/JB095iB04p04873. 2.1

Savage, J. C., and J. L. Svarc (1997), Postseismic deformation associated with the 1992 Mw = 7.3 Landers earthquake, southern California, *Journal of Geophysical Research: Solid Earth*, *102*(B4), 7565–7577, doi:10.1029/97JB00210. 2.1

Savage, J. C., J. L. Svarc, and S.-B. Yu (2007), Postseismic relaxation and aftershocks, *Journal of Geophysical Research*, *112*(B6), B06,406, doi:10.1029/2006JB004584. 2.5.1

Stein, S., and M. Liu (2009), Long aftershock sequences within continents and implications for earthquake hazard assessment., *Nature*, *462*(7269), 87–9, doi:10.1038/nature08502. 2.5.1

Taylor, G., S. Rost, and G. Houseman (2016), Crustal Imaging Across the North Anatolian Fault Zone from the Auto-Correlation of Ambient Seismic Noise, *Geophysical Research Letters*. 2.5.3

Utsu, T. (1957), Magnitude of Earthquakes and Occurrence of their Aftershocks, *Zisin (Journal of the Seismological Society of Japan. 2nd ser.)*, *10*(1), 35. 2.3.3

Utsu, T., Y. Ogata, and R. S (1995), The Centenary of the Omori Formula for a Decay Law of Aftershock Activity., *Journal of Physics of the Earth*, *43*(1), 1–33, doi:10.4294/jpe1952.43.1. 2.5.1

Vauchez, A., and A. Tommasi (2003), Wrench faults down to the asthenosphere: geological and geophysical evidence and thermomechanical effects, *Geological Society, London, Special Publications*, *210*(1), 15–34, doi:10.1144/GSL.SP.2003.210.01.02. 2.5.3

Vergnolle, M. (2003), Constraints on the viscosity of the continental crust and mantle from GPS measurements and postseismic deformation models in western Mongolia, *Journal of Geophysical Research*, *108*(B10), 2502, doi:10.1029/2002JB002374. 2.1, 2.2

Vernant, P. (2015), What can we learn from 20 years of interseismic GPS measurements across strike-slip faults?, *Tectonophysics*, *644-645*, 22–39, doi:10.1016/j.tecto.2015.01.013. 2.5.3

Watts, A., S. Zhong, and J. Hunter (2013), The Behavior of the Lithosphere on Seismic to Geologic Timescales, *Annual Review of Earth and Planetary Sciences*, *41*(1), 443–468, doi:10.1146/annurev-earth-042711-105457. 2.1

Wessel, P., and W. H. F. Smith (1991), Free software helps map and display data, *Eos, Transactions American Geophysical Union*, *72*(41), 441–441, doi:10.1029/90EO00319. 2.5.4

Wilks, K. R., and N. L. Carter (1990), Rheology of some continental lower crustal rocks, *Tectonophysics*, *182*(1-2), 57–77, doi:10.1016/0040-1951(90)90342-6. 2.5.3

Wright, T. J., J. R. Elliott, H. Wang, and I. Ryder (2013), Earthquake cycle deformation and the Moho: Implications for the rheology of continental lithosphere, *Tectonophysics*, *609*, 504–523. 2.1, 2.4, 2.5.3

Yamasaki, T., and G. A. Houseman (2012), The crustal viscosity gradient measured from post-seismic deformation: A case study of the 1997 Manyi (Tibet) earthquake, *Earth and Planetary Science Letters*, *351-352*, 105–114, doi:10.1016/j.epsl.2012.07.030. 2.4.1, 2.5.2

Yamasaki, T., T. J. Wright, and G. A. Houseman (2014), Weak ductile shear zone beneath a major strike-slip fault: Inferences from earthquake cycle model constrained by geodetic observations of the western North Anatolian Fault Zone, *Journal of Geophysical Research: Solid Earth*, *119*(4), 3678–3699, doi:10.1002/2013JB010347. 2.4.1

Zhang, Z., Y. Wang, G. A. Houseman, T. Xu, Z. Wu, X. Yuan, Y. Chen, X. Tian, Z. Bai, and J. Teng (2014), The Moho beneath western Tibet: Shear zones and eclogitization in the lower crust, *Earth and Planetary Science Letters*, *408*, 370–377, doi:10.1016/j.epsl.2014.10.022. 2.5.3

Zhao, S., K. Lambeck, and M. Lidberg (2012), Lithosphere thickness and mantle viscosity inverted from GPS-derived deformation rates in Fennoscandia, *Geophysical Journal International*, *190*(1), 278–292, doi:10.1111/j.1365-246X.2012.05454.x. 2.1

Zhu, L. (2000), Crustal structure across the San Andreas Fault, southern California from teleseismic converted waves, *Earth and Planetary Science Letters*, *179*(1), 183–190, doi:10.1016/S0012-821X(00)00101-1. 2.5.3

Chapter 3

Constraints on the geometry and frictional properties of the Main Himalayan Thrust using co-, post- and interseismic deformation in Nepal

T. Ingleby[1], T.J. Wright[1], A. Hooper[1], T.J. Craig[1] and J.R. Elliott[1]

[1] *COMET, School of Earth and Environment, University of Leeds, United Kingdom*

In revision for the *Journal of Geophysical Research: Solid Earth*

Abstract

The geometry and frictional properties of a fault system are key parameters required to understand its seismic behaviour. The Main Himalayan Thrust in Nepal is the type example of a continental megathrust and forms part of a fault system which accommodates a significant fraction of India-Eurasia convergence. Despite extensive study of this zone of shortening, the geometry of the fault system remains controversial. Here, we use interseismic, coseismic and postseismic geodetic data in Nepal to investigate the proposed down-dip geometries. We use interseismic and coseismic data from previous studies, acquired before and during the 2015 M_w 7.8 Gorkha earthquake. We then supplement these by processing our own postseismic deformation data, acquired following the Gorkha earthquake. We find that kinematic modelling of geodetic data alone cannot easily distinguish between the previously proposed geometries. We therefore

develop a mechanical joint coseismic-postseismic slip inversion which simultaneously solves for the distribution of coseismic slip and rate-strengthening friction parameters. We run this inversion using the proposed geometries and find that they are all capable of explaining the majority of geodetic data. We find values for the rate parameter, a, from the rate-and-state friction law that are between $0.8 - 1.6 \times 10^{-3}$, depending on the geometry used. These values are in agreement with results from laboratory studies and those inferred from other earthquakes. We suggest that the limitations of earthquake cycle geodesy partly explain the continued controversy over the geometry and role of various faults in the Nepal Himalaya.

3.1 Introduction

Continental megathrusts are capable of hosting some of the largest earthquakes in the world (*Hubbard et al.*, 2015). The size of dip-slip faulting earthquakes can be controlled by the down-dip geometry of the fault system (e.g. *Elliott et al.*, 2011, *Bonini et al.*, 2014, *Hubbard et al.*, 2016), and as such, the geometry of these fault systems is important for seismic hazard analysis. In addition to geometrical complexities playing a role in rupture size, regions with different frictional properties are also thought to be significant in controlling rupture propagation and arrest (e.g. *Perfettini et al.*, 2010, *Jolivet et al.*, 2015, *Avouac et al.*, 2015).

The type example of a continental megathrust is the fault system underlying the Nepal Himalaya. India is currently converging with Eurasia at a rate of approximately 40 mm/yr, with roughly half of this convergence accommodated in the Himalaya on the southern border of the Tibetan Plateau (*Stevens and Avouac*, 2015). The way in which this convergence is accommodated remains controversial. In particular, the geometry of the system of faults over which shortening occurs is still debated (e.g. *Pandey et al.*, 1995, *Lavé and Avouac*, 2001, *Hodges et al.*, 2004, *Wobus et al.*, 2005).

The M_W 7.8 Gorkha earthquake of 25th April 2015 has presented an opportunity to learn more about the causative fault system, with a large number of studies examining the rupture in detail. Unfortunately, a consensus has not yet emerged, and instead, the earthquake has highlighted the variety of possible geometries that can be inferred from a range of data sets. Geometries used to model coseismic slip include single planes (e.g. *Avouac et al.*, 2015), faults incorporating a laterally-continuous (e.g. *Elliott et al.*, 2016) or spatially-varying (e.g. *Hubbard et al.*, 2016) mid-crustal ramp, and models including a shallow splay fault (e.g. *Whipple et al.*, 2016). Section 3.3 contains a more detailed explanation of the different proposed geometries.

Geodetic techniques such as Global Navigation Satellite Systems (GNSS), Interferometric Synthetic Aperture Radar (InSAR), SAR/optical pixel tracking and levelling are powerful tools for investigating fault geometry and slip at depth. Most of the works examining the Gorkha rupture have used geodesy to either infer the fault geometry

(*Wang and Fialko*, 2015, *Elliott et al.*, 2016, *Whipple et al.*, 2016) or constrain the distribution of slip on an assumed geometry (*Avouac et al.*, 2015, *Lindsey et al.*, 2015, *Galetzka et al.*, 2015, *Grandin et al.*, 2015, *Hubbard et al.*, 2016). *Elliott et al.* (2016) used interseismic deformation data as a further constraint in their investigation of possible fault geometries, although they solved for coseismic and interseismic geometries independently.

Here, we use geodetic data from each stage of the earthquake cycle in Nepal to test different down-dip fault geometries. We seek time-invariant fault geometries that are capable of matching surface geodetic data satisfactorily, given estimates of their uncertainties. Coseismic and interseismic deformation data are readily available for Nepal, having been acquired prior to and during the 2015 M_w 7.8 Gorkha earthquake (e.g. *Lindsey et al.*, 2015, *Galetzka et al.*, 2015, *Elliott et al.*, 2016, *Jackson and Bilham*, 1994, *Ader et al.*, 2012). However, the postseismic deformation that followed is less well studied (*Gualandi et al.*, 2016, *Sreejith et al.*, 2016, *Mencin et al.*, 2016, *Zhao et al.*, 2017, *Jiang et al.*, 2018, *Wang and Fialko*, 2018). These postseismic studies find a relatively small deformation signal, which is more dependent on the data processing methods applied. We therefore independently process GNSS and InSAR data using different approaches to previous studies over Nepal to obtain our own postseismic deformation measurements.

Deriving these postseismic deformation measurements also enables us to examine the continuing and evolving hazard following the Nepal earthquake. Palaeoseismology has shown that previous earthquakes have ruptured all the way to the surface, with many metres of slip along the Main Frontal Thrust (MFT) (*Sapkota et al.*, 2013). However, the Gorkha earthquake failed to rupture to the surface, meaning a large section of the Main Himalayan Thrust (MHT) likely remains capable of producing future damaging earthquakes. Furthermore, the region to the west of the Gorkha earthquake remains an area of concern. The last large earthquake to occur here was in 1505 and could have exceeded M_W 8.5, leading to a potential slip deficit of over 10 m (*Bilham and Wallace*, 2005, *Avouac et al.*, 2015). An alternative means of releasing strain on these portions of the MHT is through aseismic afterslip, which has been observed following a large number of earthquakes (*Hearn*, 2002, *Freed*, 2007, *Wright et al.*, 2013, *Ingleby and Wright*, 2017). Determining which parts of the MHT are slipping aseismically is vital for assessing the ongoing seismic hazard in the region (*Avouac et al.*, 2015).

Furthermore, any afterslip can be used to investigate the frictional properties of the sliding faults (e.g. *Perfettini and Avouac*, 2004, *Barbot and Fialko*, 2010, *Copley and Jolivet*, 2016, *Wimpenny et al.*, 2017). Using the geometries constrained by earthquake cycle geodesy, we can obtain the stress transferred to other regions of the fault due to the earthquake. The relationship between the calculated stress change in these regions and the resulting inferred afterslip allows us to place constraints on frictional properties

on the major faults in Nepal.

We begin by obtaining measurements of the postseismic deformation following the Gorkha event using GNSS and InSAR. Following this, we investigate possible fault geometries within Nepal in light of deformation data from various stages of the earthquake cycle. Finally, we use these geometries as a starting point for determining the frictional properties of the fault system by inverting for a self-consistent mechanical model of coseismic and postseismic slip.

3.2 Measurements of Postseismic Deformation

3.2.1 Previous Studies

There have been a number of postseismic deformation studies following the Gorkha event. *Gualandi et al.* (2016) used continuous GNSS stations in Nepal to study the transient postseismic deformation up until November 2015. They isolated the postseismic signal using Independent Component Analysis and found that GNSS stations showed predominantly southwards motion with the amount of motion increasing to a maximum of approximately 65 mm at CHLM. *Mencin et al.* (2016) also used GNSS stations to examine deformation following the Gorkha earthquake. They isolated the postseismic signal using a combination of interseismic and hydrological loading models and found a similar pattern of deformation to *Gualandi et al.* (2016). One problem faced by both of these studies is the lack of GNSS data on the Tibetan plateau. This means that inferred postseismic deformation models are largely unconstrained north of the Himalayan range. *Zhao et al.* (2017) and *Jiang et al.* (2018) supplemented GNSS stations south of the Himalayan range with a small number of stations operating in southern Tibet. These far-field stations record small postseismic displacements towards the rupture zone, whilst the stations south of the range show similar displacements to other studies.

Sreejith et al. (2016) used InSAR, combined with four GNSS station time series to examine postseismic deformation up to 88 days after the main shock. Their InSAR data provides further constraints to the north of the Himalayan range and supplements the GNSS data constraints. The InSAR results show a range decrease of 10 - 15 cm consistent with uplift north of the coseismic rupture. This is in broad agreement with GNSS stations showing increasing deformation to the north. *Wang and Fialko* (2018) present the most comprehensive range of postseismic deformation data to date, with GNSS data south of the Himalayan range up until March 2017 and InSAR data from several satellite tracks. Their results agree with the picture given by previous studies, and their InSAR data suggest relatively localised uplift north of the coseismic rupture.

Here, we use a combination of GNSS and InSAR data to measure the surface deformation following the Gorkha event. We use a Bayesian technique to estimate the GNSS

postseismic position uncertainties and construct an InSAR time series using StaMPS (*Hooper et al.*, 2012).

3.2.2 Data Sets

GNSS Data

We use GNSS stations which were deployed and maintained through a collaboration between California Institute of Technology and the Department of Mines and Geology (Nepal). Some additional stations were deployed by Roger Bilham, Rebecca Bendick, and David Mencin following the 2015 Gorkha earthquake. We use the 24-hour final daily position time series processed by the Nevada Geodetic Laboratory (`http://geodesy.unr.edu/`; last accessed on 23/8/2017) for all stations within the Nepal region. These daily solutions are processed using GIPSY/OASIS-ii Version 6.1.1 developed by JPL and are provided in the IGS08 reference frame. Full details of the processing are available online (`http://geodesy.unr.edu/gps/ngl.acn.txt`). We supplement the data available from the Nevada Geodetic Laboratory with some data provided by A. Gualandi, used in *Gualandi et al.* (2016).

The position time series obtained are the result of a number of signals which need to be accounted for in order to extract a transient, postseismic signal. These signals include a linear deformation rate, annual and semi-annual loading and offsets in the time series caused by equipment changes or earthquakes. In order to remove these signals, we fit a function to stations that had been recording for at least one year prior to the earthquake of the following form:

$$y(t)_{preseismic} = A + Bt + C\sin(2\pi t) + D\cos(2\pi t) + E\sin(4\pi t) + F\cos(4\pi t) + \mathcal{H}(t) \quad (3.1)$$

where A is a universal offset for the entire time series, Bt represents a linear rate, the sin and cos functions represent annual and semi-annual signals and $\mathcal{H}(t)$ is the Heaviside function, used to model offsets in the time series. If the offset times are known then the equation becomes linear and can be solved using a linear least squares inversion. Offset times at each station were obtained from the potential step discontinuities database maintained at the Nevada Geodetic Laboratory (`http://geodesy.unr.edu/NGLStationPages/steps.txt`). Manual inspection of the time series confirmed most of these step discontinuities were present. Extra offset times were added for stations MKLU, GRHI, XYAK and BNDP at 0.57 years after the earthquake and at ODRE at 0.95 years after the earthquake. If there were many offset times within a short time span, we collapsed these to a single offset time to avoid overfitting the data.

We use a similar approach to previous studies (*Gualandi et al.*, 2016, *Wang and Fialko*, 2018) and spatially interpolate the linear and seasonal fitting coefficients to

those stations that were not recording for at least one year before the earthquake (see Figure B.1 for details). Fitting coefficients are mostly consistent, but we exclude stations CTWN, NAST and KIRT when performing the linear interpolation as their fitting coefficients appeared to be anomalously different to other stations around them. The resulting interpolated coefficients were used to remove signals not associated with postseismic deformation from the remaining GNSS sites. The resulting GNSS time series show evidence of transient postseismic deformation, with the clearest signal visible at station CHLM (see Figure 3.1). The remaining time series should only contain transient postseismic deformation, but some sites show slight sinusoidal variations still. We therefore include some sinusoidal terms when extracting the postseismic signal in order to avoid fitting residual seasonal deformation as though it were postseismic.

$$y(t)_{postseismic} = \alpha \ln(1 + t/\tau) + \beta \sin(2\pi t) + \gamma \cos(2\pi t) + \mathcal{H}(t) + \delta \tag{3.2}$$

This equation includes a universal offset (δ), step discontinuities represented by the Heaviside function ($\mathcal{H}(t)$), seasonal terms (β and γ) and a logarithmic postseismic function. We use a Bayesian inversion technique to calculate a range of acceptable values for each of the unknowns. We use uniform prior probability distributions for each parameter and use the data misfit as our likelihood function, assuming Gaussian errors on the data. Once the inversion has passed the 'burn-in' stage, we keep a record of accepted models. We can then use these accepted models to predict displacements associated with each term in equation 3.2. In order to extract an estimate of postseismic deformation at any time after the earthquake, we predict displacements caused by all the terms in equation 3.2, except the logarithmic term. These predicted 'non-postseismic' displacements are subtracted from the postseismic time series and then we extract all GNSS displacements within 6 days of the desired time. This is done for all accepted model fits to obtain a range of possible postseismic displacements, which we take the mean and standard deviation of. We estimate the displacement at each station at the time of each InSAR acquisition and after one and two years. This approach enables us to largely isolate the postseismic signal, without underestimating the error on that signal from both random noise and other sources of deformation. The resulting postseismic displacements after one year and two years are shown in the maps in Figure 3.1. The map of postseismic displacements shows most deformation is concentrated near the coseismic rupture with very little deformation at large distances, where coseismic stress changes will be small. The fact that GNSS stations far from the coseismic rupture show little movement in our extracted postseismic displacements suggest our method is working as expected.

Postseismic InSAR

We use SAR images captured by the EU Copernicus satellite Sentinel-1a, operated by the European Space Agency (ESA). Sentinel-1a acquired images on both ascending and descending tracks covering the area of interest with a relatively short revisit time (12 - 36 days). Images were acquired in Interferometric Wide Swath mode with a footprint approximately 250 km wide and consist of a series of sub-images known as bursts which we combined to form a larger mosaic. We formed small baseline interferograms with higher coherence using the Gamma software (`http://www.gamma-rs.ch/`), implemented within a modified version of LiCSAR (*Wright et al.*, 2016) and prepared for input into a modified version of StaMPS for time series analysis (*Hooper et al.*, 2012). We chose to use images from descending track 19 up until 8 September 2015 and ascending track 85 up until 23 November 2015. We ended our time series at these times due to a change in acquisition strategy causing a large time gap between these dates and the next data available on each track, thus reducing coherence. Furthermore, GNSS data from CHLM indicate that 43% of the displacement recorded after two years is accumulated by the end 8th September 2015, even though this is only 18% of the two year observation period.

Initial inspection of the InSAR time series revealed very large signals (over 15 cm LOS) that were often correlated with topography. We suspected these signals were atmospheric signals and so investigated the effects of the atmosphere on InSAR signals in the area. We used the ERA-Interim (ERA-I) weather model re-analysis product (*Jolivet et al.*, 2011, *Bekaert et al.*, 2015a) and GNSS station estimates of atmospheric delay (*Herring et al.*, 2013) to estimate the atmospheric signals present in the InSAR time series. Full details of our analysis can be found in the supplement. The temporal variability of the atmosphere is highly changeable over the study area with much greater temporal variability in the Ganges basin compared to the Tibetan plateau, even after seasonal signals are removed.

We attempted to remove the atmospheric signal using both empirical approaches (*Elliott et al.*, 2008) and weather model results (*Jolivet et al.*, 2011, *Bekaert et al.*, 2015a). Unfortunately, neither approach provided a satisfactory correction to our InSAR data (see text S1 for more details). We therefore take a different approach and only use part of our InSAR data. GNSS stations and ERA-I nodes both show much lower temporal variability at greater heights (Figure B.3). This is simply due to the fact that at higher elevations, the lower troposphere (where the largest delay variations occur) is thinner, thus introducing less opportunity to build up large variability (*Bekaert et al.*, 2015b). As well as the temporal variability, the atmosphere becomes more spatially variable over longer length scales and over large changes in topography. This suggests that analysing a smaller region on one side of the large topographic change caused by the Himalayas would reduce the impact of large atmospheric variations. We

therefore decided to only analyse InSAR data for heights over 4000 m on the Tibetan plateau. We chose 4000 m as a cut off height as this provides a good balance between the number of available InSAR pixels and their atmospheric variability (see Figure B.3d). Analysing data from the plateau has a number of advantages, such as generally higher coherence, less atmospheric variation and greater resolving power for the northward extent of postseismic deformation. Whilst this approach means we discard large amounts of potentially useful data, we are less likely to misinterpret atmospheric or hydrological loading signals as tectonic ones. This approach also removes the risk of possible unwrapping errors over the Himalayas affecting our results. The resulting InSAR data are complementary to the GNSS data available at lower altitudes.

Initial analysis of the data shows a region of range decrease in the same location as found by *Wang and Fialko* (2018). In order to improve the signal-to-noise ratio of the plateau data, we apply a simple height based atmospheric correction:

$$\phi = ah + bx + cy + d \tag{3.3}$$

where h is the height, and x and y are InSAR pixel coordinates in kilometres. This correction simultaneously solves for a linear correlation between phase and topography and a bilinear ramp using only data from the plateau and excluding data in the deforming region. The inclusion of a bilinear ramp allows for the removal of any long wavelength atmospheric signals uncorrelated with topography. An example corrected interferogram covering the period 29 April 2015 - 15 August 2015 is shown in Figure 3.1 as well as profiles through the InSAR time series.

3.2.3 Observations Summary

Some GNSS stations show a clear postseismic transient, indicating that postseismic deformation is taking place but is limited in its spatial extent (see Figure 3.1). The affected GNSS stations surround the coseismic rupture with stations to the north showing the greatest deformation (e.g. CHLM). These observations are in agreement with previously published work (*Gualandi et al.*, 2016, *Mencin et al.*, 2016, *Zhao et al.*, 2017, *Jiang et al.*, 2018).

Ascending and descending Sentinel-1a interferograms show significant surface deformation on the Tibetan plateau and provide a constraint on the northward extent of the postseismic deformation. They show that deformation is relatively localised and agree with the picture given by the GNSS stations alone. The InSAR deformation is clearest in the descending track (Track 019), with a lobe of motion towards the satellite just to the north of the coseismic rupture. This signal is similar to that seen by *Sreejith et al.* (2016) although smaller in extent, but is in good agreement with *Wang and Fialko* (2018). The ascending track (Track 085) also shows signals that may be caused by postseismic deformation, but these signals are not as consistent through time. We

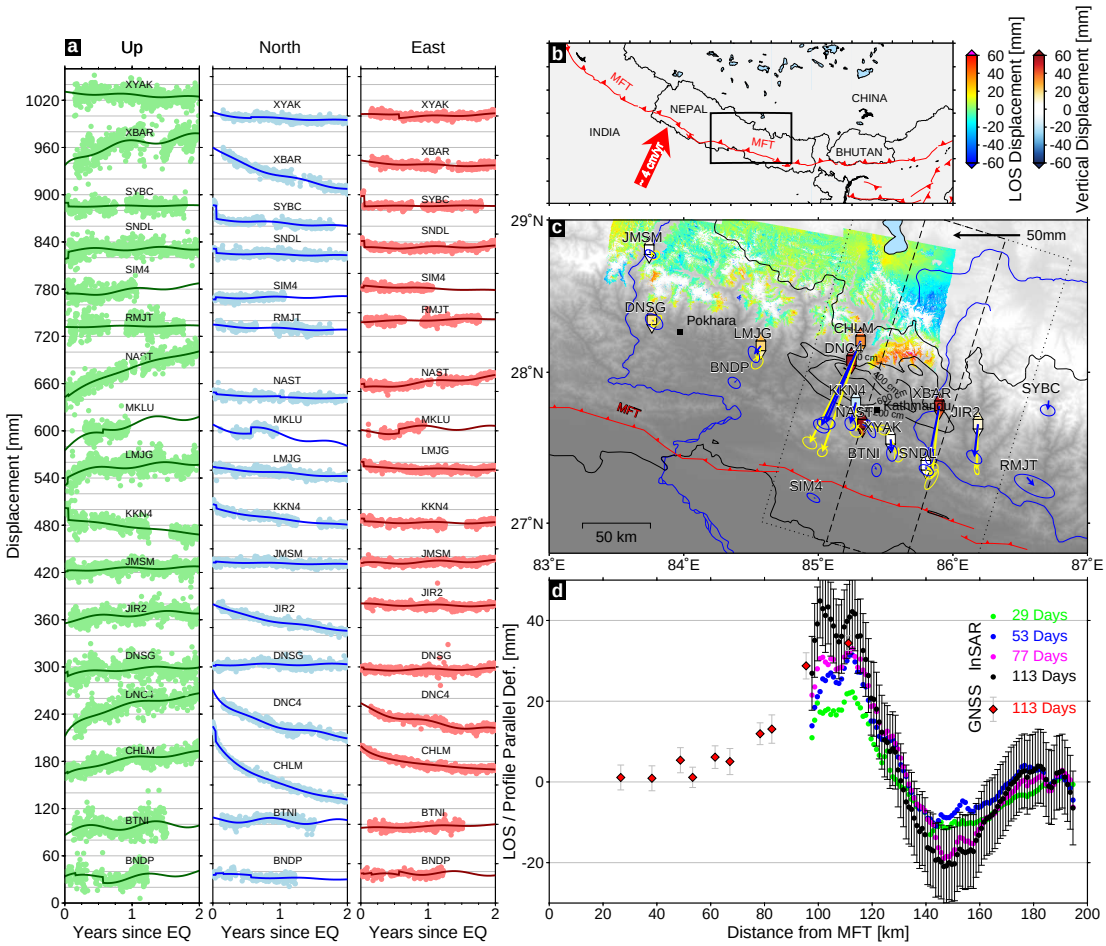

Figure 3.1: Postseismic deformation recorded by GNSS stations and InSAR. a) Postseismic time series for each component at each station. Dots show the detrended postseismic position and solid lines show the fit. b) Location map. Red arrow shows Indian plate convergence. Black rectangle is area shown in panel c. c) Map view of postseismic deformation showing GNSS displacements 1 year (blue) and 2 years (yellow) after the Gorkha earthquake. Colour map shows a Sentinel-1 interferogram spanning 29 April 2015 - 15 August 2015. Red colours correspond to movement towards the satellite (i.e. range decrease). Vertical GNSS displacements are represented as squares with triangles showing the 1-sigma range of values. Grey lines show coseismic slip contoured every 2 metres from *Elliott et al.* (2016). Dashed and dotted boxes show the swath profiles used when sampling the InSAR and GNSS respectively. d) Profile through postseismic deformation. Red dots with errorbars show profile-parallel GNSS. Coloured and black dots show line-of-sight deformation along the profile from different times after the earthquake. Black errorbars show standard deviation of phase from an undeforming part of the Tibetan plateau for the 113 days interferogram. The earlier interferogram profiles have smaller error bars but these are omitted for clarity.

therefore choose to use only the descending data in our modelling. All data-sets agree that deformation is primarily to the north of the centre of coseismic deformation and is relatively focused (see Figure 3.1), in agreement with previous work.

3.2.4 Deformation Mechanism

Various different postseismic deformation mechanisms may be responsible for the observed surface displacements (*Ingleby and Wright*, 2017). Distinguishing between afterslip and viscoelastic relaxation can be challenging (e.g. *Savage*, 1990, *Perfettini and Avouac*, 2004, *Ryder et al.*, 2007, *Hao et al.*, 2012, *Wright et al.*, 2013). However, the combination of spatial and temporal modelling of surface displacements can be used to determine which deformation mechanism is primarily responsible (e.g. *Jónsson et al.*, 2003, *Freed*, 2007, *Freed et al.*, 2007).

The spatial location and extent of postseismic surface deformation for the Gorkha earthquake suggests that slip down-dip of the coseismic rupture is a likely cause of the observations, as inferred by previous authors (*Gualandi et al.*, 2016, *Sreejith et al.*, 2016, *Mencin et al.*, 2016, *Zhao et al.*, 2017, *Jiang et al.*, 2018, *Wang and Fialko*, 2018). We used VISCO-1D (*Pollitz*, 1997) to perform simple viscoelastic relaxation calculations. We tested a number of different viscosities and found that all models produce a much broader, lower amplitude surface deformation signal, with the opposite sense of motion to that seen in the data (see Figure B.4 in the supplement and accompanying details in Text B.1 for further information). Previous work has found that limited viscoelastic relaxation is possible, but is masked by the larger afterslip signal (*Wang and Fialko*, 2018). *Zhao et al.* (2017) suggest that some viscoelastic relaxation helps to explain far-field GNSS stations in southern Tibet and causes the spatial distribution of afterslip to have a more plausible extent. We therefore assume that the predominant cause of the near-field postseismic deformation we observe is afterslip. With this in mind, we use these postseismic deformation measurements in our investigation of the faults beneath Nepal.

3.3 Geometry of the Himalayan Fault System

3.3.1 Proposed Geometries

The 3D geometry of the Himalayan fault system is still vigorously debated. The variety of geometries proposed fall in to three broad categories. These categories can be illustrated by summarising the geometries used in slip inversions for the Gorkha earthquake (see Figure 3.4 for a cross section showing the geometries).

Firstly, a number of authors have used a single, shallowly dipping fault plane to explain observations in the earthquake (e.g. *Wang and Fialko*, 2015, *Avouac et al.*, 2015, *Lindsey et al.*, 2015, *Galetzka et al.*, 2015, *Grandin et al.*, 2015). This simple model is

able to explain most of the coseismic observations, as well as the largest aftershock and postseismic deformation observed using GNSS (*Gualandi et al.*, 2016).

Secondly, some authors have used a flat-ramp-flat geometry to model slip in the Gorkha event (e.g. *Elliott et al.*, 2016, *Hubbard et al.*, 2016, *Sreejith et al.*, 2016). This geometry is also able to explain most of the observations and is generally chosen due to its ability to explain other aspects of the Himalayan orogeny such as the location of microseismicity (*Pandey et al.*, 1995), the location of a rapid change in uplift rates (*Lavé and Avouac*, 2001), and the geology (e.g. *Hubbard et al.*, 2016). The complexity of these geometries varies from a single geometry along strike (*Elliott et al.*, 2016, *Sreejith et al.*, 2016) to full 3D models with multiple ramps and along-strike variation (*Hubbard et al.*, 2016, *Qiu et al.*, 2016, *Zhang et al.*, 2017). Laterally continuous flat-ramp-flat models have also been used to model postseismic deformation by *Mencin et al.* (2016) and *Sreejith et al.* (2016).

Thirdly, *Whipple et al.* (2016) have used a single, shallowly dipping fault plane with a steeper splay fault to explain detailed aspects of the geodetic data in the Gorkha event. This model is also able to explain other aspects of the Himalayan orogeny since it advocates out of sequence thrusting as a mechanism for the rapid change in uplift rates and the building of topography (e.g. *Hodges et al.*, 2004, *Wobus et al.*, 2005).

3.3.2 Inverting for Fault Geometry

Method

Here, we use geodetic data from all three stages of the earthquake cycle in Nepal to determine geometries that are capable of matching all three stages simultaneously. We use ALOS InSAR data from *Lindsey et al.* (2015) and Sentinel-1 InSAR data from *Elliott et al.* (2016), which record coseismic deformation. For the postseismic period, we use the postseismic GNSS displacements accrued by 2015/08/15 and the interferogram covering the period 2015/04/29 – 2015/08/15. Finally, we use horizontal GNSS velocities compiled for the Global Strain Rate Model by *Kreemer et al.* (2014) and vertical GNSS velocities from *Ader et al.* (2012), along with vertical velocities from levelling (*Jackson and Bilham*, 1994) as estimates of the interseismic deformation. Figure 3.2 shows a summary of the data sets obtained as well as the location of profiles taken through each data set.

For several reasons, we choose to focus on profiles through the data. Firstly, the interseismic levelling data (*Jackson and Bilham*, 1994) and GNSS data (*Ader et al.*, 2012, *Kreemer et al.*, 2014) are mostly in the form of orogen perpendicular profiles due to accessibility. Secondly, the down-dip structure of the fault zone is primarily constrained by fault-perpendicular observations. Thirdly, modelling individual profiles allows us to see if there is discernible variation along strike (*Hubbard et al.*, 2016). Finally, modelling profiles is computationally faster, with fewer data points and model

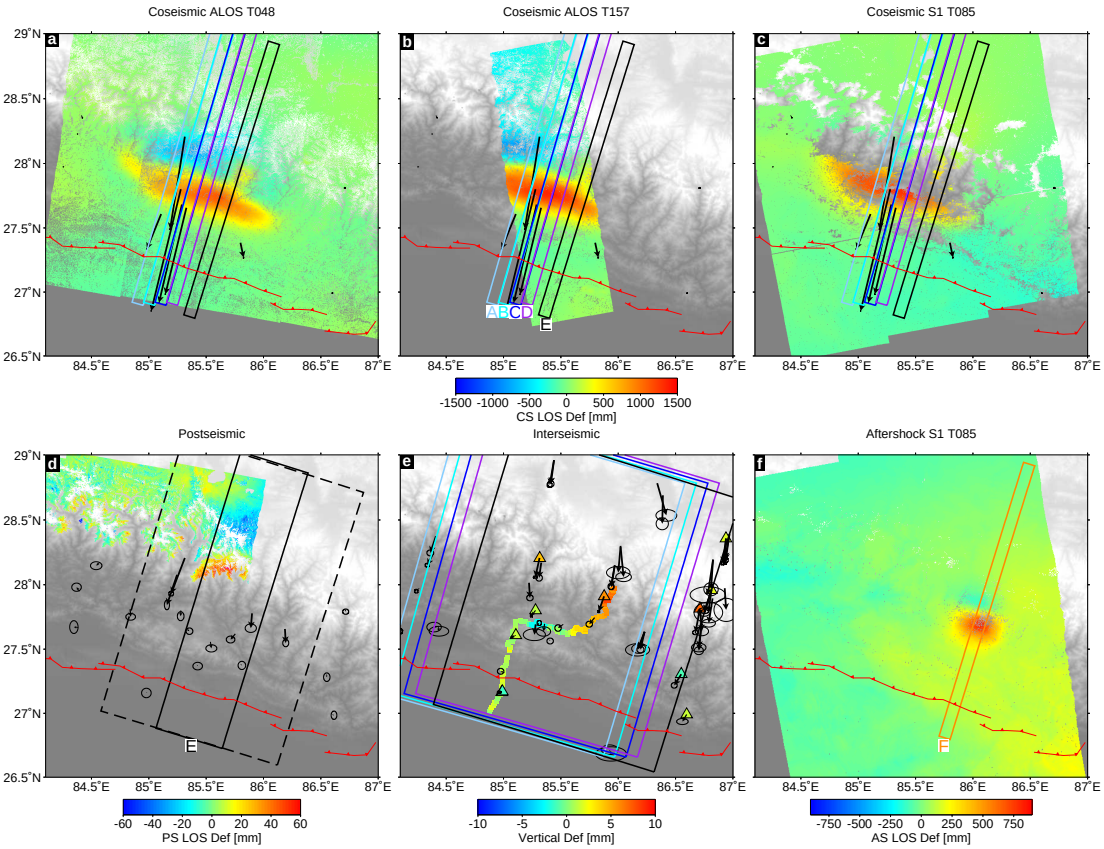

Figure 3.2: Summary of geodetic data used from each stage of the earthquake cycle. a-c) Examples of coseismic data from ALOS (*Lindsey et al.*, 2015) and Sentinel-1 (*Elliott et al.*, 2016), as well as GNSS coseismic offsets as black arrows (*Galetzka et al.*, 2015). Red saw-tooth line is the surface trace of the Main Frontal Thrust (*Taylor and Yin*, 2009). Rectangles show swath profiles used in modeling labeled A-E in panel b). d) Postseismic data from Sentinel-1 and GNSS displacements. Dashed line shows the wider swath used to obtain GNSS displacements. e) Interseismic data: coloured squares are vertical velocities obtained from levelling (*Jackson and Bilham*, 1994), coloured triangles represent vertical GNSS velocities from (*Ader et al.*, 2012). Arrows are horizontal velocities from *Kreemer et al.* (2014). f) Example of aftershock data from Sentinel-1. Orange rectangle, labeled F is profile used in aftershock modeling.

parameters. We use profiles taken perpendicular to the average strike of the surface trace of the MFT (287 degrees), which are shown in Figure 3.2.

We begin by modelling data from each stage of the earthquake cycle independently to find the location of fault slip suggested by each data set. We use a number of profiles along-strike to allow us to capture coseismic, postseismic and interseismic deformation maxima as well as deformation due to the largest Gorkha aftershock (M_w7.1 on 12th April 2015). InSAR data along the profiles are averaged in successive bins to reduce the computational cost, whilst the covariance matrix of each InSAR data set is constructed using an empirical variogram (e.g. *Lohman and Simons*, 2005, *Oliver and Webster*, 2014). We use a bin spacing of 2 km for the coseismic InSAR but only 1 km for the postseismic InSAR to increase the number of postseismic data available in our inversions. We project GNSS displacements (or interseismic GNSS velocities) into profile-parallel and profile-perpendicular components, with the profile-parallel component used in the modelling. The swaths used for the postseismic and interseismic deformation are wider than the coseismic swath since there are fewer geodetic measurements available. We remove the subsidence signal seen in the interseismic levelling data near Kathmandu, which is likely due to water extraction (*Jackson and Bilham*, 1994). We also remove levelling data south of the MFT surface projection, because signals here are unlikely to be associated with motion on the main Himalayan fault system (*Bettinelli et al.*, 2006, *Grandin et al.*, 2012).

Initially, we find the single best uniform slip elastic dislocation (*Okada*, 1985) for each stage of the earthquake cycle independently. For the interseismic deformation, we consider a creeping dislocation which continues deep into Tibet (*Vergne et al.*, 2001, *Elliott et al.*, 2016). We then move on to using coseismic, interseismic and postseismic data together to invert for satisfactory geometries. We use a Bayesian inversion scheme implemented using a Monte Carlo Markov Chain method incorporating the Metropolis-Hastings algorithm (*Mosegaard and Tarantola*, 1995). Our inversion method begins by using simulated annealing to determine a high likelihood starting point for the Bayesian inversion (*Bagnardi and Hooper*, 2017). The step size is adjusted within the inversion if acceptance rates become too high or too low (*Amey et al.*, 2018). Each elastic dislocation has five parameters in our inversions: distance from MFT to top of the dislocation, top depth, bottom depth, dip angle and slip. We use uniform prior probability distributions for each parameter.

In all our inversions, we assume a homogeneous elastic half-space. *Wang and Fialko* (2018) showed that including topography and heterogeneous elastic properties can change surface displacement patterns by approximately 10%. Inversions including these effects suggested very similar fault slip patterns for a fixed fault geometry with differences of up to approximately 10% in slip magnitudes. However, we chose to use a homogeneous half space to enable more rapid calculation of the Greens functions for each each new trial geometry. *Wang and Fialko* (2018) also found that the differ-

ence between models using homogeneous and heterogeneous elastic structures and/or topography is reduced for smoother slip distributions, indicating that other factors affect the inference of slip at depth. These other factors include different geometries, different layered velocity structures and different degrees of smoothing. Our inversions account for the uncertainty in geometry and solve for the degree of smoothing where appropriate. However, we do not account for any other uncertainties in the forward model, such as errors in elastic structure (*Duputel et al.*, 2014, *Ragon et al.*, 2018) or those introduced by failing to account for topography (*Wang and Fialko*, 2018, *Ben Thompson and Meade*, 2018). Inclusion of such model errors would increase the final uncertainties in our results.

We keep a record of each accepted model, providing us with probability distribution functions (PDF) for each model parameter. We combine the various geometric parameter PDFs (dips, depths and distances) to construct a picture of likely fault models at depth. We determine where a fault model intersects a grid of 1 x 1 km squares beneath Nepal and produce a grid showing the possible geometries (see Figures 3.5 and 3.6).

Independent Coseismic, Postseismic and Interseismic Inversions

Figure 3.3 shows the results of our inversions for each stage of the earthquake cycle independently. The majority of the surface deformation data can be explained using shallowly dipping elastic dislocations. Coseismic data from western profiles (A and B) are best fit using a dislocation dipping at 9.5 – 10.5 degrees. Interseismic geodetic observations from throughout Nepal are best fit by a creeping interseismic dislocation which extends from near the lower-edge of the coseismic rupture with a similar dip (8 - 14 degrees). Postseismic data from profile E are best fit by a shallowly dipping fault with a similar geometry to that suggested by interseismic deformation. Furthermore, data from the M_w 7.1 aftershock (profile F) also suggest a fault with a similar geometry.

Combining the results of all these geodetic inversions, we see that most of the deformation is best fit by slip on a shallowly dipping (10 degrees) fault. The most significant deviation from this geometry (best-fit dip of 35 degrees) is suggested by coseismic data from profile E that passes through the uplift anomaly identified by *Whipple et al.* (2016). This change in dip may be real and highlight a variable geometry along strike, as has been suggested by previous authors (e.g. *Hubbard et al.*, 2016, *Zhang et al.*, 2017). Alternatively, rather than the dip of a single, planar MHT changing along strike, a more complicated down-dip geometry may be able to explain the data from profile E. We therefore try a series of more complex geometries to model data from profile E in subsequent sections. These more complex geometries are not precluded by our analysis so far, and may be hinted at by the higher density of aftershocks in the east (*Adhikari et al.*, 2015, *Bai et al.*, 2016).

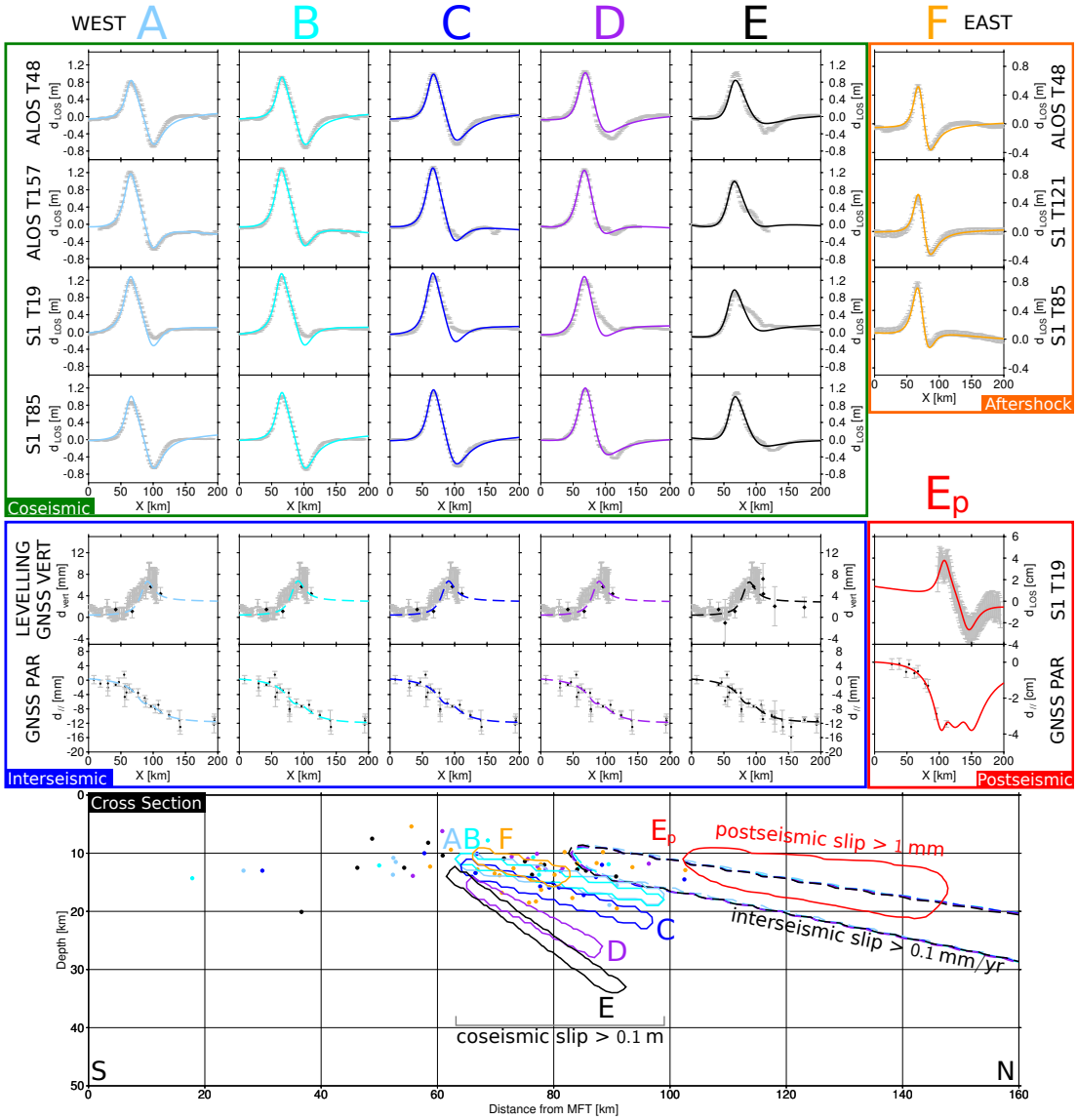

Figure 3.3: Profile data and model results. Letters correspond to profile labels in Figure 3.2. Far-right panels show aftershock profile data and postseismic data. Coloured lines show the model fit with the corresponding location of causative slip shown in the same colour as a polygon on the cross section below. Coloured dots are aftershocks from (*Bai et al.*, 2016) from each profile.

3.3.3 Joint Coseismic, Postseismic and Interseismic Inversions

We focus on testing the three classes of geometric model discussed in section 3.3: planar models, mid-crustal ramp models and splay models. We first test the exact down-dip geometries proposed by *Elliott et al.* (2016), *Whipple et al.* (2016) and *Hubbard et al.* (2016) by solving for distributed slip on each fixed geometry. We construct the geometries based on the geometric parameters provided in *Elliott et al.* (2016) and *Whipple et al.* (2016), and take a profile through the geometry of *Hubbard et al.* (2016). We split the down-dip geometries into 5 km square fault patches and solve for the amount of slip on each patch in each stage of the earthquake cycle. We use a Bayesian inversion and apply smoothing to each stage of the earthquake cycle separately by using a Laplacian operator and solving for the degree of smoothing in the inversion (*Fukuda and Johnson*, 2008). We found that all three geometries gave similar total variance reductions (see Figure B.14 in the supplement). Each of the geometries could fit the coseismic data reasonably well, although the geometries proposed by *Elliott et al.* (2016) and *Hubbard et al.* (2016) gave slightly higher variance reduction values (Figure B.14). However, the geometries of *Elliott et al.* (2016) and *Hubbard et al.* (2016) could not reproduce the postseismic deformation particularly well (Figures B.13 and B.14), particularly the wavelength of the signal. This is likely due to their proposed geometries being relatively deep in the location where postseismic slip is required.

We therefore solve for our own version of each type of geometry, allowing the positions of ramps and splays to vary. We use coseismic, interseismic and postseismic data from the easternmost profile in a joint inversion for the optimal model geometries. We then test whether slip on faults with these geometries can explain data from the westernmost profile. We perform the joint inversions in a Bayesian sense, where the likelihood of each model is calculated using the fits to the coseismic, postseismic and interseismic data. We use the same inversion procedure as described in section 3.3.2 with uniform priors for each parameter. The bounds of these priors, as well as any other constraints, are explained in the appropriate subsequent sections. We again produce a grid of the possible geometries in cross-section, as described in section 3.3.2 and show the range of slip values in each earthquake cycle stage at different distances along the profile (see Figure 3.5).

We consider there to be two end-member approaches when determining the likelihood of a proposed geometry. The first approach uses the data errors alone as weights in the inversion (as done in section 3.3.2). In this case, the fit to the coseismic data ends up dominating the inversion as there are more coseismic data and the signal-to-noise ratio is much higher. A second approach uses the data errors and additional weighting factors to balance the contributions from different earthquake cycle data sets. This approach is necessary to account for incorrect model assumptions favouring a fit to one data set at the expense of all others. These weighting factors are implemented by

scaling the coseismic and interseismic data variance-covariance matrices with respect to the postseismic data variance-covariance matrix. This maintains the relative errors between the data sets (e.g. InSAR and GNSS) in each stage of the earthquake cycle, but alters the relative weighting between stages of the earthquake cycle (e.g. coseismic and postseismic). We determined the relative weights by calculating the weighted residual for a 1% error on all data from each stage of the earthquake cycle. For example, the weighted residual for the coseismic data is calculated as:

$$R_{cs} = (\mathbf{d_{cs}} - 0.99\mathbf{d_{cs}})^{\top}\mathbf{C_{cs}^{-1}}(\mathbf{d_{cs}} - 0.99\mathbf{d_{cs}}) \tag{3.4}$$

where d_{cs} is the coseismic data vector and C_{cs}^{-1} is the inverse of the coseismic variance-covariance matrix. This is repeated for the postseismic and interseismic data. We then divide the postseismic residuals by the coseismic and interseismic residuals and use these ratios as weights such that $w_{ps} = 1$, $w_{cs} = R_{ps}/R_{cs}(= 0.0095)$, and $w_{is} = R_{ps}/R_{is}(= 0.1557)$.

We tested both approaches in our inversions and compared the results for the different geometries. We found that downweighting the coseismic and interseismic data had little effect on the overall quality of the fit to these data. In contrast, there was a noticeable improvement in the fit to the postseismic data when they played a greater role in the inversion. Artificially increasing the errors on the coseismic and interseismic data allowed a greater spread of acceptable models. Whilst this greater range of acceptable geometries is due to our artificial increase of the coseismic and interseismic data errors, we suggest that a larger range of acceptable models is preferable given that we have not formally considered model errors in the inversion. We found that the inversion using data errors alone gave an optimal geometry that was different to that obtained using the weighted inversion, although they generally agreed within error. We therefore proceed using the results of our inversions with approximately equal weights for each stage of the earthquake cycle. Results of inversions using data weights alone can be found in the supplementary material.

Planar Geometry

We first tried solving for the best fit single planar geometry using coseismic, postseismic and interseismic data from profile E. The range of acceptable geometries from this inversion are shown in Figure 3.5 as a gray-scale grid with darker shades representing the most likely geometry. The range of acceptable geometries is similar to the majority of best-fitting faults in section 3.3.2. The corresponding data fits are shown in Figure 3.6. The range of acceptable models overlaps with the best-fit models inferred using the data errors alone and agrees with the geometry used by *Avouac et al.* (2015).

Uniform slip can explain most of the data well, but struggles to explain eastern coseismic data from profile E. We therefore split the geometry into a series of smaller

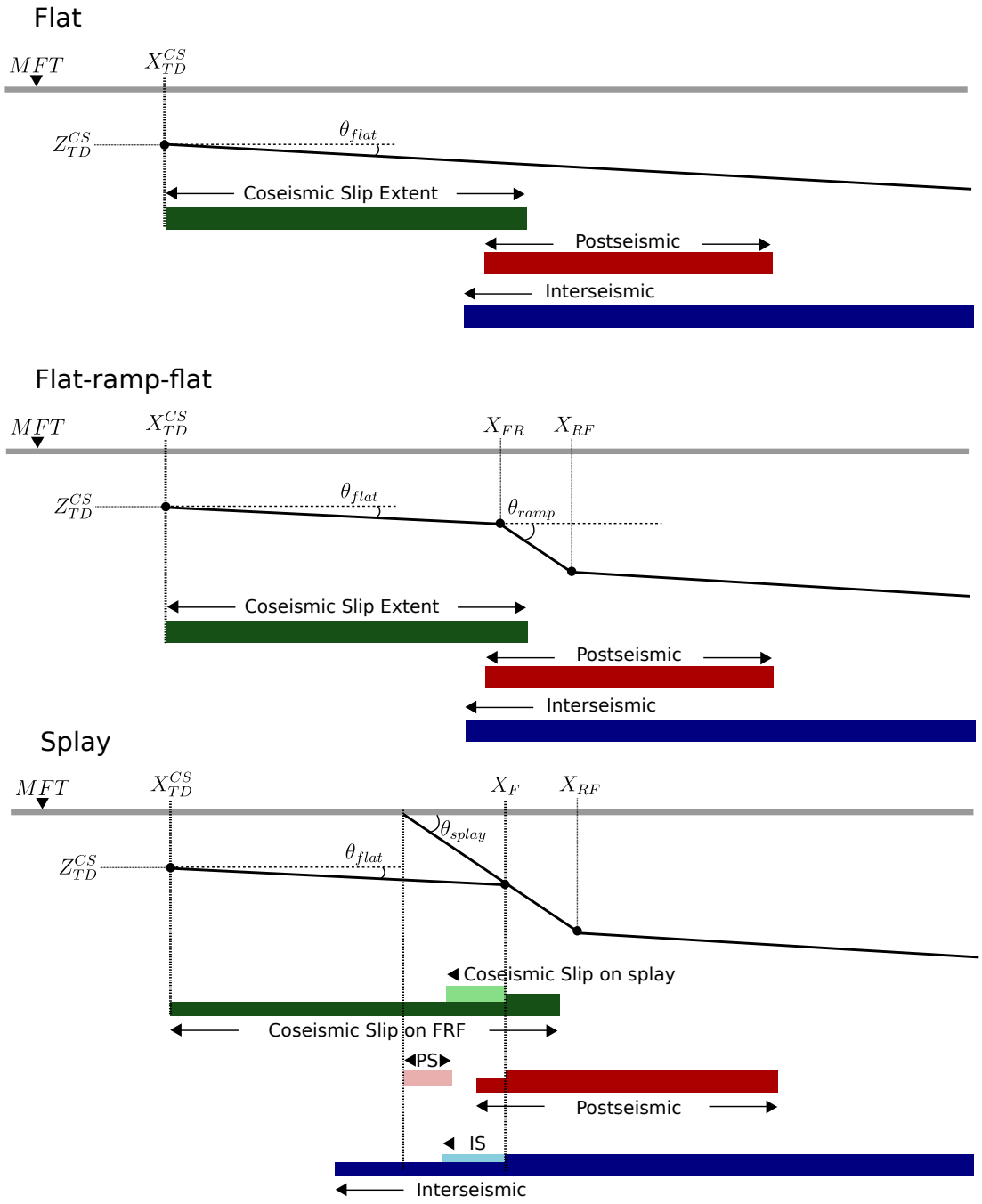

Figure 3.4: Diagram explaining the model set-up with associated parameters. Top panel shows a parameterisation of the single flat model. Middle panel shows the flat-ramp-flat geometry (similar to *Elliott et al.* (2016)). Lower panel shows a flat-ramp-flat geometry with a splay similar to *Whipple et al.* (2016). CS, PS and IS refer to coseismic, postseismic and interseismic respectively. TD refers to top depth and MFT is the Main Frontal Thrust surface trace.

fault patches, solving for distributed slip in a Bayesian sense for each stage of the earthquake cycle. Creating a discretized fault plane limits our ability to exactly reproduce the maximum likelihood geometry suggested by uniform slip. Instead, we use a geometry which is similar to the mean geometry suggested by our uniform slip inversions. The fixed geometry dips at 8 degrees from the surface trace of the MFT and is split into 40 patches with down-dip width of 5 km and is shown in Figure 3.5. We model data from both east and west Nepal (profiles E and A respectively) to check whether models obtained using the eastern Nepal data are still capable of matching the western Nepal data. Full details of all our distributed slip inversions can be found in the supplementary information. We find that distributed slip models made only minimal improvements in the fit to the data. In some cases, the variance reduction provided by distributed slip is worse than that given by uniform slip. This is likely due to the fixed geometry we choose not necessarily matching the maximum likelihood geometry suggested by uniform slip. Furthermore, a slightly worse fit may be caused by the edges of the discretized fault patch boundaries not aligning with the edges of the uniform slip dislocations and the addition of smoothing.

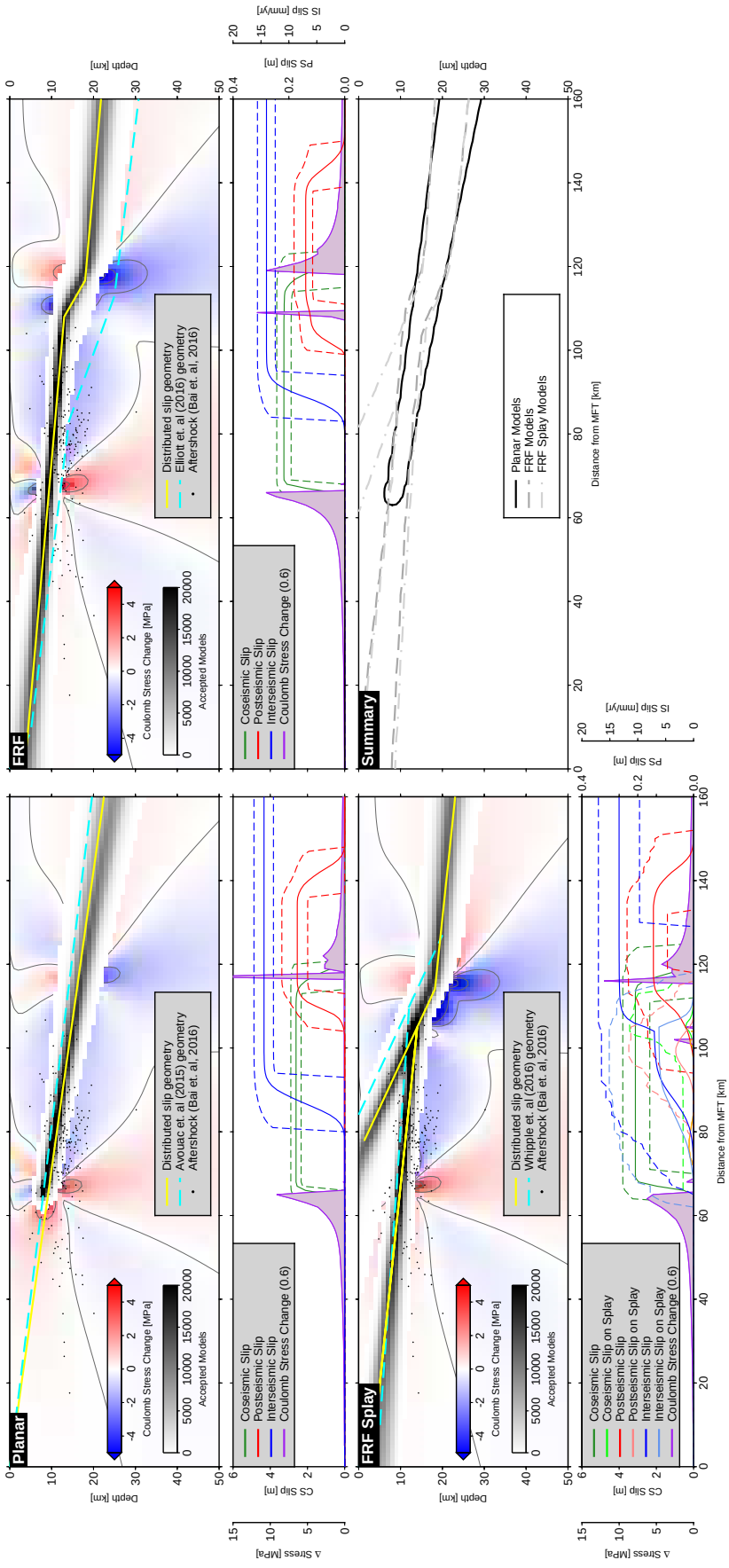

Figure 3.5: Summary of different inferred geometries. For each geometry, the top panel shows a cross section beneath Nepal and the lower panel shows slip and stress changes on the inferred faults. The cross section shows the range of possible geometries obtained using the inversion with equal weight given to each earthquake cycle stage. The yellow lines correspond to the geometry used for distributed slip modelling in subsequent sections. Cyan lines are similar geometries from other studies. Slip in each stage of the earthquake cycle is shown by the mean (solid line) and the 95% confidence interval (dashed lines) in the lower panels. The summary figure shows the region with > 1000 accepted models for each geometry.

Flat-ramp-flat (FRF) Geometry

Next, we try a system involving three faults connected down-dip, illustrated in the middle panel of Figure 3.4. The top and bottom faults are given the same, shallow dip (between 2 and 15 degrees) while the middle fault can have a different dip, which is allowed to reach steeper dip angles (2 to 30 degrees). This means these three faults are capable of producing geometries ranging from a single, planar geometry through to a flat-ramp-flat (FRF) geometry. We use data from the eastern profile (profile E) to solve for the optimal geometry. The geometry of the fault system as well as the extent and magnitude of slip in each earthquake cycle stage is varied in each trial.

Figures 3.5 and 3.6 show the range of acceptable models and the fit to the data. The addition of a mid-crustal ramp enables a better fit to the coseismic data using uniform slip but has minimal effect on the fit to the interseismic and postseismic data. Our range of acceptable models places the mid-crustal ramp 20 - 30 km further north than the model proposed by *Elliott et al.* (2016). This discrepancy can be explained by our inclusion of postseismic data when resolving the best fit geometry, and the range of acceptable models suggested by *Elliott et al.* (2016) (e.g. see Figure 3 of *Elliott et al.* (2016)). When coseismic data contribute more to our inversion, the best-fit ramp moves further south but with little visible improvement in fit to the data. We then fix the geometry as shown in Figure 3.5 and split this into a number of patches. We solve for distributed slip both in the east and west as discussed above. We find that the distributed slip model is capable of fitting both eastern and western data, but that the improvement in overall fit is even smaller than the planar case.

Flat-ramp-flat splay Geometry

Finally, we try a flat-ramp-flat geometry with the ramp extending towards the surface as a splay, illustrated in the lower panel of Figure 3.4. This model resembles that used in *Whipple et al.* (2016) and allows for out of sequence thrusting in the earthquake cycle. The flat-ramp-flat geometric parameters are similar to the flat-ramp-flat model, but the parameter ranges are restricted to be similar to the model of *Whipple et al.* (2016). The splay has the same dip as the ramp and can reach up to the surface. The slip on the splay is solved for as a fraction of the slip on the main flat-ramp-flat fault for each earthquake cycle stage. Coseismic slip on the splay is forced to have a bottom depth at the base of the splay but can have a top depth anywhere up to the surface. Postseismic slip can be anywhere on the splay with no constraints. Interseismic slip on the splay extends from the base of the splay up. Furthermore, the total interseismic slip rate on the splay and up-dip of the junction on the main flat-ramp-flat fault must be less than or equal to the slip rate below the junction.

We once again combine all deformation data together and solve for a consistent geometry. Results of these inversions are shown in Figures 3.5 and 3.6. The inferred

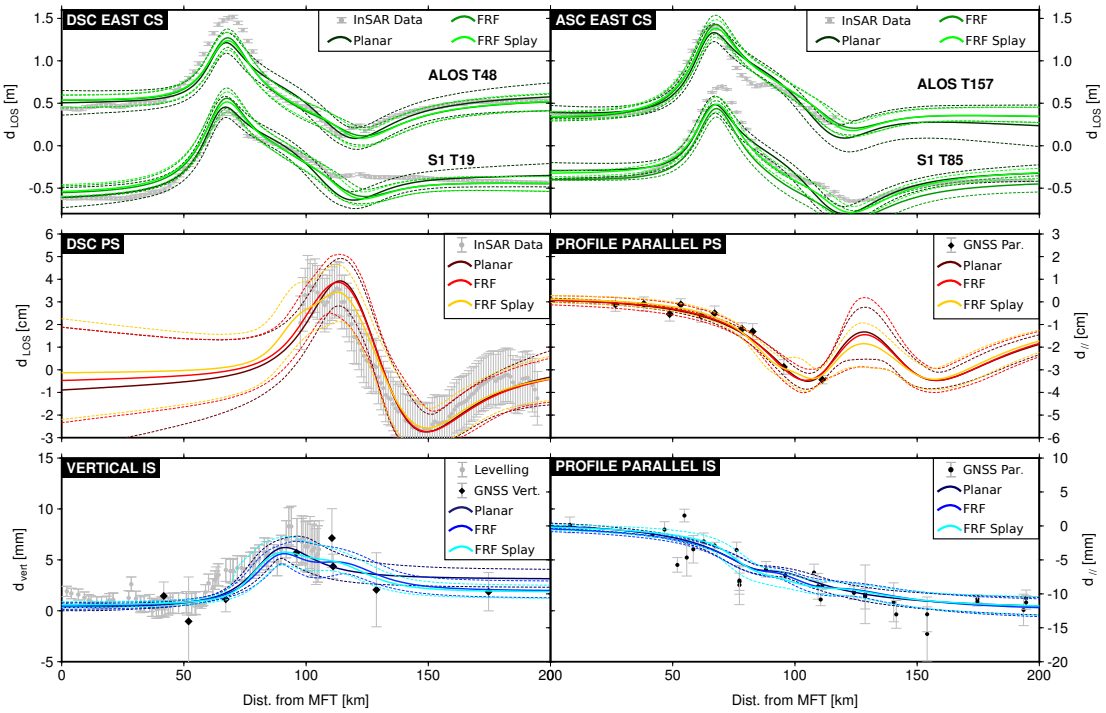

Figure 3.6: Summary of model fits to coseismic(CS), postseismic (PS) and interseismic (IS) data profiles. Thick, solid lines show the mean model fit and similarly coloured thin dashed lines show the corresponding 95% confidence interval. All three geometric models produce very similar fits to all data sets.

geometry is similar to that suggested by *Whipple et al.* (2016) but the most likely location of the ramp/splay is approximately 10 km further south, similar to our flat-ramp-flat geometry. Coseismic and postseismic slip on the splay is minimal, but the inversion places interseismic slip on the splay to give a sharper change in uplift rates. We then split this geometry into a number of patches down-dip and solve for slip as in previous examples. More patches are required to construct this geometry due to the splay fault. The distributed slip inversion again provides only a minor improvement in fit.

3.3.4 Assessing the Geometries

We have now tested the three main candidate geometries against geodetic data from throughout the earthquake cycle. We compare the fits of each model quantitatively using the weighted percentage variance reduction (VR) achieved by each model (e.g. *Huang et al.*, 2016), defined as:

$$VR = \left[1 - \frac{(\mathbf{d}-\hat{\mathbf{d}})^\top \mathbf{C^{-1}} (\mathbf{d}-\hat{\mathbf{d}})}{\mathbf{d}^\top \mathbf{C^{-1}} \mathbf{d}}\right] \times 100 \tag{3.5}$$

where d is the data vector, $\hat{d}$ is the data predicted by the model and C^{-1} is the

inverse of the variance-covariance matrix. We calculate the VR for our two inversion weighting schemes and compare the results. All three geometries are capable of high total variance reduction ($> 90\%$), and the difference between them is minimal however the inversion is weighted (see Figure B.11). Our kinematic slip inversion results offer no clear best candidate geometry. This goes some way to explaining why the geometry of the Himalayan thrust system remains controversial: different model geometries are capable of producing similar fits to surface deformation data.

An alternative approach to determine the best geometry is to test the physical consistency of each model. One way of doing this is to use the relationship between coseismic slip and postseismic afterslip. Afterslip is a function of the coseismic stress change (determined by coseismic slip), fault geometry and frictional properties (e.g. *Barbot et al.*, 2009, *Rousset et al.*, 2012, *Feng et al.*, 2016). We can therefore use a stress transfer based model of afterslip to test the proposed geometries. We next use geodetic data and mechanical afterslip models to attempt to distinguish between the proposed geometries and infer the frictional properties of the faults beneath Nepal.

3.4 Frictional Properties of the Main Himalayan Thrust

3.4.1 Method

Many previous studies have used postseismic deformation as a means of determining the frictional properties of faults (e.g. *Hearn*, 2002, *Perfettini and Avouac*, 2004, *Barbot et al.*, 2009, *Chang et al.*, 2013, *Hussain et al.*, 2016). Most of these studies assume a rate-and-state friction law (*Marone*, 1998) where fault friction is related to sliding rate and the state of the fault (e.g. contact time). Often, the law is simplified using a rate-strengthening approximation when modelling afterslip (e.g. *Perfettini and Avouac*, 2004, *Barbot et al.*, 2009, *Chang et al.*, 2013, *Feng et al.*, 2016). The complexity of the rate-strengthening model used varies. The simplest models solve for uniform frictional properties for a fault using the time dependence of a single GNSS station (*Perfettini and Avouac*, 2004). More complex models use the spatial and temporal variation of displacements to solve for uniform frictional properties on the fault (*Feng et al.*, 2016, *Wimpenny et al.*, 2017). The most complex models solve for spatially variable frictional properties over the fault (*Barbot et al.*, 2009, *Chang et al.*, 2013).

In all these cases, postseismic afterslip is driven by the coseismic stress change caused by the earthquake. This stress change is obtained using the coseismic slip distribution (*Barbot et al.*, 2009, *Chang et al.*, 2013, *Feng et al.*, 2016, *Wimpenny et al.*, 2017) or an estimate of the average stress change caused by the earthquake in the region slipping postseismically (*Perfettini and Avouac*, 2004). In all these cases, the coseismic stress change is assumed as a known term. However, this stress change strongly depends on the earthquake slip distribution, which is not perfectly known. Some stud-

ies take account of this uncertainty by collapsing the coseismic slip distribution to a smaller region and rescaling the slip to maintain seismic moment (*Barbot et al.*, 2009, *Wimpenny et al.*, 2017). Others use a variety of slip distributions from different authors to investigate the effects of these differences (*Chang et al.*, 2013).

Here, we take account of the uncertainty in the coseismic slip distribution explicitly by jointly solving for both coseismic slip and the frictional properties of the fault. We smooth the coseismic slip using a Laplacian operator, but also solve for the degree of smoothing in the inversion as a hyperparameter (*Fukuda and Johnson*, 2008). Joint coseismic and postseismic slip inversions have been performed before (e.g. *Wang et al.*, 2012), but without a mechanical link between the coseismic slip and postseismic slip. We use a generalised version of the rate-strengthening friction law (*Barbot et al.*, 2009, *Rousset et al.*, 2012, *Feng et al.*, 2016) to link coseismic slip and postseismic slip via the coseismic stress change and frictional parameters, assuming steady state:

$$V(t) = 2V_0 \sinh \frac{\Delta\tau(t)}{a\sigma} \tag{3.6}$$

This model provides fault sliding velocities, V, at a time, t, after an earthquake. Velocities are multiplied by a specified time step to give the displacement accrued over a short time interval. These displacements are then used to recalculate the total driving stress. V_0 is a reference slip rate (not equivalent to the interseismic slip rate) that controls the timescale of afterslip evolution (*Barbot et al.*, 2009) - larger values of V_0 give larger stress-driven displacements in a specified time step, leading to faster stress relaxation. a is the rate dependence of friction from the rate- and state-friction laws, and σ is the normal stress. The steady state assumption is true when the total slip is much greater than the critical slip distance, D_c. In our inversions, cumulative postseismic slip is on the order of $10^{-2} - 10^{-1}$ m whereas laboratory derived values for D_c are on the order of 10^{-5} m (*Scholz*, 1988), i.e. total slip $\gg D_c$. $\Delta\tau(t)$ is the total shear stress change at time t after the earthquake, which we calculate as:

$$\Delta\tau(t) = \Delta\tau_{coseismic} + \Delta\tau_{aftershock} + \Delta\tau_{afterslip}(t) \tag{3.7}$$

This shear stress change is made up of a shear stress change from the earthquake, a shear stress change from the largest aftershock and ongoing shear stress changes from the evolving afterslip. We calculate the incremental displacements at each time step using a fixed time step of one day (e.g. *Chang et al.*, 2013). The incremental shear stress change caused by the incremental afterslip is added to the current total stress and used to drive further afterslip. This allows for the spreading out of postseismic deformation through time and allows postseismic slip to migrate into areas which may have slipped coseismically.

We assume the fault is entirely rate strengthening and solve for positive values of a. We acknowledge that parts of the fault must be rate weakening in order for

earthquakes to nucleate. With a rate-strengthening only friction law, patches with little or no postseismic slip can be produced by giving those patches very low values of V_0 and/or high values of a (see equation 3.6). These patches are likely rate-weakening and locked. σ is the normal stress at each patch, which is assumed to be lithostatic using an average rock density of 2670 kg m^{-3}. As in *Feng et al.* (2016), we assume that the normal stress change is small ($\approx$ 0.1 MPa) compared to the total normal stress ($\approx$ 350 MPa) and therefore that the Coulomb stress change can be well approximated by the shear stress change alone.

All our kinematic slip inversions suggest that postseismic slip is restricted to areas down-dip of the coseismic rupture. However, shear stresses are increased both down-dip and up-dip of the earthquake, which would produce afterslip up-dip of the rupture as well on a fault with uniform rate-strengthening properties. Previous studies using stress-driven afterslip models for the Gorkha earthquake have had to only allow post-seismic slip down-dip of the rupture (*Zhao et al.*, 2017, *Wang and Fialko*, 2018). We account for this need to have different amounts of slip up-dip and down-dip of the rupture by solving for depth-dependent frictional properties. In the very shallow crust (depth $<$ 5 km), we set a to be very high in order to prevent postseismic slip and numerical instability caused by low lithostatic normal stresses. Below these depths, we solve for a single value of a, but we incorporate a depth dependence in V_0. This enables the transition from negligible afterslip (low values of V_0) to significant afterslip (higher values of V_0) to be determined in the inversion rather than imposed a priori, thus enabling uncertainties to be fully propagated. We use a logistic function to parameterise the depth dependence as a sigmoid:

$$V_0(z) = \frac{V_0}{1 + \exp(-k(z - z_0))} \tag{3.8}$$

We solve for the midpoint (z_0) and the steepness (k) of the sigmoid in the inversion. We used a smooth function to define the depth dependence to aid the inversion. We found that functions with a sharp transition depth caused problems in inversions with discrete down-dip patches. Solving for the parameters z_0 and k allows for a range of depth dependent V_0 curves. We allow V_0 to reach values up to 0.1 m/yr as previous work has found V_0 to be on the order of the interseismic loading rate (*Barbot et al.*, 2009, *Wimpenny et al.*, 2017). Given the lack of shallow afterslip in kinematic inversions, we set a to be very high for patches at depths shallower than 5 km to prevent postseismic slip and numerical instability in these patches with low lithostatic normal stresses.

Our novel approach enables us to use coseismic and postseismic observations together in the inversion, therefore allowing uncertainties in coseismic slip to propagate into uncertainties in our afterslip parameters. We use four coseismic interferograms (ALOS T48 and T157 (*Lindsey et al.*, 2015) and Sentinel-1 T85 and T19 (*Elliott et al.*, 2016)), downsampled using a quadtree approach (*Decriem et al.*, 2010). We also include

coseismic GNSS offsets from *Galetzka et al.* (2015) in the inversion, and solve for slip in the largest aftershock (M_w7.1 on 12th April 2015) using ALOS T48 and Sentinel-1 T85 and T121 interferograms. We use the Sentinel-1 T19 postseismic deformation time series obtained in this study with all displacements relative to the first date (29th April 2015). The lower signal-to-noise ratio of these data made a quadtree based downsampling approach impractical since noise was often also highlighted by this gradient based approach. Instead we use a downsampling scheme with more sampling near the region of postseismic deformation. Postseismic GNSS displacements are also extracted at each of these InSAR epochs using the method described in section 3.2.2. Whilst our models calculate displacements using a daily time step, we only compare with postseismic data (GNSS and InSAR) at the InSAR acquisition times.

We use the fault geometries obtained in our earlier kinematic inversions as the input for the joint coseismic-postseismic slip inversion. These geometries are extended along strike and then split into multiple square patches with length 10 km. We use the formulations of *Okada* (1985, 1992) to calculate the necessary elastic kernels used for both the expected stress and surface displacements from slip of 1 m on a fault patch. We first use simulated annealing to solve for the optimal coseismic and aftershock slip distributions. We then use this optimal model and use simulated annealing to solve for the associated optimal frictional properties. Having determined reasonable values for all parameters, we proceed to the joint inversion, using a Bayesian inversion scheme to simultaneously solve for coseismic and aftershock slip as well as the frictional properties and InSAR offsets. We use a Monte Carlo Markov Chain method where the step size is adjusted if acceptance rates become too high or too low (*Amey et al.*, 2018). However, the step size is fixed once the burn-in has been passed and samples are drawn from the posterior probability distribution.

3.4.2 Results

We performed a synthetic test to validate the new model and examine trade-offs between various parameters. A more detailed analysis of these results can be found in the supplement. The synthetic earthquake and associated afterslip can be well retrieved by the inversion and the frictional properties and depth dependence can be retrieved within error. Having tested the model and understood some of the trade-offs, we proceeded to use it on real data.

We use the best fixed geometries inferred in section 3.3.3, extended along strike and divided in to 10 km square patches. After the simulated annealing stages, the Bayesian inversion algorithm keeps a record of model samples. After completion of the inversion and removal of any burn-in, the kept models provide joint probability distributions for all model parameters. Results for the planar geometry are shown in Figures 3.7, 3.8, 3.9 and 3.10.

All three geometries are capable of explaining the majority of coseismic, aftershock

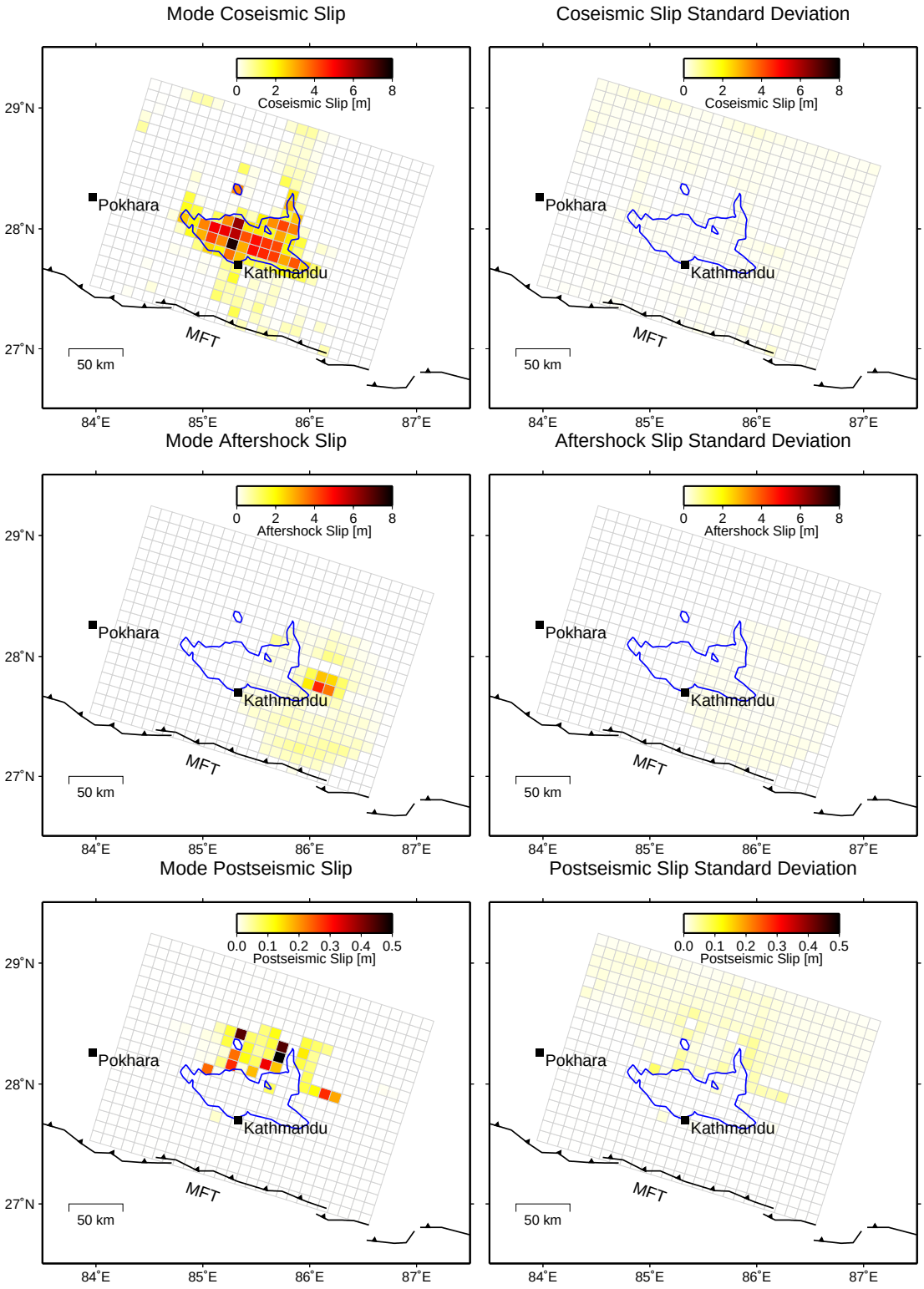

Figure 3.7: Results for the single planar geometry. Note colourbar is different for coseismic and postseismic slip. Blue line shows the 2 metre contour of mean coseismic slip. Top row: mode and standard deviation of coseismic slip. Middle row: mode and standard deviation of aftershock slip. Bottom row: mode and standard deviation of postseismic slip on 8th September 2015.

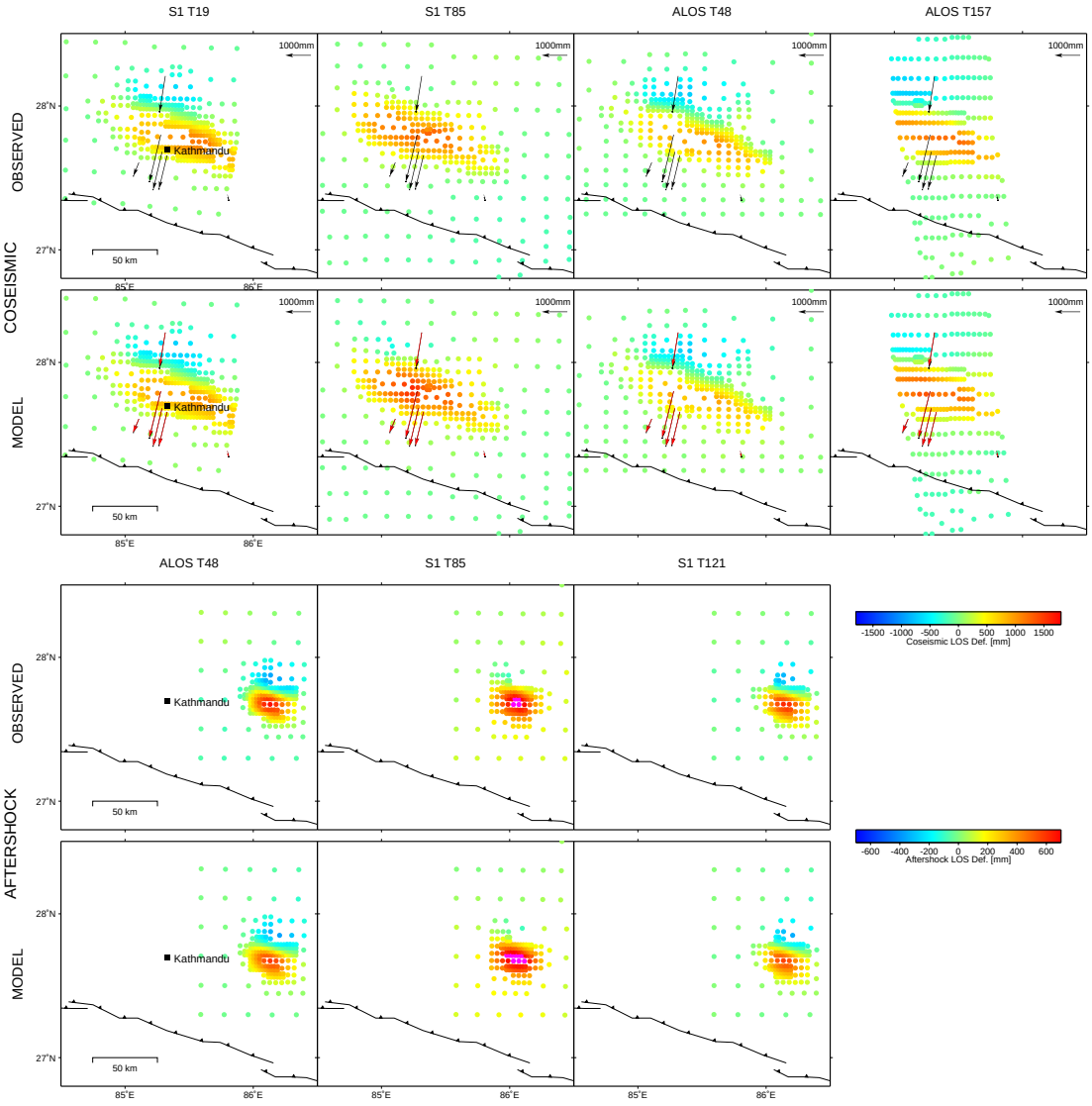

Figure 3.8: Coseismic and aftershock displacements for the single planar geometry. Top rows show the InSAR and GNSS displacements from the main shock as well as the mean model fit. Note that red, predicted GNSS arrows overlie black, observed arrows in the model displacements. Bottom rows shows the InSAR displacements from the aftershock and corresponding mean model fit.

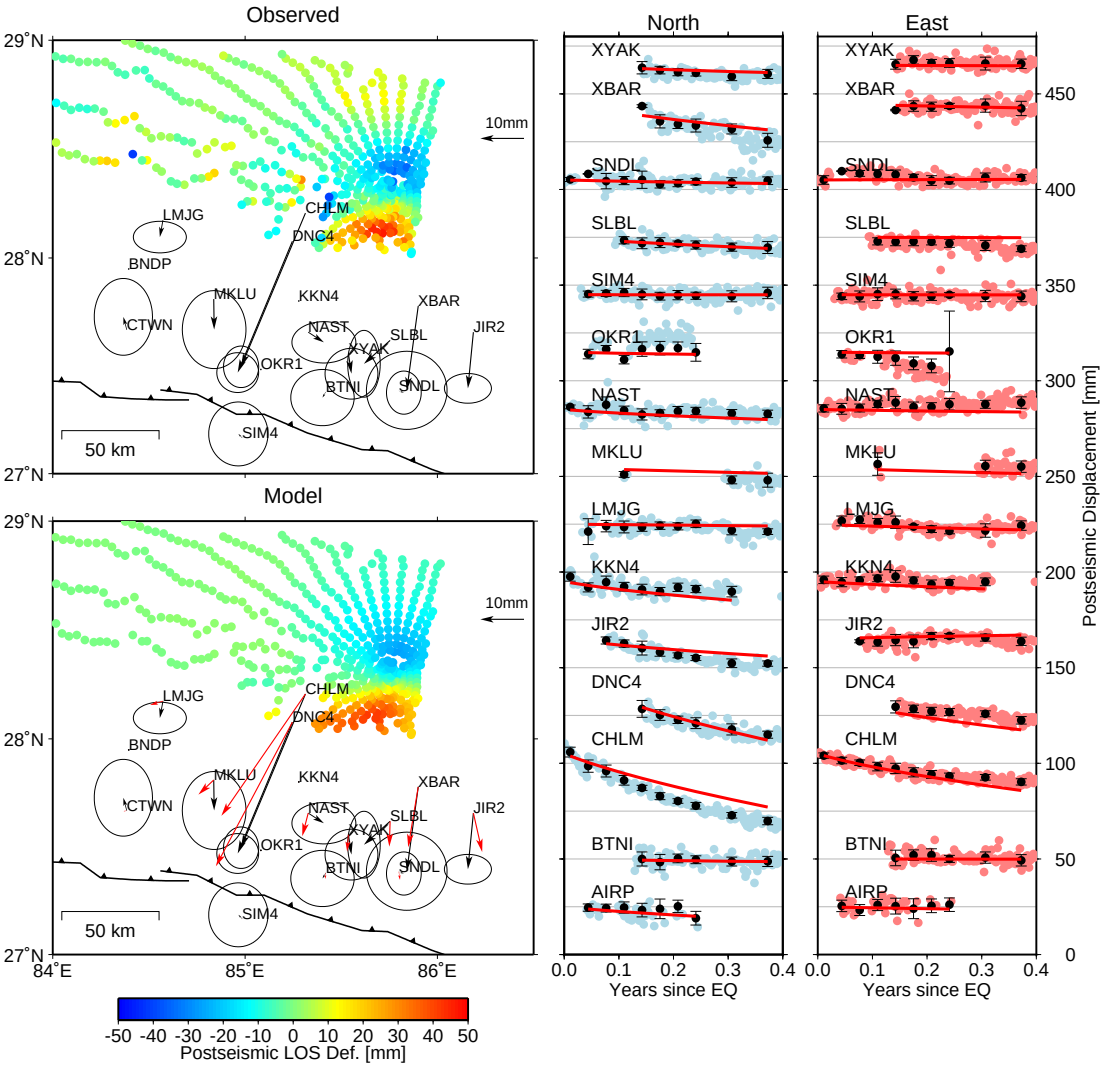

Figure 3.9: Postseismic displacements from stress-driven afterslip model. Top left panel show the final postseismic InSAR and GNSS displacements (8th September 2015). Bottom left panel shows the InSAR and GNSS (red arrows) displacements at the same date predicted by the mean model. Panels on the right show the GNSS time series for stations close to the coseismic rupture, with data points used in the inversion as black errorbars and the model fit as a red line. Note, no vertical GNSS displacements were used in the inversion.

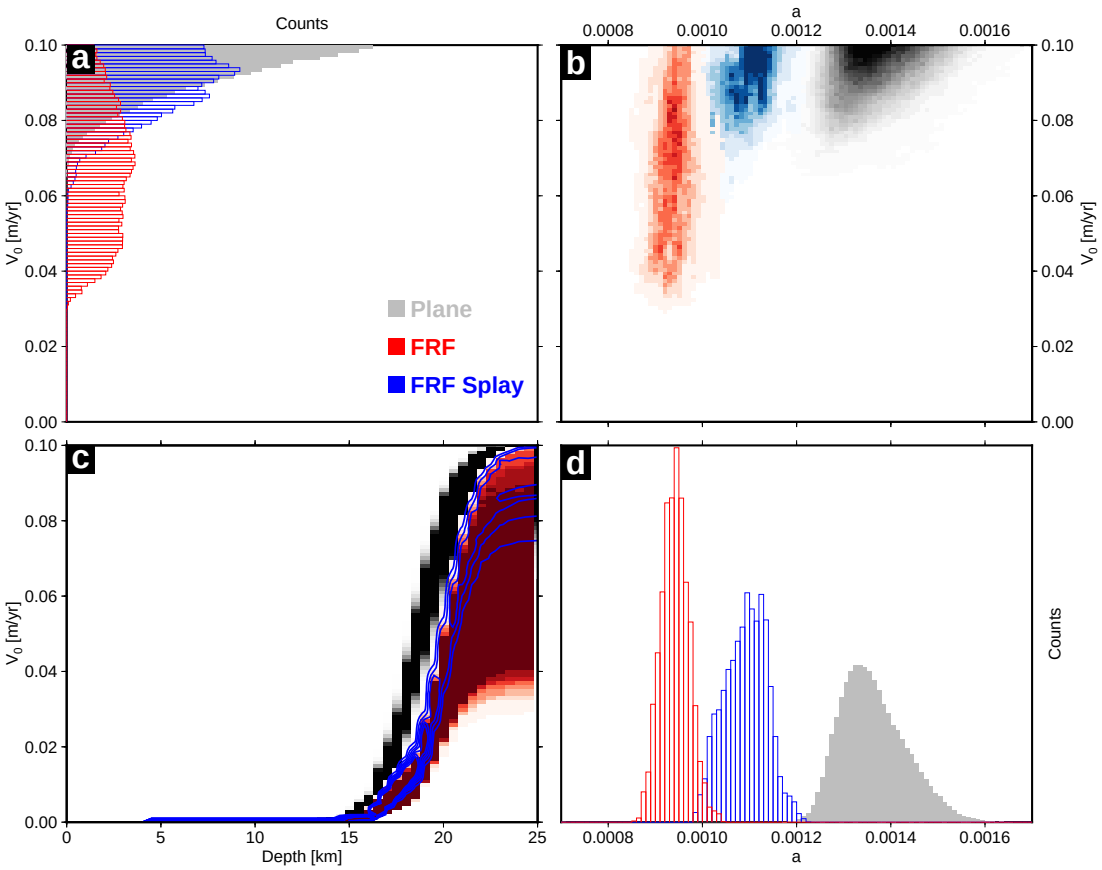

Figure 3.10: Comparison between the distributions of frictional properties for each geometry. a) Probability density function (PDF) of V_0. b) Joint PDFs for V_0 and a. c) Variation of V_0 with depth. d) PDF of a.

and postseismic data with variance reduction of over 99% for all three models. Furthermore, examination of the spatial distribution of residuals does not clearly favour one geometry over any other (see Figure B.17). Coseismic slip distributions for all three geometries are similar except where deeper slip in the planar and FRF models is mapped on to the shallow splay in the FRF splay model. Postseismic slip is primarily down-dip of the coseismic rupture in all cases, with the majority of slip fringing the down-dip edge of the main rupture. The FRF splay model has some possible shallow postseismic slip on the splay, probably caused by the low normal stresses on the fault at these depths. A similar mechanism may explain the shallow afterslip seen on the Main Dun thrust by *Elliott et al.* (2016).

Figure 3.10 shows a comparison between the values of a and V_0 inferred for each geometry. The results for the FRF and FRF-splay models are very similar and within error of one another but distinct from the results for the planar geometry. This suggests that the inclusion of a ramp has a significant effect on the inferred frictional properties, requiring lower values for both a and V_0.

3.5 Discussion

3.5.1 Postseismic Deformation

Our assessment of the postseismic deformation following the Gorkha event largely agrees with previous work (*Gualandi et al.*, 2016, *Mencin et al.*, 2016, *Sreejith et al.*, 2016, *Zhao et al.*, 2017, *Jiang et al.*, 2018, *Wang and Fialko*, 2018). GNSS and InSAR measurements show that postseismic deformation is relatively localised and predominantly north (down-dip) of the coseismic deformation. Our measurements confirm there is very little motion to the south of the Gorkha coseismic slip region. *Elliott et al.* (2016) observed limited afterslip ($<$ 6 cm LOS) on the Main Dun Thrust using Sentinel-1 interferograms, which we confirm is also visible in ALOS interferograms. *Bai et al.* (2016) suggested the aftershocks with steep nodal planes may have occurred on splay faults above the main ramp, suggesting possible activity following the earthquake. Postseismic slip on thrust faults may play a role in the development of topography (e.g. *Nishimura et al.*, 2008, *Copley and Reynolds*, 2014, *Copley*, 2014), and may contribute to the maintenance of taper in a critical taper wedge.

Modelling of the deformation reveals that rate-strengthening afterslip can explain the majority of geodetic data (VR $>$ 99%), although some limited viscoelastic relaxation is possible. The inferred afterslip does not extend significantly along strike, with most deformation directly down-dip of the coseismic rupture. This means the region to the west of the Gorkha event highlighted by *Avouac et al.* (2015) has not released significant seismic moment as afterslip. *Mencin et al.* (2016) argue that this limited afterslip points to strain reservoirs in the Himalaya which may contribute to large, surface-rupturing events along the MFT. Areas up-dip and along strike of the Gorkha event could still release their accumulated strain in future earthquakes.

3.5.2 Geometry of the Himalayan Fault System

We have presented the key constraints provided by seismic cycle geodesy in Nepal and discussed the variety of models which are permitted. As pointed out by *Taylor* (2016), different solutions can be obtained depending upon the philosophical approach used (see Figures 3.5 and 3.6). We have sought geometric models which are simultaneously capable of matching geodetic data from coseismic, postseismic and interseismic data. Such an approach can be used more generally to determine the range of fault geometries permitted in different tectonic settings.

Coseismic data requires there to be a shallowly dipping fault, extending from near the MFT surface trace to approximately 80 km north of the MFT. All of the proposed geometries, and our own inversions, agree on this aspect of the geometry (see Figures 3.5 and B.12). Slip in the largest aftershock also agrees with this geometry. It does not seem necessary to include a shallow splay fault, as proposed by *Whipple et al.*

(2016), to explain the 'uplift anomaly' they identify in the coseismic deformation field. This anomaly is seen in profiles through the eastern section of the coseismic InSAR data as a secondary hump to the north of the primary coseismic uplift signal. This welt of uplift is seen more clearly in some InSAR tracks than others, and is difficult to explain perfectly in all InSAR tracks with any of our models. All of the proposed models explain the uplift anomaly to a similar degree. Planar models do so by placing slip further north on the flat and FRF and FRF-splay models do so by having some slip on the ramp and/or splay fault (see Figure 3.6 and Figure B.17 in the supplementary material).

Postseismic and interseismic deformation suggest there is a shallowly dipping plane extending northwards with a depth of approximately 20 km between 120 and 140 km from the MFT. Geometries with deeper faults at these distances (e.g. *Elliott et al.*, 2016, *Hubbard et al.*, 2016) cannot reproduce the relatively short wavelength of the postseismic deformation field.

Any geometry for the Himalayan fault system therefore needs to contain two shallowly dipping fault segments at slightly different depths to explain both the coseismic and postseismic data. Unfortunately, our current suite of geodetic data cannot readily distinguish between the various proposals for how these two segments are connected. A single plane can explain the data reasonably well, but so can a geometry involving one or multiple ramps and splays.

In addition, our assumption that there is a single structure which accommodates strain throughout the earthquake cycle may be too simplistic. The apparent mismatch between the location of the mid-crustal ramp inferred using coseismic data (*Elliott et al.*, 2016) and that suggested by our modelling may hint at different structures active at different times (compare yellow and cyan lines for the FRF geometry in Figure 3.5). It may be that one ramp was active during the earthquake, and a more northerly ramp was active following the earthquake. Such a combination of active ramps could be indicative of a duplexing process, as inferred by studies of interseismic deformation (*Grandin et al.*, 2012, *Lindsey et al.*, 2018).

To make further progress, the constraints provided by geodesy need to be combined with those provided by other data sets in order to distinguish between various proposed geometries. For example, whilst a single planar geometry can reproduce the geodetic data, it offers no explanation for the spatial variation in long term uplift rates seen in the Himalaya (e.g. *Lavé and Avouac*, 2001, *Hodges et al.*, 2004, *Wobus et al.*, 2005). Therefore, geometries including a mid-crustal ramp, or out-of-sequence thrusting on splay faults are proposed as explanations, both of which also satisfy the geodetic data. Additional data sets can also be used, such as surface geology (*Hubbard et al.*, 2016), microseismicity (*Pandey et al.*, 1995) or seismic imaging (*Duputel et al.*, 2016), each of which provide different constraints on allowable geometries.

Multidisciplinary studies are therefore necessary if we are to fully constrain the

geometry and tectonics of the faults beneath Nepal. The geological modelling approach used by *Hubbard et al.* (2016) may be one way of conducting such interdisciplinary studies. Their model satisfies the constraints provided by geology and is corroborated by the distribution of slip in the Gorkha earthquake (*Grandin et al.*, 2015, *Qiu et al.*, 2016), potential dip variations in the earthquake itself (*Zhang et al.*, 2017) and the locations of aftershocks (*Wang et al.*, 2017). However, corroboration is not necessarily equivalent to confirmation of such a model. *Riesner et al.* (2017) highlight the need to include various data sets and account for their relative uncertainties when constructing such geological models. In order to do this, future multidisciplinary studies should not only use multiple kinds of data, but also contain the expertise necessary to account for the range of permissible models that can fit such data. This strategy should also be used more generally, where possible, to provide tighter constraints on fault geometries in a variety of tectonic contexts.

3.5.3 Frictional Properties

We developed a joint inversion algorithm that simultaneously solves for coseismic slip and fault frictional properties assuming rate-strengthening friction. We demonstrated that the inversion could successfully retrieve the frictional properties and coseismic slip distribution for a synthetic earthquake model. This method allows for the propagation of errors from the coseismic slip inversion in to errors in the inferred frictional properties. Our approach is generally applicable to fault systems undergoing frictional afterslip in response to coseismic stress transfer and could be adapted for use in other areas where we have both coseismic and postseismic deformation data.

Our model implementation depends on a number of simplifying assumptions such as perfect elasticity in a uniform half-space, minimal viscoelastic relaxation, lithostatic normal stresses, and a simplification of the rate- and state-friction laws. We applied our joint inversion to coseismic and postseismic data from Nepal, retrieving values for a in the range $0.8 - 1.6 \times 10^{-3}$, depending on the geometry of the fault system. These values are at the lower end of those retrieved from laboratory experiments, which are typically on the order of 10^{-3} to 10^{-2} (*Marone*, 1998, *van den Ende et al.*, 2018).

Wang and Fialko (2018) used a similar rate-strengthening friction law to explain postseismic deformation and found values for V_0 and a of 10 m/yr and 6.5×10^{-2} respectively. They used a locking width to force slip only down-dip of the rupture and found that a locking width of 110 km provides the best fit, which is in reasonable agreement with our results. We also found that our values for a and V_0 were significantly smaller than those inferred by *Wang and Fialko* (2018). This may be due to the slightly different geometries, different locking widths, different model set-up or different input data. However, our results for the planar geometry are consistent with those found in other studies of postseismic deformation, where $a\sigma$ is on the order of 0.1 - 10 MPa and V_0 on the order of the interseismic loading rate (*Barbot et al.*, 2009, *Chang et al.*, 2013,

Rollins et al., 2015, *Feng et al.*, 2016, *Wimpenny et al.*, 2017).

We found that all three geometries were capable of reproducing the majority of main shock, aftershock and postseismic displacements using physically coupled coseismic and postseismic slip. Variance reduction for all three geometries was over 99% with only small differences between them. The addition of a shallow splay fault gives a slight increase in variance reduction, as might be expected given the extra complexity of the model (81 more slip patches and an additional V_0 value). Overall though, we suggest that the minor differences in variance reduction mean that the three geometries are equally capable of explaining the observations both kinematically and dynamically.

The inferred frictional properties depend on the geometry used, primarily on whether a mid-crustal ramp is included in the model. A mid crustal ramp means patches down-dip of the Gorkha rupture are deeper, and thus have a higher lithostatic normal stress in our models. Furthermore, the more steeply dipping ramp affects the stress change experienced by all patches on and below the ramp as well as the impact that slip on these patches has on the surface deformation field. This combination of factors means that a different set of frictional properties are required in order to match the surface deformation observations.

3.5.4 Long-term Slip Budget

To test whether the long-term slip budget is balanced, we compared the results of our rate-strengthening afterslip model with the interseismic slip rates suggested by our kinematic modelling of profiles. We used the results for the planar geometry and calculated the total seismic and aseismic slip for different scenarios. We used the mode coseismic slip and mean frictional properties for each patch on the planar geometry, and then take the average of patches along strike to give down-dip coseismic and postseismic slip distributions. Firstly, we assumed that the 1833 earthquake released all the slip deficit in the region of the 2015 Gorkha event, and that the two events were similar in nature (*Mencin et al.*, 2016). The 1833 event had a similar magnitude to the 2015 event (M_w 7.5 - 7.9) and occurred near to Kathmandu, failing to rupture the surface (*Bilham*, 1995, *Mugnier et al.*, 2013). We compared the accumulated interseismic slip between the 1833 earthquake with the coseismic and postseismic slip in the Gorkha event (Figure 3.11a). In this scenario, the coseismic and postseismic slip lead to a slip surplus for distances greater than approximately 70 km from the MFT. Such a situation seems unlikely, and arises because our kinematic models suggest significant interseismic slip occurs over a similar range as both coseismic and postseismic slip (e.g. see Figure 3.5).

We therefore tried a different approach, where we calculated the interseismic rate at different distances from the MFT by assuming no net slip deficit or surplus for distances greater than 80 km from the MFT. We used the time between the 1833 and 2015 earthquakes as our observation period and obtained the interseismic slip rate at

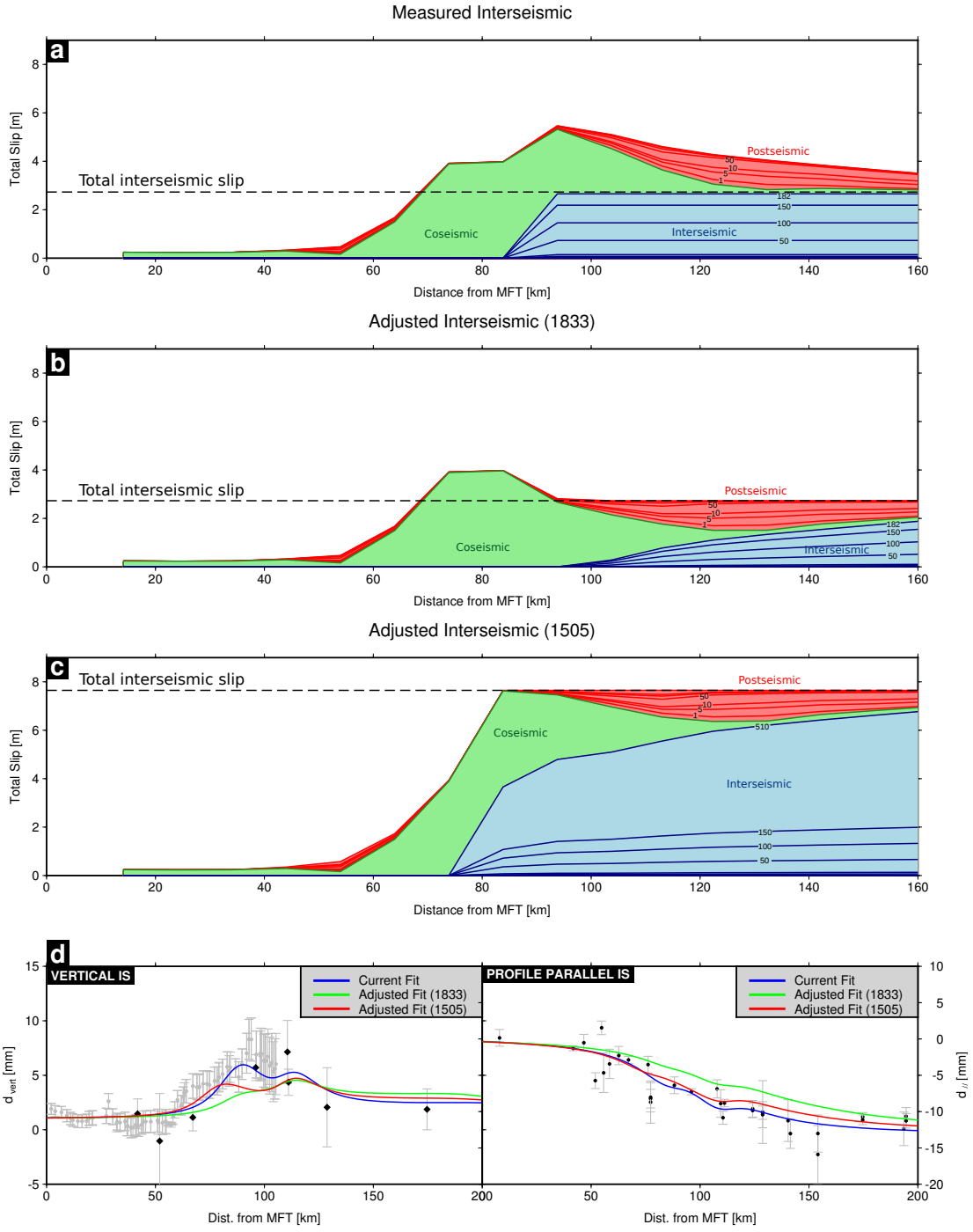

Figure 3.11: Slip budget for different scenarios in Nepal. a) Total slip between the 1833 and 2015 earthquakes. Different colours refer to slip in different parts of the earthquake cycle. Small numbers along slip contours correspond to the number of years over which the slip has accrued. Dashed line is the total slip which needs to be released over the period. b) Same as a), except the interseismic slip rate is adjusted at each point to balance the slip budget. c) Same as b), but using a convergence rate of 20 mm/yr to balance the slip budget. d) Fit of the different interseismic slip models to interseismic data prior to the 2015 Gorkha earthquake.

each point as:

$$V_{IS} = (V_{conv} t_{rec} - (U_{CS} + U_{PS}))/t_{rec} \tag{3.9}$$

where V_{IS} is the adjusted interseismic slip rate at each point and V_{conv} is the convergence rate (assumed as 15 mm/yr). U_{CS} is the coseismic displacement in the Gorkha earthquake and U_{PS} is the total postseismic displacement over the observation period, whilst t_{rec} is the recurrence interval (182 years between 1833 and 2015). The results for this scenario are shown in Figure 3.11b, and show a small slip surplus in the region of highest coseismic slip, but no surplus north of this. The transition from locked to freely sliding here is further from the MFT and much more gradual than suggested by our kinematic models, even when using distributed slip inversions for the interseismic deformation. We compared the predicted surface deformation using such an interseismic locking pattern with that recorded by GNSS and levelling (Figure 3.11d), finding a poor fit, particularly to the levelling data.

In order to improve the fit to the interseismic deformation data, the interseismic transition needs to be closer to the MFT. In other words, interseismic deformation needs to play a greater role in closing the slip budget at shorter distances from the MFT. This can be achieved by increasing the overall convergence rate, thereby increasing the fraction of the total displacement accommodated by interseismic slip at each point. We therefore increased the convergence rate to 20 mm/yr (e.g. *Stevens and Avouac*, 2015) and recalculated the interseismic velocities required to balance the slip budget (Figure 3.11c). In this situation, the interseismic rates are better able to match the GNSS and levelling data, although still not as effectively as our best-fit kinematic model. Furthermore, the amount of coseismic slip in the earthquake is approximately equal to the accumulated slip over the interseismic period in this model. If the time between earthquakes was longer, then interseismic slip would extend closer to the MFT, potentially improving the fit to the interseismic surface deformation data.

In all our models, there are parts of the fault which either show a slip surplus or a slip deficit. *Stevens and Avouac* (2015) have shown that the long term slip rates, measured geologically along the Himalayan arc, closely resemble the short term convergence rates measured using geodesy. This suggests the seismic cycle should approximately balance, with almost all convergence being transferred to the frontal thrusts along the MFT. Small, local slip surpluses or deficits may be present in our models because our models do not cover a long enough time period, or because of our geometric simplifications and averaging along-strike. Alternatively, small slip surpluses may indicate permanent deformation which is not transferred all the way to the front, thereby proving a means of growing topography (*Meade*, 2010).

Whatever assumptions are used for our models, a significant slip deficit exists updip of the Gorkha coseismic rupture. If the 1833 earthquake ruptured to the front

and released any accumulated strain there, then the total up-dip slip deficit is equal to the convergence rate multiplied by the total time. Convergence rates of 15 - 20 mm/yr give slip deficits of 2.7 - 3.7 m up-dip of the Gorkha rupture. On the other hand, if the 1833 event did not rupture to the front, but was instead similar to the Gorkha event, then the last time slip was released to the front may have been 1505. Using the same convergence rates as above gives slip deficits of 7.7 - 10.3 m. *Mencin et al.* (2016) have highlighted the role that Gorkha type events may play in transferring strain to the frontal portion of the Himalayan fold and thrust belt, accruing a large strain reservoir which could rupture in future events. We can estimate an approximate magnitude range for possible future earthquakes which rupture the whole region up-dip of the Gorkha event (rupture length of 110 km and down-dip width of 70 km). We obtain moment magnitudes (M_w) in the range 7.8 - 8.2 for the different slip deficits discussed above. However, larger events would be possible, either due to the slip deficit being higher, or due to this up-dip region slipping as part of an earthquake nucleating deeper in the fault system, in a similar location to the Gorkha event.

3.6 Conclusions

We processed InSAR and GNSS data to obtain measurements of near-field postseismic deformation following the M_w7.8 Gorkha earthquake in Nepal. We obtained a similar deformation field to previous studies (*Gualandi et al.*, 2016, *Mencin et al.*, 2016, *Sreejith et al.*, 2016, *Zhao et al.*, 2017, *Jiang et al.*, 2018, *Wang and Fialko*, 2018), which is dominantly produced by afterslip. Furthermore, this afterslip does not reduce any of the slip deficit up-dip of the coseismic rupture, and this deficit may be many metres and capable of producing earthquakes with moment magnitudes in the range 7.8 - 8.2.

We then combined these data with coseismic and interseismic geodetic data to investigate the geometry of the Himalayan fault system. We found that the data required a shallowly dipping fault until at least 80 km north of the MFT surface trace. Our combined data could not conclusively distinguish between different possible geometries north of this point.

We developed a joint inversion which seeks models which simultaneously fit the coseismic, aftershock and postseismic deformation fields. The inversion uses a rate-strengthening friction law to link the coseismic and postseismic slip by solving for the frictional properties (a and V_0). We found that afterslip, caused by stress changes associated with the main shock and aftershock, could explain most of the postseismic data. We found a to be between $0.8 - 1.6 \times 10^{-3}$, in agreement with laboratory experiments and postseismic deformation studies of other earthquakes. This range of a values could be used in future simulations of the earthquake cycle in the Nepal Himalaya to better understand potential hazards in the region.

All three proposed geometries are capable of explaining over 99% of the data vari-

ance, and thus fail to provide an alternative way of distinguishing the most appropriate model. It therefore seems necessary to increase the quantity, quality and diversity of data in the Nepal Himalaya. Furthermore, these data need to be correctly integrated by multidisciplinary teams with the expertise to understand the errors and limitations of each data set. New models are also required to adequately model each of the data sets and tie them together.

Acknowledgments

TI is funded by the UK Natural Environment Research Council (NERC) through the Leeds-York NERC Doctoral Training Program (NE/L002574/1). TJC thanks the Royal Commission for the Exhibition of 1851 for financial support through a Research Fellowship. JRE acknowledges support from the Royal Society through a University Research Fellowship (UF150282). This work was supported by NERC through the Centre for the Observation and Modelling of Earthquakes, Volcanoes and Tectonics (COMET, GA/13/M/031, http://comet.nerc.ac.uk) and via the Looking Inside the Continents (LiCS) project (NE/K011006/1). GNSS time series data were acquired from the Nevada Geodetic Laboratory (http://geodesy.unr.edu/) and from *Gualandi et al.* (2016). Stations were deployed and maintained through a collaboration between Caltech and the Department of Mines and Geology (Nepal). Some stations were deployed by Roger Bilham, Rebecca Bendick, and David Mencin after the 2015 Gorkha earthquake. Coseismic GNSS displacements are from *Galetzka et al.* (2015) and GNSS interseismic horizontal velocities were acquired from the Global Strain Rate Model (http://gsrm2.unavco.org/intro/intro.html, *Kreemer et al.* (2014)). Vertical interseismic GNSS velocities were obtained from *Ader et al.* (2012) and levelling data from (*Jackson and Bilham*, 1994). Meteorological data were provided by ECMWF (http://apps.ecmwf.int/datasets/), the Nevada Geodetic Laboratory, and produced using GNSS data provided by UNAVCO (http://www.unavco.org/). The Sentinel-1A interferograms were produced by *Elliott et al.* (2016) or in this study and are a derived work of Copernicus data, subject to the ESA use and distribution conditions. ALOS-2 data were provided by *Lindsey et al.* (2015) online at http://topex.ucsd.edu/nepal/. Postseismic InSAR and GNSS data from this study can be found in the supplementary material. Most figures were made using the Generic Mapping Tools (GMT) (*Wessel and Smith*, 1991). We thank Pablo J Gonzalez for his help with InSAR processing and the use of the LiCSAR system. We thank the editor, Paul Tregoning, Associate Editor, Emma Hill, and two anonymous reviewers for their helpful comments which improved the manuscript.

References

Ader, T., J.-P. Avouac, J. Liu-Zeng, H. Lyon-Caen, L. Bollinger, J. Galetzka, J. Genrich, M. Thomas, K. Chanard, S. N. Sapkota, S. Rajaure, P. Shrestha, L. Ding, and M. Flouzat (2012), Convergence rate across the Nepal Himalaya and interseismic coupling on the Main Himalayan Thrust: Implications for seismic hazard, *Journal of Geophysical Research*, *117*(B4), B04,403, doi:10.1029/2011JB009071. 3.1, 3.3.2, 3.3.2, 3.2, 3.6

Adhikari, L., U. Gautam, B. Koirala, M. Bhattarai, T. Kandel, R. Gupta, C. Timsina, N. Maharjan, K. Maharjan, T. Dahal, R. Hoste-Colomer, Y. Cano, M. Dandine, A. Guilhem, S. Merrer, P. Roudil, and L. Bollinger (2015), The aftershock sequence of the 2015 April 25 GorkhaNepal earthquake, *Geophysical Journal International*, *203*(3), 2119–2124, doi:10.1093/gji/ggv412. 3.3.2

Amey, R. M. J., A. Hooper, and R. J. Walters (2018), A Bayesian Method for Incorporating Self-Similarity Into Earthquake Slip Inversions, *Journal of Geophysical Research: Solid Earth*, doi:10.1029/2017JB015316. 3.3.2, 3.4.1

Avouac, J.-P., L. Meng, S. Wei, T. Wang, and J.-P. Ampuero (2015), Lower edge of locked Main Himalayan Thrust unzipped by the 2015 Gorkha earthquake, *Nature Geoscience*, *8*(9), 708–711, doi:10.1038/ngeo2518. 3.1, 3.3.1, 3.3.3, 3.5.1

Bagnardi, M., and A. J. Hooper (2017), GBIS (Geodetic Bayesian Inversion Software): Rapid Inversion of InSAR and GNSS Data to Estimate Surface Deformation Source Parameters and Uncertainties, in *American Geophysical Union, Fall Meeting 2017, abstract #G23A-0881.* 3.3.2

Bai, L., H. Liu, J. Ritsema, J. Mori, T. Zhang, Y. Ishikawa, and G. Li (2016), Faulting structure above the Main Himalayan Thrust as shown by relocated aftershocks of the 2015 M_w 7.8 Gorkha, Nepal, earthquake, *Geophysical Research Letters*, *43*(2), 637–642, doi:10.1002/2015GL066473. 3.3.2, 3.3, 3.5.1

Barbot, S., and Y. Fialko (2010), A unified continuum representation of post-seismic relaxation mechanisms: semi-analytic models of afterslip, poroelastic rebound and viscoelastic flow, *Geophysical Journal International*, *182*(3), 1124–1140, doi:10.1111/j.1365-246X.2010.04678.x. 3.1

Barbot, S., Y. Fialko, and Y. Bock (2009), Postseismic deformation due to the M w 6.0 2004 Parkfield earthquake: Stress-driven creep on a fault with spatially variable rate-and-state friction parameters, *Journal of Geophysical Research*, *114*(B7), B07,405, doi:10.1029/2008JB005748. 3.3.4, 3.4.1, 3.4.1, 3.4.1, 3.5.3

Bekaert, D., R. Walters, T. Wright, A. Hooper, and D. Parker (2015a), Statistical comparison of InSAR tropospheric correction techniques, *Remote Sensing of Environment*, *170*, 40–47, doi:10.1016/j.rse.2015.08.035. 3.2.2

Bekaert, D. P. S., A. Hooper, and T. J. Wright (2015b), A spatially-variable power-law tropospheric correction technique for InSAR data, *Journal of Geophysical Research: Solid Earth*, pp. n/a–n/a, doi:10.1002/2014JB011558. 3.2.2

Ben Thompson, T., and B. J. Meade (2018), Topography and the shallow slip deficit inference, doi:10.31223/OSF.IO/PUZ84. 3.3.2

Bettinelli, P., J.-P. Avouac, M. Flouzat, F. Jouanne, L. Bollinger, P. Willis, and G. R. Chitrakar (2006), Plate Motion of India and Interseismic Strain in the Nepal Himalaya from GPS and DORIS Measurements, *Journal of Geodesy*, *80*(8-11), 567–589, doi:10.1007/s00190-006-0030-3. 3.3.2

Bilham, R. (1995), Location and magnitude of the 1833 Nepal earthquake and its relation to the rupture zones of contiguous great Himalayan earthquakes, doi:10.2307/24097233. 3.5.4

Bilham, R., and K. Wallace (2005), Future Mw>8 earthquakes in the Himalaya: implications from the 26 Dec 2004 Mw=9.0 earthquake on India's eastern plate margin, *Geol. Surv. Ind. Spl. Pub*, *85*(85), 1–14. 3.1

Bonini, L., G. Toscani, and S. Seno (2014), Three-dimensional segmentation and different rupture behavior during the 2012 Emilia seismic sequence (Northern Italy), *Tectonophysics*, *630*, 33–42, doi:10.1016/j.tecto.2014.05.006. 3.1

Chang, S.-H., J.-P. Avouac, S. Barbot, and J.-C. Lee (2013), Spatially variable fault friction derived from dynamic modeling of aseismic afterslip due to the 2004 Parkfield earthquake, *Journal of Geophysical Research: Solid Earth*, *118*(7), 3431–3447, doi:10.1002/jgrb.50231. 3.4.1, 3.4.1, 3.5.3

Copley, A. (2014), Postseismic afterslip 30 years after the 1978 Tabas-e-Golshan (Iran) earthquake: observations and implications for the geological evolution of thrust belts, *Geophysical Journal International*, *197*(2), 665–679, doi:10.1093/gji/ggu023. 3.5.1

Copley, A., and R. Jolivet (2016), Fault rheology in an aseismic fold-thrust belt (Shahdad, eastern Iran), *Journal of Geophysical Research: Solid Earth*, *121*(1), 412–431, doi:10.1002/2015JB012431. 3.1

Copley, A., and K. Reynolds (2014), Imaging topographic growth by long-lived postseismic afterslip at Sefidabeh, east Iran, *Tectonics*, *33*(3), 330–345, doi:10.1002/2013TC003462. 3.5.1

Decriem, J., T. Árnadóttir, A. Hooper, H. Geirsson, F. Sigmundsson, M. Keiding, B. G. Ófeigsson, S. Hreinsdóttir, P. Einarsson, P. LaFemina, and R. A. Bennett (2010), The 2008 May 29 earthquake doublet in SW Iceland, *Geophysical Journal International*, doi:10.1111/j.1365-246X.2010.04565.x. 3.4.1

Duputel, Z., P. S. Agram, M. Simons, S. E. Minson, and J. L. Beck (2014), Accounting for prediction uncertainty when inferring subsurface fault slip, *Geophysical Journal International*, *197*(1), 464–482, doi:10.1093/gji/ggt517. 3.3.2

Duputel, Z., J. Vergne, L. Rivera, G. Wittlinger, V. Farra, and G. Hetényi (2016), The 2015 Gorkha earthquake: A large event illuminating the Main Himalayan Thrust fault, *Geophysical Research Letters*, *43*(6), 2517–2525, doi:10.1002/2016GL068083. 3.5.2

Elliott, J., R. Jolivet, P. J. González, J.-P. Avouac, J. Hollingsworth, M. P. Searle, and V. Stevens (2016), Himalayan megathrust geometry and relation to topography revealed by the Gorkha earthquake, *Nature Geoscience*, *9*(2), 174–180, doi:10.1038/ngeo2623. 3.1, 3.1, 3.3.1, 3.3.2, 3.2, 3.3.2, 3.3.3, 3.4, 3.3.3, 3.4.1, 3.4.2, 3.5.1, 3.5.2, 3.6

Elliott, J. R., J. Biggs, B. Parsons, and T. J. Wright (2008), InSAR slip rate determination on the Altyn Tagh Fault, northern Tibet, in the presence of topographically correlated atmospheric delays, *Geophysical Research Letters*, *35*(12), n/a–n/a, doi:10.1029/2008GL033659. 3.2.2

Elliott, J. R., B. Parsons, J. A. Jackson, X. Shan, R. A. Sloan, and R. T. Walker (2011), Depth segmentation of the seismogenic continental crust: The 2008 and 2009 Qaidam earthquakes, *Geophysical Research Letters*, *38*(6), n/a–n/a, doi:10.1029/2011GL046897. 3.1

Feng, L., S. Barbot, E. M. Hill, I. Hermawan, P. Banerjee, and D. H. Natawidjaja (2016), Footprints of past earthquakes revealed in the afterslip of the 2010 M_w 7.8 Mentawai tsunami earthquake, *Geophysical Research Letters*, *43*(18), 9518–9526, doi:10.1002/2016GL069870. 3.3.4, 3.4.1, 3.4.1, 3.5.3

Freed, A. M. (2007), Afterslip (and only afterslip) following the 2004 Parkfield, California, earthquake, *Geophysical Research Letters*, *34*(6), L06,312, doi:10.1029/2006GL029155. 3.1, 3.2.4

Freed, A. M., R. Bürgmann, and T. Herring (2007), Far-reaching transient motions after Mojave earthquakes require broad mantle flow beneath a strong crust, *Geophysical Research Letters*, *34*(19), L19,302, doi:10.1029/2007GL030959. 3.2.4

Fukuda, J., and K. M. Johnson (2008), A Fully Bayesian Inversion for Spatial Distribution of Fault Slip with Objective Smoothing, *Bulletin of the Seismological Society of America*, *98*(3), 1128–1146, doi:10.1785/0120070194. 3.3.3, 3.4.1

Galetzka, J., D. Melgar, J. F. Genrich, J. Geng, S. Owen, E. O. Lindsey, X. Xu, Y. Bock, J.-P. Avouac, L. B. Adhikari, B. N. Upreti, B. Pratt-Sitaula, T. N. Bhattarai, B. P. Sitaula, A. Moore, K. W. Hudnut, W. Szeliga, J. Normandeau, M. Fend, M. Flouzat, L. Bollinger, P. Shrestha, B. Koirala, U. Gautam, M. Bhatterai, R. Gupta, T. Kandel, C. Timsina, S. N. Sapkota, S. Rajaure, and N. Maharjan (2015), Slip pulse and resonance of the Kathmandu basin during the 2015 Gorkha earthquake, Nepal, *Science*, *349*(6252). 3.1, 3.3.1, 3.2, 3.4.1, 3.6

Grandin, R., M.-P. Doin, L. Bollinger, B. Pinel-Puyssegur, G. Ducret, R. Jolivet, S. N. Sapkota, S. H., C. J., H. B.-S., and H. P. (2012), Long-term growth of the Himalaya inferred from interseismic InSAR measurement, *Geology*, *40*(12), 1059–1062, doi:10.1130/G33154.1. 3.3.2, 3.5.2

Grandin, R., M. Vallée, C. Satriano, R. Lacassin, Y. Klinger, M. Simoes, and L. Bollinger (2015), Rupture process of the M_w =7.9 2015 Gorkha earthquake (Nepal): Insights into Himalayan megathrust segmentation, *Geophysical Research Letters*, *42*(20), 8373–8382, doi:10.1002/2015GL066044. 3.1, 3.3.1, 3.5.2

Gualandi, A., J.-P. Avouac, J. Galetzka, J. F. Genrich, G. Blewitt, L. Bijaya Adhikari, B. Prasad Koirala, R. Gupta, B. Nath Upreti, B. Pratt-Sitaula, and J. Liu-Zeng (2016), Pre-and post-seismic deformation related to the 2015, Mw 7.8 Gorkha earthquake, Nepal, *Tectonophysics*, doi:10.1016/j.tecto.2016.06.014. 3.1, 3.2.1, 3.2.2, 3.2.2, 3.2.3, 3.2.4, 3.3.1, 3.5.1, 3.6, 3.6

Hao, M., Z.-K. Shen, Q. Wang, and D. Cui (2012), Postseismic deformation mechanisms of the 1990 Mw 6.4 Gonghe, China earthquake constrained using leveling measurements, *Tectonophysics*, *532-535*, 205–214, doi:10.1016/j.tecto.2012.02.005. 3.2.4

Hearn, E. H. (2002), Dynamics of Izmit Earthquake Postseismic Deformation and Loading of the Duzce Earthquake Hypocenter, *Bulletin of the Seismological Society of America*, *92*(1), 172–193, doi:10.1785/0120000832. 3.1, 3.4.1

Herring, T. A., R. W. King, and S. C. McClusky (2013), Introduction to GAMIT-GLOBK Release 10.5, *Tech. rep.* 3.2.2

Hodges, K. V., C. Wobus, K. Ruhl, T. Schildgen, and K. Whipple (2004), Quaternary deformation, river steepening, and heavy precipitation at the front of the Higher Himalayan ranges, *Earth and Planetary Science Letters*, *220*(3-4), 379–389, doi:10.1016/S0012-821X(04)00063-9. 3.1, 3.3.1, 3.5.2

Hooper, A., D. Bekaert, K. Spaans, and M. Arkan (2012), Recent advances in SAR interferometry time series analysis for measuring crustal deformation, *Tectonophysics*, *514-517*, 1–13, doi:10.1016/j.tecto.2011.10.013. 3.2.1, 3.2.2

Huang, M.-H., H. Tung, E. J. Fielding, H.-H. Huang, C. Liang, C. Huang, and J.-C. Hu (2016), Multiple fault slip triggered above the 2016 M_w 6.4 MeiNong earthquake in Taiwan, *Geophysical Research Letters*, *43*(14), 7459–7467, doi:10.1002/2016GL069351. 3.3.4

Hubbard, J., S. Barbot, E. M. Hill, and P. Tapponnier (2015), Coseismic slip on shallow décollement megathrusts: implications for seismic and tsunami hazard, *Earth-Science Reviews*, *141*, 45–55, doi:10.1016/J.EARSCIREV.2014.11.003. 3.1

Hubbard, J., R. Almeida, A. Foster, S. N. Sapkota, P. Bürgi, and P. Tapponnier (2016), Structural segmentation controlled the 2015 M_w 7.8 Gorkha earthquake rupture in Nepal, *Geology*, *44*(8), 639–642, doi:10.1130/G38077.1. 3.1, 3.3.1, 3.3.2, 3.3.2, 3.3.3, 3.5.2

Hussain, E., T. J. Wright, R. J. Walters, D. Bekaert, A. Hooper, and G. A. Houseman (2016), Geodetic observations of postseismic creep in the decade after the 1999 Izmit earthquake, Turkey: Implications for a shallow slip deficit, *Journal of Geophysical Research: Solid Earth*, *121*(4), 2980–3001, doi:10.1002/2015JB012737. 3.4.1

Ingleby, T., and T. J. Wright (2017), Omori-like decay of postseismic velocities following continental earthquakes, *Geophysical Research Letters*, *44*(7), 3119–3130, doi:10.1002/2017GL072865. 3.1, 3.2.4

Jackson, M., and R. Bilham (1994), Constraints on Himalayan deformation inferred from vertical velocity fields in Nepal and Tibet, *Journal of Geophysical Research: Solid Earth*, *99*(B7), 13,897–13,912, doi:10.1029/94JB00714. 3.1, 3.3.2, 3.3.2, 3.2, 3.6

Jiang, Z., L. Yuan, D. Huang, Z. Yang, and A. Hassan (2018), Postseismic deformation associated with the 2015 Mw 7.8 Gorkha earthquake, Nepal: investigating ongoing afterslip and constraining crustal rheology, *Journal of Asian Earth Sciences*, doi:10.1016/J.JSEAES.2017.12.039. 3.1, 3.2.1, 3.2.3, 3.2.4, 3.5.1, 3.6

Jolivet, R., R. Grandin, C. Lasserre, M.-P. Doin, and G. Peltzer (2011), Systematic InSAR tropospheric phase delay corrections from global meteorological reanalysis data, *Geophysical Research Letters*, *38*(17), n/a–n/a, doi:10.1029/2011GL048757. 3.2.2

Jolivet, R., M. Simons, P. S. Agram, Z. Duputel, and Z.-K. Shen (2015), Aseismic slip and seismogenic coupling along the central San Andreas Fault, *Geophysical Research Letters*, *42*(2), 297–306, doi:10.1002/2014GL062222. 3.1

Jónsson, S., P. Segall, R. Pedersen, and G. Björnsson (2003), Post-earthquake ground movements correlated to pore-pressure transients, *Nature*, *424*(6945), 179–183, doi:10.1038/nature01776. 3.2.4

Kreemer, C., G. Blewitt, and E. C. Klein (2014), A geodetic plate motion and Global Strain Rate Model, *Geochemistry, Geophysics, Geosystems*, *15*(10), 3849–3889, doi:10.1002/2014GC005407. 3.3.2, 3.3.2, 3.2, 3.6

Lavé, J., and J. P. Avouac (2001), Fluvial incision and tectonic uplift across the Himalayas of central Nepal, *Journal of Geophysical Research: Solid Earth*, *106*(B11), 26,561–26,591, doi:10.1029/2001JB000359. 3.1, 3.3.1, 3.5.2

Lindsey, E. O., R. Natsuaki, X. Xu, M. Shimada, M. Hashimoto, D. Melgar, and D. T. Sandwell (2015), Line-of-sight displacement from ALOS-2 interferometry: M w 7.8 Gorkha Earthquake and M w 7.3 aftershock, *Geophysical Research Letters*, *42*(16), 6655–6661, doi:10.1002/2015GL065385. 3.1, 3.3.1, 3.3.2, 3.2, 3.4.1, 3.6

Lindsey, E. O., R. Almeida, R. Mallick, J. Hubbard, K. Bradley, L. L. H. Tsang, Y. Liu, R. Burgmann, and E. M. Hill (2018), Structural Control on Downdip Locking Extent of the Himalayan Megathrust, *Journal of Geophysical Research: Solid Earth*, *123*(6), 5265–5278, doi:10.1029/2018JB015868. 3.5.2

Lohman, R. B., and M. Simons (2005), Some thoughts on the use of InSAR data to constrain models of surface deformation: Noise structure and data downsampling, *Geochemistry, Geophysics, Geosystems*, *6*(1), n/a–n/a, doi:10.1029/2004GC000841. 3.3.2

Marone, C. (1998), Laboratory-derived friction laws and their application to seismic faulting, *Annual Review of Earth and Planetary Sciences*, *26*, 643–696. 3.4.1, 3.5.3

Meade, B. J. (2010), The signature of an unbalanced earthquake cycle in Himalayan topography?, *Geology*, *38*(11), 987–990, doi:10.1130/G31439.1. 3.5.4

Mencin, D., R. Bendick, B. N. Upreti, D. P. Adhikari, A. Gajurel, R. R. Bhattarai, H. R. Shrestha, T. N. Bhattarai, N. Manandhar, J. Galetzka, E. Knappe, B. Pratt-Sitaula, A. Aoudia, and R. Bilham (2016), Himalayan strain reservoir inferred from limited afterslip following the Gorkha earthquake, *Nature Geoscience*, *9*(7), 533–537, doi:10.1038/ngeo2734. 3.1, 3.2.1, 3.2.3, 3.2.4, 3.3.1, 3.5.1, 3.5.4, 3.5.4, 3.6

Mosegaard, K., and A. Tarantola (1995), Monte Carlo sampling of solutions to inverse problems, *Journal of Geophysical Research: Solid Earth*, *100*(B7), 12,431–12,447, doi:10.1029/94JB03097. 3.3.2

Mugnier, J.-L., A. Gajurel, P. Huyghe, R. Jayangondaperumal, F. Jouanne, and B. Upreti (2013), Structural interpretation of the great earthquakes of the last millennium in the central Himalaya, *Earth-Science Reviews*, *127*, 30–47, doi:10.1016/J.EARSCIREV.2013.09.003. 3.5.4

Nishimura, T., M. Tobita, H. Yarai, T. Amagai, M. Fujiwara, H. Une, and M. Koarai (2008), Episodic growth of fault-related fold in northern Japan observed by SAR interferometry, *Geophysical Research Letters*, *35*(13), L13,301, doi:10.1029/2008GL034337. 3.5.1

Okada, Y. (1985), Surface deformation due to shear and tensile faults in a half-space, *Bulletin of the Seismological Society of America*, *75*(4), 1135–1154. 3.3.2, 3.4.1

Okada, Y. (1992), Internal deformation due to shear and tensile faults in a half-space, *Bulletin of the Seismological Society of America*, *82*(2), 1018–1040. 3.4.1

Oliver, M., and R. Webster (2014), A tutorial guide to geostatistics: Computing and modelling variograms and kriging, *CATENA*, *113*, 56–69, doi:10.1016/j.catena.2013.09.006. 3.3.2

Pandey, M. R., R. P. Tandukar, J. P. Avouac, J. Lavé, and J. P. Massot (1995), Interseismic strain accumulation on the Himalayan crustal ramp (Nepal), *Geophysical Research Letters*, *22*(7), 751–754, doi:10.1029/94GL02971. 3.1, 3.3.1, 3.5.2

Perfettini, H., and J.-P. Avouac (2004), Postseismic relaxation driven by brittle creep: A possible mechanism to reconcile geodetic measurements and the decay rate of aftershocks, application to the Chi-Chi earthquake, Taiwan, *Journal of Geophysical Research*, *109*(B2), B02,304, doi:10.1029/2003JB002488. 3.1, 3.2.4, 3.4.1

Perfettini, H., J.-P. Avouac, H. Tavera, A. Kositsky, J.-M. Nocquet, F. Bondoux, M. Chlieh, A. Sladen, L. Audin, D. L. Farber, and P. Soler (2010), Seismic and aseismic slip on the Central Peru megathrust, *Nature*, *465*(7294), 78–81, doi:10.1038/nature09062. 3.1

Pollitz, F. F. (1997), Gravitational viscoelastic postseismic relaxation on a layered spherical Earth, *Journal of Geophysical Research: Solid Earth*, *102*(B8), 17,921–17,941, doi:10.1029/97JB01277. 3.2.4

Qiu, Q., E. M. Hill, S. Barbot, J. Hubbard, W. Feng, E. O. Lindsey, L. Feng, K. Dai, S. V. Samsonov, and P. Tapponnier (2016), The mechanism of partial rupture of a locked megathrust: The role of fault morphology, *Geology*, *44*(10), 875–878, doi:10.1130/G38178.1. 3.3.1, 3.5.2

Ragon, T., A. Sladen, and M. Simons (2018), Accounting for uncertain fault geometry in earthquake source inversions I: theory and simplified application, *Geophysical Journal International*, *214*(2), 1174–1190, doi:10.1093/gji/ggy187. 3.3.2

Riesner, M., P. DurandRiard, J. Hubbard, A. Plesch, and J. H. Shaw (2017), Building Objective 3D Fault Representations in Active Tectonic Settings, *Seismological Research Letters*, *88*(3), 831–839, doi:10.1785/0220160192. 3.5.2

Rollins, C., S. Barbot, and J.-P. Avouac (2015), Postseismic Deformation Following the 2010 M = 7.2 El Mayor-Cucapah Earthquake: Observations, Kinematic Inversions, and Dynamic Models, *Pure and Applied Geophysics*, doi:10.1007/s00024-014-1005-6. 3.5.3

Rousset, B., S. Barbot, J.-P. Avouac, and Y.-J. Hsu (2012), Postseismic deformation following the 1999 Chi-Chi earthquake, Taiwan: Implication for lower-crust rheology, *Journal of Geophysical Research: Solid Earth*, *117*(B12), n/a–n/a, doi:10.1029/2012JB009571. 3.3.4, 3.4.1

Ryder, I., B. Parsons, T. J. Wright, and G. J. Funning (2007), Post-seismic motion following the 1997 Manyi (Tibet) earthquake: InSAR observations and modelling, *Geophysical Journal International*, *169*(3), 1009–1027, doi:10.1111/j.1365-246X.2006.03312.x. 3.2.4

Sapkota, S. N., L. Bollinger, Y. Klinger, P. Tapponnier, Y. Gaudemer, and D. Tiwari (2013), Primary surface ruptures of the great Himalayan earthquakes in 1934 and 1255, *Nature Geoscience*, *6*, 71–76. 3.1

Savage, J. C. (1990), Equivalent strike-slip earthquake cycles in half-space and lithosphere-asthenosphere earth models, *Journal of Geophysical Research*, *95*(B4), 4873, doi:10.1029/JB095iB04p04873. 3.2.4

Scholz, C. H. (1988), The critical slip distance for seismic faulting, *Nature*, *336*(6201), 761–763, doi:10.1038/336761a0. 3.4.1

Sreejith, K. M., P. S. Sunil, R. Agrawal, A. P. Saji, D. S. Ramesh, and A. S. Rajawat (2016), Coseismic and early postseismic deformation due to the 25 April 2015, M_w 7.8 Gorkha, Nepal, earthquake from InSAR and GPS measurements, *Geophysical Research Letters*, *43*(7), 3160–3168, doi:10.1002/2016GL067907. 3.1, 3.2.1, 3.2.3, 3.2.4, 3.3.1, 3.5.1, 3.6

Stevens, V. L., and J. P. Avouac (2015), Interseismic coupling on the main Himalayan thrust, *Geophysical Research Letters*, *42*(14), 5828–5837, doi:10.1002/2015GL064845. 3.1, 3.5.4

Taylor, M., and A. Yin (2009), Active structures of the Himalayan-Tibetan orogen and their relationships to earthquake distribution, contemporary strain field, and Cenozoic volcanism, *Geosphere*, *5*(3), 199–214, doi:10.1130/GES00217.1. 3.2

Taylor, M. H. (2016), Tales of Himalayan topography, *Nature Geoscience*, *9*(9), 649–651, doi:10.1038/ngeo2805. 3.5.2

van den Ende, M., J. Chen, J.-P. Ampuero, and A. Niemeijer (2018), A comparison between rate-and-state friction and microphysical models, based on numerical simulations of fault slip, *Tectonophysics*, *733*, 273–295, doi:10.1016/J.TECTO.2017.11.040. 3.5.3

Vergne, J., R. Cattin, and J. P. Avouac (2001), On the use of dislocations to model interseismic strain and stress build-up at intracontinental thrust faults, *Geophysical Journal International*, *147*(1), 155–162, doi:10.1046/j.1365-246X.2001.00524.x. 3.3.2

Wang, K., and Y. Fialko (2015), Slip model of the 2015 M w 7.8 Gorkha (Nepal) earthquake from inversions of ALOS-2 and GPS data, *Geophysical Research Letters*, *42*(18), 7452–7458, doi:10.1002/2015GL065201. 3.1, 3.3.1

Wang, K., and Y. Fialko (2018), Observations and Modeling of Coseismic and Postseismic Deformation Due To the 2015 M_w 7.8 Gorkha (Nepal) Earthquake, *Journal of Geophysical Research: Solid Earth*, doi:10.1002/2017JB014620. 3.1, 3.2.1, 3.2.2, 3.2.2, 3.2.3, 3.2.4, 3.3.2, 3.4.1, 3.5.1, 3.5.3, 3.6

Wang, L., S. Hainzl, G. Zöller, and M. Holschneider (2012), Stress- and aftershock-constrained joint inversions for coseismic and postseismic slip applied to the 2004 M6.0 Parkfield earthquake, *Journal of Geophysical Research: Solid Earth*, *117*(B7), n/a–n/a, doi:10.1029/2011JB009017. 3.4.1

Wang, X., S. Wei, and W. Wu (2017), Double-ramp on the Main Himalayan Thrust revealed by broadband waveform modeling of the 2015 Gorkha earthquake sequence, *Earth and Planetary Science Letters*, *473*, 83–93, doi:10.1016/j.epsl.2017.05.032. 3.5.2

Wessel, P., and W. H. F. Smith (1991), Free software helps map and display data, *Eos, Transactions American Geophysical Union*, *72*(41), 441–441, doi:10.1029/90EO00319. 3.6

Whipple, K. X., M. Shirzaei, K. V. Hodges, and J. R. Arrowsmith (2016), Active shortening within the Himalayan orogenic wedge implied by the 2015 Gorkha earthquake, *Nature Geoscience*, *9*, 711–716. 3.1, 3.3.1, 3.3.2, 3.3.3, 3.4, 3.3.3, 3.5.2

Wimpenny, S., A. Copley, and T. Ingleby (2017), Fault mechanics and post-seismic deformation at Bam, SE Iran, *Geophysical Journal International*, *209*(2), 1018–1035, doi:10.1093/gji/ggx065. 3.1, 3.4.1, 3.4.1, 3.5.3

Wobus, C., A. Heimsath, K. Whipple, and K. Hodges (2005), Active out-of-sequence thrust faulting in the central Nepalese Himalaya, *Nature*, *434*(7036), 1008–1011, doi:10.1038/nature03499. 3.1, 3.3.1, 3.5.2

Wright, T. J., J. R. Elliott, H. Wang, and I. Ryder (2013), Earthquake cycle deformation and the Moho: Implications for the rheology of continental lithosphere, *Tectonophysics*, *609*, 504–523. 3.1, 3.2.4

Wright, T. J., P. J. Gonzalez, R. J. Walters, E. L. Hatton, K. Spaans, and A. J. Hooper (2016), LiCSAR: Tools for automated generation of Sentinel-1 frame interferograms, *American Geophysical Union, Fall General Assembly 2016, abstract #G23A-1037*. 3.2.2

Zhang, Y., R. Wang, T. R. Walter, W. Feng, Y. Chen, and Q. Huang (2017), Significant lateral dip changes may have limited the scale of the 2015 Mw 7.8 Gorkha earthquake, *Geophysical Research Letters*, *44*(17), 8847–8856, doi:10.1002/2017GL074095. 3.3.1, 3.3.2, 3.5.2

Zhao, B., R. Bürgmann, D. Wang, K. Tan, R. Du, and R. Zhang (2017), Dominant Controls of Downdip Afterslip and Viscous Relaxation on the Postseismic Displacements Following the M_w 7.9 Gorkha, Nepal, Earthquake, *Journal of Geophysical Research: Solid Earth*, *122*(10), 8376–8401, doi:10.1002/2017JB014366. 3.1, 3.2.1, 3.2.3, 3.2.4, 3.4.1, 3.5.1, 3.6

Chapter 4

Fold and Thrust Belt Growth from over 25 years of InSAR Data

T. Ingleby[1], T.J. Wright[1], J. Weiss[1] and V. Butterworth[1]

[1] *COMET, School of Earth and Environment, University of Leeds, United Kingdom*

Abstract

The relationship between short-term earthquake-cycle processes and the long-term development of topography remains unclear. A more complete understanding of this relationship would allow us to access measurements of earthquake cycle deformation recorded in topography and contribute to our knowledge of mountain building. Here, we study the relationship between tectonics and topography in part of the Sulaiman fold and thrust belt near Sibi, Pakistan. We use three generations of InSAR satellites to construct an InSAR time series which spans 25 years and includes the 1997 Sibi earthquake. We find that combining these different InSAR data sets enables us to separate deformation associated with each stage of the earthquake cycle. We find that a combination of coseismic and postseismic deformation can reproduce the shape of the topography near the toe of the fold and thrust belt to first order. Assuming this combination of coseismic and postseismic deformation is characteristic for the region, we estimate that approximately 1000 such earthquakes could reproduce the observed topography. Furthermore, the topographic gradient near the toe of the wedge can be reproduced by this combination of coseismic and postseismic deformation, suggesting that some wedges may maintain their taper in a single earthquake cycle.

4.1 Introduction

4.1.1 Tectonics and Topography

It has long been recognised that the earthquake cycle must play a significant role in the development of topography and geological structures in tectonically active regions (*King et al.*, 1988, *Stein et al.*, 1988, *Ainscoe et al.*, 2017). However, the way in which the earthquake cycle generates topography remains poorly understood. For example, some earthquakes have caused regions of long term uplift to subside (*Elliott et al.*, 2016, *Melnick*, 2016), requiring other mechanisms to counteract this in the long term.

In order to determine the roles that various mechanisms play in the construction and destruction of topography, we need high resolution, long time-span measurements. Global Navigation Satellite System (GNSS) measurements can provide an understanding of the broad patterns of deformation associated with tectonics in a region over a relatively long time span (e.g. *Beavan et al.*, 2010, *Ader et al.*, 2012). Levelling lines provide transects of vertical deformation and have been used for long time-span observations, even if sampled more infrequently (e.g. *Lammali et al.*, 1997, *Ching et al.*, 2011). However, both these techniques only provide point or linear measurements of deformation, in easily accessible areas.

Remote sensing techniques such as interferometric synthetic aperture radar (InSAR) provide measurements of motion with a dense spatial resolution on the order of tens of metres over areas which span tens to hundreds of kilometres. Measurements are not made continuously in time, as for continuous GNSS receivers, but are often acquired more frequently than campaign GNSS surveys or levelling. Spaceborne InSAR also enables measurements to be made in otherwise inaccessible regions, opening up more opportunities to examine the relationship between tectonics and topography.

4.1.2 Region of Interest

We chose to investigate the relationship between tectonics and topography in part of the actively deforming, sub-aerial Sulaiman fold and thrust belt in Pakistan. The Sulaiman is part of a series of tectonic structures which accommodate strain associated with the western margin of Indo-Eurasian convergence. As India translates along this margin, motion is accommodated through a combination of left-lateral shear along the Chaman fault zone and thrusting in the Kirthar and Sulaiman fold and thrust belts (e.g. *Banks and Warburton*, 1986, *Humayon et al.*, 1991, *Jadoon et al.*, 1994). These structures are thin-skinned, with extensive deformation in the thick sediments overlying a rigid basement. The lobate nature of the Sulaiman fold and thrust belt and the reentrant near Sibi is thought to result from either the translation of a rigid block along the Chaman fault zone (*Haq and Davis*, 1997) or the presence of a deep basin towards the apex of the lobe preferentially enhancing propagation of the belt (*Macedo and Marshak*,

1999, *Reynolds et al.*, 2015).

The Sulaiman remains seismically active, with most seismicity being shallow and focused around the edges of the belt, away from the thickened sedimentary interior (*Reynolds et al.*, 2015, *Khan et al.*, 2018). We choose to focus on part of the fold and thrust belt near the town of Sibi, where an earthquake occurred in 1997 (*Nissen et al.*, 2016). This enables us to examine contributions to the topography from different parts of the earthquake cycle.

The syntaxis near Sibi experiences a combination of thrust faulting (*Szeliga et al.*, 2009, *Nissen et al.*, 2016) and strike-slip faulting (*Pinel-Puysségur et al.*, 2014) as it accommodates shear and compression. The major geological divisions in the area are shown in Figure 4.2 and are split between a Triassic-Eocene marine shelf sequence, and later molasse and superficial deposits (*Maldonado et al.*, 2011). Unfortunately, this region is sparsely populated and difficult to access. These challenges mean there are few ground based measurements of deformation in our area of interest near Sibi. A small number of campaign GNSS stations, available in the compilation used in the Global Strain Rate Model (*Kreemer et al.*, 2014), show the overall southward motion of the belt with respect to stable India (Figure 4.1). However, these sparse measurements do not have the resolution in time or space to examine the motion of individual faults and folds or how strain rates vary in time. Whilst the arid environment leads to difficulties conducting ground based measurements of surface deformation, it lends itself well to InSAR. Dry environments tend to maintain coherence over longer periods, enabling long InSAR time series to be constructed without introducing too much decorrelation noise. We therefore used space-borne satellite radar to obtain high resolution, spatially dense line of sight (LOS) deformation measurements over the belt. Combining data from ERS-1, ERS-2, Envisat and Sentinel-1a and b, we can observe deformation over a period of 25 years.

4.2 InSAR Data and Methods

InSAR has been used to study ground deformation since the late 1980s (*Gabriel et al.*, 1989) and has been applied in the study of earthquakes (e.g. *Massonnet et al.*, 1993, *Wright*, 2002, *Wang and Fialko*, 2015), volcanoes (e.g. *Pritchard and Simons*, 2004, *Biggs et al.*, 2014), subsidence (e.g. *Cabral-Cano et al.*, 2008, *Jones et al.*, 2016) and landslides (e.g. *Hilley et al.*, 2004, *Sun et al.*, 2015). The signal in an individual interferogram is the sum of a number of contributing factors including ground deformation, atmospheric delay, orbital errors and random noise. Error sources such as the atmosphere mean that small ground deformation signals are often hidden in individual interferograms. In order to extract small deformation signals, and study the evolution of the fold and thrust belt through time, we constructed a number of InSAR time series. We combined data from three generations of European Space Agency (ESA) SAR

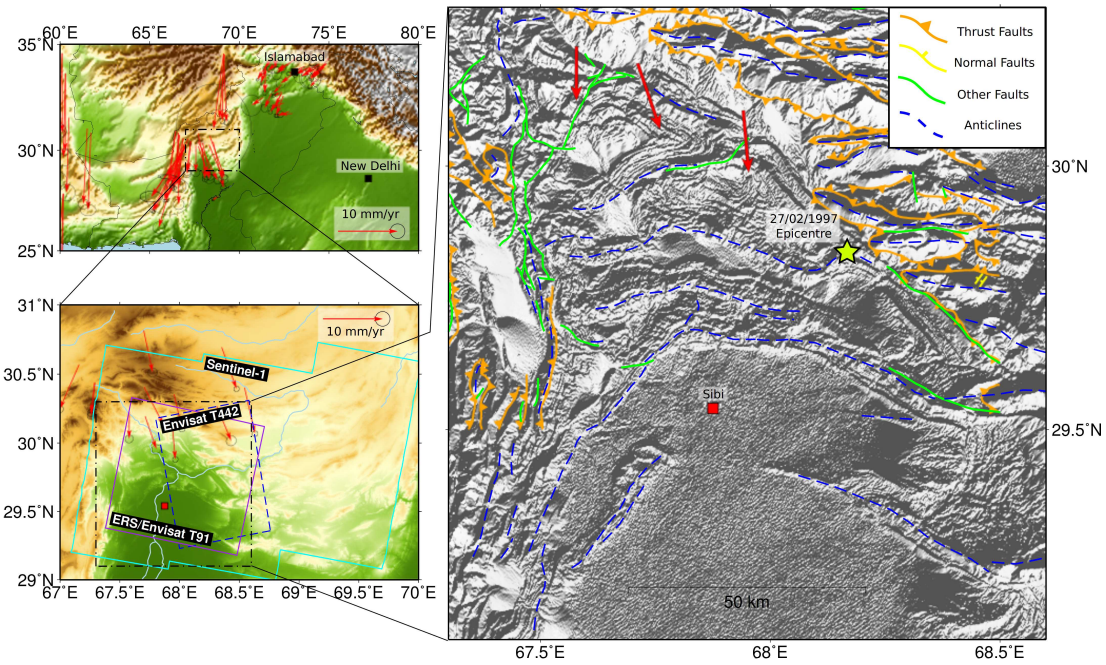

Figure 4.1: Tectonic setting. Top left: regional map showing the study location in the context of India-Eurasia convergence. Arrows show GNSS velocities with respect to stable India (*Kreemer et al.*, 2014). Bottom left: study area near Sibi. Coloured polygons shows the extent of each InSAR data set. Right: structural map of the study area showing faults and anticline fold axes from *Nissen et al.* (2016).

satellites: ERS-1/2, Envisat and Sentinel-1a/b. Most of these data were acquired after a M_w 7.1 earthquake struck the area in 1997 (*Nissen et al.*, 2016).

We used ROI-PAC (*Rosen et al.*, 2004) to focus the ERS and Envisat data and form SLC images. Interferograms were then formed in a small baseline approach using DORIS scripts implemented in StaMPS (*Hooper et al.*, 2012). Sentinel-1 data are provided as SLCs by ESA and we formed small baseline interferograms using Gamma (http://www.gamma-rs.ch/), implemented within a modified version of LiCSAR (*Wright et al.*, 2016). The resulting small baseline networks for each satellite are shown in Figure 4.3 and show the significant decrease in perpendicular and temporal baselines achieved by Sentinel-1. We then used these small baseline networks in a modified version of StaMPS (*Hooper et al.*, 2012) to invert for a single master time series for each individual satellite data set. We used a height-based empirical correction to remove topographically-correlated atmospheric signal (e.g. *Elliott et al.*, 2008). As well as solving for the correlation between phase and topography, we simultaneously solve for a bilinear ramp in each interferogram. We masked out the areas of possible deformation in each interferogram and used far-field pixels in our estimation of the atmospheric noise.

We then use these atmospherically-corrected time series to solve for a linear deformation rate at each pixel for each satellite data set. ERS data were split into

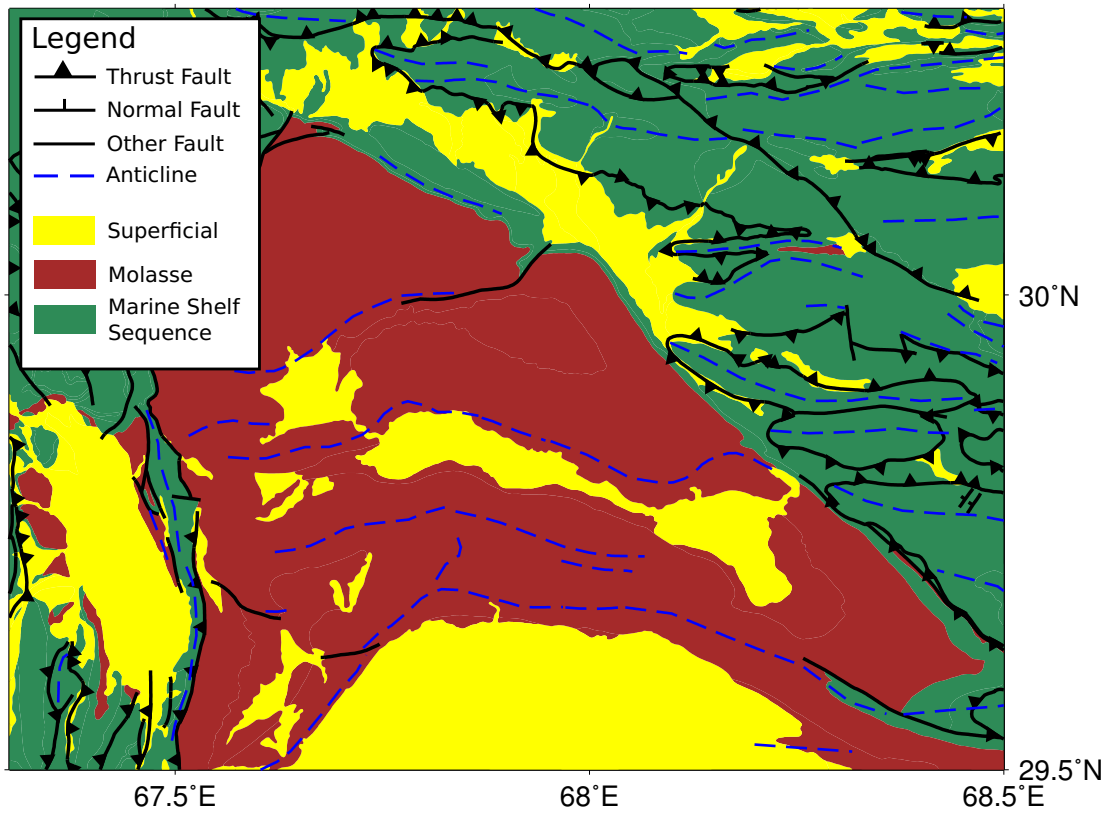

Figure 4.2: Geological map showing the major geological divisions in the area studied. Map is based on USGS Open File Report 2011-1093 (*Maldonado et al.*, 2011) and includes anticline fold axes from *Nissen et al.* (2016).

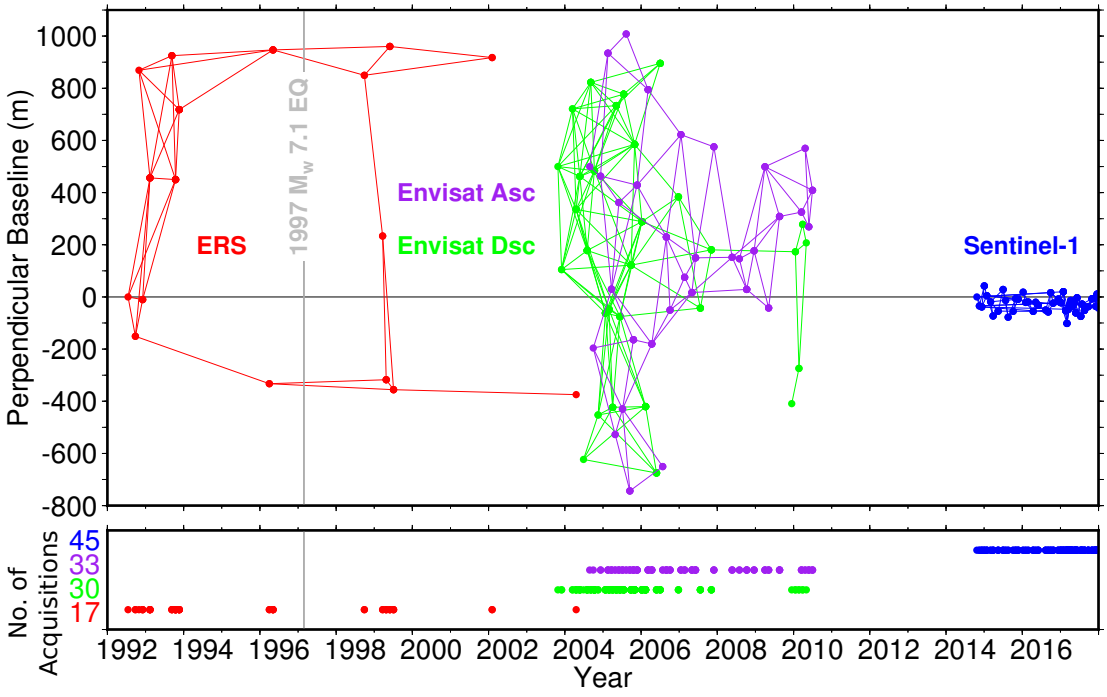

Figure 4.3: Baseline plot for each InSAR data set. Top: perpendicular baselines plotted against temporal baseline for each satellite track. Bottom: satellite acquisition times.

data before the earthquake (preseismic) and data after the earthquake (postseismic). Sentinel-1 data were cut to the same region as the ERS data to remove the effects of very long wavelength atmospheric noise. Fully accounting for the spatial correlation of residual atmospheric noise would make solving for a linear deformation rate at each pixel computationally intractable (*González and Fernández*, 2011). We therefore estimated the average residual atmospheric noise in each interferogram by calculating the phase variance in non-deforming regions. We calculated the phase variance for each slave date in each single master time series as the phase variance of the master-slave interferogram. We then used the average variance of all the slave dates as an estimate for the variance of the master date. These variances were used as weights in a weighted, linear least squares inversion to calculate the average velocity of each pixel independently. We then estimated the error on the velocity of each pixel using a bootstrapping approach with 100 random realisations of the data for each pixel. The standard deviation of the resulting velocity estimates provide an estimate of the uncertainty for each pixel (Figure C.1 in the supplementary material).

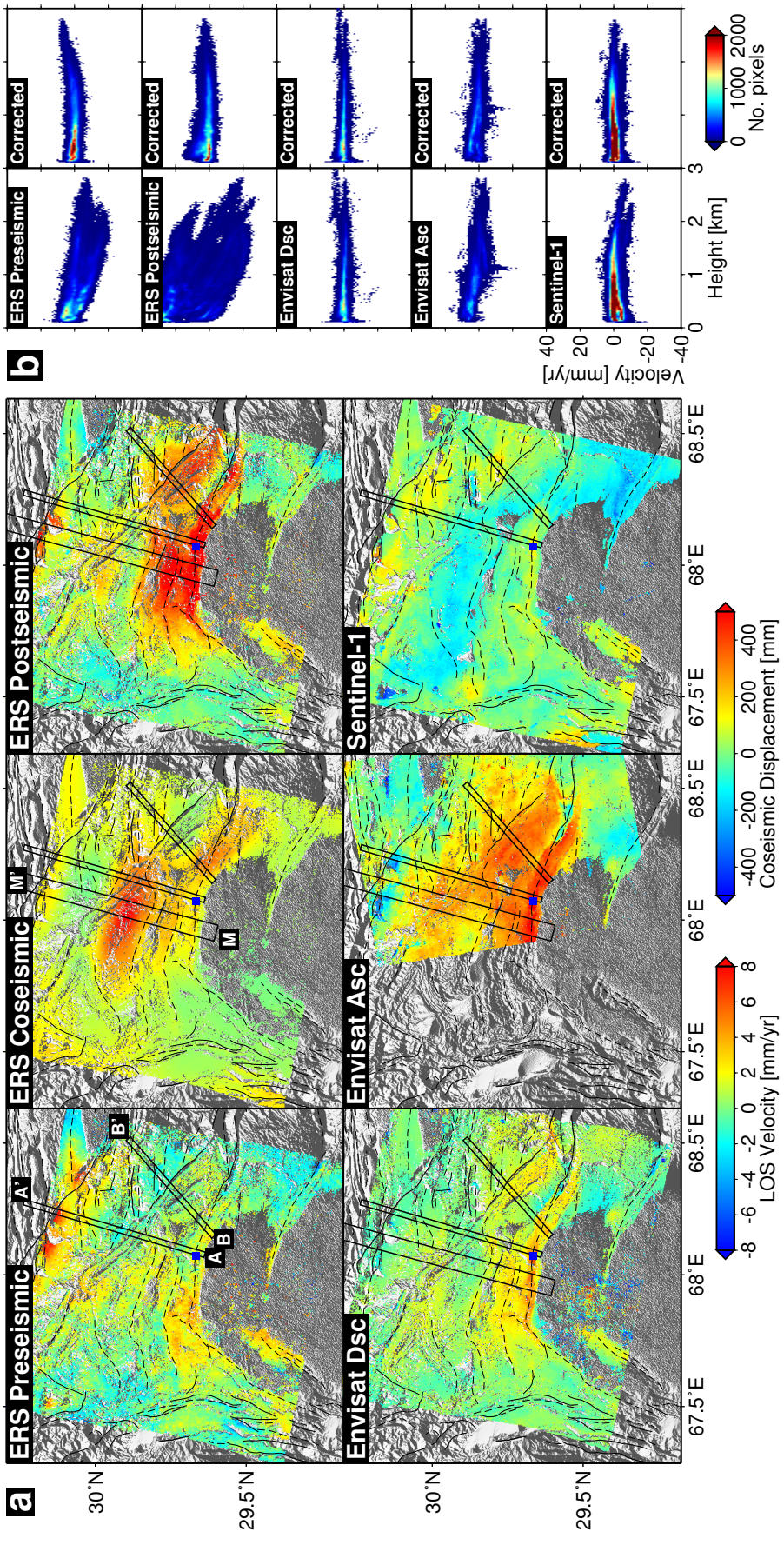

Figure 4.4: a: Linear velocity maps for each InSAR dataset and the earthquake spanning ERS interferogram. Note the change in colour scale between the coseismic interferogram and all other images. Solid lines are faults and dashed lines are fold axes from *Nissen et al.* (2016). Rectangles A and B show the location and extent of swath profiles shown in Figure 4.5. Rectangle M shows the swath profile used for modelling the coseismic and postseismic deformation (Figure 4.6). Blue square is the location of the time series plotted in Figure 4.7. Accompanying error maps for each data set can be found in Figure C.1 in the supplementary material. b: Correlation between LOS velocity and topography for each velocity map. All panels have the same axes. Left column shows relationship for uncorrected velocity maps and right column shows relationship in velocity maps which have been corrected as described in the main text.

Figure 4.4 shows the average linear deformation rate of each pixel for each satellite data set. Many of the signals in these velocity maps are correlated with topography even after removing topographically correlated atmosphere. We are confident that the signals we see are due to deformation and not residual uncorrected atmosphere for the following reasons. Firstly, the overall correlation between LOS velocity and topography is minimal in the corrected velocity maps (see Figure 4.4b). Larger topographic features do not show similar signals in the velocity maps or profiles through the data (see Figures 4.4 and 4.5). Secondly, independent ERS, Envisat ascending and Envisat descending postseismic velocities show similar features. The similarity between these different datasets suggest predominantly vertical deformation. Thirdly, the deformation signals we see following the 1997 earthquake surround the region of coseismic uplift in areas which were likely to experience a stress increase from the earthquake. Finally, the inferred linear deformation rates for the postseismic signals decrease with time since the earthquake, as expected for postseismic deformation (*Ingleby and Wright*, 2017). Sharp discontinuities in the deformation rate maps (see Figures 4.4 and 4.5) suggest faults that are creeping following the earthquake and again show decreasing creep rates through time. As well as these short wavelength deformation features, longer wavelength, lower amplitude signals can also be seen, indicative of deeper deformation sources.

4.3 Earthquake Cycle Deformation

4.3.1 Fault Modelling

Our InSAR time series contains a number of surface deformation signals, most of which can be related to the earthquake cycle. We used the surface deformation revealed by InSAR to determine the geometry of the fault system at depth. The large number of signals, particularly in the postseismic velocity maps, means care is required in model construction and inversion technique. We therefore chose to start our modelling using profiles taken perpendicular to the strike of the fold and thrust belt. This reduces the number of signals we are attempting to explain and the number of model parameters. We then modelled these profiles using uniform slip on dislocations in an elastic half space (*Okada*, 1985, *Wright*, 2003). We used simulated annealing with adaptive step size to find the best fitting fault plane parameters (*Bagnardi and Hooper*, 2018, *Amey et al.*, 2018). We then explored the uncertainties in each parameter by using a Bayesian inversion, implemented using a Monte Carlo Markov Chain (*Mosegaard and Tarantola*, 1995), to construct the probability densities for each parameter. The probability densities for the fault plane parameters can be used to produce a cross section with the likely locations and geometries of modelled faults (see Figure 4.6).

We began by modelling the coseismic deformation, using the earthquake spanning ERS interferogram. Our profile is taken perpendicular to the strike of the main co-

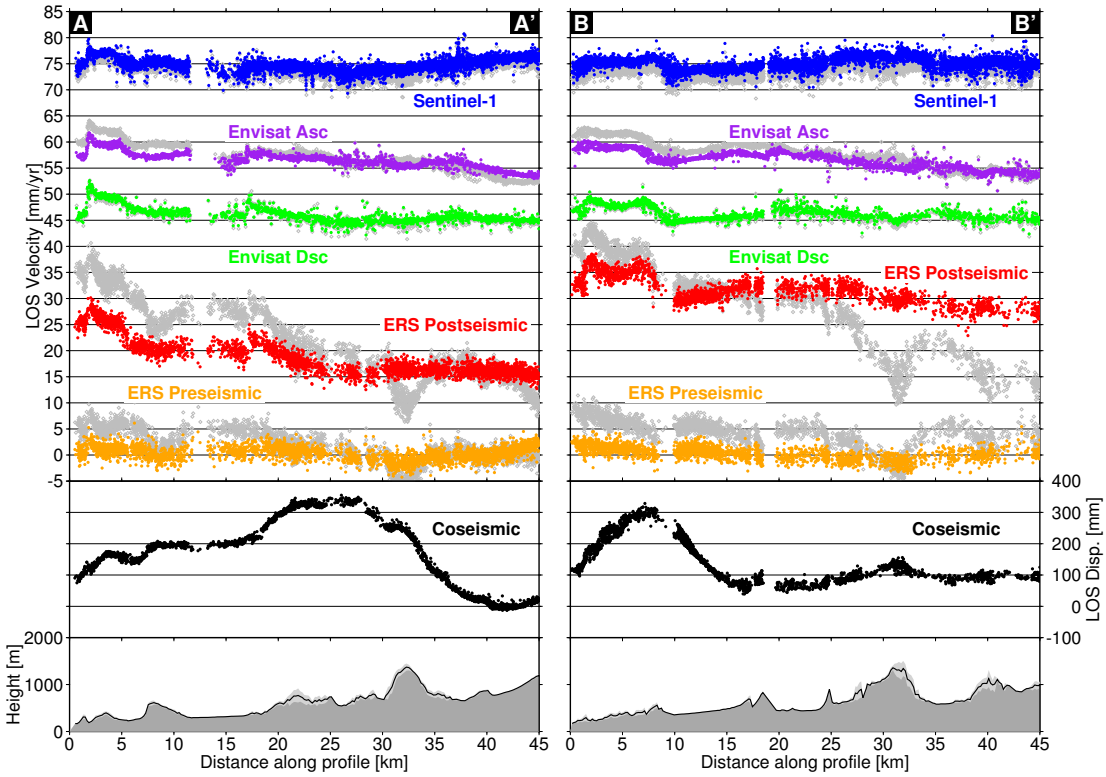

Figure 4.5: Profiles of LOS deformation recorded by ERS, Envisat and Sentinel-1 compared with topography. Gray diamonds show profiles through uncorrected velocity maps and coloured dots show corresponding profiles extracted from the corrected velocity maps shown in Figure 4.4. Profiles are shifted by a constant offset to enable clearer plotting. Topography is shown as the mean topography in the swath profile (black line) plus/minus the standard deviation (light gray and dark gray polygons respectively).

seismic and postseismic deformation signals. The ERS interferogram includes over a year of postseismic deformation, which is particularly evident at the southern end of the profile. The northern end of the profile is affected by a large change in topography, which is correlated with a change in LOS delay. We therefore excluded data from these regions when modelling the coseismic deformation and instead concentrated on fitting the main lobe of coseismic range decrease. This lobe is best explained by a fault dipping at 24.7 - 31.6 degrees with thrust faulting slip of 1.25 - 1.75 m extending from 6 km to 12.7 km depth (all at 95% confidence, see Figure 4.6). Our coseismic fault has a similar dip to the dip of 21 degrees inferred by *Nissen et al.* (2016), but a different depth range and slip magnitude. Seismological solutions from source catalogues which treat the doublet as a single event give dips in the range 7 - 16 degrees (*Nissen et al.*, 2016); smaller than our geodetic estimate. However, these seismological solutions provide similar depths to our estimate (7 - 15 km). The greatest residuals to our model are seen in the southern and northern parts of the profile (see Figure C.2 in the supplementary material). The southern residuals have a similar appearance to the postseismic deformation seen in later interferograms, suggesting that our removal of this signal when modelling the coseismic deformation was appropriate and necessary. The northern residual is correlated with the high topography and is likely caused by topographically correlated atmosphere (e.g. *Elliott et al.*, 2008).

We then sought to model the more complicated postseismic deformation field. Postseismic range decrease is seen along at least two folds south of the coseismic rupture, and possibly three. There is also a broad range decrease signal north of the coseismic rupture, which may be associated with deeper slip. We therefore constructed a fault model containing five faults, arranged as shown in Figure C.3 in the supplementary material. This system of faults is pinned to the top and bottom of the coseismic fault plane, thereby reducing the number of free parameters. We simultaneously fit the Envisat ascending and descending data as well as the ERS data in a joint inversion. We solve for an ERS scaling factor for each fault, in order to take account of the faster velocities in the ERS velocity map. This model is capable of reproducing the postseismic deformation over all wavelengths along the profile by placing slip on the faults down-dip and up-dip of the coseismic rupture (Figure 4.6). Up-dip of the rupture, the inversion requires a very shallowly dipping fault (0 - 1.5 degrees) with a slip rate of approximately 2 - 6 mm/yr during the Envisat observation period. Splays dipping at 35 - 60 degrees underlie each of the short wavelength uplifting folds and have a strong trade-off between fault depth and fault slip rate for each splay. Down-dip of the rupture, the fault geometry is poorly resolved but could have higher slip rates than the upper flat. A down-dip extension of the coseismic fault would agree with the locations and mechanisms of some of the larger aftershocks constrained by *Nissen et al.* (2016) using body waveform modelling.

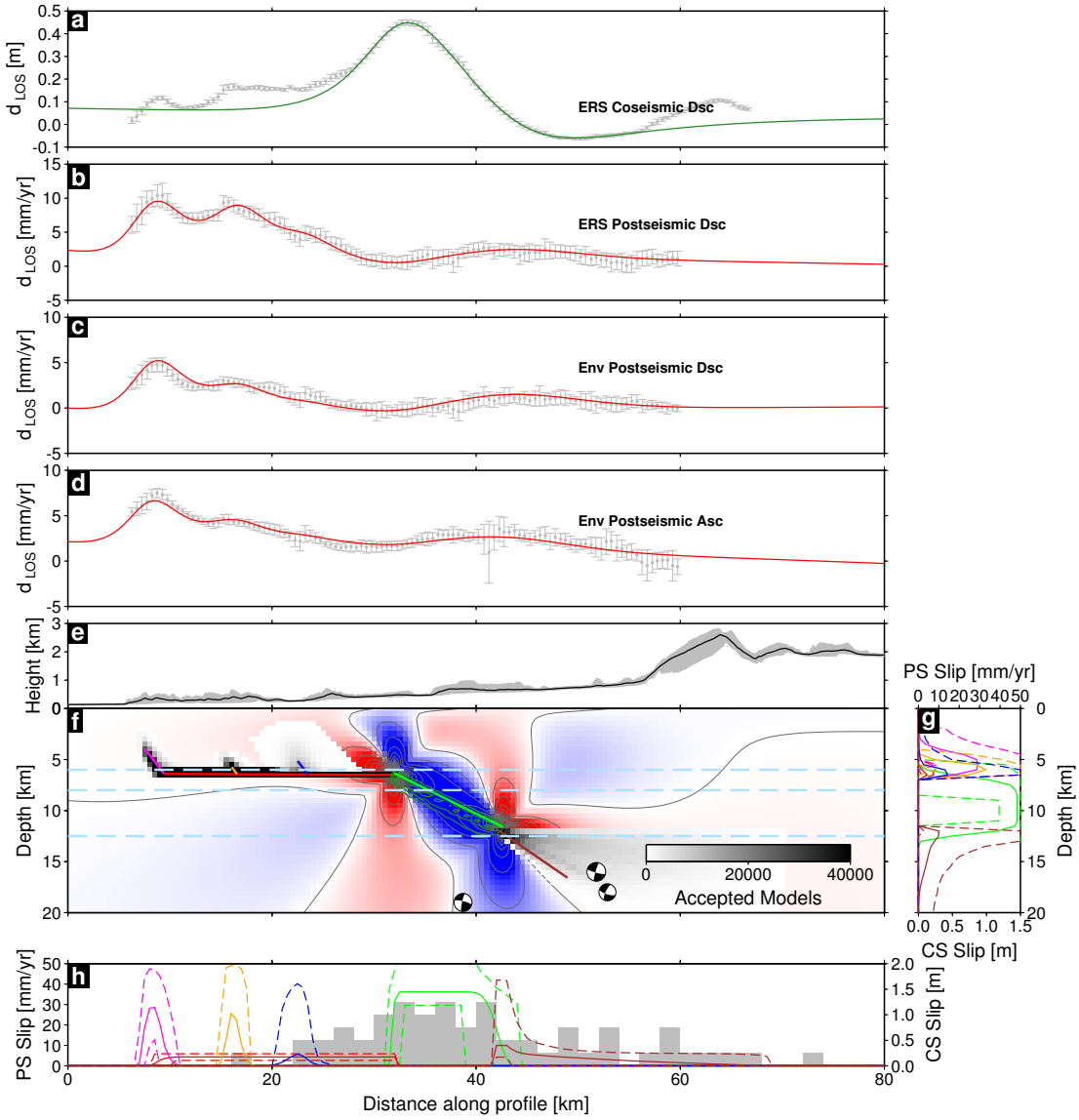

Figure 4.6: Results from inversion of coseismic and postseismic data for the fault geometry along profile M. Panels a-d show the fit to the coseismic and postseismic data by the fault geometry shown in panel f. e: topography along profile M. f: fault geometry from coseismic and postseismic inversions. Background color map shows Coulomb stress change from the earthquake. Green contours show range of coseismic fault models. Green line shows maximum likelihood coseismic fault. Grey shading shows range of postseismic fault geometries. Colored lines correspond to the maximum likelihood fault geometry. Dashed blue horizontal lines show the depths of potential detachment horizons in the generalised stratigraphic column provided by *Nissen et al.* (2016). Focal mechanisms are for aftershocks constrained with body waveform modelling in *Nissen et al.* (2016). g and h: slip on each fault, projected onto the X and Y axes. Colors correspond to colored faults in panel f. Grey histogram in h are aftershock locations with no depth constraint from *Nissen et al.* (2016).

4.3.2 Coseismic, Postseismic and Interseismic Deformation from InSAR

We next turned our attention to deriving a more complete picture of how the fold and thrust belt is evolving throughout the earthquake cycle. We did this by combining the different satellite data sets together in a single time series. We resampled pixels from each descending data set to the ERS pixel locations and then tied the data sets together using a predetermined functional fit. We fit the different satellite time series at each pixel using a simple ground deformation model, similar to those used when fitting GNSS time series in regions affected by earthquake cycle deformation:

$$u(t) = \alpha + vt + \beta\mathcal{H}(t-t_{eq}) + \gamma\mathcal{H}(t-t_{eq}) \cdot ln[1+\frac{t-t_{eq}}{\tau}] + \kappa\mathcal{H}(t-t_{Env}) + \epsilon\mathcal{H}(t-t_{S1}) \quad (4.1)$$

where α is an offset, v is a linear rate, β is the offset in the 1997 earthquake and the logarithmic term (γ) accounts for postseismic deformation with time constant τ. κ and ϵ are the offsets between the ERS time series and the Envisat and Sentinel-1 data respectively. $\mathcal{H}$ terms refer to the Heaviside function used in the coseismic offset, postseismic term and for the offsets between different satellite time series. When the offset time and postseismic time constant are known, the above equation is linear and can be rapidly solved for the thousands of pixels in the InSAR data sets.

Whilst we only used descending data in our combined time series, we need to consider the effect of the different viewing geometries of each satellite. The ERS and Envisat data have very similar headings (averages of $-168.3°$ and $-168.23°$) and incidence angles (averages of $23.41°$ and $22.74°$), meaning that similar surface deformation will give similar LOS deformation patterns. However, Sentinel-1 has a significantly different incidence angle ($40°$) , causing surface deformation to be imaged from a different perspective. One way to handle the varied looking geometries is to convert the LOS deformation into vertical and east-west deformation, assuming no north-south motion (e.g. *Wright et al.*, 2004). However, given the orientation of the fold and thrust belt, we expect significant north-south motion. Furthermore, this would require ascending and descending data over our entire area of interest throughout the period covered.

We therefore take a different approach and assume that most of the motion recorded in our InSAR is in one direction. In a fold and thrust belt, we might expect deformation to be predominantly vertical and parallel with the direction of convergence. We can therefore assume that there is negligible motion parallel to fold hinges, leaving us with two deformation directions. Fortunately, the convergence direction in the Sibi fold and thrust belt is approximately perpendicular to the LOS vector for the descending satellites, meaning that our data are nearly completely insensitive to convergence parallel deformation. This leaves only vertical deformation as an expected and observable signal in the descending data. In this case, the LOS deformation at each pixel, seen by

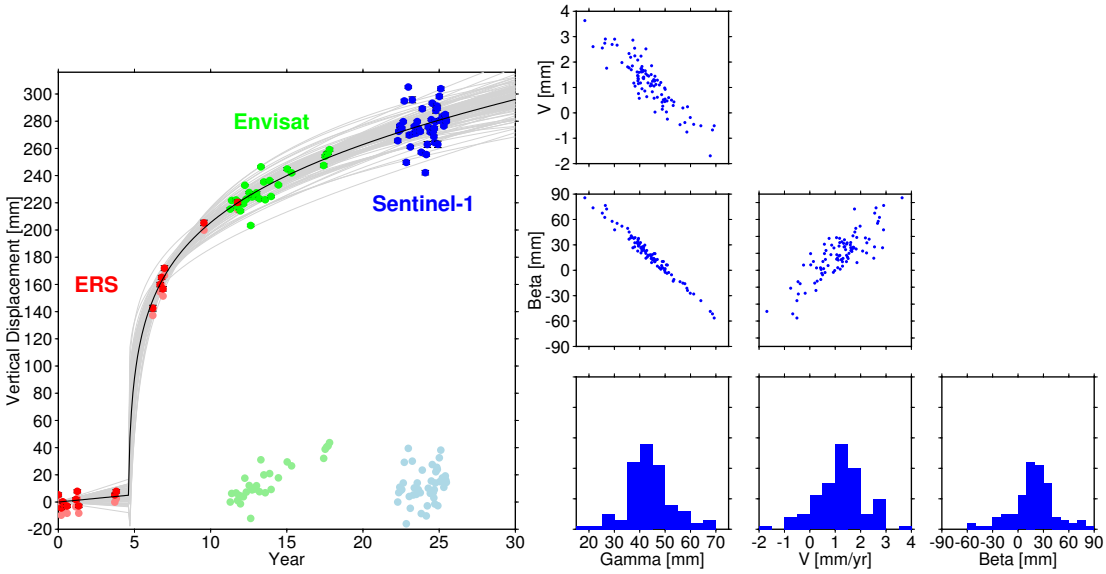

Figure 4.7: Example time series for pixels in the region highlighted in Figure 4.4. LOS deformation has been converted to assumed vertical deformation using the vertical component of the look vector for each satellite. Faded colours show original satellite time series and bright colours show the full time series constructed by tying the different data sets together using equation 4.1. Histograms and scatter plots show the range of possible values for the time series parameters in equation 4.1 as well as trade offs determined using bootstrapping.

each satellite is simply related to the angle between the vertical and the satellite look direction at that pixel. The look vector is the unit vector point from the ground to the satellite at any location, and we use the vertical component of this vector to account for the different viewing geometries of ERS/Envisat and Sentinel-1. In the rest of this paper, we assume that all observable deformation is vertical.

We used weighted least squares to solve for each of the time series parameters. We initially performed the inversion with different values of the postseismic time constant (τ) and found the value of τ which gave the minimum misfit for each pixel. We found that pixels with a clear postseismic deformation signal were best fit using a time constant of 0.1 years (see Figure C.6 in the supplementary material). We therefore reran the inversion and fixed the time constant at 0.1 years for all pixels to prevent trade offs between the time constant, τ and the amplitude of the postseismic coefficient γ. We referenced all InSAR data to the first ERS acquisition using this model and constructed a time series spanning 25 years. The last ERS acquisition in this area occurred after Envisat had begun acquiring, allowing us to check that our method is achieving the expected results. Figure 4.7 shows an example time series of pixels from one of the folds which show a strong postseismic deformation signal. The final ERS data point agrees with the shifted location of the first Envisat points, suggesting our approach is successfully combining the different time series. We used bootstrapping to estimate the errors in each of the parameters and obtained a range of time dependent model curves which fit the InSAR time series for each pixel. Bootstrapping reveals trade-offs

between the linear rate, postseismic coefficient and coseismic offset terms (see Figure 4.7), due to the long time span between preseismic and postseismic SAR acquisitions and the small amount of preseismic data.

We solved for the coefficients in equation 4.1 at every pixel and plotted the results in map form to show how different parts of the fold and thrust belt grow (Figure 4.8). The earthquake-spanning interferogram includes more than a year of postseismic deformation, which may contaminate the coseismic signal (*Nissen et al.*, 2016). A map of the coseismic offset (β) from the time series fit is similar to this earthquake-spanning interferogram, but shows less deformation to the south of the main deformation lobe (see Figure C.5 in the supplementary material). The postseismic coefficient (γ) map has a similar appearance to the ERS and Envisat postseismic rate maps. Postseismic deformation surrounds the region of coseismic deformation, with the strongest signals seen up-dip of the two lobes of coseismic uplift. Broader, low amplitude signals are seen down-dip of the two coseismic deformation signals. The linear rate map (v) is less well resolved due to the small amount of data acquired before the earthquake and is similar in appearance to the ERS preseismic velocity map. It appears to show uplift signals along parts of the frontal fold and towards the rear of the fold and thrust belt. However, these possible signals are of a similar magnitude to the noise (see Figure 4.8) and therefore need to be interpreted with caution.

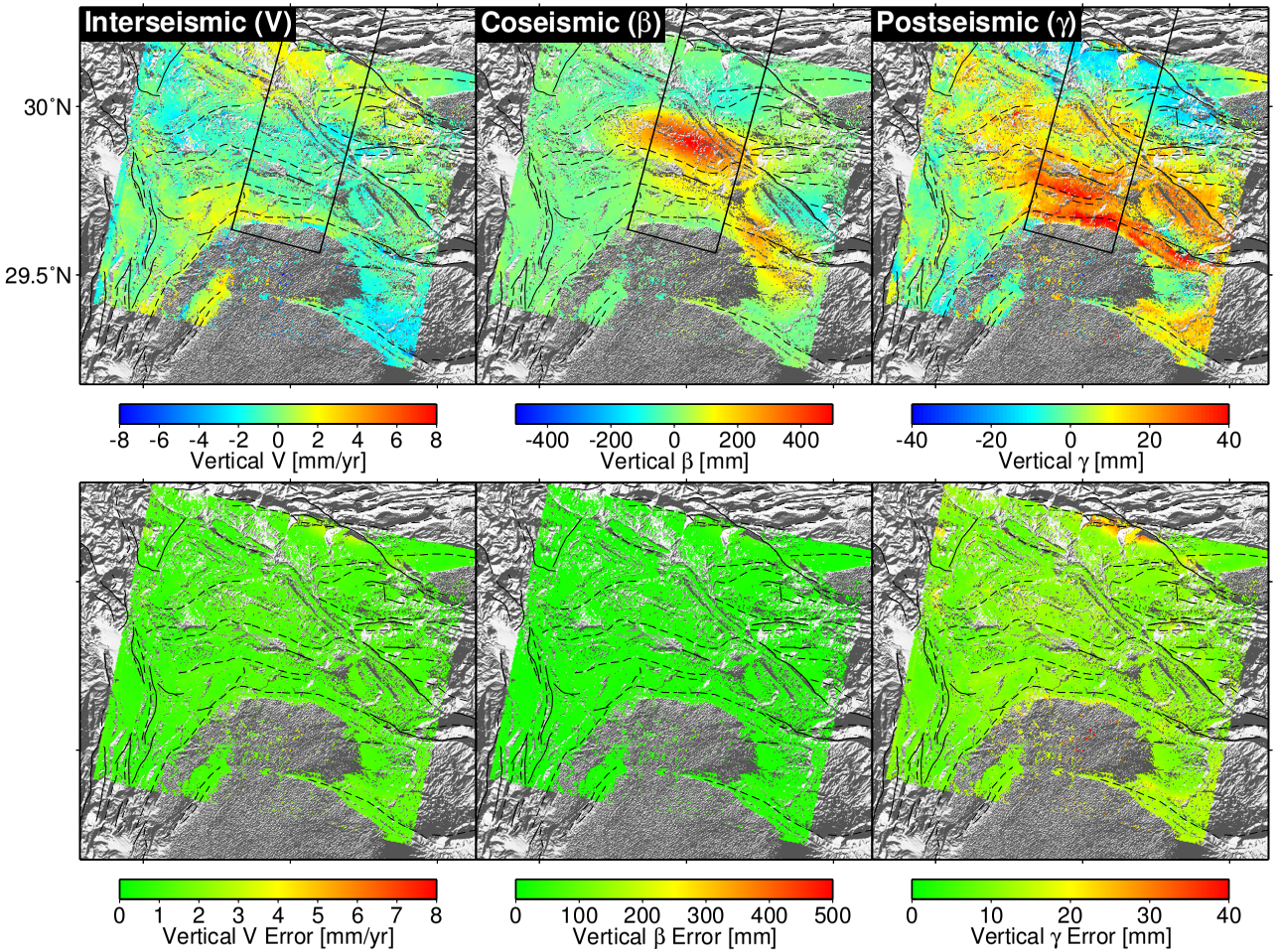

Figure 4.8: Maps for three coefficients related to the earthquake cycle calculated using 4.1. Note that these are assumed to be purely vertical deformation in each stage of the earthquake cycle. Associated error maps are calculated using bootstrapping. Black rectangle shows the swath profile used for comparing vertical deformation and topography in Figure 4.9.

4.4 Topographic Growth

4.4.1 Earthquake Cycle Contributions

Our InSAR measurements allow us to estimate the contributions of different parts of the earthquake cycle to the generation of topography in the fold and thrust belt near Sibi. Coseismic slip in the 1997 earthquake generated uplift approximately 30 km into the fold and thrust belt. However, as in other examples, the earthquake caused subsidence in some areas of higher elevation (see Figures 4.5 and 4.9). If the topography in the fold and thrust belt is generated by the earthquake cycle, then the higher elevations must be caused by other processes such as deeper, or more northward, earthquakes.

Interseismic deformation may also play a role in generating these higher elevations. Interseismic deformation shows range decreases consistent with uplift to the north of the centre of coseismic uplift, which could contribute to the building of topography if some of this is anelastic and permanent. South of the coseismic uplift, the western end of the frontal fold structure also shows signals consistent with uplift. However, the interseismic deformation is the least well observed, and as such, these possible uplift measurements should not be considered robust. Similar signals can be seen in ERS preseismic data and Sentinel-1 data as well as in the interseismic component of the earthquake cycle inversion. However, the same signals are not clearly visible in the descending Envisat time series which covers a longer observation period and has generally lower noise.

Postseismic deformation is well imaged by ERS, Envisat and Sentinel-1. Postseismic uplift is concentrated along short wavelength folds, particularly to the south of the coseismic uplift signal. Similar short wavelength fold growth has been observed following a number of earthquakes in Iran (*Copley and Reynolds*, 2014, *Copley*, 2014, *Copley and Jolivet*, 2016, *Zhou et al.*, 2018). Figure 4.9 shows peaks in postseismic uplift either side of the peak in coseismic uplift, consistent with afterslip occurring both up-dip and down-dip of the coseismic rupture.

We tested whether deformation from these three stages can sum to give something resembling the topography we observe today. We compared the deformation observed by InSAR with the topography along the swath profile (Figure 4.9). Postseismic deformation strongly resembles the short wavelength topography near the front of the fold and thrust belt. We tested the similarity of the deformation and the topography by by normalising both profiles by the average value of points in the region of maximum coseismic uplift. We subtracted a height of 140 m from the topographic profile, which corresponds to the background height of the belt above sea level. Figure 4.9b shows this comparison for both coseismic deformation and the sum of coseismic and aseismic deformation 20 years after an earthquake. The overall shape of this section of the fold and thrust belt can be reproduced by a combination of coseismic and postseismic deformation. Differences between the two normalised profiles may be due to incorrectly

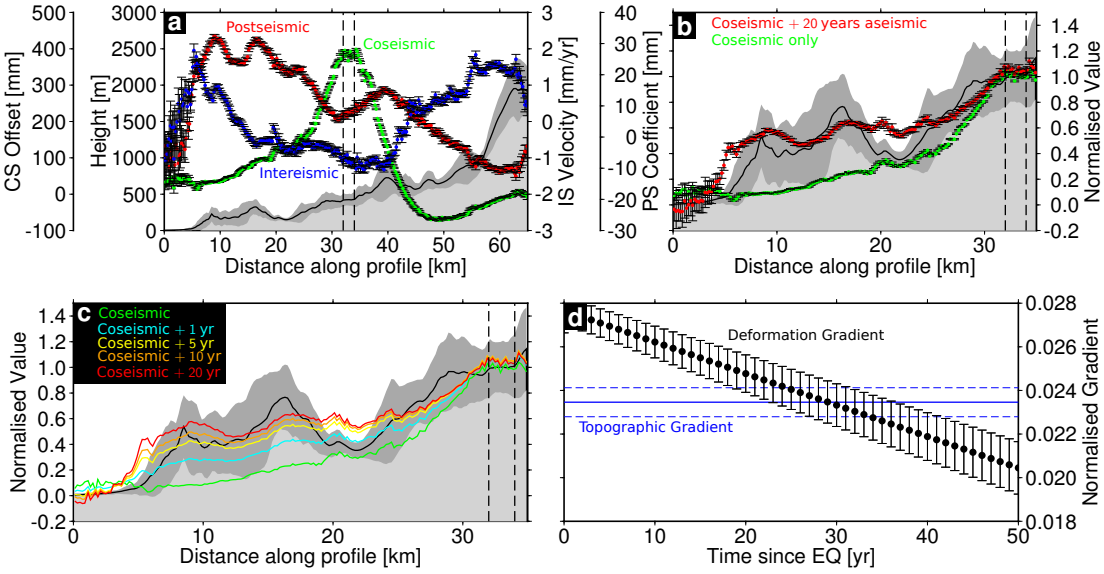

Figure 4.9: Comparison between earthquake cycle deformation and topography. a) Topography and earthquake cycle parameters along the swath profile shown in Figure 4.8. Deformation is represented as the weighted mean of the swath and error bars show the error on the weighted mean. Black line is mean topography whilst dark gray and light gray polygons show mean topography plus/minus topographic standard deviation in the swath. Dashed vertical lines are normalisation region. b) Normalised topography compared with normalised coseismic deformation (green) and normalised total deformation after 20 years (red). c) Similar to b), but showing the evolution of the total normalised deformation through time from coseismic only (green) to total deformation after 20 years (red). d) Comparison between the gradient of the normalised topography and the normalised deformation. Blue solid line is the estimated topographic gradient with standard deviation given by the blue dashed lines. Black points with error bars show how the gradient of the normalised total deformation field varies with time.

assuming purely vertical deformation, longer term isostatic effects and the effects of erosion. However, the overall similarity between the profiles suggests that the frontal section of this fold and thrust belt could be built by repeated earthquake cycles of a similar nature to that observed here.

4.4.2 Development of Topography

If we assume that the 1997 earthquake was characteristic for this frontal section of the fold and thrust belt, then we can infer aspects of the long term tectonics from the topography. We use a simple model to link deformation in an earthquake cycle to the construction of long term topography:

$$h = d_{IS}t + d_{CS}\frac{t}{t_r} + d_{PS}\frac{t}{t_r}ln(1 + \frac{t_r}{\tau}) + h_0 \tag{4.2}$$

where d_{IS}, d_{CS} and d_{PS} are the earthquake cycle parameters obtained in section 4.3.2, t is the total time of tectonic activity, t_r is the earthquake recurrence interval, τ is the postseismic time constant and h_0 is the height in undeforming regions. We used a value

of 0.1 years for τ, equivalent to the value obtained in section 4.3.2. We fixed h_0 to be 140 m (as above) and removed this from the topographic profile. We then performed a grid search over values of t and t_r, calculating the misfit for each parameter pairing.

We found that including the possible interseismic deformation observed at the western end of the frontal fold prevented a good fit to the topography. This interseismic deformation is the least well constrained from our InSAR observations, is only seen in the western section of the frontal fold, and if real, may only be a transient creep event. We therefore chose to remove the interseismic deformation from the model and perform the grid search again. Figure 4.10 shows the fit of the minimum misfit models to the topographic profile, as well as plots showing how misfit varies over parameter space. The misfit plots show a strong trade off between t and t_r, where longer total deformation times require longer earthquake recurrence intervals. In other words, we can only constrain the number of earthquakes (with their associated postseismic deformation) that have occurred. The topography is best reproduced by approximately 1000 earthquakes and their associated postseismic deformation.

4.5 Discussion

4.5.1 Fold and Thrust Belt Growth

We measured surface deformation associated with different parts of the earthquake cycle near Sibi. Coseismic deformation in the 1997 earthquake consisted of two lobes of uplift with associated subsidence signals of smaller amplitude (Figure 4.8). The main uplift lobe had a peak which does not coincide with any one particular fold, whilst the secondary event to the south-east shows uplift closely associated with a fold axis (*Nissen et al.*, 2016). Coseismic fold growth has been inferred from geomorphological and structural measurements (*Walker et al.*, 2015) as well as seismic reflection profiles combined with borehole measurements (*Leon et al.*, 2007). However, geodetic measurements of coseismic deformation often reveal an unclear relationship between coseismic deformation and surface folding. *Parsons et al.* (2006) observed a broad uplift signal associated with the 1994 Sefidabeh earthquakes in Iran, in contrast with the short wavelength topographic ridges. *Elliott et al.* (2015) found that coseismic deformation in the Khaki-Shonbe earthquake (Iran) revealed by InSAR, was of a similar along-strike length to a fold, but that the peak uplift signal was offset in a strike-perpendicular sense.

In our results, coseismic deformation caused subsidence in some areas of higher elevation (e.g. Figure 4.9a). The apparent destruction of topographic highs in earthquakes has been observed geodetically in the Gorkha earthquake (*Elliott et al.*, 2016) and in great Andean subduction zone earthquakes (*Melnick*, 2016). Furthermore, a net destruction of topography in earthquakes has been argued for using a mass balance be-

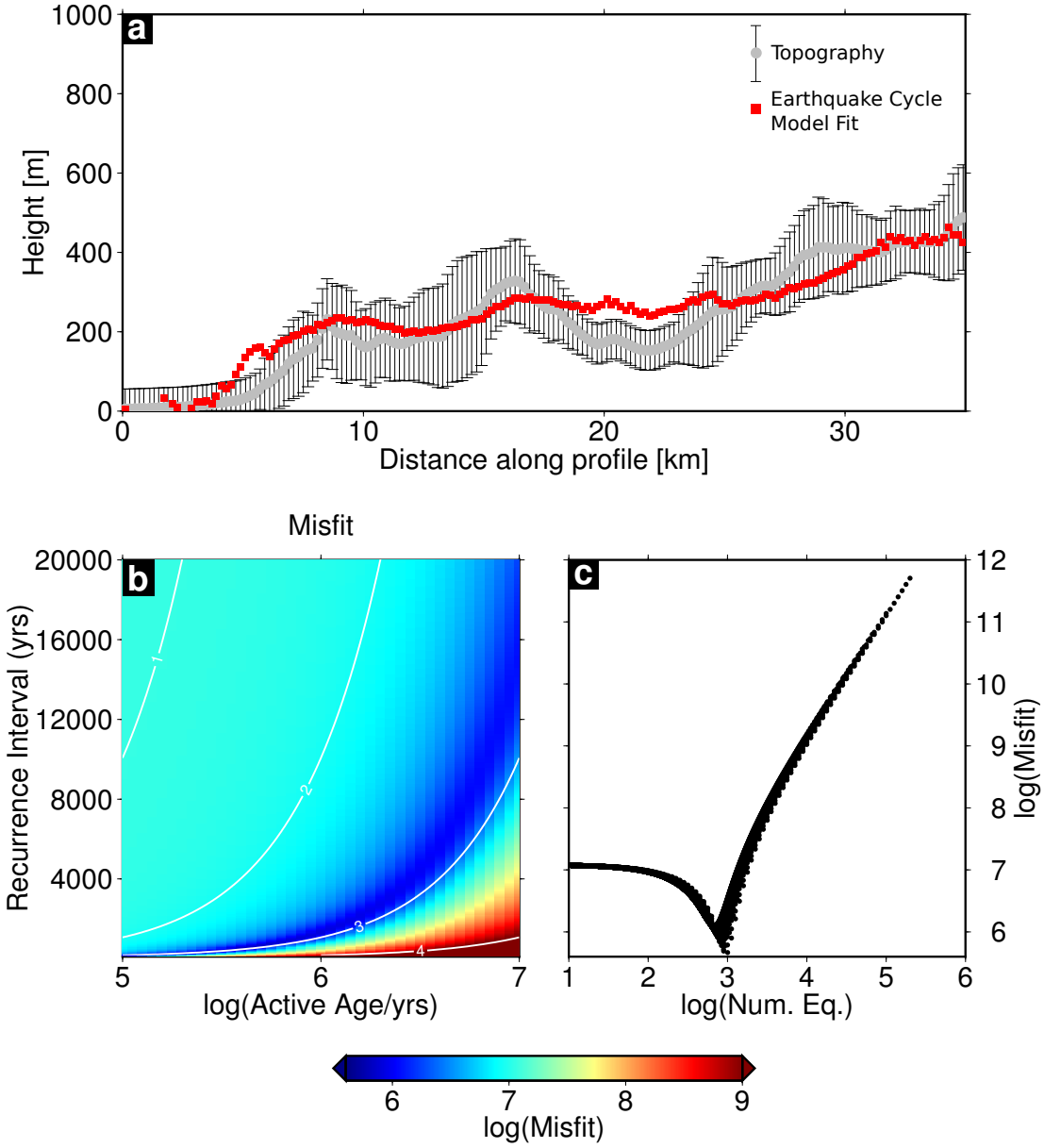

Figure 4.10: Modelling topography as a result of earthquake cycle deformation in the frontal section of the fold and thrust belt. a) Comparison of the observed topography and the earthquake cycle prediction produced by the best fit combination of parameters. b) Misfit as a function of the age of the fold and thrust belt and the earthquake recurrence interval. White contours show log_{10} of the total number of earthquakes. c) Misfit against total number of earthquake cycles.

tween coseismic uplift and landslides for the 2008 Wenchuan earthquake (*Parker et al.*, 2011). These observations clearly require uplift to occur in other parts of the seismic cycle if topographic highs are to be created and sustained over geological timescales. *Melnick* (2016) suggest that moderate, deeper subduction zone earthquakes could explain the rise of the Andean coast. A similar mechanism may operate here and lead to uplift further into the fold and thrust belt.

Another possibility for creating high topography is via interseismic deformation between earthquakes. Even though our interseismic measurements are the least well constrained, they suggest this mechanism may be operating here. They offer a way of counteracting the subsidence experienced in earthquakes like the 1997 event (see Figure 4.9a), provided that some of this strain is permanent rather than elastic. The role of interseismic deformation in generating topography is also suggested by GNSS data from the Southern Alps in New Zealand, where vertical uplift rates closely resemble the shape of the topography over wavelengths of approximately 60 km (*Beavan et al.*, 2010). A combination of levelling data and GNSS reveals a dome shaped uplift pattern for Taiwan, centred over the interior mountain ranges, with many similarities between short term vertical rates and longer term rates derived from radiometric dating (*Ching et al.*, 2011).

The clearest relationship between tectonics and topography in our results is seen in the comparison between postseismic deformation and short wavelength folds. Postseismic deformation closely resembles the shape of fold hinges in map view (Figure 4.8) and has a similar wavelength to the topography associated with these folds (Figure 4.9). These observations add to a growing body of literature where short wavelength folds have been seen to grow following an earthquake (*Fielding et al.*, 2004, *Nishimura et al.*, 2008, *Copley and Reynolds*, 2014, *Copley*, 2014, *Copley and Jolivet*, 2016, *Wimpenny et al.*, 2017). Such structures are often thought to result from shallow fault slip triggered by coseismic stress changes and controlled by the rate-and-state friction laws. This shallow afterslip offers a way of building permanent, short wavelength topography. In fact, it may represent the only way of building such topography in regions where the shallow fault is rate-strengthening and in the stress shadow of a portion of locked, deeper fault (*Almeida et al.*, 2018).

However, our results need to be interpreted with a degree of caution and cannot give the complete picture over how the range near Sibi has developed. The structural geology (see Figure 4.2) reveals a number of different structures and features which cannot all be explained by the surface deformation we observe in our InSAR results. Our InSAR captures decadal deformation in the most recent structures and is potentially biased by the large fraction of the time series dominated by coseismic and postseismic deformation. Furthermore, the deformation we observe may not be controlled by faults but instead be the result of more distributed folding and ductile deformation processes. The sharp discontinuities in the InSAR velocity maps (see Figure 4.4) require relatively

localised deformation, but this may be along small faults or due to bedding plane slip (*Berberian et al.*, 2000, *Zhou et al.*, 2018). Even if the deformation is controlled by faults, these faults need not be controlled by the rate-and-state friction laws, but may instead be sliding via pressure solution creep (*Gratier et al.*, 2014).

Despite these caveats, some conclusions can be drawn regardless of the mechanism that may be producing the deformation we see. Our results show that a combination of coseismic and postseismic deformation can recreate the shape of the topography to first order (Figure 4.10). This agreement suggests that at least some of the coseismic and postseismic deformation produced outweighs the effects of interseismic strain, leading to permanent deformation. It also suggests that earthquakes like the 1997 event may be representative of the region, since repeats of such events can reproduce the longer term record of deformation provided by topography. Whilst the 1997 event highlighted the danger of making assumptions about limits on earthquake rupture (*Nissen et al.*, 2016), this may only apply in the along-strike sense here. The down-dip extent of rupture may well be controlled by the presence of detachment horizons (*Banks and Warburton*, 1986) which have slipped aseismically following the earthquake. Figure 4.6 shows how coseismic slip ends at the approximate depths of detachment horizons from *Nissen et al.* (2016), shown as light-blue dashed lines. These may provide a physical reason for why an earthquake such as the 1997 event may be representative for the region.

4.5.2 Implications for Critical Tapers

As well as considering the short wavelength topography in a fold and thrust belt, our results also have implications for longer lengthscales of topography. At longer lengthscales, uncertainties in InSAR tend to increase due to the increasing variability of the atmosphere as well as possible effects of the ionosphere and orbital errors (*Lohman and Simons*, 2005, *Fattahi and Amelung*, 2014, *Bekaert et al.*, 2015). These factors mean that long wavelength signals need to be interpreted with greater caution. Nevertheless, we proceed to outline the possible implications for long wavelength deformation in the context of critical taper wedge mechanics.

Critical taper wedge mechanics treats a fold and thrust belt analogously to a pile of sand or snow being pushed up a shallow incline by a bulldozer (*Davis et al.*, 1983, *Dahlen et al.*, 1984, *Dahlen*, 1990). The topographic slope of the fold and thrust belt is controlled by the dip and strength of the underlying decollement and the strength of the wedge material. For a critical wedge, a strong decollement or weak wedge material will result in a steeper topographic slope. Critical taper models have been applied to active orogenic wedges such as Taiwan (*Davis et al.*, 1983, *Carena et al.*, 2002, *Suppe*, 2007), the Longmen Shan (*Hubbard et al.*, 2010) and the Alps (*von Hagke et al.*, 2014) as well as accretionary wedges around Barbados (*Suppe*, 2007) and offshore South America (*Cubas et al.*, 2013).

Fold and thrust belts which have reached a critical taper are in a steady state, where the topographic slope of the wedge is maintained through time. In other words, critical wedges grow in a self similar manner in order to maintain their taper. However, a single earthquake within these actively deforming tapers often produces a pattern of uplift with a different slope to the topography. For example, the 1999 Chi Chi (*Yu et al.*, 2004, *Suppe*, 2007) earthquake, 2008 Wenchuan earthquake (*de Michele et al.*, 2010, *Hubbard et al.*, 2010) and 2015 Gorkha earthquake (*Elliott et al.*, 2016, *Searle et al.*, 2017) all occurred in orogenic wedges which have been modelled as critical tapers. All of these earthquakes only caused uplift in part of the wedge, resulting in a deformation gradient which is different to the topographic gradient. Maintenance of the topographic slope through time therefore requires uplift in other parts of the wedge. For example, an earthquake in the interior of the wedge produces uplift towards the rear of the wedge and therefore increases the overall taper. Earthquakes near the toe of the wedge and the propagation of the wedge into the foreland decrease the taper of the wedge. Critical taper theory therefore suggests that fold and thrust belts maintain taper by the appropriate balance of these uplift sources combined with the effects of erosion (*Davis et al.*, 1983).

Modelling a fold and thrust belt as a critical taper rests on a number of significant assumptions. In particular, the wedge is modeled as having uniform properties, and on the verge of failure by faulting everywhere within the wedge. The Sulaiman fold and thrust belt as a whole cannot be modeled as a single critical taper due to the variety of earthquake mechanisms (*Reynolds et al.*, 2015). However, over short lengthscales than the entire range, it is more appropriate to use a simple wedge model since the degree of variability in both lithology and faulting will be less. We argue that the Sibi fold and thrust belt is at critical taper from the toe of the wedge for at least 35 km along the strike-perpendicular profile. *Hubbard et al.* (2010) argue that the Longmen Shan is at critical taper because of the propagation of the wedge into the foreland basin, the presence of active thrusts throughout the belt and overall wedge shape of the topography. All of these elements are present in the Sibi fold and thrust belt: active folds can be seen in the Sibi basin (Figures 4.1 and 4.2), numerous thrust faults are seen to be active in our InSAR observations (Figure 4.4) and the topography has an overall wedge shape (Figure 4.9a). Furthermore, critical taper theory suggests that the whole wedge is on the verge of failure. *von Hagke et al.* (2014) argue that the Alps are on the verge of failure by pointing to induced seismicity caused by a number of natural and human causes. We observe multiple examples of failure following stress changes in the Sibi fold and thrust belt. The first seismic event in the 1997 doublet triggered a second event at large distances, suggesting the wedge was on the verge of failure. The earthquake also generated pervasive postseismic deformation with slip on a number of thrust faults throughout the wedge. We therefore suggest that the Sibi fold and thrust belt is behaving as a wedge at critical taper.

Our InSAR observations show that postseismic deformation can play a key role in maintaining the taper of a wedge. Coseismic deformation increased the taper of the Sibi wedge through uplift in the interior of the fold and thrust belt (see Figure 4.9d). In order to maintain critical taper, the overall taper of the wedge must be lowered. Figure 4.9d shows how postseismic deformation produced uplift towards the toe of the wedge, thus reducing the taper again and reproducing the overall shape of the topography. This self similar growth, even in a single earthquake cycle, is also indicative of a critical taper wedge. Our observations show that it is possible to grow topography and maintain critical taper using a single earthquake and associated postseismic deformation.

4.6 Conclusions

We combined ERS, Envisat and Sentinel-1 data to investigate the development of topography in a fold and thrust belt throughout the earthquake cycle. The resulting surface deformation maps showed the contributions of coseismic, postseismic and interseismic deformation to the generation of topography over various lengthscales. We found a clear relationship between shallow postseismic deformation and the development of short wavelength anticlines, in agreement with a number of previous studies elsewhere. The growth of such structures following an earthquake provides a way by which critical taper wedges can maintain taper without the need for future earthquakes nearer the toe of the wedge. We found that repeating the 1997 event, with its associated postseismic deformation, approximately 1000 times can reproduce the topography near the front of the fold and thrust belt. Our results have implications for how earthquakes and aseismic deformation in fold and thrust belts contribute to their development, as well as to the field of critical taper wedge mechanics.

Acknowledgments

TI is funded by the UK Natural Environment Research Council (NERC) through the Leeds-York NERC Doctoral Training Program (NE/L002574/1). This work was supported by NERC through the Centre for the Observation and Modelling of Earthquakes, Volcanoes and Tectonics (COMET, GA/13/M/031, `http://comet.nerc.ac.uk`) and via the Looking Inside the Continents (LiCS) project (NE/K011006/1). GNSS interseismic velocities were acquired from the Global Strain Rate Model (`http://gsrm2.unavco.org/intro/intro.html`, *Kreemer et al.* (2014)). Sentinel-1A interferograms are a derived work of Copernicus data, subject to the ESA use and distribution conditions. ERS and Envisat data were provided by ESA to TI (project no. 28753). We thank R. Amey, K. Spaans and J. Elliott for useful discussions and assistance and E. Nissen for providing the locations of faults and fold axes in the study area.

References

Ader, T., J.-P. Avouac, J. Liu-Zeng, H. Lyon-Caen, L. Bollinger, J. Galetzka, J. Genrich, M. Thomas, K. Chanard, S. N. Sapkota, S. Rajaure, P. Shrestha, L. Ding, and M. Flouzat (2012), Convergence rate across the Nepal Himalaya and interseismic coupling on the Main Himalayan Thrust: Implications for seismic hazard, *Journal of Geophysical Research*, *117*(B4), B04,403, doi:10.1029/2011JB009071. 4.1.1

Ainscoe, E. A., J. R. Elliott, A. Copley, T. J. Craig, T. Li, B. E. Parsons, and R. T. Walker (2017), Blind Thrusting, Surface Folding, and the Development of Geological Structure in the M_w 6.3 2015 Pishan (China) Earthquake, *Journal of Geophysical Research: Solid Earth*, *122*(11), 9359–9382, doi:10.1002/2017JB014268. 4.1.1

Almeida, R., E. O. Lindsey, K. Bradley, J. Hubbard, R. Mallick, and E. M. Hill (2018), Can the Updip Limit of Frictional Locking on Megathrusts Be Detected Geodetically? Quantifying the Effect of Stress Shadows on Near-Trench Coupling, *Geophysical Research Letters*, *45*(10), 4754–4763, doi:10.1029/2018GL077785. 4.5.1

Amey, R. M. J., A. Hooper, and R. J. Walters (2018), A Bayesian Method for Incorporating Self-Similarity Into Earthquake Slip Inversions, *Journal of Geophysical Research: Solid Earth*, doi:10.1029/2017JB015316. 4.3.1

Bagnardi, M., and A. Hooper (2018), Inversion of Surface Deformation Data for Rapid Estimates of Source Parameters and Uncertainties: A Bayesian Approach, *Geochemistry, Geophysics, Geosystems*, *19*(7), 2194–2211, doi:10.1029/2018GC007585. 4.3.1

Banks, C., and J. Warburton (1986), Passive-roof' duplex geometry in the frontal structures of the Kirthar and Sulaiman mountain belts, Pakistan, *Journal of Structural Geology*, *8*(3), 229–237, doi:10.1016/0191-8141(86)90045-3. 4.1.2, 4.5.1

Beavan, J., P. Denys, M. Denham, B. Hager, T. Herring, and P. Molnar (2010), Distribution of present-day vertical deformation across the Southern Alps, New Zealand, from 10 years of GPS data, *Geophysical Research Letters*, *37*(16), n/a–n/a, doi:10.1029/2010GL044165. 4.1.1, 4.5.1

Bekaert, D., R. Walters, T. Wright, A. Hooper, and D. Parker (2015), Statistical comparison of InSAR tropospheric correction techniques, *Remote Sensing of Environment*, *170*, 40–47, doi:10.1016/j.rse.2015.08.035. 4.5.2

Berberian, M., J. A. Jackson, M. Qorashi, M. Talebian, M. Khatib, and K. Priestley (2000), The 1994 Sefidabeh earthquakes in eastern Iran: blind thrusting and bedding-plane slip on a growing anticline, and active tectonics of the Sistan suture zone, *Geophysical Journal International*, *142*(2), 283–299, doi:10.1046/j.1365-246x.2000.00158.x. 4.5.1

Biggs, J., S. K. Ebmeier, W. P. Aspinall, Z. Lu, M. E. Pritchard, R. S. J. Sparks, and T. A. Mather (2014), Global link between deformation and volcanic eruption quantified by satellite imagery, *Nature Communications*, *5*(1), 3471, doi:10.1038/ncomms4471. 4.2

Cabral-Cano, E., T. H. Dixon, F. Miralles-Wilhelm, O. Diaz-Molina, O. Sanchez-Zamora, and R. E. Carande (2008), Space geodetic imaging of rapid ground subsidence in Mexico City, *Geological Society of America Bulletin*, *120*(11-12), 1556–1566, doi:10.1130/B26001.1. 4.2

Carena, S., J. Suppe, and H. Kao (2002), Active detachment of Taiwan illuminated by small earthquakes and its control of first-order topography, *Geology*, *30*(10), 935, doi:10.1130/0091-7613(2002)030¡0935:ADOTIB¿2.0.CO;2. 4.5.2

Ching, K.-E., M.-L. Hsieh, K. M. Johnson, K.-H. Chen, R.-J. Rau, and M. Yang (2011), Modern vertical deformation rates and mountain building in Taiwan from precise leveling and continuous GPS observations, 20002008, *Journal of Geophysical Research*, *116*(B8), B08,406, doi:10.1029/2011JB008242. 4.1.1, 4.5.1

Copley, A. (2014), Postseismic afterslip 30 years after the 1978 Tabas-e-Golshan (Iran) earthquake: observations and implications for the geological evolution of thrust belts, *Geophysical Journal International*, *197*(2), 665–679, doi:10.1093/gji/ggu023. 4.4.1, 4.5.1

Copley, A., and R. Jolivet (2016), Fault rheology in an aseismic fold-thrust belt (Shahdad, eastern Iran), *Journal of Geophysical Research: Solid Earth*, *121*(1), 412–431, doi:10.1002/2015JB012431. 4.4.1, 4.5.1

Copley, A., and K. Reynolds (2014), Imaging topographic growth by long-lived postseismic afterslip at Sefidabeh, east Iran, *Tectonics*, *33*(3), 330–345, doi:10.1002/2013TC003462. 4.4.1, 4.5.1

Cubas, N., J.-P. Avouac, P. Souloumiac, and Y. Leroy (2013), Megathrust friction determined from mechanical analysis of the forearc in the Maule earthquake area, *Earth and Planetary Science Letters*, *381*, 92–103, doi:10.1016/J.EPSL.2013.07.037. 4.5.2

Dahlen, F. A. (1990), Critical Taper Model of Fold-And-Thrust Belts and Accretionary Wedges, *Annual Review of Earth and Planetary Sciences*, *18*(1), 55–99, doi:10.1146/annurev.ea.18.050190.000415. 4.5.2

Dahlen, F. A., J. Suppe, and D. Davis (1984), Mechanics of fold-and-thrust belts and accretionary wedges: Cohesive Coulomb Theory, *Journal of Geophysical Research: Solid Earth*, *89*(B12), 10,087–10,101, doi:10.1029/JB089iB12p10087. 4.5.2

Davis, D., J. Suppe, and F. A. Dahlen (1983), Mechanics of fold-and-thrust belts and accretionary wedges, *Journal of Geophysical Research*, *88*(B2), 1153, doi:10.1029/JB088iB02p01153. 4.5.2

de Michele, M., D. Raucoules, J. de Sigoyer, M. Pubellier, and N. Chamot-Rooke (2010), Three-dimensional surface displacement of the 2008 May 12 Sichuan earthquake (China) derived from Synthetic Aperture Radar: evidence for rupture on a blind thrust, *Geophysical Journal International*, *183*(3), 1097–1103, doi:10.1111/j.1365-246X.2010.04807.x. 4.5.2

Elliott, J., R. Jolivet, P. J. González, J.-P. Avouac, J. Hollingsworth, M. P. Searle, and V. Stevens (2016), Himalayan megathrust geometry and relation to topography revealed by the Gorkha earthquake, *Nature Geoscience*, *9*(2), 174–180, doi:10.1038/ngeo2623. 4.1.1, 4.5.1, 4.5.2

Elliott, J. R., J. Biggs, B. Parsons, and T. J. Wright (2008), InSAR slip rate determination on the Altyn Tagh Fault, northern Tibet, in the presence of topographically correlated atmospheric delays, *Geophysical Research Letters*, *35*(12), n/a–n/a, doi:10.1029/2008GL033659. 4.2, 4.3.1

Elliott, J. R., E. A. Bergman, A. C. Copley, A. R. Ghods, E. K. Nissen, B. Oveisi, M. Tatar, R. J. Walters, and F. Yamini-Fard (2015), The 2013 M_w 6.2 Khaki-Shonbe (Iran) Earthquake: Insights into seismic and aseismic shortening of the Zagros sedimentary cover, *Earth and Space Science*, *2*(11), 435–471, doi:10.1002/2015EA000098. 4.5.1

Fattahi, H., and F. Amelung (2014), InSAR uncertainty due to orbital errors, *Geophysical Journal International*, *199*(1), 549–560, doi:10.1093/gji/ggu276. 4.5.2

Fielding, E. J., T. J. Wright, J. Muller, B. E. Parsons, and R. Walker (2004), Aseismic deformation of a fold-and-thrust belt imaged by synthetic aperture radar interferometry near Shahdad, southeast Iran, *Geology*, *32*(7), 577, doi:10.1130/G20452.1. 4.5.1

Gabriel, A. K., R. M. Goldstein, and H. A. Zebker (1989), Mapping small elevation changes over large areas: Differential radar interferometry, *Journal of Geophysical Research*, *94*(B7), 9183, doi:10.1029/JB094iB07p09183. 4.2

González, P. J., and J. Fernández (2011), Error estimation in multitemporal InSAR deformation time series, with application to Lanzarote, Canary Islands, *Journal of Geophysical Research*, *116*(B10), B10,404, doi:10.1029/2011JB008412. 4.2

Gratier, J. P., F. Renard, and B. Vial (2014), Postseismic pressure solution creep: Evidence and time-dependent change from dynamic indenting experiments, *Journal of Geophysical Research: Solid Earth*, *119*(4), 2764–2779, doi:10.1002/2013JB010768. 4.5.1

Haq, S. S. B., and D. M. Davis (1997), Oblique convergence and the lobate mountain belts of western Pakistan, *Geology*, *25*(1), 23, doi:10.1130/0091-7613(1997)025¡0023:OCATLM¿2.3.CO;2. 4.1.2

Hilley, G. E., R. Bürgmann, A. Ferretti, F. Novali, and F. Rocca (2004), Dynamics of slow-moving landslides from permanent scatterer analysis., *Science (New York, N.Y.)*, *304*(5679), 1952–5, doi:10.1126/science.1098821. 4.2

Hooper, A., D. Bekaert, K. Spaans, and M. Arkan (2012), Recent advances in SAR interferometry time series analysis for measuring crustal deformation, *Tectonophysics*, *514-517*, 1–13, doi:10.1016/j.tecto.2011.10.013. 4.2

Hubbard, J., J. H. Shaw, and Y. Klinger (2010), Structural Setting of the 2008 Mw 7.9 Wenchuan, China, Earthquake, *Bulletin of the Seismological Society of America*, *100*(5B), 2713–2735, doi:10.1785/0120090341. 4.5.2

Humayon, M., R. J. Lillie, and R. D. Lawrence (1991), Structural interpretation of the Eastern Sulaiman Foldbelt and Foredeep, Pakistan, *Tectonics*, *10*(2), 299–324, doi:10.1029/90TC02133. 4.1.2

Ingleby, T., and T. J. Wright (2017), Omori-like decay of postseismic velocities following continental earthquakes, *Geophysical Research Letters*, *44*(7), 3119–3130, doi:10.1002/2017GL072865. 4.2

Jadoon, I. A., R. D. Lawrence, and K. Shahid Hassan (1994), Mari-Bugti pop-up zone in the central Sulaiman fold belt, Pakistan, *Journal of Structural Geology*, *16*(2), 147–158, doi:10.1016/0191-8141(94)90101-5. 4.1.2

Jones, C. E., K. An, R. G. Blom, J. D. Kent, E. R. Ivins, and D. Bekaert (2016), Anthropogenic and geologic influences on subsidence in the vicinity of New Orleans, Louisiana, *Journal of Geophysical Research: Solid Earth*, *121*(5), 3867–3887, doi:10.1002/2015JB012636. 4.2

Khan, S., M. Waseem, M. A. Khan, and W. Ahmed (2018), Updated earthquake catalogue for seismic hazard analysis in Pakistan, *Journal of Seismology*, *22*(4), 841–861, doi:10.1007/s10950-018-9736-y. 4.1.2

King, G. C. P., R. S. Stein, and J. B. Rundle (1988), The Growth of Geological Structures by Repeated Earthquakes 1. Conceptual Framework, *Journal of Geophysical Research: Solid Earth*, *93*(B11), 13,307–13,318, doi:10.1029/JB093iB11p13307. 4.1.1

Kreemer, C., G. Blewitt, and E. C. Klein (2014), A geodetic plate motion and Global Strain Rate Model, *Geochemistry, Geophysics, Geosystems*, *15*(10), 3849–3889, doi:10.1002/2014GC005407. 4.1.2, 4.1, 4.6

Lammali, K., M. Bezzeghoud, F. Oussadou, D. Dimitrov, and H. Benhallou (1997), Postseismic deformation at El Asnam (Algeria) in the seismotectonic context of northwestern Algeria, *Geophysical Journal International*, *129*(3), 597–612, doi:10.1111/j.1365-246X.1997.tb04496.x. 4.1.1

Leon, L. A., S. A. Christofferson, J. F. Dolan, J. H. Shaw, and T. L. Pratt (2007), Earthquake-by-earthquake fold growth above the Puente Hills blind thrust fault, Los Angeles, California: Implications for fold kinematics and seismic hazard, *Journal of Geophysical Research*, *112*(B3), B03S03, doi:10.1029/2006JB004461. 4.5.1

Lohman, R. B., and M. Simons (2005), Some thoughts on the use of InSAR data to constrain models of surface deformation: Noise structure and data downsampling, *Geochemistry, Geophysics, Geosystems*, *6*(1), n/a–n/a, doi:10.1029/2004GC000841. 4.5.2

Macedo, J., and S. Marshak (1999), Controls on the geometry of fold-thrust belt salients, *Geological Society of America Bulletin*, *111*(12), 1808–1822, doi:10.1130/0016-7606(1999)111¡1808:COTGOF¿2.3.CO;2. 4.1.2

Maldonado, F., J. Mengal, S. Khan, and J. Thomas (2011), Digital geologic map and Landsat image map of parts of Loralai, Sibi, Quetta, and Khuzar Divisions, Balochistan Province, west-central Pakistan. 4.1.2, 4.2

Massonnet, D., M. Rossi, C. Carmona, F. Adragna, G. Peltzer, K. Feigl, and T. Rabaute (1993), The displacement field of the Landers earthquake mapped by radar interferometry, *Nature*, *364*(6433), 138–142, doi:10.1038/364138a0. 4.2

Melnick, D. (2016), Rise of the central Andean coast by earthquakes straddling the Moho, *Nature Geoscience*, *9*(5), 401–407, doi:10.1038/ngeo2683. 4.1.1, 4.5.1

Mosegaard, K., and A. Tarantola (1995), Monte Carlo sampling of solutions to inverse problems, *Journal of Geophysical Research: Solid Earth*, *100*(B7), 12,431–12,447, doi:10.1029/94JB03097. 4.3.1

Nishimura, T., M. Tobita, H. Yarai, T. Amagai, M. Fujiwara, H. Une, and M. Koarai (2008), Episodic growth of fault-related fold in northern Japan observed by SAR interferometry, *Geophysical Research Letters*, *35*(13), L13,301, doi:10.1029/2008GL034337. 4.5.1

Nissen, E., J. R. Elliott, R. A. Sloan, T. J. Craig, G. J. Funning, A. Hutko, B. E. Parsons, and T. J. Wright (2016), Limitations of rupture forecasting exposed by instantaneously triggered earthquake doublet, *Nature Geoscience 2016 9:4*, *9*(4), 330, doi:10.1038/ngeo2653. 4.1.2, 4.1, 4.2, 4.2, 4.4, 4.3.1, 4.3.1, 4.6, 4.3.2, 4.5.1

Okada, Y. (1985), Surface deformation due to shear and tensile faults in a half-space, *Bulletin of the Seismological Society of America*, *75*(4), 1135–1154. 4.3.1

Parker, R. N., A. L. Densmore, N. J. Rosser, M. de Michele, Y. Li, R. Huang, S. Whadcoat, and D. N. Petley (2011), Mass wasting triggered by the 2008 Wenchuan earthquake is greater than orogenic growth, *Nature Geoscience*, *4*(7), 449–452, doi:10.1038/ngeo1154. 4.5.1

Parsons, B., T. Wright, P. Rowe, J. Andrews, J. Jackson, R. Walker, M. Khatib, M. Talebian, E. Bergman, and E. R. Engdahl (2006), The 1994 Sefidabeh (eastern Iran) earthquakes revisited: new evidence from satellite radar interferometry and carbonate dating about the growth of an active fold above a blind thrust fault, *Geophysical Journal International*, *164*(1), 202–217, doi:10.1111/j.1365-246X.2005.02655.x. 4.5.1

Pinel-Puysségur, B., R. Grandin, L. Bollinger, and C. Baudry (2014), Multifaulting in a tectonic syntaxis revealed by InSAR: The case of the Ziarat earthquake sequence (Pakistan), *Journal of Geophysical Research: Solid Earth*, *119*(7), 5838–5854, doi:10.1002/2013JB010564. 4.1.2

Pritchard, M. E., and M. Simons (2004), An InSAR-based survey of volcanic deformation in the central Andes, *Geochemistry, Geophysics, Geosystems*, *5*(2), n/a–n/a, doi:10.1029/2003GC000610. 4.2

Reynolds, K., A. Copley, and E. Hussain (2015), Evolution and dynamics of a fold-thrust belt: the Sulaiman Range of Pakistan, *Geophysical Journal International*, *201*(2), 683–710, doi:10.1093/gji/ggv005. 4.1.2, 4.5.2

Rosen, P. A., S. Hensley, G. Peltzer, and M. Simons (2004), Updated repeat orbit interferometry package released, *Eos, Transactions American Geophysical Union*, *85*(5), 47–47, doi:10.1029/2004EO050004. 4.2

Searle, M., J.-P. Avouac, J. Elliott, and B. Dyck (2017), Ductile shearing to brittle thrusting along the Nepal Himalaya: Linking Miocene channel flow and critical wedge tectonics to 25th April 2015 Gorkha earthquake, *Tectonophysics*, *714-715*, 117–124, doi:10.1016/J.TECTO.2016.08.003. 4.5.2

Stein, R. S., G. C. P. King, and J. B. Rundle (1988), The Growth of Geological Structures by Repeated Earthquakes 2. Field Examples of Continental Dip-Slip Faults, *Journal of Geophysical Research: Solid Earth*, *93*(B11), 13,319–13,331, doi:10.1029/JB093iB11p13319. 4.1.1

Sun, Q., L. Zhang, X. Ding, J. Hu, Z. Li, and J. Zhu (2015), Slope deformation prior to Zhouqu, China landslide from InSAR time series analysis, *Remote Sensing of Environment*, *156*, 45–57, doi:10.1016/J.RSE.2014.09.029. 4.2

Suppe, J. (2007), Absolute fault and crustal strength from wedge tapers, *Geology*, *35*(12), 1127, doi:10.1130/G24053A.1. 4.5.2

Szeliga, W., R. Bilham, D. Schelling, D. M. Kakar, and S. Lodi (2009), Fold and thrust partitioning in a contracting fold belt: Insights from the 1931 Mach earthquake in Baluchistan, *Tectonics*, *28*(5), n/a–n/a, doi:10.1029/2008TC002265. 4.1.2

von Hagke, C., O. Oncken, and S. Evseev (2014), Critical taper analysis reveals lithological control of variations in detachment strength: An analysis of the Alpine basal detachment (Swiss Alps), *Geochemistry, Geophysics, Geosystems*, *15*(1), 176–191, doi:10.1002/2013GC005018. 4.5.2

Walker, R., M. Khatib, A. Bahroudi, A. Rodés, C. Schnabel, M. Fattahi, M. Talebian, and E. Bergman (2015), Co-seismic, geomorphic, and geologic fold growth associated with the 1978 Tabas-e-Golshan earthquake fault in eastern Iran, *Geomorphology*, *237*, 98–118, doi:10.1016/J.GEOMORPH.2013.02.016. 4.5.1

Wang, K., and Y. Fialko (2015), Slip model of the 2015 M_w 7.8 Gorkha (Nepal) earthquake from inversions of ALOS-2 and GPS data, *Geophysical Research Letters*, *42*(18), 7452–7458, doi:10.1002/2015GL065201. 4.2

Wimpenny, S., A. Copley, and T. Ingleby (2017), Fault mechanics and post-seismic deformation at Bam, SE Iran, *Geophysical Journal International*, *209*(2), 1018–1035, doi:10.1093/gji/ggx065. 4.5.1

Wright, T. J. (2002), Remote monitoring of the earthquake cycle using satellite radar interferometry., *Philosophical transactions. Series A, Mathematical, physical, and engineering sciences*, *360*(1801), 2873–88, doi:10.1098/rsta.2002.1094. 4.2

Wright, T. J. (2003), Source model for the M w 6.7, 23 October 2002, Nenana Mountain Earthquake (Alaska) from InSAR, *Geophysical Research Letters*, *30*(18), 1974, doi:10.1029/2003GL018014. 4.3.1

Wright, T. J., B. E. Parsons, and Z. Lu (2004), Toward mapping surface deformation in three dimensions using InSAR, *Geophysical Research Letters*, *31*(1), L01,607, doi:10.1029/2003GL018827. 4.3.2

Wright, T. J., P. J. Gonzalez, R. J. Walters, E. L. Hatton, K. Spaans, and A. J. Hooper (2016), LiCSAR: Tools for automated generation of Sentinel-1 frame interferograms, *American Geophysical Union, Fall General Assembly 2016, abstract #G23A-1037*. 4.2

Yu, S.-B., L.-C. Kuo, Y.-J. Hsu, H.-H. Su, C.-C. Liu, C.-S. Hou, J.-F. Lee, T.-C. Lai, C.-C. Liu, C.-L. Liu, T.-F. Tseng, C.-S. Tsai, and T.-C. Shin (2004), Preseismic Deformation and Coseismic Displacements Associated with the 1999 Chi-Chi, Taiwan, Earthquake, *Bulletin of the Seismological Society of America*, *91*(5), 995–1012, doi:10.1785/0120000722. 4.5.2

Zhou, Y., M. Y. Thomas, B. Parsons, and R. T. Walker (2018), Time-dependent postseismic slip following the 1978 Mw 7.3 Tabas-e-Golshan, Iran earthquake revealed by over 20 years of ESA InSAR observations, *Earth and Planetary Science Letters*, *483*, 64–75, doi:10.1016/J.EPSL.2017.12.005. 4.4.1, 4.5.1

Chapter 5

Discussion and Conclusions

In this final chapter, I discuss the results from chapters 2 - 4 and consider some of the recurring themes from this thesis. I then move on to suggest avenues for possible further research based on the findings of this thesis and the opportunities currently available.

5.1 Summary of Work

5.1.1 Chapter 2: Omori Decay of Postseismic Velocities

In chapter 2, I presented a compilation of near-field postseismic velocity measurements. I gathered 151 postseismic velocity measurements from 45 publications spanning 34 continental earthquakes/earthquake sequences. I found that the compilation shows a clear temporal pattern, with velocities decaying as $1/t$, where t is the time since the earthquake. In other words, the compilation showed that postseismic displacements grow logarithmically for points near the coseismic fault. The remarkably simple pattern holds over multiple timescales, covering periods from hours after an earthquake to nearly a century later.

I then compared these observations with various models routinely used to explain postseismic deformation. I found that linear viscoelastic relaxation models with only a single relaxation time were unable to explain the temporal evolution of the velocities. Including a second relaxation time (such as in a Burgers body) enables a linear viscoelastic model to explain the observations within the scatter of the data, but does not reproduce the temporal decay I observed. The addition of further relaxation times (e.g. through a continuously varying depth-dependent viscosity) may enable a better fit to the data. In contrast with linear viscoelastic models, I found that processes associated with fault zones such as frictional afterslip and power-law creep were better able to explain the observations. Frictional afterslip can provide the required $1/t$ evolution of postseismic velocities, whilst power-law creep with high stress exponents is also able to reproduce such temporal variation.

I suggested that these results imply that fault zone processes can dominate near-field surface deformation over the entire postseismic period. This means that studies seeking to obtain viscosity estimates for the mantle or lower crust need to take care not to misinterpret surface deformation in tectonically active regions.

5.1.2 Chapter 3: Nepal Seismic Cycle Geodesy

In chapter 3, I used geodesy to study the seismic cycle in Nepal and make inferences about the geometry and frictional properties of the Himalayan fault system. I processed Sentinel-1 data to produce an InSAR time series to study postseismic deformation following the M_w 7.8 Gorkha earthquake in Nepal. I combined these measurements with GNSS data and inferred that afterslip down-dip of the coseismic rupture was the predominant mechanism operating in the first few months after the earthquake, as found in previous studies (*Gualandi et al.*, 2016, *Sreejith et al.*, 2016, *Mencin et al.*, 2016, *Zhao et al.*, 2017, *Jiang et al.*, 2018, *Wang and Fialko*, 2018).

I then combined these postseismic measurements with interseismic and coseismic geodetic data to try and distinguish between competing models for the geometry of the Himalayan fault system. I found that geodetic data alone were incapable of distinguishing the various suggestions, even with the requirement that the geometry be consistent with data from these different earthquake cycle stages. I therefore tried to place extra constraints on the geometry by seeking a geometry which is capable of explaining both coseismic and postseismic deformation tied together by a mechanical model. I developed and applied a rate-strengthening friction model (*Barbot et al.*, 2009, *Rousset et al.*, 2012, *Feng et al.*, 2016) and inverted coseismic and postseismic displacements to seek models which could explain both simultaneously. I found that all three of the geometric models I tested were able to explain the data equally well.

I suggested that this inability to resolve the geometry with geodesy partly contributes to the controversy over the structure of the Himalayan fault system. Future studies need to combine geodetic data with additional constraints and determine the most appropriate structure using an interdisciplinary approach. This will require a team with expertise in each of the available data sets such that the errors on each can be correctly accounted for and an overall conclusion reached.

5.1.3 Chapter 4: Fold and Thrust Belt Growth from 25 Years of InSAR

In chapter 4, I examined the relationship between the earthquake cycle and the development of topography in a fold and thrust belt near Sibi, Pakistan. I combined ERS, Envisat and Sentinel-1 data to produce an InSAR time series over 25 years long. This long, spatially dense time series enabled me to study the evolution of individual folds and faults as well as the overall motion in the fold and thrust belt.

I tied together the different SAR datasets by using a ground deformation model, similar to those used when fitting GNSS time series. This exercise enabled me to separate out the contributions of different parts of the earthquake cycle to the overall surface deformation field. I then used the resulting earthquake cycle deformation maps to discuss the role of coseismic, postseismic and interseismic deformation in shaping topography. I found that postseismic deformation closely resembled the shape of short wavelength folds, as seen in previous studies (*Fielding et al.*, 2004, *Nishimura et al.*, 2008, *Copley and Reynolds*, 2014, *Copley*, 2014, *Copley and Jolivet*, 2016, *Wimpenny et al.*, 2017). I also showed that a combination of coseismic and postseismic deformation closely resembled the topography near the front of the fold and thrust belt, suggesting that repeating this combined deformation field many times could reproduce the topography seen today.

I determined that the topography near the front of the fold and thrust belt can be reconstructed with approximately 1000 repeats of the 1997 earthquake, with associated postseismic deformation. I suggested that the 1997 earthquake may be representative for the region because the down-dip extent may have been controlled by the presence of detachment horizons. I also suggested that these results have implications for the way by which the overall shape of a fold and thrust belt is maintained. Critical taper wedge mechanics suggests that fold and thrust belts grow in a self-similar way, maintaining taper (total angle between surface slope and decollement dip) over time. I showed how taper can be maintained within a single earthquake cycle through postseismic deformation near the toe of the wedge.

5.1.4 Aims and Objectives Revisited

I now return to the aims and objectives stated at the beginning of this thesis and evaluate progress against each of them.

Collate geodetic measurements of the seismic cycle from a number of previously studied dip-slip earthquakes.

I have collated measurements of postseismic deformation from both strike-slip and dip-slip earthquakes. I have also collated measurements of coseismic, interseismic and postseismic deformation for two case studies in Nepal and Pakistan.

Use InSAR to produce new surface deformation measurements around dip-slip faults.

I have constructed an InSAR time series to study postseismic deformation following the Gorkha earthquake. I have used ERS, Envisat and Sentinel-1 data to produce an InSAR time series covering significant aspects of the seismic cycle in a fold and thrust belt in Pakistan.

Combine all of these geodetic data from multiple stages of the earthquake cycle to build up a full picture of deformation around dip-slip faults.

I have combined postseismic geodetic data from multiple timescales to study the temporal evolution of surface velocities following continental earthquakes. This has enabled a clearer picture of postseismic deformation to be developed. The combination of interseismic, coseismic and postseismic geodetic data in Nepal provides a reasonably full picture of the earthquake cycle there. However, surface displacements from a large, surface rupturing earthquake and the accompanying postseismic deformation remain to be observed. My work on the Sibi fold and thrust belt has shown the potential for InSAR to provide a thorough picture of earthquake cycle deformation in both time and space. If the 1997 earthquake is representative of earthquakes in the region, then we have a fairly good understanding of what the earthquake cycle looks like here. However, interseismic deformation in this example remains uncertain and more long-term observations will be required to better constrain this aspect of the seismic cycle.

Determine an appropriate model to explain observations from throughout the seismic cycle. Develop additional models as required to explain the observations.

My compilation of postseismic deformation measurements suggests that fault zone processes are important when explaining near field postseismic deformation over a variety of timescales. Case studies in Nepal and Pakistan have further highlighted the role of faults in explaining earthquake cycle deformation. Observations from throughout the earthquake cycle in Nepal can be explained using elastic dislocation models. InSAR results over the Sibi fold and thrust belt clearly show the important role of faults in both coseismic and postseismic deformation.

Given the importance of faults in the seismic cycle, I developed a joint coseismic-postseismic fault model. The model uses rate-strengthening friction to mechanically couple coseismic and postseismic slip. This model can account for uncertainties in the coseismic slip model when trying to model postseismic deformation and provides uncertainties on the frictional parameters of the faults involved.

Examine the relationship between earthquake cycle deformation and topography in a dip-slip fault setting to see how topography is grown in these regions.

I examined the relationship between topography and the earthquake cycle using InSAR over the Sibi fold and thrust belt. I found that the clearest relationship between the two can be seen in the postseismic deformation field. Coseismic deformation can contribute to the longer wavelength development of topography, whilst interseismic deformation

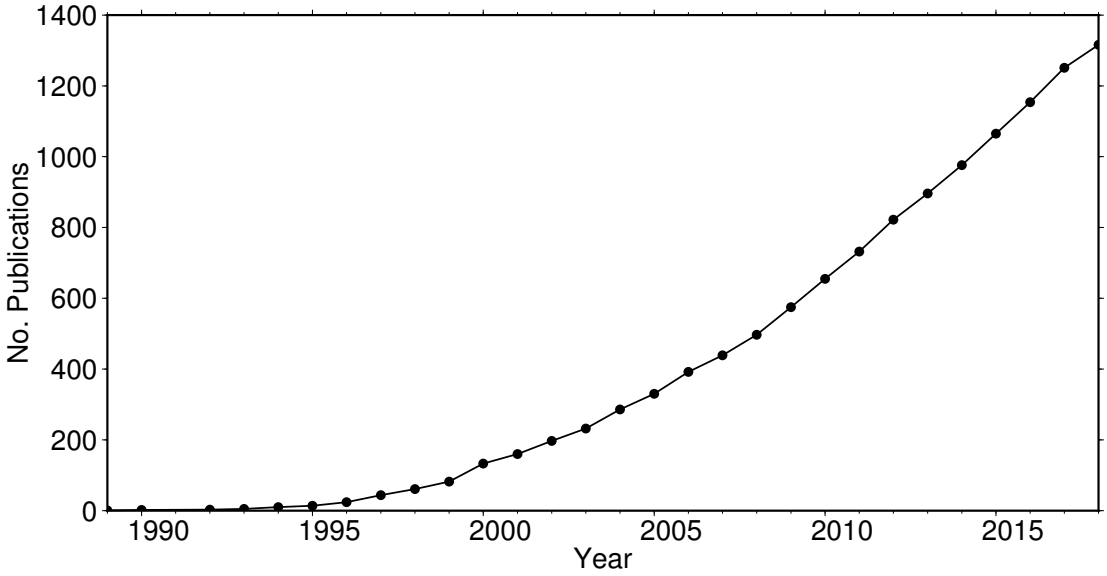

Figure 5.1: Number of earthquakes/tectonics related publications associated with InSAR. Results obtained using Scopus (`https://www.scopus.com`), searching for publications containing any of the following in their title, abstract or key words: InSAR, radar interferometry or SAR interferometry and any of a number of earthquakes/tectonics keywords.

may play a role in the generation and maintenance of topography towards the rear of the fold and thrust belt.

5.2 Using InSAR to study the Earthquake Cycle

I have used InSAR to study different parts of the earthquake cycle in every chapter in this thesis. This is representative of the increasing usage of InSAR by the tectonics community. Figure 5.1 shows the growing number of tectonics/earthquake publications using InSAR since the late 1990s. Usage is expected to keep growing due to the launch of satellites such as Sentinel-1a/b that acquire data regularly over most tectonic regions on the planet, and for which the data is freely distributed.

I have shown both the strengths and weaknesses of InSAR for tectonics in this thesis. InSAR provided postseismic velocity measurements for over a third (55/151) of the data points used in the compilation in chapter 2. InSAR played an important role in providing measurements of postseismic deformation over longer timescales in remote regions (e.g *Ryder et al.*, 2014, *Copley*, 2014). The high spatial resolution of InSAR also enables the identification of postseismic fault creep (e.g *Hussain et al.*, 2016). In chapter 3, I used InSAR to obtain postseismic deformation measurements from the Tibetan plateau where GNSS stations are sparsely available. In chapter 4, I showed how InSAR can be used to construct geodetic data sets covering large regions, over long time scales, at high spatial resolution.

However, InSAR has significant limitations. Firstly, many regions remain unsuitable

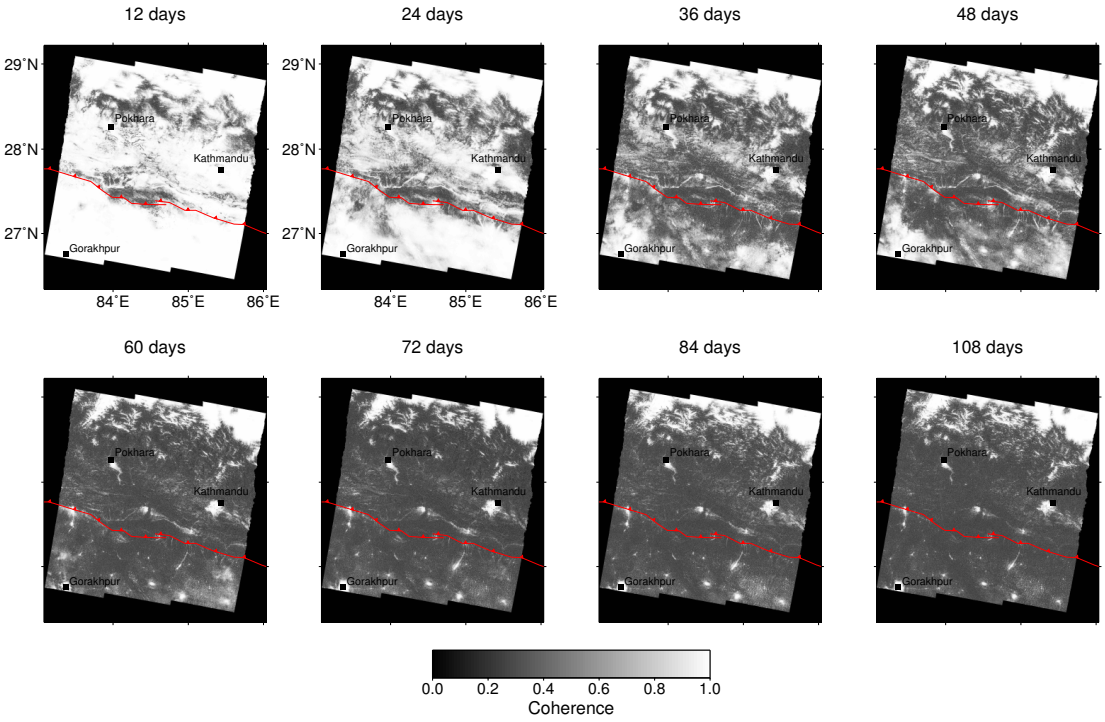

Figure 5.2: Time series of coherence change over Nepal. White areas are high coherence whereas darker regions have low coherence. Red line is the surface trace of the Main Frontal Thrust (*Taylor and Yin*, 2009)

.

for InSAR due to a lack of coherence. Figure 5.2 shows how coherence decreases rapidly over most of Nepal. Even after only 36 days, most of the image has become incoherent, leaving only the Tibetan plateau (in the north of the image) and the urban areas such as Kathmandu, Pokhara and Gorakhpur with high coherence. This is not only a problem in Nepal, but also in many other parts of the world (*Funning and Garcia*, 2017).

Secondly, InSAR is affected by a number of noise sources, as discussed in chapter 1. The most significant of these noise sources is the atmosphere, which can swamp deformation signals in individual interferograms (*Dawson and Tregoning*, 2007, *Funning and Garcia*, 2017) and even in InSAR time series analysis (*Fattahi and Amelung*, 2015). Figure B.3 in the appendix shows the significant atmospheric delays present in Nepal which show a seasonal signal overlaid with random smaller perturbations. The size of this signal is large enough to swamp postseismic deformation signals in the Ganges basin and was one of the reasons for excluding this data in chapter 3.

InSAR data, and geodesy more generally, cannot provide a full picture of the earthquake cycle. In chapter 3, I showed the limitations of surface geodetic data when seeking to address questions around the geometry of the faults beneath Nepal. Even with a variety of different geodetic data sets, no geometry was clearly favoured. Such a conclusion highlights the necessity for interdisciplinary work when tackling such questions.

5.3 The Role of Fault Geometry

In the introduction, I discussed the possible role of fault geometry in controlling various aspects of the earthquake cycle. Throughout this thesis, fault geometry has played a role in a number of ways.

5.3.1 Postseismic Response

In chapter 2, I compared the temporal variation of postseismic velocities for both strike-slip and dip-slip earthquakes. There appears to be no significant difference between the different faulting environments, with strike-slip, normal and thrust faults all showing similar temporal patterns (Figure 2.2). This suggests that a similar mechanism is responsible for the postseismic deformation observed. Modelling suggests this mechanism is fault-zone related, such as frictional afterslip or power-law creep (*Montési*, 2004).

The different postseismic responses seen following the Sibi and Gorkha earthquakes may also be controlled by fault geometry. The Gorkha earthquake was followed by afterslip down-dip of the rupture, with very little shallow afterslip. In contrast, the Sibi earthquake was followed by postseismic deformation indicative of both down- and up-dip afterslip. The two earthquakes were both thrust faulting events, although different in size, depth range and geometry. The more pervasive shallow afterslip following the Sibi event may be due to the shallower nature of the rupture (5 - 10 km rather than 10 - 15 km in Gorkha) or the geometry of the fault system. In Sibi, the coseismic rupture occurred on a ramp with a flatter decollement at shallower levels (see Figure 4.6). In contrast, the Gorkha earthquake occurred on a relatively flat segment of the Main Himalayan Thrust and may have been surrounded by steep ramps (*Hubbard et al.*, 2016). Alternatively, the different responses may reflect different lithologies and fault strengths in each case. Further work is required to disentangle the various possible explanations for such different postseismic responses.

5.3.2 Fault Geometry and Tectonics in Nepal

In chapter 3 I discussed the different geometries proposed for the Himalayan fault system beneath Nepal. I concluded that our current suite of geodetic data were unable to distinguish between the different suggestions. However, the question remains important and should be tackled using different tools. The geometry of the faults beneath Nepal have consequences for the way in which topography is generated and strain accommodated (e.g. *Pandey et al.*, 1995, *Lavé and Avouac*, 2001, *Hodges et al.*, 2004, *Wobus et al.*, 2005, *Grandin et al.*, 2012). Furthermore, recent work has shown how fault geometry may control the extent of deformation in different stages of the earthquake cycle. *Hubbard et al.* (2016) constructed a 3D geometry for the Main Himalayan Thrust beneath Nepal using geological modelling. They found that the extent of coseismic slip in the 2015 Gorkha earthquake closely followed the shape of a flat between two ramps

in the fault structure. *Lindsey et al.* (2018) compared the location of the interseismic locking line with the location of the lower ramp from the same geological model. They found close agreement between the two for eastern and central Nepal, suggesting the ramp may control the location of interseismic locking.

5.3.3 Coseismic Containment in the Sibi Fold and Thrust Belt

In chapter 4, I presented InSAR results over the Sibi fold and thrust belt. Coseismic InSAR reveals an elongate region of surface deformation that is much longer along strike than it is down-dip (see Figure 4.4). The aspect ratio of this surface deformation suggests that slip propagated further along strike than down dip. Elastic dislocation modelling confirms this, with slip inferred to have occurred over approximately 40 km along strike and 10 km down dip. A similarly long, thin rupture for this event was inferred by *Nissen et al.* (2016) and confirms an aspect ratio (L/W) of 4, which is at the high end of values for dip-slip earthquakes (*Weng and Yang*, 2017). Long, thin ruptures have been observed in other locations (*Elliott et al.*, 2015) and depth-limited seismicity seen in a number of cases (*Elliott et al.*, 2011, 2013, *Bonini et al.*, 2014, *Hubbard et al.*, 2016). In these cases, the depth extent of seismic slip is thought to have been controlled by geological structures.

Structural control may be exerted through lithological layering or fault interaction, for example through the role of detachment horizons and fault geometry in controlling rupture propagation. To test this, I compared the depth range of seismicity with the approximate depths of potential detachment horizons within shale units (*Nissen et al.*, 2016). In chapter 4, I modelled the coseismic deformation recorded by ERS in the 1997 Sibi earthquake. The upper limit of coseismic slip agrees with the depth of one of the detachment horizons, at approximately 6 km depth (Figure 4.6). The second earthquake in the 1997 doublet has coseismic slip reaching to similar depths, suggesting a laterally continuous barrier to rupture propagation. The lower limit of coseismic slip in both events is at approximately 10 - 12 km depth in reasonable agreement with the depth of another potential detachment horizon (Figure 4.6). Postseismic afterslip is seen both above and below the coseismic rupture, suggesting that the material up- and down-dip is rate strengthening and therefore difficult to rupture seismically. Detachment horizons of rate-strengthening material, such as over-pressured shales (*Kohli and Zoback*, 2013, *Reynolds et al.*, 2015), could therefore explain the depth extent of coseismic slip.

Alternatively, the geometry of the fault system may have arrested rupture. Both events were followed by afterslip on shallow faults beneath short wavelength folds. When these faults are projected down-dip, some intersect with the approximate location of the up-dip limit of coseismic slip. Fault intersections and junctions may be places of focused damage which inhibit ruptures (*Andrews*, 1989, *Gartrell et al.*, 2004, *Qi et al.*, 2011). A change in dip of the fault without any other fault intersections, may have also

inhibited further rupture (*Hubbard et al.*, 2016).

If fault intersections or detachment horizons act as persistent barriers to earthquake rupture, then we might consider slip between these barriers to be characteristic of earthquakes in Sibi. If this is the case, then it provides a physical reason for why the topography might be constructed from multiple earthquakes which are similar to this (see chapter 4). These barriers would only control the vertical extent of rupture and allow a variety of along-strike rupture scenarios. The 1997 earthquake shows how even a vertically contained rupture can become large by dynamic triggering of adjacent faults (*Nissen et al.*, 2016). Using such barriers as a means of assessing maximum earthquake magnitudes is therefore problematic.

5.4 The Importance of Afterslip

Afterslip has been a significant part of every chapter in this thesis. In chapter 2 I showed that frictional afterslip could explain the temporal variation of near-field postseismic velocities over multiple time scales. In chapter 3 I concluded that down-dip afterslip was the dominant deformation mechanism following the 2015 Gorkha earthquake, and in chapter 4 I inferred that afterslip was likely responsible for the postseismic deformation observed. Figure 5.3 shows an updated version of Figure 2.1, which includes postseismic velocities from both Nepal and Sibi. These examples agree with the previous compilation, showing a $1/t$ decay of velocities following the earthquake. This relationship has also been found to hold in recent papers looking at postseismic velocity evolution in Iran (*Zhou et al.*, 2018) and Turkey (*Hussain et al.*, 2018).

Figure 5.4 shows geodetic measurements of afterslip in the two regions examined in this thesis. The examples show the different length scales of deformation that can be produced by afterslip. The Gorkha postseismic deformation field is centred down-dip of the coseismic deformation, with a relatively long wavelength signal (80 km). In contrast, the postseismic deformation near Sibi is primarily up-dip of the main rupture and consists of both long wavelength signals and short wavelength signals over folds.

Afterslip also plays a significant role in developing topography. In chapter 4, I showed how short wavelength folds appeared to be growing following the Sibi earthquake. This mechanism of topographic growth is being observed more frequently (*Fielding et al.*, 2004, *Nishimura et al.*, 2008, *Copley and Reynolds*, 2014, *Copley*, 2014, *Copley and Jolivet*, 2016, *Wimpenny et al.*, 2017) and further study may be able to establish how important it is globally. Results from Nepal suggest that afterslip can partly counteract the subsidence produced in the Gorkha earthquake, although the peak postseismic uplift signal is still southward of the highest topography (see Figure 5.4). This suggests that other mechanisms are required to grow and maintain such high topography. Furthermore, despite the common occurrence of afterslip and its ability explain a number of different observations, other postseismic mechanisms are required

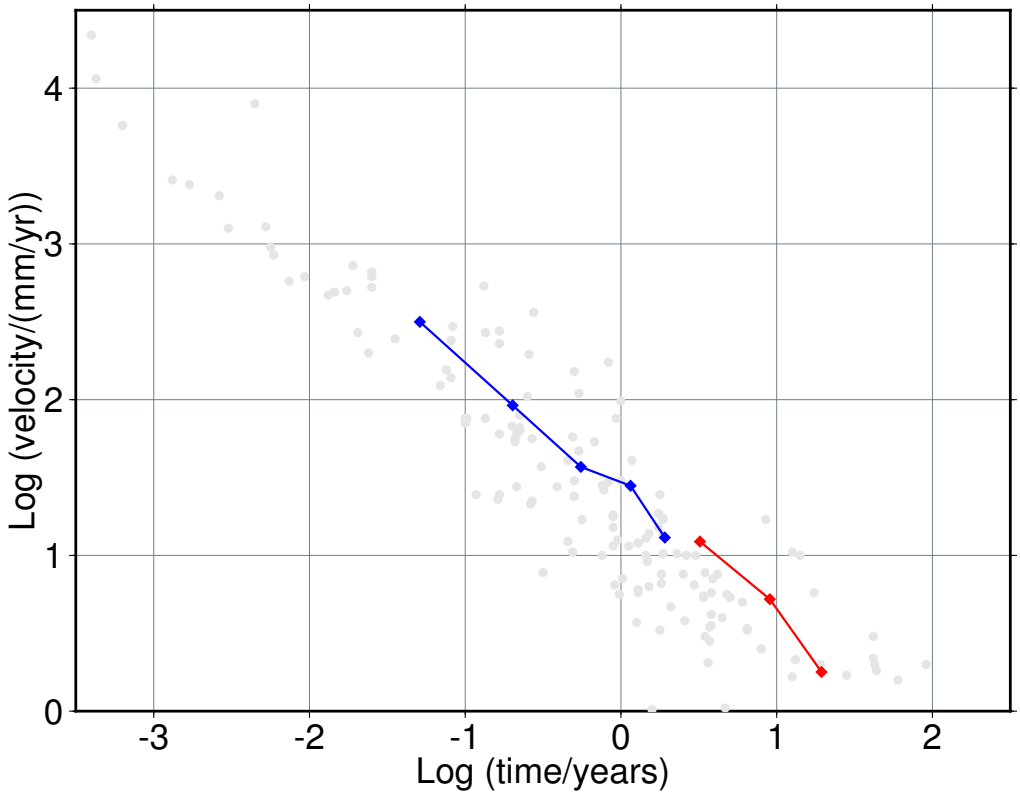

Figure 5.3: Temporal variation of postseismic velocities, as in Figure 2.1, updated with velocities from other work presented in this thesis. Grey dots are the original data points presented in *Ingleby and Wright* (2017). Blue line shows velocites obtained from a piecewise linear fit to the southward component of motion at GNSS station CHLM. Red line shows LOS velocities from ERS, Envisat and Sentinel-1 data over the frontal fold in the Sibi fold and thrust belt.

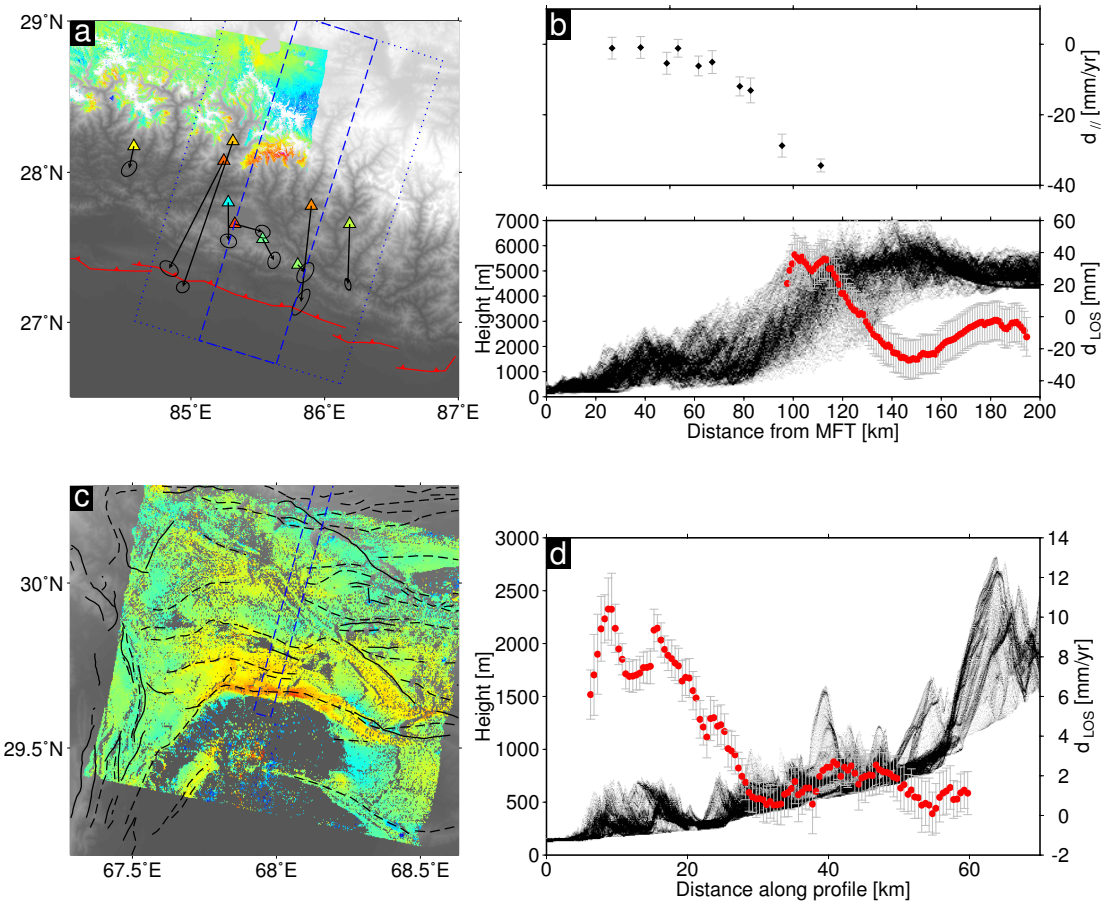

Figure 5.4: Examples of afterslip observed in two regions of thrust faulting. a) Map of the Nepalese Himalaya overlaid with postseismic deformation measurements following the 2015 M_w7.8 Gorkha earthquake. Arrows are GNSS displacements 2 years after the earthquake. InSAR data show postseismic displacements 113 days after the earthquake. Blue dashed rectangle shows extent of swath profile for InSAR whilst dotted rectangle shows extent of GNSS swath profile. b) Comparison between postseismic deformation and topography. Top panel is profile parallel GNSS covering same period as InSAR; lower panel shows InSAR LOS displacements. c) Map of a part of the Sulaiman fold and thrust belt near Sibi, Pakistan with a velocity map formed from Envisat data acquired after the earthquake. Black solid lines are faults and black dashed lines are anticline fold axes (*Nissen et al.*, 2016). Blue dashed box shows location of swath profile. d) Envisat LOS velocities compared with topography.

to fully explain the postseismic deformation field following earthquakes (*Jónsson et al.*, 2003, *Fialko*, 2004, *Freed et al.*, 2006, 2007).

5.5 Frictional Properties of Faults

I have shown the importance of localised deformation on faults throughout this thesis. The strength and seismogenic potential of faults depends upon their frictional properties. The total stress a fault can maintain before failing in an earthquake is dependent upon the static coefficient of friction, μ. Stronger faults have higher friction coefficients and can maintain higher stresses before brittle failure (*Byerlee*, 1978). However, fault friction has been found to also depend on the rate of fault motion as well as the time of contact between opposing fault surfaces (*Dieterich*, 1979, *Ruina*, 1983). These observations have been summarised in the rate and state friction laws, which describe how the coefficient of friction varies as a function of sliding rate and contact time (*Marone*, 1998).

5.5.1 Rate Strengthening Parameter from Afterslip

In chapter 3, I used the rate and state friction laws to develop an inversion which uses coseismic and postseismic deformation simultaneously to infer frictional properties of faults. I found a range of values for the rate parameter (a) between $0.7 - 1.6 \times 10^{-3}$, at the lower end of those retrieved from laboratory experiments which are usually between 10^{-3} and 10^{-2} (*Marone*, 1998, *van den Ende et al.*, 2018). However, these results are consistent with those found in other studies of postseismic deformation, where $a\sigma$ is on the order of 0.1 - 10 MPa (*Barbot et al.*, 2009, *Chang et al.*, 2013, *Rollins et al.*, 2015, *Feng et al.*, 2016, *Wimpenny et al.*, 2017).

The compilation of postseismic velocities presented in Figure 5.3 offers an opportunity to determine the range of frictional properties suggested by the decay of postseismic velocities. Assuming the velocity evolution is controlled by brittle creep and is primarily driven by the coseismic shear stress change, it is possible to use the velocity evolution proposed by *Perfettini and Avouac* (2004) to model the velocity compilation. I normalised the results as described in chapter 2, and used equation 24 in *Perfettini and Avouac* (2004) to model the velocity evolution $V(t)$ of a 1D spring slider system. I modify the equation to model only postseismic velocities by subtracting the interseismic slip rate:

$$V(t) = V_i \frac{d \exp(\frac{t}{t_r})}{1 + d\frac{V_i}{V_0}(\exp(\frac{t}{t_r}) - 1)} - V_0 \tag{5.1}$$

where V_i is the initial postseismic velocity, V_0 is the interseismic slip rate, t_r is the relaxation time of the system and d can be calculated as $d = \exp(\Delta\tau / a\sigma)$. $\delta\tau$ is the

shear stress change caused by the earthquake and $a\sigma$ is the rate parameter multiplied by the normal stress. The relaxation time is calculated as:

$$t_r = \frac{a\sigma}{kV_0} \tag{5.2}$$

where most parameters have previously been defined, except for k which is the average stiffness of the system. Since I am using a compilation of postseismic velocity measurements, many of these terms are unknown and certain assumptions need to be made about reasonable values. I therefore used a Bayesian inversion, using prior probability density functions (PDF) for each of the unknown parameters. I used a uniform prior PDF for each parameter, assigning equal probability to parameter values between reasonable bounds. I allowed $a\sigma$ to vary between 0.1 and 10 MPa and the shear stress change ($\Delta\tau$) to be between 0.1 and 10 MPa, assuming that the shear stress change is of similar size to typical earthquake stress drops. The initial velocity was allowed to be anything between 0 and 10000 mm/yr whilst the interseismic velocity was between 0 and 50 mm/yr. The stiffness of the material was allowed to be between 0 and 0.1 MPa/mm, where the average stiffness of a deforming area is defined as $k = G/h$. A stiffness of 0.1 MPa/mm corresponds to a deforming area with $h = 100$ m and a shear modulus, $G = 10$ GPa. Larger stiffness values would be possible with a larger shear modulus or smaller deforming area but other studies inferring values for k (*Fletcher and McGarr*, 2006, *Steer et al.*, 2011, *Rolandone et al.*, 2018) or which use a typical value (*Marone et al.*, 1991) have values less than 0.1 MPa/mm. I then used a Monte Carlo Markov Chain (*Mosegaard and Tarantola*, 1995), to sample the posterior PDFs for each parameter.

Figure 5.5 shows the maximum likelihood model fit to the velocity compilation and Figure 5.6 shows the posterior PDFs for each parameter, as well as the joint PDFs for each combination of parameters. The stress change and initial velocity are unconstrained by the data, with a posterior PDF equivalent to the prior PDF. The data prefer generally higher values of average stiffness, but only weakly. The most well constrained parameters are the interseismic velocity and $a\sigma$. The interseismic velocity tends towards very low values, whilst $a\sigma$ ranges between 0.2 and 1.54 MPa (at 95% confidence). This range of values is similar to the values for $a\sigma$ obtained in chapter 3 for Nepal (0.36 - 0.72 MPa, assuming a lithostatic normal stress of 450 MPa at 15 km depth).

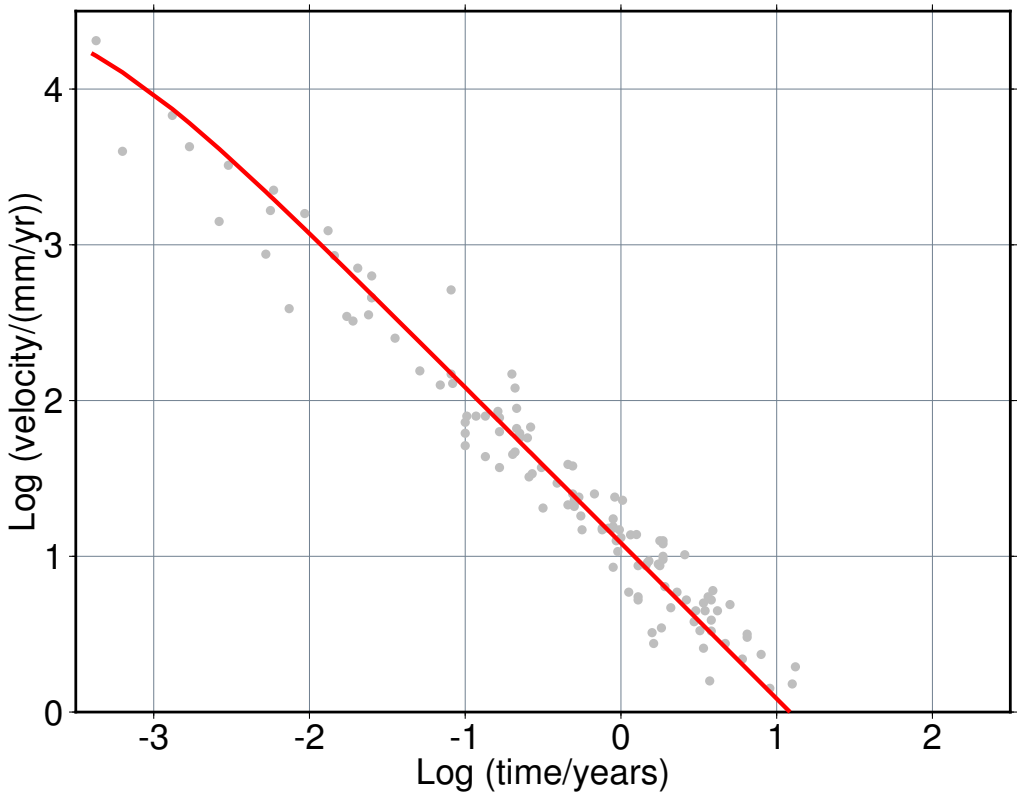

Figure 5.5: Temporal variation of postseismic velocities updated with velocities from other work presented in this thesis, normalised as in Figure 2.1. Grey dots are the normalised data. Red line shows the maximum likelihood model fit for a 1D spring-slider model (*Perfettini and Avouac*, 2004).

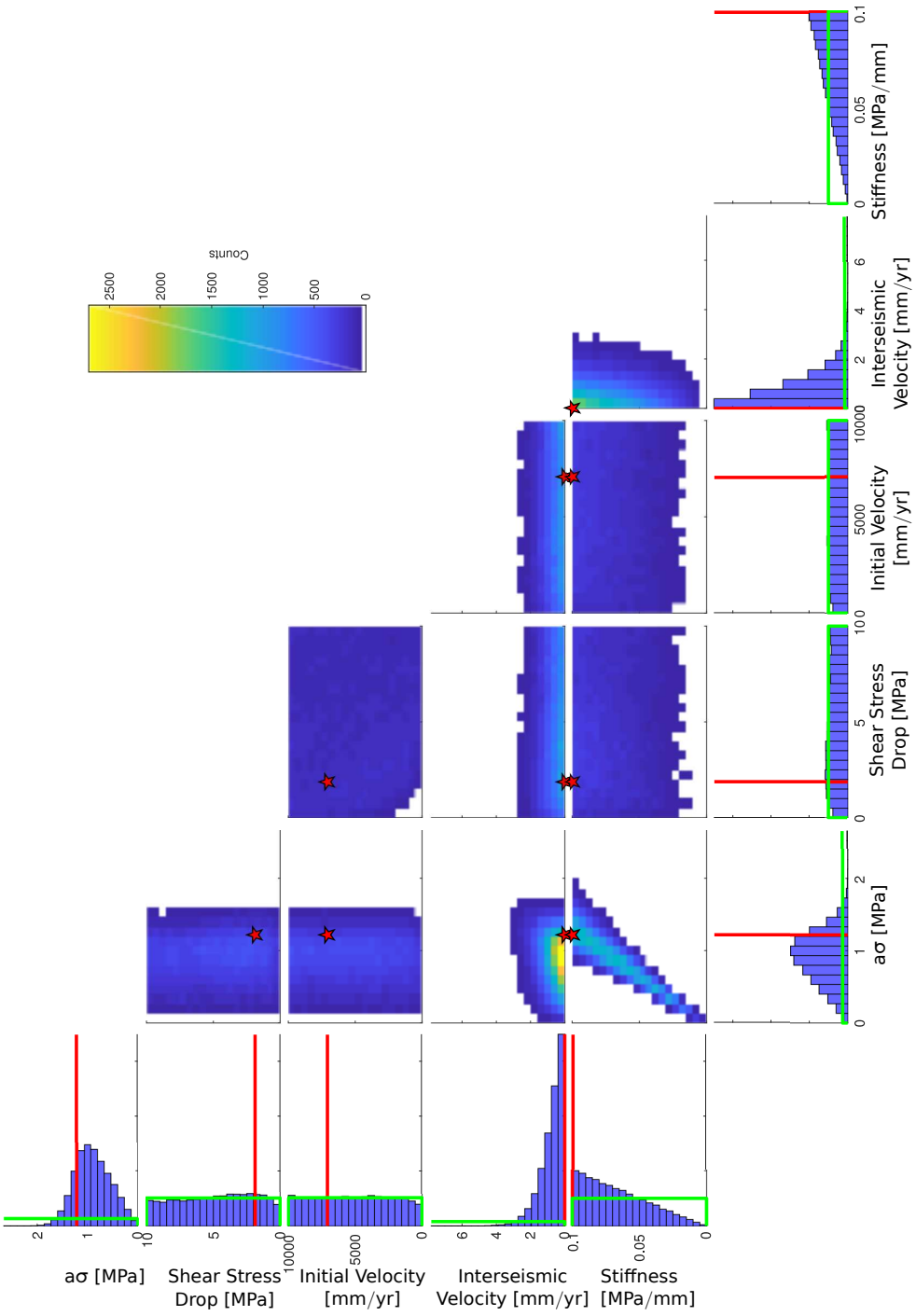

Figure 5.6: Probability density functions (PDF) for each of the parameters used in the 1D spring slider model, as well as joint PDFs for each pair of parameters. Green boxes show prior PDFs used in the Bayesian inversion, whilst red lines/stars show the maximum likelihood values.

These results lend support to the rate-and-state friction paradigm. The rate-and-state formulation of fault friction is based on an empirical fit to laboratory data. The ability for these laws to reproduce postseismic geodetic data from a variety of natural examples corroborates the work in the laboratory. Assuming lithostatic normal stresses in Nepal suggests low values of a ($10^{-4} - 10^{-3}$). Lower values of a result in smaller increases in fault friction for a given increase in velocity (see equation 1.3). The key stability condition for whether a fault can nucleate an earthquake is the value of $(a - b)$. If $(a - b) < 0$ then the fault is rate-weakening and can nucleate earthquakes, whereas values of $(a - b)$ greater than zero are rate-strengthening and cannot nucleate earthquakes. However, if $(a - b)$ is close to 0, then rate-strengthening faults can be ruptured through (*Kaneko et al.*, 2010, *Noda and Lapusta*, 2013). The values we obtain for a in Nepal are close to 0, meaning that it may be possible for seismic ruptures to continue in to these apparently rate-strengthening regions (*Dublanchet et al.*, 2013, *Zhou et al.*, 2018).

5.5.2 Static Friction Coefficient from Critical Taper Analysis

In order to obtain a more complete picture of the frictional properties of faults, I also need to estimate the static friction coefficient. I have previously argued that the toe of the Sibi fold and thrust belt is behaving as a critical taper in chapter 4. Here, I use critical taper analysis to constrain the frictional properties of the decollement underlying this fold and thrust belt. I used the equation for a sub-aerial critical taper (*Dahlen*, 1990):

$$\alpha + \beta \approx \frac{\beta + \mu_b(1 - \lambda_b) + S_b/\rho g H}{1 + 2(1 - \lambda)[\frac{\sin\phi}{1-\sin\phi}] + C/\rho g H} \tag{5.3}$$

where α is the topographic slope and β is the decollement dip (both in radians). The numerator contains a number of terms associated with the strength of the decollement: μ_b is the friction coefficient, λ_b is the Hubbert-Rubey fluid pressure ratio (*Hubbert and Rubey*, 1959) for the decollement and S_b is the basal cohesion. The denominator has similar terms which determine the strength of the wedge: λ is the Hubbert-Rubey fluid pressure ratio in the wedge, ϕ is the internal friction angle such that $\mu = \sin\phi$ and C is the wedge cohesion. The only other terms relate to the lithostatic pressure in the wedge where ρ is the average wedge density, g is acceleration due to gravity and H is the thickness of the wedge.

Equation 5.3 enabled me to estimate various parameters for the Sibi fold and thrust belt using the shape of the topography and the dip of the decollement. I used an affine invariant Bayesian inversion (*Goodman and Weare*, 2010) to determine the range of parameter values which reproduce the topographic slope. This inversion uses multiple walkers to explore parameter space and allows for the efficient exploration of probability distributions even when parameters are highly correlated. The algorithm has been

extensively tested in previous work (*Foreman-Mackey et al.*, 2013) and applied in a number of contexts (*Hou et al.*, 2012, *Hussain et al.*, 2016). Using this approach, I was able to generate probability distributions for each parameter, similar to *Cubas et al.* (2013).

I used uniform prior distributions for each parameter. My investigations of the fault geometry beneath the Sibi fold and thrust belt suggests a very shallowly dipping decollement at approximately 6 km depth beneath the toe of the wedge (Figure 4.6). I therefore allowed dips up to two degrees for the parameter β. I used the same parameter ranges as *Hubbard et al.* (2010) for wedge cohesion, basal cohesion, internal friction coefficient and the decollement friction coefficient. I assumed that the wedge and the decollement have Hubbert-Rubey fluid pressure ratios equivalent to hydrostatic pore fluid pressure (*Hubbard et al.*, 2010) and a typical crustal density for the average wedge density. The thickness of the wedge was calculated as the depth of the decollement (6 km) plus the height of the topography at the back of the modelled wedge.

I initially modelled the toe of the wedge, using the shape of the topography from $x = 6.5$ km to $x = 35$ km along the profile. These values correspond to the start of the fold and thrust belt and the end of the shallow decollement respectively. I extracted the mean and standard deviation of the height in the swath profile in steps of approximately 200 m. The critical taper model can be used to predict a topographic slope for any set of taper parameters. In order to compare the predicted slope with topographic measurements, an offset (k) is added to the prediction such that $d_{pred} = \beta x + k$. I found that most parameters are unconstrained by the inversion such that their posterior probability distribution was identical to their prior probability distribution. However, the offset k and basal coefficient of friction μ_b were somewhat constrained by the data. The basal coefficient of friction is constrained to be < 0.6 and between 0.04 and 0.49 at 95% confidence (see Figure 5.7).

The decollement friction coefficient is in agreement with the values obtained in other studies using critical taper wedge analysis, with values between 0.04 and 0.4 (*Carena et al.*, 2002, *Suppe*, 2007, *Hubbard et al.*, 2010, *Cubas et al.*, 2013). These results suggest that the decollement is weak and add to the body of evidence suggesting this for a wide variety of decollements. Whilst most rocks have a coefficient of friction of around 0.6 (*Byerlee*, 1978), some earth materials such as phylosillicates have significantly lower friction coefficients. Furthermore, there is growing evidence that faults have effective friction coefficients less than 0.3 (*Copley*, 2018). Overpressured shales often contain low angle decollements and have been found to have frictional strength of approximately 0.1 (*Suppe*, 2007, *von Hagke et al.*, 2014). The presence of such shales in the Sulaiman fold and thrust belt has been suggested by previous authors (*Reynolds et al.*, 2015, *Nissen et al.*, 2016) and I suggest one such layer is responsible for the shallow, low friction decollement we observe.

The decollement in Sibi also slips aseismically following the earthquake, suggesting

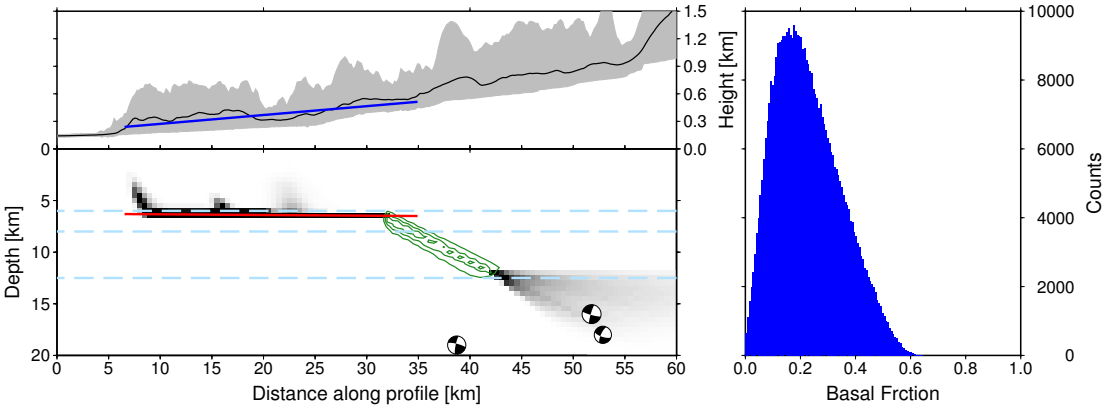

Figure 5.7: Set-up and results for the wedge modelling. Left-hand panels show the fault geometry and topography used in the modelling. Solid red line is the maximum likelihood decollement geometry obtained from the wedge modelling. Solid blue line is the average fit to the topographic slope produced by the wedge modelling. Histogram shows the range of acceptable basal friction coefficients.

it is rate strengthening. *Ikari et al.* (2011) found a systematic relationship between fault strength and the rate-and-state $(a - b)$ value. They found that materials with a coefficient of friction < 0.5 were always rate-strengthening in their laboratory tests, whereas stronger materials could be either rate-strengthening or rate-weakening. *Kohli and Zoback* (2013) found this relationship to also be true for shale samples from hydrocarbon reservoirs, showing a dependence of both parameters on the total clay and organic content. My modelling results therefore agree with laboratory experiments suggesting that rocks, particularly shales, with low strength are also rate-strengthening.

Combining the static friction coefficient with the rate-and-state parameters can provide a more complete picture of fault friction (*Chang et al.*, 2013, *Copley and Jolivet*, 2016). For example, whilst low angle decollements offer a large potential rupture area and may pose a significant seismic hazard (*Hubbard et al.*, 2015), my results for the Sibi decollement suggest it has low friction and is rate-strengthening, implying a lower risk of large seismic ruptures. *Hubbard et al.* (2010) argue that the tow of the wedge associated with the Wenchuan earthquake is likely incapable of storing sufficient elastic energy to generate large earthquakes due to its low friction coefficient. The friction coefficient obtained for the Sibi decollement, and many other faults, is much lower than that obtained for most forms of intact rock (*Byerlee*, 1978). Faults therefore represent weak zones within a stronger substrate, explaining why strain localises on pre-existing faults and why fault reactivation is so prevalent (*Copley*, 2018). These faults also cannot maintain large stresses, supporting the idea that earthquake stress drops represent complete stress release (*Copley*, 2018).

5.6 Recommendations and Future work

5.6.1 Fully Exploiting InSAR Data

Sentinel-1

The launch of Sentinel-1 marked the start of a new era of satellite geodesy. Sentinel-1a and b can produce images over hundreds of kilometres wide with pixel resolution of 5 m by 20 m and a revisit time as small as six days in many tectonic regions. These data are open source, allowing anybody to access them and use them for free. These characteristics make Sentinel-1 ideally placed to study remote, inaccessible regions and increase the breadth of environments contributing to our understanding of the earthquake cycle.

Another advantage of Sentinel-1 is its acquisition mode: Terrain Observation by Progressive Scans (TOPS). Data are acquired as bursts in three parallel sub swaths, which are then combined to form a mosaicked image. Bursts are arranged in such a way that there is overlap between them in both the range and azimuth directions. In these overlap regions the ground is imaged at least twice, with different viewing geometries which allow measurements of surface deformation in multiple directions (*Grandin et al.*, 2016). When observations from both ascending and descending satellite tracks are combined, certain points on the ground are imaged from at least three different viewing directions (Figure 5.8). The deformation observed in each of these directions can be combined to give three dimensional displacements, similar to those obtained from a network of Global Navigation Satellite System (GNSS) receivers but without the need for deployment and servicing.

Despite the great benefits of the Sentinel-1, the satellite constellation has only been active since 2015 and therefore has not yet generated the long time series required to observe very slow tectonic motions in most regions. The short time span also means that the number of earthquake phenomena captured by Sentinel-1 is still relatively small. However, the short repeat time and open data policy mean that a large proportion of earthquakes which can be studied using Sentinel-1 have been.

ESA Archive

Previous ESA SAR satellites (ERS-1/2 and Envisat) have provided more sporadic surface deformation measurements between 1992 and 2010. Whilst these satellites have finished operations, the archive of SAR data is readily available. This archive can provide 18 years of InSAR data for studying earthquake cycle deformation and compliments the shorter, denser time series generated using Sentinel-1 images. Combining all these SAR datasets together would allow the construction of time series over 25 years long (e.g. chapter 4).

Much of the ESA SAR archive remains unused, despite the potential wealth of information contained within it. This is partly due to the fact that producing an InSAR

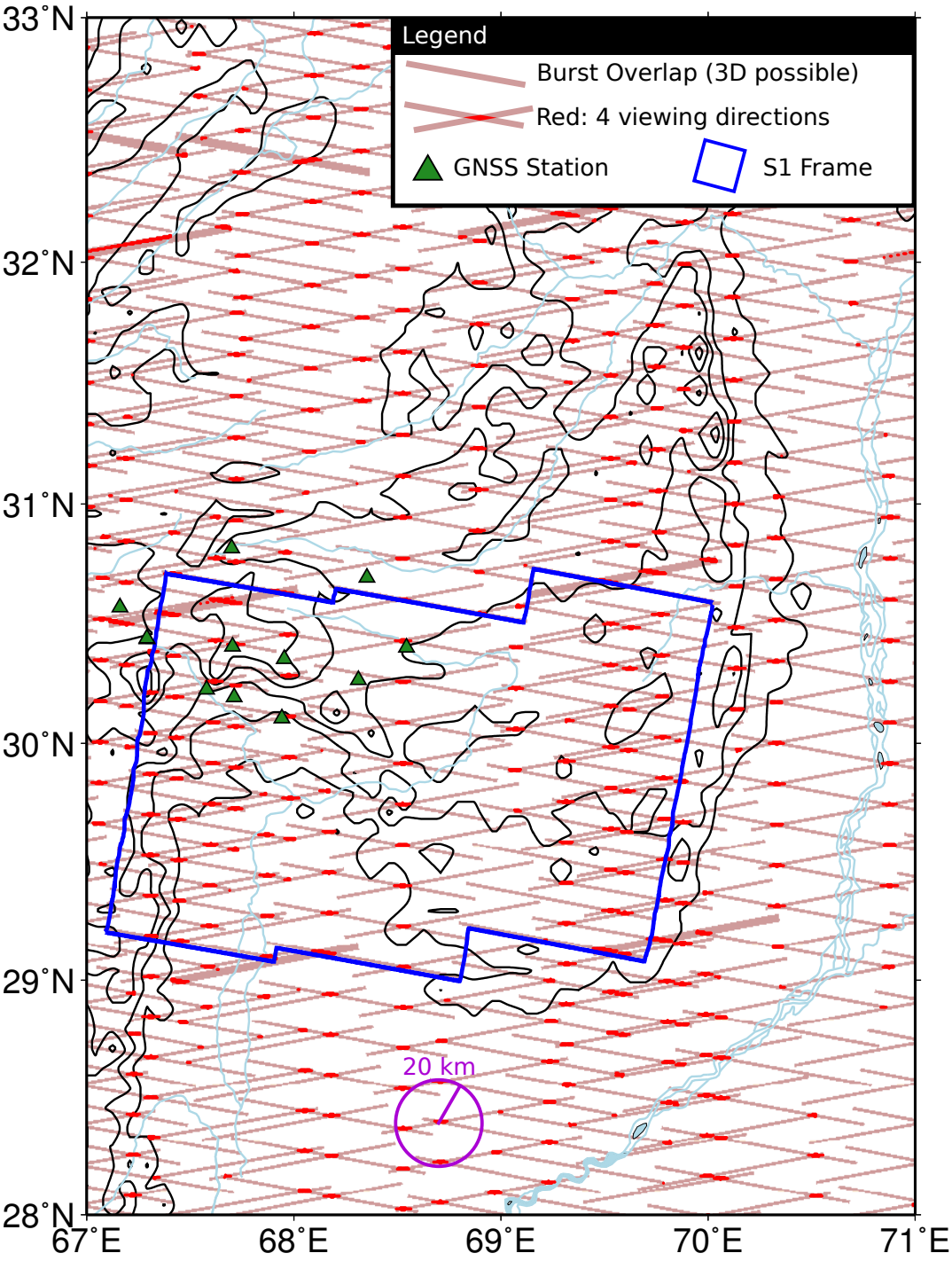

Figure 5.8: Map showing the locations where 3D displacements can be obtained using Sentinel-1 over the Sulaiman fold and thrust belt. Black contours show the topography of the belt. GNSS stations from the Global Strain Rate Model (*Kreemer et al.*, 2014) are shown as green triangles. The average distance between GNSS stations in densely instrumented Japan is shown using the purple circle.

time series is time consuming, requiring a number of intermediate steps. The archive could be more fully exploited by automating the processing required to transform SAR images into interferograms. This would allow more time to be spent interpreting the observations and likely lead to serendipitous discoveries.

The huge volume of data acquired by Sentinel-1 has necessitated the automation of SAR processing. The COMET group have developed an automatic InSAR processing system as part of the 'Looking Inside the Continents from Space' (LiCS) project. The processor (LiCSAR) is currently producing interferograms over the Alpine-Himalayan belt and providing the products to the community via a portal (`http://comet.nerc.ac.uk/COMET-LiCS-portal/`). Greater use of the ESA SAR archive could be facilitated by the development of an automated InSAR processor for these data. Many aspects of the LiCSAR processor could be translated for use in an ERS and Envisat automatic processor.

The opportunities provided by the Sentinel-1 TOPS acquisition mode are also not currently being regularly and fully exploited. Deformation measurements made in multiple viewing geometries could be automatically processed and combined to provide the full 3D deformation field at particular locations. These measurements could be generated as part of the LiCSAR processing chain and made available to the community. These points could be treated in a similar way to campaign GNSS stations and used to study earthquake displacements as well as long-term steady motion.

5.6.2 Dip Slip Faulting

Monitoring Continental Collision Zones

Continental collision zones, with their associated fold and thrust belts, present an excellent initial target for the greater exploitation of SAR data. The work presented in chapter 4 has shown the great potential for combining different generations of satellite data to study the earthquake cycle. This approach, combined with the 3D surface deformation measurements made with Sentinel-1, could be repeated for other fold and thrust belts around the world. These measurements can then be used to examine the various hazards posed by these deforming belts. Seismic hazard can be examined by seeing how various faults are moving through time; those which steadily creep perhaps pose less danger than those which are locked and accumulating elastic energy. Furthermore, these belts are regions of active uplift as folds grow and earthquakes occur. This uplift can produce unstable slopes, leading to landslides, which can be monitored using InSAR time series.

As well as monitoring of hazards, surface deformation time series can provide insights into the physical properties of faults and the crust. The 25 year long time series over the Sulaiman fold and thrust belt showed that sections of the belt are growing in a self-similar way, as expected by models of deformation which are analogous to a

bulldozer pushing sand up a ramp (*Dahlen*, 1990). Surface deformation measurements can also be used to infer the frictional properties of faults by seeing how they respond to stress changes in earthquakes, such as I have done in chapter 3.

Geometric Controls on the Earthquake Cycle

I have previously discussed the role of fault geometry in controlling various aspects of the seismic cycle. Future work could focus on this more, particularly investigating the role that fault intersections and changes in dip angle may contain the extent of coseismic rupture. Significant work has already been done on this in map view (e.g. *Biasi and Wesnousky*, 2016), but there has been little work on the role of geometry in controlling earthquake ruptures in cross section. *DeDontney and Hubbard* (2012) used dynamic rupture models in a fold and thrust belt with forces constrained by critical taper wedge mechanics. Similar studies could be carried out, exploring a wide variety of possible geometries. Such studies could use either numerical modelling (as in *DeDontney and Hubbard* (2012)) or through the use of analogue material modelling.

Furthermore, the postseismic response to earthquakes with different rupture geometries could be explored. Assuming a set of frictional properties, elastic properties and rupture properties, it is possible to simulate the expected afterslip on a rate strengthening fault. Different rupture scenarios could be tested where the angle between the coseismic fault and postseismic fault is varied, as well as other parameters of interest. Such work could inform a broader understanding of why certain fault systems show extensive postseismic afterslip whilst others do not. Such an understanding could help with seismic hazard analysis, particularly in understanding the potential evolving hazard following an earthquake.

Finally, all the case studies examined in this thesis have been in thrust faulting environments. Similar work could be carried out in normal faulting environments to establish the similarities and differences with the earthquake cycle at thrust faults.

5.7 Conclusions

In this thesis, I have presented measurements and models of the earthquake cycle at continental dip-slip faults. I have shown how InSAR can be used as a useful tool in tectonics research, but also that other measurements are necessary to add further constraints to our models. Interdisciplinary research teams, with experts in each kind of measurement, are often required to elucidate the most appropriate model that can satisfy a suite of measurements within error. I found that afterslip is pervasive: it has played a significant role in both case studies examined here and can explain the compilation of postseismic velocities presented in chapter 2. Such afterslip can be explained using rate-strengthening faults with values of $a\sigma$ between approximately 0.1 and 1.5 MPa. I have investigated the relationship between the earthquake cycle and

topography in a fold and thrust belt, finding a clear role for postseismic deformation in the development of short wavelength topography.

Despite the limitations of InSAR, the launch of satellites such as Sentinel-1 present a golden opportunity for tectonics research. Combining these measurements with the underused ESA archive of ERS and Envisat data can provide spatially dense, decadal time series in deforming areas. The development of automatic processing systems for the ESA archive and the full exploitation of 3D measurements from Sentinel-1 would open up a wealth of new geodetic observations of the earthquake cycle. Combining such measurements with observations from seismology, geology, topography and appropriate models could clarify the role of various earthquake parameters in controlling tectonic deformation.

References

Andrews, D. J. (1989), Mechanics of fault junctions, *Journal of Geophysical Research*, *94*(B7), 9389, doi:10.1029/JB094iB07p09389. 5.3.3

Barbot, S., Y. Fialko, and Y. Bock (2009), Postseismic deformation due to the M w 6.0 2004 Parkfield earthquake: Stress-driven creep on a fault with spatially variable rate-and-state friction parameters, *Journal of Geophysical Research*, *114*(B7), B07,405, doi:10.1029/2008JB005748. 5.1.2, 5.5.1

Biasi, G. P., and S. G. Wesnousky (2016), Steps and Gaps in Ground Ruptures: Empirical Bounds on Rupture Propagation, *Bulletin of the Seismological Society of America*, *106*(3), 1110–1124, doi:10.1785/0120150175. 5.6.2

Bonini, L., G. Toscani, and S. Seno (2014), Three-dimensional segmentation and different rupture behavior during the 2012 Emilia seismic sequence (Northern Italy), *Tectonophysics*, *630*, 33–42, doi:10.1016/j.tecto.2014.05.006. 5.3.3

Byerlee, J. (1978), Friction of rocks, *Pure and Applied Geophysics PAGEOPH*, *116*(4-5), 615–626, doi:10.1007/BF00876528. 5.5, 5.5.2

Carena, S., J. Suppe, and H. Kao (2002), Active detachment of Taiwan illuminated by small earthquakes and its control of first-order topography, *Geology*, *30*(10), 935, doi:10.1130/0091-7613(2002)030¡0935:ADOTIB¿2.0.CO;2. 5.5.2

Chang, S.-H., J.-P. Avouac, S. Barbot, and J.-C. Lee (2013), Spatially variable fault friction derived from dynamic modeling of aseismic afterslip due to the 2004 Parkfield earthquake, *Journal of Geophysical Research: Solid Earth*, *118*(7), 3431–3447, doi:10.1002/jgrb.50231. 5.5.1, 5.5.2

Copley, A. (2014), Postseismic afterslip 30 years after the 1978 Tabas-e-Golshan (Iran) earthquake: observations and implications for the geological evolution of thrust belts, *Geophysical Journal International*, *197*(2), 665–679, doi:10.1093/gji/ggu023. 5.1.3, 5.2, 5.4

Copley, A. (2018), The strength of earthquake-generating faults, *Journal of the Geological Society*, *175*(1), 1–12, doi:10.1144/jgs2017-037. 5.5.2

Copley, A., and R. Jolivet (2016), Fault rheology in an aseismic fold-thrust belt (Shahdad, eastern Iran), *Journal of Geophysical Research: Solid Earth*, *121*(1), 412–431, doi:10.1002/2015JB012431. 5.1.3, 5.4, 5.5.2

Copley, A., and K. Reynolds (2014), Imaging topographic growth by long-lived postseismic afterslip at Sefidabeh, east Iran, *Tectonics*, *33*(3), 330–345, doi:10.1002/2013TC003462. 5.1.3, 5.4

Cubas, N., J.-P. Avouac, P. Souloumiac, and Y. Leroy (2013), Megathrust friction determined from mechanical analysis of the forearc in the Maule earthquake area, *Earth and Planetary Science Letters*, *381*, 92–103, doi:10.1016/J.EPSL.2013.07.037. 5.5.2, 5.5.2

Dahlen, F. A. (1990), Critical Taper Model of Fold-And-Thrust Belts and Accretionary Wedges, *Annual Review of Earth and Planetary Sciences*, *18*(1), 55–99, doi:10.1146/annurev.ea.18.050190.000415. 5.5.2, 5.6.2

Dawson, J., and P. Tregoning (2007), Uncertainty analysis of earthquake source parameters determined from InSAR: A simulation study, *Journal of Geophysical Research*, *112*(B9), B09,406, doi:10.1029/2007JB005209. 5.2

DeDontney, N., and J. Hubbard (2012), Applying Wedge Theory to Dynamic Rupture Modeling of Fault Junctions, *Bulletin of the Seismological Society of America*, *102*(4), 1693–1711, doi:10.1785/0120110190. 5.6.2

Dieterich, J. H. (1979), Modeling of rock friction: 1. Experimental results and constitutive equations, *Journal of Geophysical Research*, *84*(B5), 2161, doi:10.1029/JB084iB05p02161. 5.5

Dublanchet, P., P. Bernard, and P. Favreau (2013), Interactions and triggering in a 3-D rate-and-state asperity model, *Journal of Geophysical Research: Solid Earth*, *118*(5), 2225–2245, doi:10.1002/jgrb.50187. 5.5.1

Elliott, J., A. Copley, R. Holley, K. Scharer, and B. Parsons (2013), The 2011 Mw 7.1 Van (Eastern Turkey) earthquake, *Journal of Geophysical Research: Solid Earth*, *118*(4), 1619–1637, doi:10.1002/jgrb.50117. 5.3.3

Elliott, J. R., B. Parsons, J. A. Jackson, X. Shan, R. A. Sloan, and R. T. Walker (2011), Depth segmentation of the seismogenic continental crust: The 2008 and 2009 Qaidam earthquakes, *Geophysical Research Letters*, *38*(6), n/a–n/a, doi:10.1029/2011GL046897. 5.3.3

Elliott, J. R., E. A. Bergman, A. C. Copley, A. R. Ghods, E. K. Nissen, B. Oveisi, M. Tatar, R. J. Walters, and F. Yamini-Fard (2015), The 2013 M_w 6.2 Khaki-Shonbe (Iran) Earthquake: Insights into seismic and aseismic shortening of the Zagros sedimentary cover, *Earth and Space Science*, *2*(11), 435–471, doi:10.1002/2015EA000098. 5.3.3

Fattahi, H., and F. Amelung (2015), InSAR bias and uncertainty due to the systematic and stochastic tropospheric delay, *Journal of Geophysical Research: Solid Earth*, *120*(12), 8758–8773, doi:10.1002/2015JB012419. 5.2

Feng, L., S. Barbot, E. M. Hill, I. Hermawan, P. Banerjee, and D. H. Natawidjaja (2016), Footprints of past earthquakes revealed in the afterslip of the 2010 M_w 7.8 Mentawai tsunami earthquake, *Geophysical Research Letters*, *43*(18), 9518–9526, doi:10.1002/2016GL069870. 5.1.2, 5.5.1

Fialko, Y. (2004), Evidence of fluid-filled upper crust from observations of postseismic deformation due to the 1992 M w 7.3 Landers earthquake, *Journal of Geophysical Research: Solid Earth*, *109*(B8), n/a–n/a, doi:10.1029/2004JB002985. 5.4

Fielding, E. J., T. J. Wright, J. Muller, B. E. Parsons, and R. Walker (2004), Aseismic deformation of a fold-and-thrust belt imaged by synthetic aperture radar interferometry near Shahdad, southeast Iran, *Geology*, *32*(7), 577, doi:10.1130/G20452.1. 5.1.3, 5.4

Fletcher, J. B., and A. McGarr (2006), Distribution of stress drop, stiffness, and fracture energy over earthquake rupture zones, *Journal of Geophysical Research: Solid Earth*, *111*(B3), n/a–n/a, doi:10.1029/2004JB003396. 5.5.1

Foreman-Mackey, D., D. W. Hogg, D. Lang, and J. Goodman (2013), emcee : The MCMC Hammer, *Publications of the Astronomical Society of the Pacific*, *125*(925), 306–312, doi:10.1086/670067. 5.5.2

Freed, A. M., R. Bürgmann, E. Calais, J. Freymueller, and S. Hreinsdóttir (2006), Implications of deformation following the 2002 Denali, Alaska, earthquake for postseismic relaxation processes and lithospheric rheology, *Journal of Geophysical Research*, *111*(B1), B01,401, doi:10.1029/2005JB003894. 5.4

Freed, A. M., R. Bürgmann, and T. Herring (2007), Far-reaching transient motions after Mojave earthquakes require broad mantle flow beneath a strong crust, *Geophysical Research Letters*, *34*(19), L19,302, doi:10.1029/2007GL030959. 5.4

Funning, G., and A. Garcia (2017), A systematic study of earthquake detectability using Sentinel-1 Interferometric Wide-Swath data, *EarthArXiv*, doi:10.31223/OSF.IO/9WG8S. 5.2

Gartrell, A., Y. Zhang, M. Lisk, and D. Dewhurst (2004), Fault intersections as critical hydrocarbon leakage zones: integrated field study and numerical modelling of an example from the Timor Sea, Australia, *Marine and Petroleum Geology*, *21*(9), 1165–1179, doi:10.1016/J.MARPETGEO.2004.08.001. 5.3.3

Goodman, J., and J. Weare (2010), Ensemble samplers with affine invariance, *Communications in Applied Mathematics and Computational Science*, *5*(1), 65–80, doi:10.2140/camcos.2010.5.65. 5.5.2

Grandin, R., M.-P. Doin, L. Bollinger, B. Pinel-Puyssegur, G. Ducret, R. Jolivet, S. N. Sapkota, S. H., C. J., H. B.-S., and H. P. (2012), Long-term growth of the Himalaya inferred from interseismic InSAR measurement, *Geology*, *40*(12), 1059–1062, doi:10.1130/G33154.1. 5.3.2

Grandin, R., E. Klein, M. Métois, and C. Vigny (2016), 3D displacement field of the 2015 M w 8.3 Illapel earthquake (Chile) from across- and along-track Sentinel-1 TOPS interferometry, *Geophysical Research Letters*, *43*(6), n/a–n/a, doi:10.1002/2016GL067954. 5.6.1

Gualandi, A., J.-P. Avouac, J. Galetzka, J. F. Genrich, G. Blewitt, L. Bijaya Adhikari, B. Prasad Koirala, R. Gupta, B. Nath Upreti, B. Pratt-Sitaula, and J. Liu-Zeng (2016), Pre-and post-seismic deformation related to the 2015, Mw 7.8 Gorkha earthquake, Nepal, *Tectonophysics*, doi:10.1016/j.tecto.2016.06.014. 5.1.2

Hodges, K. V., C. Wobus, K. Ruhl, T. Schildgen, and K. Whipple (2004), Quaternary deformation, river steepening, and heavy precipitation at the front of the Higher Himalayan ranges, *Earth and Planetary Science Letters*, *220*(3-4), 379–389, doi:10.1016/S0012-821X(04)00063-9. 5.3.2

Hou, F., J. Goodman, D. W. Hogg, J. Weare, and C. Schwab (2012), An Affine-Invariant Sampler for Exoplanet Fitting and Discovery in Radial Velocity Data, *The Astrophysical Journal*, *745*(2), 198, doi:10.1088/0004-637X/745/2/198. 5.5.2

Hubbard, J., J. H. Shaw, and Y. Klinger (2010), Structural Setting of the 2008 Mw 7.9 Wenchuan, China, Earthquake, *Bulletin of the Seismological Society of America*, *100*(5B), 2713–2735, doi:10.1785/0120090341. 5.5.2, 5.5.2

Hubbard, J., S. Barbot, E. M. Hill, and P. Tapponnier (2015), Coseismic slip on shallow décollement megathrusts: implications for seismic and tsunami hazard, *Earth-Science Reviews*, *141*, 45–55, doi:10.1016/J.EARSCIREV.2014.11.003. 5.5.2

Hubbard, J., R. Almeida, A. Foster, S. N. Sapkota, P. Bürgi, and P. Tapponnier (2016), Structural segmentation controlled the 2015 M_w 7.8 Gorkha earthquake rupture in Nepal, *Geology*, *44*(8), 639–642, doi:10.1130/G38077.1. 5.3.1, 5.3.2, 5.3.3

Hubbert, M. K., and W. W. Rubey (1959), Role of fluid pressure in mechanics of overthrust faulting, *GSA Bulletin*, *70*(2), 115–166, doi:10.1130/0016-7606(1959)70[115:rofpim]2.0.co;2. 5.5.2

Hussain, E., T. J. Wright, R. J. Walters, D. Bekaert, A. Hooper, and G. A. Houseman (2016), Geodetic observations of postseismic creep in the decade after the 1999 Izmit earthquake, Turkey: Implications for a shallow slip deficit, *Journal of Geophysical Research: Solid Earth*, *121*(4), 2980–3001, doi:10.1002/2015JB012737. 5.2, 5.5.2

Hussain, E., T. J. Wright, R. J. Walters, D. P. S. Bekaert, R. Lloyd, and A. Hooper (2018), Constant strain accumulation rate between major earthquakes on the North Anatolian Fault, *Nature Communications*, *9*(1), 1392, doi:10.1038/s41467-018-03739-2. 5.4

Ikari, M. J., C. Marone, and D. M. Saffer (2011), On the relation between fault strength and frictional stability, *Geology*, *39*(1), 83–86, doi:10.1130/G31416.1. 5.5.2

Ingleby, T., and T. J. Wright (2017), Omori-like decay of postseismic velocities following continental earthquakes, *Geophysical Research Letters*, *44*(7), 3119–3130, doi:10.1002/2017GL072865. 5.3

Jiang, Z., L. Yuan, D. Huang, Z. Yang, and A. Hassan (2018), Postseismic deformation associated with the 2015 Mw 7.8 Gorkha earthquake, Nepal: investigating ongoing afterslip and constraining crustal rheology, *Journal of Asian Earth Sciences*, doi:10.1016/J.JSEAES.2017.12.039. 5.1.2

Jónsson, S., P. Segall, R. Pedersen, and G. Björnsson (2003), Post-earthquake ground movements correlated to pore-pressure transients, *Nature*, *424*(6945), 179–183, doi:10.1038/nature01776. 5.4

Kaneko, Y., J.-P. Avouac, and N. Lapusta (2010), Towards inferring earthquake patterns from geodetic observations of interseismic coupling, *Nature Geoscience*, *3*(5), 363–369, doi:10.1038/ngeo843. 5.5.1

Kohli, A. H., and M. D. Zoback (2013), Frictional properties of shale reservoir rocks, *Journal of Geophysical Research: Solid Earth*, *118*(9), 5109–5125, doi:10.1002/jgrb.50346. 5.3.3, 5.5.2

Kreemer, C., G. Blewitt, and E. C. Klein (2014), A geodetic plate motion and Global Strain Rate Model, *Geochemistry, Geophysics, Geosystems*, *15*(10), 3849–3889, doi:10.1002/2014GC005407. 5.8

Lavé, J., and J. P. Avouac (2001), Fluvial incision and tectonic uplift across the Himalayas of central Nepal, *Journal of Geophysical Research: Solid Earth*, *106*(B11), 26,561–26,591, doi:10.1029/2001JB000359. 5.3.2

Lindsey, E. O., R. Almeida, R. Mallick, J. Hubbard, K. Bradley, L. L. H. Tsang, Y. Liu, R. Burgmann, and E. M. Hill (2018), Structural Control on Downdip Locking Extent of the Himalayan Megathrust, *Journal of Geophysical Research: Solid Earth*, *123*(6), 5265–5278, doi:10.1029/2018JB015868. 5.3.2

Marone, C. (1998), Laboratory-derived friction laws and their application to seismic faulting, *Annual Review of Earth and Planetary Sciences*, *26*, 643–696. 5.5, 5.5.1

Marone, C. J., C. H. Scholtz, and R. Bilham (1991), On the mechanics of earthquake afterslip, *Journal of Geophysical Research*, *96*(B5), 8441, doi:10.1029/91JB00275. 5.5.1

Mencin, D., R. Bendick, B. N. Upreti, D. P. Adhikari, A. Gajurel, R. R. Bhattarai, H. R. Shrestha, T. N. Bhattarai, N. Manandhar, J. Galetzka, E. Knappe, B. Pratt-Sitaula, A. Aoudia, and R. Bilham (2016), Himalayan strain reservoir inferred from limited afterslip following the Gorkha earthquake, *Nature Geoscience*, *9*(7), 533–537, doi:10.1038/ngeo2734. 5.1.2

Montési, L. G. J. (2004), Controls of shear zone rheology and tectonic loading on postseismic creep, *Journal of Geophysical Research*, *109*(B10), B10,404, doi:10.1029/2003JB002925. 5.3.1

Mosegaard, K., and A. Tarantola (1995), Monte Carlo sampling of solutions to inverse problems, *Journal of Geophysical Research: Solid Earth*, *100*(B7), 12,431–12,447, doi:10.1029/94JB03097. 5.5.1

Nishimura, T., M. Tobita, H. Yarai, T. Amagai, M. Fujiwara, H. Une, and M. Koarai (2008), Episodic growth of fault-related fold in northern Japan observed by SAR interferometry, *Geophysical Research Letters*, *35*(13), L13,301, doi:10.1029/2008GL034337. 5.1.3, 5.4

Nissen, E., J. R. Elliott, R. A. Sloan, T. J. Craig, G. J. Funning, A. Hutko, B. E. Parsons, and T. J. Wright (2016), Limitations of rupture forecasting exposed by instantaneously triggered earthquake doublet, *Nature Geoscience 2016 9:4*, *9*(4), 330, doi:10.1038/ngeo2653. 5.3.3, 5.4, 5.5.2

Noda, H., and N. Lapusta (2013), Stable creeping fault segments can become destructive as a result of dynamic weakening, *Nature*, *493*(7433), 518–521, doi:10.1038/nature11703. 5.5.1

Pandey, M. R., R. P. Tandukar, J. P. Avouac, J. Lavé, and J. P. Massot (1995), Interseismic strain accumulation on the Himalayan crustal ramp (Nepal), *Geophysical Research Letters*, *22*(7), 751–754, doi:10.1029/94GL02971. 5.3.2

Perfettini, H., and J.-P. Avouac (2004), Postseismic relaxation driven by brittle creep: A possible mechanism to reconcile geodetic measurements and the decay rate of aftershocks, application to the Chi-Chi earthquake, Taiwan, *Journal of Geophysical Research*, *109*(B2), B02,304, doi:10.1029/2003JB002488. 5.5.1, 5.5

Qi, W., Q. Xuejun, L. Qigui, J. Freymueller, Y. Shaomin, X. Caijun, Y. Yonglin, Y. Xinzhao, T. Kai, and C. Gang (2011), Rupture of deep faults in the 2008 Wenchuan earthquake and uplift of the Longmen Shan, *Nature Geoscience*, *4*(9), 634–640, doi:10.1038/ngeo1210. 5.3.3

Reynolds, K., A. Copley, and E. Hussain (2015), Evolution and dynamics of a fold-thrust belt: the Sulaiman Range of Pakistan, *Geophysical Journal International*, *201*(2), 683–710, doi:10.1093/gji/ggv005. 5.3.3, 5.5.2

Rolandone, F., J.-M. Nocquet, P. A. Mothes, P. Jarrin, M. Vallée, N. Cubas, S. Hernandez, M. Plain, S. Vaca, and Y. Font (2018), Areas prone to slow slip events impede earthquake rupture propagation and promote afterslip, *Science Advances*, *4*(1), eaao6596, doi:10.1126/sciadv.aao6596. 5.5.1

Rollins, C., S. Barbot, and J.-P. Avouac (2015), Postseismic Deformation Following the 2010 M = 7.2 El Mayor-Cucapah Earthquake: Observations, Kinematic Inversions, and Dynamic Models, *Pure and Applied Geophysics*, doi:10.1007/s00024-014-1005-6. 5.5.1

Rousset, B., S. Barbot, J.-P. Avouac, and Y.-J. Hsu (2012), Postseismic deformation following the 1999 Chi-Chi earthquake, Taiwan: Implication for lower-crust rheology, *Journal of Geophysical Research: Solid Earth*, *117*(B12), n/a–n/a, doi:10.1029/2012JB009571. 5.1.2

Ruina, A. (1983), Slip instability and state variable friction laws, *Journal of Geophysical Research*, *88*(B12), 10,359, doi:10.1029/JB088iB12p10359. 5.5

Ryder, I., H. Wang, L. Bie, and A. Rietbrock (2014), Geodetic imaging of late postseismic lower crustal flow in Tibet, *Earth and Planetary Science Letters*, *404*, 136–143, doi:10.1016/j.epsl.2014.07.026. 5.2

Sreejith, K. M., P. S. Sunil, R. Agrawal, A. P. Saji, D. S. Ramesh, and A. S. Rajawat (2016), Coseismic and early postseismic deformation due to the 25 April 2015, M_w 7.8 Gorkha, Nepal, earthquake from InSAR and GPS measurements, *Geophysical Research Letters*, *43*(7), 3160–3168, doi:10.1002/2016GL067907. 5.1.2

Steer, P., A. Bigot, R. Cattin, and R. Soliva (2011), In-situ characterization of the effective elasticity of a fault zone, and its relationship to fracture spacing, *Journal of Structural Geology*, *33*, 1541–1553, doi:10.1016/j.jsg.2011.09.009. 5.5.1

Suppe, J. (2007), Absolute fault and crustal strength from wedge tapers, *Geology*, *35*(12), 1127, doi:10.1130/G24053A.1. 5.5.2

Taylor, M., and A. Yin (2009), Active structures of the Himalayan-Tibetan orogen and their relationships to earthquake distribution, contemporary strain field, and Cenozoic volcanism, *Geosphere*, *5*(3), 199–214, doi:10.1130/GES00217.1. 5.2

van den Ende, M., J. Chen, J.-P. Ampuero, and A. Niemeijer (2018), A comparison between rate-and-state friction and microphysical models, based on numerical simulations of fault slip, *Tectonophysics*, *733*, 273–295, doi:10.1016/J.TECTO.2017.11.040. 5.5.1

von Hagke, C., O. Oncken, and S. Evseev (2014), Critical taper analysis reveals lithological control of variations in detachment strength: An analysis of the Alpine basal detachment (Swiss Alps), *Geochemistry, Geophysics, Geosystems*, *15*(1), 176–191, doi:10.1002/2013GC005018. 5.5.2

Wang, K., and Y. Fialko (2018), Observations and Modeling of Coseismic and Postseismic Deformation Due To the 2015 M_w 7.8 Gorkha (Nepal) Earthquake, *Journal of Geophysical Research: Solid Earth*, doi:10.1002/2017JB014620. 5.1.2

Weng, H., and H. Yang (2017), Seismogenic width controls aspect ratios of earthquake ruptures, *Geophysical Research Letters*, *44*(6), 2725–2732, doi:10.1002/2016GL072168. 5.3.3

Wimpenny, S., A. Copley, and T. Ingleby (2017), Fault mechanics and post-seismic deformation at Bam, SE Iran, *Geophysical Journal International*, *209*(2), 1018–1035, doi:10.1093/gji/ggx065. 5.1.3, 5.4, 5.5.1

Wobus, C., A. Heimsath, K. Whipple, and K. Hodges (2005), Active out-of-sequence thrust faulting in the central Nepalese Himalaya, *Nature*, *434*(7036), 1008–1011, doi:10.1038/nature03499. 5.3.2

Zhao, B., R. Bürgmann, D. Wang, K. Tan, R. Du, and R. Zhang (2017), Dominant Controls of Downdip Afterslip and Viscous Relaxation on the Postseismic Displacements Following the M_w 7.9 Gorkha, Nepal, Earthquake, *Journal of Geophysical Research: Solid Earth*, *122*(10), 8376–8401, doi:10.1002/2017JB014366. 5.1.2

Zhou, Y., M. Y. Thomas, B. Parsons, and R. T. Walker (2018), Time-dependent postseismic slip following the 1978 Mw 7.3 Tabas-e-Golshan, Iran earthquake revealed by over 20 years of ESA InSAR observations, *Earth and Planetary Science Letters*, *483*, 64–75, doi:10.1016/J.EPSL.2017.12.005. 5.4, 5.5.1

Appendix A

Supplementary material for Chapter 2

The supporting information includes Figures A.1 and A.2 and the data tables (Tables A.1 - A.4) which contain all the data used in this study. A full table with all of the results in can be found online, as an Excel file, within the supplementary information (`https://agupubs.onlinelibrary.wiley.com/doi/abs/10.1002/2017GL072865`).

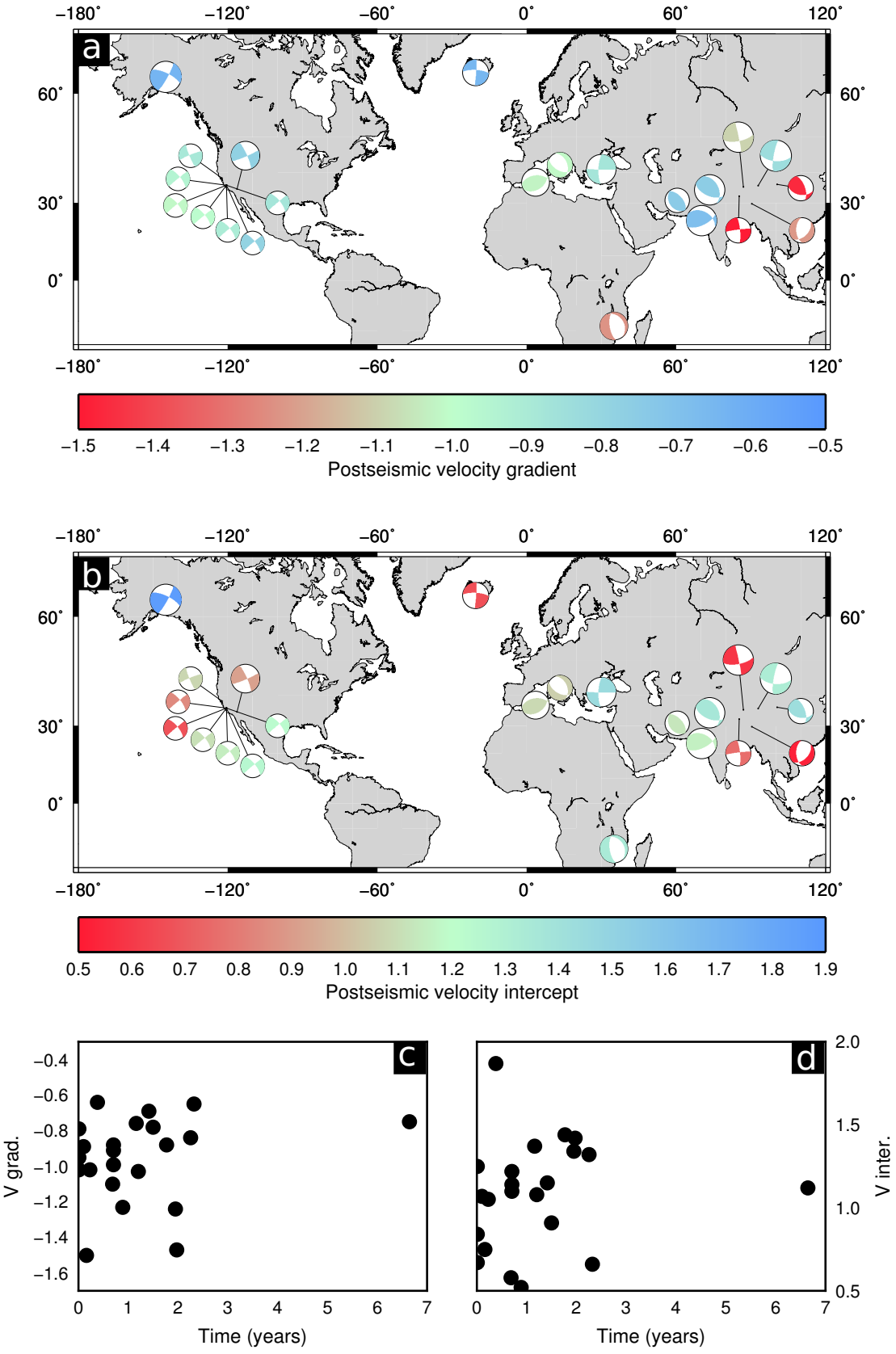

Figure A.1: a) Map showing the locations of earthquakes used in our compilation. Focal mechanism is representative of the dominant earthquake mechanism (strike-slip, normal or thrust). Symbol size is representative of earthquake magnitude and the colour corresponds to the best-fit postseismic velocity gradient for each individual earthquake where postseismic velocities are available from at least three time periods. b) Same as a) but with colour determined by the best-fit value of log(postseismic velocity) at log(t) = 0 (i.e. the intercept of the best-fit line). c) Velocity gradient values (as in a) plotted against the mid-point of the observation period (in years). d) Velocity intercept values (as in b) plotted against the mid-point of the observation period (in years).

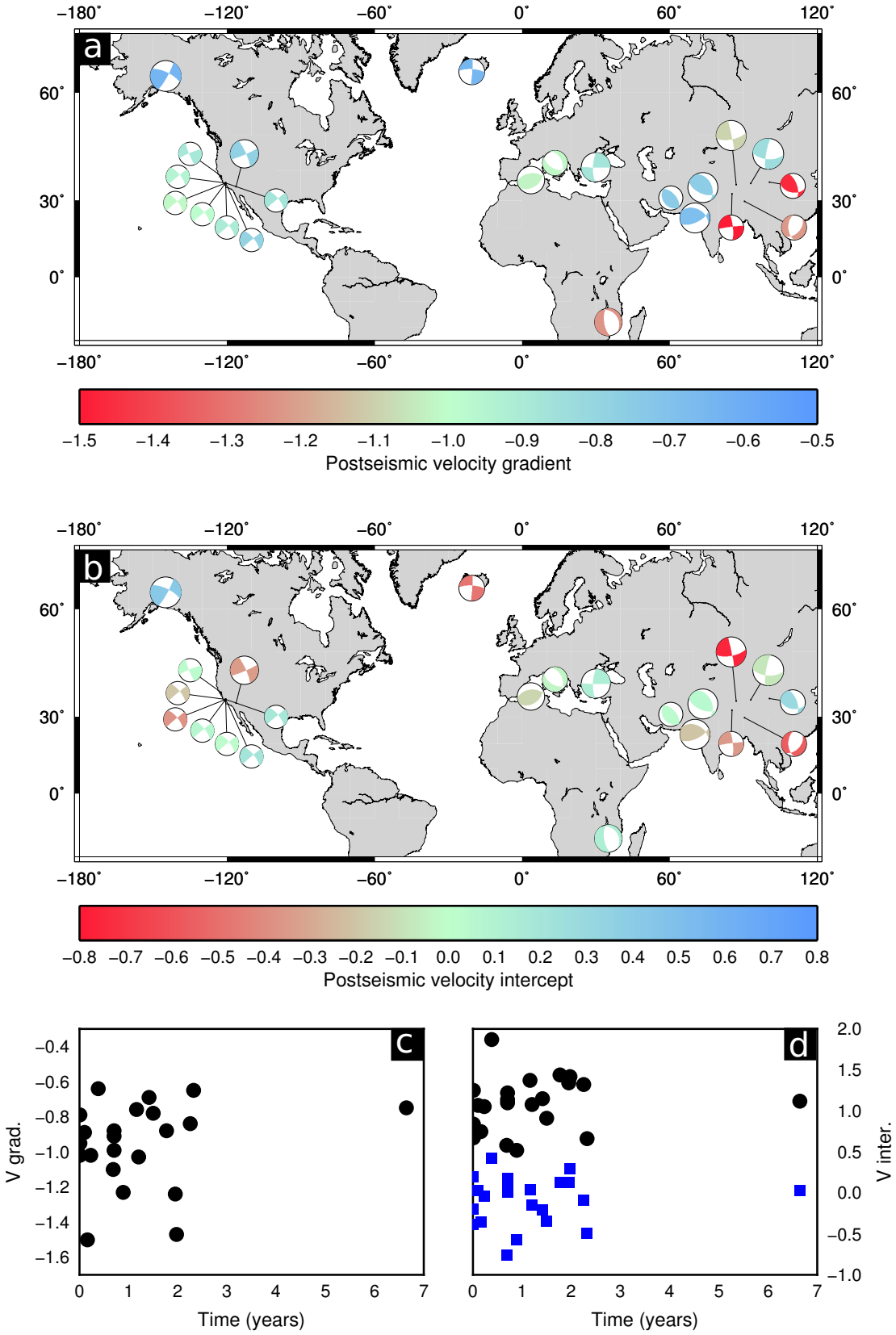

Figure A.2: Same as Figure A.1, except using linear fits to each individual earthquake after the normalisation described in section 2.3.1. This did not change the gradients, but the intercepts now cluster around 0 (blue dots).

Earthquake	Date	Type	Mw	D	EQ Lat	EQ Lon	Tech	Sig Lon	Sig Lat	ID	PD	Mech	t1 (yr)	t2 (yr)	t	d1 (mm)	d2 (mm)	V (mm/yr)	log(t)	log(v)	Reference
Athens	07/09/1999	N	5.9	15	37.87	23.64	I	23.6	38.5	-	5	A	0.04	2.53	1.29	0.00	30.00	12.05	0.11	1.08	Atzori et al (2008)
Damxung	06/10/2008	N	6.3	12	29.66	90.50	I	90.4	29.7	-	1.5	A	0.08	0.25	0.16	1.25	5.20	23.09	-0.79	1.36	Bie et al (2013)
Damxung	06/10/2008	N	6.3	12	29.66	90.50	I	90.4	29.7	-	1.5	A	0.08	0.73	0.40	5.20	10.18	7.65	-0.40	0.88	Bie et al (2013)
Damxung	06/10/2008	N	6.3	12	29.66	90.50	I	90.4	29.7	-	1.5	A	0.08	1.11	0.59	10.18	12.68	2.42	-0.23	0.38	Bie et al (2013)
Damxung	06/10/2008	N	6.3	12	29.66	90.50	I	90.4	29.7	-	1.5	A	0.08	1.40	0.74	12.68	13.75	0.81	-0.13	-0.09	Bie et al (2013)
Damxung	06/10/2008	N	6.3	12	29.66	90.50	I	90.4	29.7	-	1.5	A	0.08	1.88	0.98	13.75	14.11	0.20	-0.01	-0.70	Bie et al (2013)
Fucino	03/01/1915	N	6.7	-	-	-	L	13.83	42.17	Popoli	40	VR	35.00	85.00	60.00	0.00	80.00	1.60	1.78	0.20	Amoruso et al (2005)
Hebgen Lake	17/08/1959	N	7.3	-	-	-	L	-111.1	44.65	West Yellowstone	20	VR	0.00	1.00	0.50	0.00	150.00	150.00	-0.30	2.18	Reilinger (1986)
Hebgen Lake	17/08/1959	N	7.3	-	-	-	L	-111.1	44.65	West Yellowstone	20	VR	1.00	24.00	12.50	0.00	240.00	10.43	1.10	1.02	Reilinger (1986)
Hebgen Lake	17/08/1959	N	7.3	-	-	-	L	-111.1	44.65	West Yellowstone	20	A,VR	0.20	28.00	14.10	0.00	280.00	10.07	1.15	1.00	Nishimura & Thatcher (2003)
Irpinia	23/11/1980	N	6.9	13.7	40.82	15.39	L	15.25	40.76	-	3	VR	0.50	4.50	2.50	0.00	30.00	7.50	0.40	0.88	Dalla Via et al (2005)
L'Aquila	06/04/2009	N	6.3	12	42.29	13.35	I,CG	13.43	42.39	-	0.75	A	0.02	0.15	0.08	0.00	18.00	136.88	-1.09	2.14	D'Agostino et al (2012)
L'Aquila	06/04/2009	N	6.3	12	42.29	13.35	I,CG	13.43	42.39	-	0.75	A	0.02	0.28	0.15	18.00	26.00	30.42	-0.83	1.48	D'Agostino et al (2012)
L'Aquila	06/04/2009	N	6.3	12	42.29	13.35	I,CG	13.43	42.39	-	0.75	A	0.02	0.50	0.26	26.00	32.00	12.44	-0.59	1.09	D'Agostino et al (2012)
Mozambique	22/02/2006	N	7	12	-21.20	33.33	I	33.36	-21.26	-	0	A	0.20	0.30	0.25	0.00	10.00	104.29	-0.60	2.02	Copley et al (2012)
Mozambique	22/02/2006	N	7	12	-21.20	33.33	I	33.36	-21.26	-	0	A	0.84	2.86	1.85	0.00	35.00	17.36	0.27	1.24	Copley et al (2012)
Mozambique	22/02/2006	N	7	12	-21.20	33.33	I	33.36	-21.26	-	0	A	0.84	4.62	2.73	35.00	40.00	1.32	0.44	0.12	Copley et al (2012)
Nima-Gaize	09/01/2008	N	6.4	12.65	32.30	85.32	I	85.29	32.46	-	0	A	0.02	0.15	0.08	0.00	30.00	238.14	-1.09	2.38	Ryder et al (2010)
Nima-Gaize	09/01/2008	N	6.4	12.65	32.30	85.32	I	85.29	32.46	-	0	A	0.10	0.30	0.20	0.00	13.00	67.79	-0.70	1.83	Ryder et al (2010)
Nima-Gaize	09/01/2008	N	6.4	12.65	32.30	85.32	I	85.29	32.46	-	0	A	0.06	0.35	0.21	0.00	16.00	55.62	-0.68	1.75	Ryder et al (2010)
Umbria-Marche sequence	26/09/1997	N	6	15	43.01	12.86	G	12.89	42.97	POPO	0.5	A,VR	3.00	4.00	3.50	0.00	7.78	7.78	0.54	0.89	Riva et al (2007)
Umbria-Marche sequence	26/09/1997	N	6	15	43.01	12.86	G	12.89	42.97	POPO	0.5	A,VR	4.00	5.67	4.83	0.00	9.44	5.66	0.68	0.75	Riva et al (2007)

Table A.1: Table containing all normal faulting data used in chapter 2. Modified from the Excel spreadsheet available in the online supplement for space reasons. Table contains: earthquake name; date of earthquake; primary focal mechanism (strike-slip (SS), normal (N), thrust (T) or a variety (V)); moment magnitude; Harvard CMT depth; CMT latitude; CMT longitude; the observation technique(s) used: InSAR (I), GNSS (G), continuous GNSS (CG), levelling (L); signal longitude; signal latitude; GNSS station/benchmark ID; the perpendicular distance between the surface fault trace and the observation location; the postseismic deformation mechanism(s) inferred by the study referenced: afterslip (A), viscoelastic relaxation (VR), poroelastic rebound (P); the observation window start time (years since earthquake); observation window end time; the mid-point of the observation time window; initial displacement; final displacements (if displacements rather than velocities are given); observed velocities (either directly, or from piecewise fit); log(time in years); log(velocity in mm/yr); reference for data. Study references can be found in the references of chapter 2.

Earthquake	Date	Type	Mw	D	EQ Lat	EQ Lon	Tech	Sig Lon	Sig Lat	ID	PD	Mech	t1 (yr)	t2 (yr)	t	d1 (mm)	d2 (mm)	V (mm/yr)	log(t)	log(v)	Reference
Bhuj	26/01/2001	T	7.6	19.8	23.63	70.24	G	70.16	23.32	DHAM	13	A,VR	0.09	0.33	0.21			54.00	-0.68	1.73	Reddy et al (2012)
Bhuj	26/01/2001	T	7.6	19.8	23.63	70.24	G	69.9	23.38	LODA	13	A,VR	0.33	0.80	0.57			17.00	-0.25	1.23	Reddy et al (2012)
Bhuj	26/01/2001	T	7.6	19.8	23.63	70.24	G	70.16	23.32	DHAM	13	A,VR	0.80	1.13	0.97			12.50	-0.02	1.10	Reddy et al (2012)
Bhuj	26/01/2001	T	7.6	19.8	23.63	70.24	G	70.16	23.32	DHAM	13	A,VR	1.13	1.75	1.44			10.00	0.16	1.00	Reddy et al (2012)
Bhuj	26/01/2001	T	7.6	19.8	23.63	70.24	G	70.16	23.32	DHAM	13	A,VR	1.75	6.03	3.89			7.00	0.59	0.85	Reddy et al (2012)
Chi-Chi	21/09/1999	T	7.6	33	24.12	120.71	G	120.75	23.89	AF30	7.5	A	0.00	0.27	0.13	0.00	142.00	534.33	-0.88	2.73	Hsu et al (2002)
Chi-Chi	21/09/1999	T	7.6	33	24.12	120.71	G	120.78	23.78	I007	10	A	0.00	0.55	0.27	0.00	200.00	365.00	-0.56	2.56	Perfettini & Avouac (2004)
El Asnam	10/10/1980	T	7.1	10.1	36.25	1.36	L	1.825	35.37	-	3	A	6.00	11.00	8.50			17.00	0.93	1.23	Lammali et al (1997)
Gonghe	26/04/1990	T	6.4	15	36.25	100.57	L	100.33	36.06	DH19	8	A,VR	0.18	1.18	0.68	0.00	54.00	54.00	-0.17	1.73	Hao et al (2012)
Gonghe	26/04/1990	T	6.4	15	36.25	100.57	L	100.33	36.06	DH19	8	A,VR	1.18	2.50	1.84	0.00	10.00	7.58	0.26	0.88	Hao et al (2012)
Gonghe	26/04/1990	T	6.4	15	36.25	100.57	L	100.33	36.06	DH19	8	A,VR	2.50	4.30	3.40	0.00	10.00	5.56	0.53	0.74	Hao et al (2012)
Northridge	17/01/1994	T	6.7	16.8	34.44	-118.64	G	-118.34	34.29	-	13	VR	0.00	2.90	1.45	0.00	37.00	12.76	0.16	1.11	Deng et al (1999)
Pakistan	08/10/2005	T	7.6	12	34.38	73.47	G	73.48	34.33	PS13	8	A	0.08	0.83	0.46	0.00	30.70	40.93	-0.34	1.61	Jouanne et al (2011)
Pakistan	08/10/2005	T	7.6	12	34.38	73.47	G	73.48	34.33	PS13	8	A	0.25	0.83	0.54	0.00	27.05	46.37	-0.27	1.67	Jouanne et al (2011)
Pakistan	08/10/2005	T	7.6	12	34.38	73.47	G	73.48	34.33	PS13	8	A	0.08	1.42	0.75	0.00	37.79	28.34	-0.12	1.45	Jouanne et al (2011)
Pakistan	08/10/2005	T	7.6	12	34.38	73.47	G	73.48	34.33	PS13	8	A	0.25	1.42	0.83	0.00	34.20	29.31	-0.08	1.47	Jouanne et al (2011)
Pakistan	08/10/2005	T	7.6	12	34.38	73.47	G	73.48	34.33	PS13	8	A	0.83	1.42	1.13	0.00	6.66	11.42	0.05	1.06	Jouanne et al (2011)
Pakistan	08/10/2005	T	7.6	12	34.38	73.47	G	73.48	34.33	PS13	8	A	1.42	2.17	1.79	0.00	18.31	24.42	0.25	1.39	Jouanne et al (2011)
Pakistan	08/10/2005	T	7.6	12	34.38	73.47	G	73.48	34.33	PS13	8	A	1.42	3.83	2.63	0.00	24.42	10.11	0.42	1.00	Jouanne et al (2011)
Racha	29/04/1991	T	6.9	22.3	42.60	43.61	G	43.4	42.58	KHUR	19	A	0.23	3.44	1.84	0.00	21.00	6.54	0.26	0.82	Podgorski et al (2007)
Racha	29/04/1991	T	6.9	22.3	42.60	43.61	G	43.4	42.58	KHUR	19	A	3.44	5.41	4.43	0.00	7.90	4.01	0.65	0.60	Podgorski et al (2007)
Sefidabeh	01/02/1994	T	6.2	15	30.83	60.50	I	60.55	30.89	-	0.5	A	2.16	4.56	3.36	0.00	13.00	5.42	0.53	0.73	Copley & Reynolds (2014)
Sefidabeh	01/02/1994	T	6.2	15	30.83	60.50	I	60.55	30.89	-	0.5	A	2.25	5.33	3.79	0.00	11.00	3.58	0.58	0.55	Copley & Reynolds (2014)
Sefidabeh	01/02/1994	T	6.2	15	30.83	60.50	I	60.55	30.89	-	0.5	A	2.16	5.42	3.79	0.00	18.60	5.71	0.58	0.76	Copley & Reynolds (2014)
Sefidabeh	01/02/1994	T	6.2	15	30.83	60.50	I	60.55	30.89	-	0.5	A	2.26	5.33	3.79	0.00	12.90	4.20	0.58	0.62	Copley & Reynolds (2014)
Sefidabeh	01/02/1994	T	6.2	15	30.83	60.50	I	60.55	30.89	-	0.5	A	4.56	5.42	4.99	0.00	4.60	5.33	0.70	0.73	Copley & Reynolds (2014)
Sefidabeh	01/02/1994	T	6.2	15	30.83	60.50	I	60.55	30.89	-	0.5	A	2.25	10.70	6.48	0.00	27.90	3.31	0.81	0.52	Copley & Reynolds (2014)
Sefidabeh	01/02/1994	T	6.2	15	30.83	60.50	I	60.55	30.89	-	0.5	A	2.26	10.70	6.48	0.00	28.90	3.42	0.81	0.53	Copley & Reynolds (2014)
Sefidabeh	01/02/1994	T	6.2	15	30.83	60.50	I	60.55	30.89	-	0.5	A	5.33	10.70	8.01	0.00	13.60	2.53	0.90	0.40	Copley & Reynolds (2014)
Sefidabeh	01/02/1994	T	6.2	15	30.83	60.50	I	60.55	30.89	-	0.5	A	9.83	15.49	12.66	0.00	9.30	1.64	1.10	0.22	Copley & Reynolds (2014)
Sefidabeh	01/02/1994	T	6.2	15	30.83	60.50	I	60.55	30.89	-	0.5	A	9.83	16.55	13.19	0.00	14.30	2.13	1.12	0.33	Copley & Reynolds (2014)
Tabas-e-Golshan	16/09/1978	T	7.3	11	33.37	57.02	I	56.97	33.37	-	0.5	A	17.67	20.69	19.18			2.00	1.28	0.30	Copley (2014)
Tabas-e-Golshan	16/09/1978	T	7.3	11	33.37	57.02	I	56.97	33.37	-	0.5	A	24.52	31.33	27.93			1.70	1.45	0.23	Copley (2014)
Van	23/10/2011	T	7.2	12	38.64	43.40	I	43.44	38.61	-	1.3	A	0.00	0.01	0.00	0.00	60.00	7904.88	-2.35	3.90	Feng et al (2014)
Van	23/10/2011	T	7.2	12	38.64	43.40	I	43.44	38.61	-	1.3	A	0.01	0.14	0.08	0.00	21.00	156.43	-1.12	2.19	Feng et al (2014)
Van	23/10/2011	T	7.2	12	38.64	43.40	G	43.37	38.61	VN02	0.8	A	0.10	1.58	0.84	0.00	256.25	173.85	-0.08	2.24	Dogan et al (2014)
Zemmouri	21/05/2003	T	6.9	15	36.93	3.58	G	3.55	36.79	SFNP	9	A	0.01	0.60	0.31	0.00	21.85	37.09	-0.51	1.57	Mahsas et al (2008)
Zemmouri	21/05/2003	T	6.9	15	36.93	3.58	G	3.55	36.79	SFNP	9	A	0.61	1.19	0.90	0.00	8.85	15.02	-0.05	1.18	Mahsas et al (2008)
Zemmouri	21/05/2003	T	6.9	15	36.93	3.58	G	3.55	36.79	SFNP	9	A	1.20	1.79	1.49	0.00	5.38	9.09	0.17	0.96	Mahsas et al (2008)
Zemmouri	21/05/2003	T	6.9	15	36.93	3.58	G	3.55	36.79	SFNP	9	A	1.79	2.37	2.08	0.00	2.69	4.65	0.32	0.67	Mahsas et al (2008)
Zemmouri	21/05/2003	T	6.8	15	36.93	3.58	I ,CG	3.47	36.76	-	6	A	0.14	7.33	3.74			3.50	0.57	0.54	Cetin et al (2012)
CNSB	-	V	V	-	-	-	I,CG	-117.5	40.4	-	0	VR	37.63	45.75	41.69			3.00	1.62	0.48	Gourmelan & Amelung (2005)
CNSB	-	V	V	-	-	-	G	-118.57	39.23	-	25	VR	38.00	46.00	42.00			2.20	1.62	0.34	Hetland & Hager (2003)
CNSB	-	V	V	-	-	-	I,G	-117.8	39.02	-	110	VR	37.00	50.53	43.77			1.80	1.64	0.26	Hammond et al (2009)

Table A.2: Table containing all thrust faulting data used in chapter 2. Modified from the Excel spreadsheet available in the online supplement for space reasons. Columns as in table A.1. Study references can be found in the references of chapter 2.

Earthquake	Date	Type	Mw	D	EQ Lat	EQ Lon	Tech	Sig Lon	Sig Lat	ID	PD	Mech	t1 (yr)	t2 (yr)	t	d1 (mm)	d2 (mm)	V (mm/yr)	log(t)	log(v)	Reference
Altai	27/09/2003	SS	7.2	15	50.09	87.86	I	88.06	49.97	-	0	A	0.04	2.97	1.51	0.00	40.00	13.66	0.18	1.14	Barbot et al (2008)
Bolnay	23/07/1905	SS	8.4	-	-	-	G	-	-	Mongolian Sites	-	VR	89.00	94.00	91.50			2.00	1.96	0.30	Calais et al (2002)
Denali	03/11/2002	SS	7.9	15	63.23	-144.89	G	-144.3	62.73	DRMC	35	VR	0.02	0.25	0.13			266.67	-0.87	2.43	Pollitz (2005)
Denali	03/11/2002	SS	7.9	15	63.23	-144.89	G	-144.3	62.73	DRMC	35	VR	0.08	0.25	0.17			228.57	-0.78	2.36	Pollitz (2005)
Denali	03/11/2002	SS	7.9	15	63.23	-144.89	G	-144.3	62.73	DRMC	35	VR	0.02	0.50	0.26			195.00	-0.59	2.29	Pollitz (2005)
Denali	03/11/2002	SS	7.9	15	63.23	-144.89	G	-144.3	62.73	DRMC	35	VR	0.25	1.63	0.94			76.19	-0.03	1.88	Pollitz (2005)
Denali	03/11/2002	SS	7.9	15	63.23	-144.89	G	-143.67	62.58	ROLL	15	A,VR,P	0.00	2.00	1.00	0.00	194.35	97.18	0.00	1.99	Freed et al (2006)
Denali	03/11/2002	SS	7.9	15	63.23	-144.89	I + G	-144.45	63.91	-	50	?	0.69	1.68	1.19	0.00	40.00	40.56	0.07	1.61	Biggs et al (2009)
El Mayor-Cucapeh	04/04/2010	SS	7.2	12.8	32.31	-115.39	G	-115.73	32.76	-	12	VR	0.04	0.50	0.27			56.25	-0.57	1.75	Pollitz et al (2012)
El Mayor-Cucapeh	04/04/2010	SS	7.2	12.8	32.31	-115.39	G	-115.73	32.76	-	12	VR	0.04	1.50	0.77			26.52	-0.11	1.42	Pollitz et al (2012)
Hector Mine	16/10/1999	SS	7.1	15	34.71	-116.27	G	-116.15	34.675	-	10	VR	0.04	0.50	0.27			22.50	-0.57	1.35	Pollitz & Thatcher (2010)
Hector Mine	16/10/1999	SS	7.1	15	34.71	-116.27	G	-116.15	34.675	-	10	VR	0.50	1.00	0.75			10.00	-0.12	1.00	Pollitz & Thatcher (2010)
Hector Mine	16/10/1999	SS	7.1	15	34.71	-116.27	G	-116.15	34.675	-	10	VR	1.00	2.00	1.50			6.25	0.18	0.80	Pollitz & Thatcher (2010)
Hector Mine	16/10/1999	SS	7.1	15	34.71	-116.27	G	-116.15	34.675	-	10	VR	2.00	5.00	3.50			3.00	0.54	0.48	Pollitz & Thatcher (2010)
Imperial Valley	18/05/1940	SS	7.1	-	-	-	L	-115.6	33	-	8.5	A	1.00	34.00	17.50	0.00	190.00	5.76	1.24	0.76	Reilinger (1984)
Izmit-Duzce	17/08/1999	SS	7.4	17.5	41.01	29.97	G	30.239	40.829	BEST	15	A,VR	0.02	0.02	0.02			730.00	-1.72	2.86	Ergintav et al (2009)
Izmit-Duzce	17/08/1999	SS	7.4	17.5	41.01	29.97	G	30.303	40.785	KAZI	8.3	A,VR	0.08	0.08	0.08			293.00	-1.08	2.47	Ergintav et al (2009)
Izmit-Duzce	17/08/1999	SS	7.4	17.5	41.01	29.97	G	30.303	40.785	KAZI	8.3	A,VR	0.49	0.49	0.49			57.50	-0.31	1.76	Ergintav et al (2009)
Izmit-Duzce	17/08/1999	SS	7.4	17.5	41.01	29.97	G	30.303	40.785	KAZI	8.3	A,VR	1.00	1.00	1.00			30.00	0.00	1.48	Ergintav et al (2009)
Izmit-Duzce	17/08/1999	SS	7.4	17.5	41.01	29.97	G	30.303	40.785	KAZI	8.3	A,VR	3.00	3.00	3.00			10.00	0.48	1.00	Ergintav et al (2009)
Izmit-Duzce	17/08/1999	SS	7.4	17.5	41.01	29.97	G	30.303	40.785	KAZI	8.3	A,VR	6.00	6.00	6.00			5.00	0.78	0.70	Ergintav et al (2009)
Kokoxili	14/11/2001	SS	7.8	15	35.80	92.91	G	93.62	35.39	-	28	A,VR	0.00	0.33	0.17	0.00	91.67	275.00	-0.78	2.44	Diao et al (2010)
Kokoxili	14/11/2001	SS	7.8	15	35.80	92.91	G	93.89	35.5	BDGD	17	VR	0.08	1.00	0.54	0.00	100.37	109.49	-0.27	2.04	Ryder et al (2011)
Kokoxili	14/11/2001	SS	7.8	15	35.80	92.91	I	92	36.05	-	25	VR	1.39	2.05	1.72	0.00	10.00	15.19	0.24	1.18	Ryder et al (2011)
Kokoxili	14/11/2001	SS	7.8	15	35.80	92.91	I	92	36.05	-	25	VR	1.39	2.54	1.97	10.00	15.00	4.35	0.29	0.64	Ryder et al (2011)
Kokoxili	14/11/2001	SS	7.8	15	35.80	92.91	I	92	36.05	-	25	VR	1.39	3.31	2.35	15.00	20.00	2.61	0.37	0.42	Ryder et al (2011)
Kokoxili	14/11/2001	SS	7.8	15	35.80	92.91	I	92	36.05	-	25	VR	1.39	5.02	3.21	20.00	33.00	3.58	0.51	0.55	Ryder et al (2011)
Landers	28/06/1992	SS	7.3	15	34.65	-116.65	G	-116.67	34.45	-	13	VR	0.04	3.40	1.72	0.00	62.00	18.44	0.24	1.27	Deng et al (1998)
Manyi	08/11/1997	SS	7.6	16.4	35.33	86.96	I	87.25	35.35	-	10	VR/A	0.07	0.16	0.12	2.35	4.71	24.61	-0.93	1.39	Ryder et al (2007)
Manyi	08/11/1997	SS	7.6	16.4	35.33	86.96	I	87.25	35.35	-	10	VR/A	0.07	0.26	0.16	4.71	7.06	12.25	-0.78	1.09	Ryder et al (2007)
Manyi	08/11/1997	SS	7.6	16.4	35.33	86.96	I	87.25	35.35	-	10	VR/A	0.07	0.36	0.21	7.06	9.71	9.21	-0.67	0.96	Ryder et al (2007)
Manyi	08/11/1997	SS	7.6	16.4	35.33	86.96	I	87.25	35.35	-	10	VR/A	0.07	0.45	0.26	9.71	11.76	5.34	-0.58	0.73	Ryder et al (2007)
Manyi	08/11/1997	SS	7.6	16.4	35.33	86.96	I	87.25	35.35	-	10	VR/A	0.07	0.84	0.45	11.76	16.47	6.14	-0.34	0.79	Ryder et al (2007)
Manyi	08/11/1997	SS	7.6	16.4	35.33	86.96	I	87.25	35.35	-	10	VR/A	0.07	1.99	1.03	16.47	24.71	4.30	0.01	0.63	Ryder et al (2007)
Manyi	08/11/1997	SS	7.6	16.4	35.33	86.96	I	87.25	35.35	-	10	VR/A	0.07	3.14	1.60	24.71	25.88	0.38	0.20	-0.42	Ryder et al (2007)
Mongolia quakes	-	SS	V	-	-	-	G	-	-	Mongolian Sites	-	VR	-	-	42.50			2.00	1.63	0.30	Vergnolle et al (2003)
Napa Valley	24/08/2014	SS	6	12	38.31	-122.38	I ,G	-	-	-	0.08	A	0.02	0.05	0.04	0.00	8.00	243.33	-1.45	2.39	Floyd et al (2016)
Napa Valley	24/08/2014	SS	6	12	38.31	-122.38	I ,G	-	-	-	0.08	A	0.02	0.08	0.05	8.00	12.00	60.83	-1.28	1.78	Floyd et al (2016)
Napa Valley	24/08/2014	SS	6	12	38.31	-122.38	I ,G	-	-	-	0.08	A	0.02	0.12	0.07	12.00	14.50	25.35	-1.16	1.40	Floyd et al (2016)
Napa Valley	24/08/2014	SS	6	12	38.31	-122.38	I ,G	-	-	-	0.08	A	0.02	0.15	0.08	14.50	17.00	19.01	-1.07	1.28	Floyd et al (2016)
Napa Valley	24/08/2014	SS	6	12	38.31	-122.38	I ,G	-	-	-	0.08	A	0.02	0.18	0.10	17.00	19.00	12.17	-0.99	1.09	Floyd et al (2016)

Table A.3: Table containing half of the strike-slip faulting data used in chapter 2. Modified from the Excel spreadsheet available in the online supplement for space reasons. Columns as in table A.1. Study references can be found in the references of chapter 2.

Earthquake	Date	Type	Mw	D	EQ Lat	EQ Lon	Tech	Sig Lon	Sig Lat	ID	PD	Mech	t1 (yr)	t2 (yr)	t	d1 (mm)	d2 (mm)	V (mm/yr)	log(t)	log(v)	Reference
Parkfield	28/09/2004	SS	6	12	35.92	-120.54	G	-120.4	35.88	HUNT	1.5	A	0.00	0.05	0.03	0.00	31.00	620.00	-1.60	2.79	Barbot et al (2009)
Parkfield	28/09/2004	SS	6	12	35.92	-120.54	G	-120.47	35.9	LAND	1.7	A	0.00	0.05	0.03	0.00	33.00	660.00	-1.60	2.82	Barbot et al (2009)
Parkfield	28/09/2004	SS	6	12	35.92	-120.54	G	-120.48	35.92	POMM	0.7	A	0.00	0.05	0.03	0.00	26.00	520.00	-1.60	2.72	Barbot et al (2009)
Parkfield	28/09/2004	SS	6	12	35.92	-120.54	G	-120.4	35.88	HUNT	1.5	A	0.00	0.15	0.08	31.00	38.00	46.67	-1.12	1.67	Barbot et al (2009)
Parkfield	28/09/2004	SS	6	12	35.92	-120.54	G	-120.47	35.9	LAND	1.7	A	0.00	0.15	0.08	33.00	40.50	50.00	-1.12	1.70	Barbot et al (2009)
Parkfield	28/09/2004	SS	6	12	35.92	-120.54	G	-120.48	35.92	POMM	0.7	A	0.00	0.15	0.08	26.00	33.00	46.67	-1.12	1.67	Barbot et al (2009)
Parkfield	28/09/2004	SS	6	12	35.92	-120.54	G	-120.4	35.88	HUNT	1.5	A	0.00	0.30	0.15	38.00	50.00	40.00	-0.82	1.60	Barbot et al (2009)
Parkfield	28/09/2004	SS	6	12	35.92	-120.54	G	-120.47	35.9	LAND	1.7	A	0.00	0.30	0.15	40.50	50.00	31.67	-0.82	1.50	Barbot et al (2009)
Parkfield	28/09/2004	SS	6	12	35.92	-120.54	G	-120.48	35.92	POMM	0.7	A	0.00	0.30	0.15	33.00	42.90	33.00	-0.82	1.52	Barbot et al (2009)
Parkfield	28/09/2004	SS	6	12	35.92	-120.54	G	-120.4	35.88	HUNT	1.5	A	0.00	0.70	0.35	50.00	62.00	17.14	-0.46	1.23	Barbot et al (2009)
Parkfield	28/09/2004	SS	6	12	35.92	-120.54	G	-120.47	35.9	LAND	1.7	A	0.00	0.70	0.35	50.00	59.50	13.57	-0.46	1.13	Barbot et al (2009)
Parkfield	28/09/2004	SS	6	12	35.92	-120.54	G	-120.48	35.92	POMM	0.7	A	0.00	0.70	0.35	42.90	52.40	13.57	-0.46	1.13	Barbot et al (2009)
Parkfield	28/09/2004	SS	6	12	35.92	-120.54	G	-120.4	35.88	HUNT	1.5	A	0.00	1.10	0.55	62.00	66.60	4.18	-0.26	0.62	Barbot et al (2009)
Parkfield	28/09/2004	SS	6	12	35.92	-120.54	G	-120.47	35.9	LAND	1.7	A	0.00	1.10	0.55	59.50	66.70	6.55	-0.26	0.82	Barbot et al (2009)
Parkfield	28/09/2004	SS	6	12	35.92	-120.54	G	-120.48	35.92	POMM	0.7	A	0.00	1.10	0.55	52.40	59.50	6.45	-0.26	0.81	Barbot et al (2009)
Parkfield	28/09/2004	SS	6	12	35.92	-120.54	G	-120.4	35.88	HUNT	1.5	A	0.00	1.50	0.75	66.60	71.40	3.20	-0.12	0.51	Barbot et al (2009)
Parkfield	28/09/2004	SS	6	12	35.92	-120.54	G	-120.47	35.9	LAND	1.7	A	0.00	1.50	0.75	66.70	69.00	1.53	-0.12	0.19	Barbot et al (2009)
Parkfield	28/09/2004	SS	6	12	35.92	-120.54	G	-120.48	35.92	POMM	0.7	A	0.00	1.50	0.75	59.50	61.90	1.60	-0.12	0.20	Barbot et al (2009)
Parkfield	28/09/2004	SS	6	12	35.92	-120.54	G	-120.4	35.88	HUNT	1.5	A	0.00	2.20	1.10	71.40	83.30	5.41	0.04	0.73	Barbot et al (2009)
Parkfield	28/09/2004	SS	6	12	35.92	-120.54	G	-120.47	35.9	LAND	1.7	A	0.00	2.20	1.10	69.00	76.20	3.27	0.04	0.51	Barbot et al (2009)
Parkfield	28/09/2004	SS	6	12	35.92	-120.54	G	-120.48	35.92	POMM	0.7	A	0.00	2.20	1.10	61.90	71.40	4.32	0.04	0.64	Barbot et al (2009)
Parkfield (HUNT)	28/09/2004	SS	6	12	35.92	-120.54	G	-120.4	35.88	HUNT	1.5	A	0.00	0.00	0.00			5820.00	-3.20	3.76	Langbein et al (2006)
Parkfield (HUNT)	28/09/2004	SS	6	12	35.92	-120.54	G	-120.4	35.88	HUNT	1.5	A	0.00	0.00	0.00			2055.00	-2.58	3.31	Langbein et al (2006)
Parkfield (HUNT)	28/09/2004	SS	6	12	35.92	-120.54	G	-120.4	35.88	HUNT	1.5	A	0.00	0.01	0.01			1287.00	-2.28	3.11	Langbein et al (2006)
Parkfield (HUNT)	28/09/2004	SS	6	12	35.92	-120.54	G	-120.4	35.88	HUNT	1.5	A	0.01	0.01	0.01			572.00	-2.13	2.76	Langbein et al (2006)
Parkfield (HUNT)	28/09/2004	SS	6	12	35.92	-120.54	G	-120.4	35.88	HUNT	1.5	A	0.01	0.03	0.02			502.00	-1.76	2.70	Langbein et al (2006)
Parkfield (LAND)	28/09/2004	SS	6	12	35.92	-120.54	G	-120.47	35.9	LAND	1.7	A	0.00	0.00	0.00			21666.00	-3.40	4.34	Langbein et al (2006)
Parkfield (LAND)	28/09/2004	SS	6	12	35.92	-120.54	G	-120.47	35.9	LAND	1.7	A	0.00	0.00	0.00			2592.00	-2.88	3.41	Langbein et al (2006)
Parkfield (LAND)	28/09/2004	SS	6	12	35.92	-120.54	G	-120.47	35.9	LAND	1.7	A	0.00	0.00	0.00			1254.00	-2.52	3.10	Langbein et al (2006)
Parkfield (LAND)	28/09/2004	SS	6	12	35.92	-120.54	G	-120.47	35.9	LAND	1.7	A	0.00	0.01	0.01			852.00	-2.23	2.93	Langbein et al (2006)
Parkfield (LAND)	28/09/2004	SS	6	12	35.92	-120.54	G	-120.47	35.9	LAND	1.7	A	0.01	0.01	0.01			611.00	-2.03	2.79	Langbein et al (2006)
Parkfield (LAND)	28/09/2004	SS	6	12	35.92	-120.54	G	-120.47	35.9	LAND	1.7	A	0.01	0.02	0.01			468.00	-1.88	2.67	Langbein et al (2006)
Parkfield (LAND)	28/09/2004	SS	6	12	35.92	-120.54	G	-120.47	35.9	LAND	1.7	A	0.02	0.03	0.02			270.00	-1.69	2.43	Langbein et al (2006)
Parkfield (POMM)	28/09/2004	SS	6	12	35.92	-120.54	G	-120.48	35.92	POMM	0.7	A	0.00	0.00	0.00			11586.00	-3.37	4.06	Langbein et al (2006)
Parkfield (POMM)	28/09/2004	SS	6	12	35.92	-120.54	G	-120.48	35.92	POMM	0.7	A	0.00	0.00	0.00			2413.00	-2.77	3.38	Langbein et al (2006)
Parkfield (POMM)	28/09/2004	SS	6	12	35.92	-120.54	G	-120.48	35.92	POMM	0.7	A	0.00	0.01	0.01			949.00	-2.25	2.98	Langbein et al (2006)
Parkfield (POMM)	28/09/2004	SS	6	12	35.92	-120.54	G	-120.48	35.92	POMM	0.7	A	0.01	0.02	0.01			487.00	-1.84	2.69	Langbein et al (2006)
Parkfield (POMM)	28/09/2004	SS	6	12	35.92	-120.54	G	-120.48	35.92	POMM	0.7	A	0.02	0.03	0.02			200.00	-1.62	2.30	Langbein et al (2006)
S. Iceland	21/06/2000	SS	6.5	15	63.99	-20.47	I	-20.75	63.87	-	5	VR	0.22	0.41	0.32	0.00	1.48	7.72	-0.50	0.89	Jonsson (2008)
S. Iceland	21/06/2000	SS	6.5	15	63.99	-20.47	I	-20.75	63.87	-	5	VR	0.22	1.53	0.88	1.48	7.78	4.79	-0.06	0.68	Jonsson (2008)
S. Iceland	21/06/2000	SS	6.5	15	63.99	-20.47	I	-20.75	63.87	-	5	VR	0.22	2.05	1.14	7.78	9.50	0.94	0.06	-0.03	Jonsson (2008)
S. Iceland	21/06/2000	SS	6.5	15	63.99	-20.47	I	-20.75	63.87	-	5	VR	0.22	3.10	1.66	9.50	13.50	1.39	0.22	0.14	Jonsson (2008)
S. Iceland	21/06/2000	SS	6.5	15	63.99	-20.47	I	-20.75	63.87	-	5	VR	0.22	4.16	2.19	13.50	15.70	0.56	0.34	-0.25	Jonsson (2008)

Table A.4: Table containing the second half of the strike-slip faulting data used in chapter 2. Modified from the Excel spreadsheet available in the online supplement for space reasons. Columns as in table A.1. Study references can be found in the references of chapter 2.

Appendix B

Supplementary material for Chapter 3

B.1 Introduction

The supporting information contains extra details for different sections of the main article. The results of an analysis of atmospheric variability over Nepal are shown in Figures B.2 and B.3, with accompanying details in Text S1. Figure B.1 shows the GNSS stations which were not recording prior to the earthquake, and therefore required interpolation of the fitting coefficients from other stations. Text S2, Figure B.4 and Table B.1 give details of the viscoelastic modelling performed using VISCO-1D.

Additional inversions for the geometry of the Himalayan fault system are shown in Figures B.5-B.10. These figures show the results of different weighting schemes as well as the results of distributed slip inversions. Text accompanying these figures can be found in Text S3. Figure B.11 shows bar charts of variance reduction for each of the geometries in each stage of the earthquake cycle and for different inversion schemes.

Figure B.12 shows distributed slip inversions on the geometries proposed by *Elliott et al.* (2016), *Whipple et al.* (2016) and *Hubbard et al.* (2016), whilst Figure B.13 shows the corresponding fits to the data. Figure B.14 compares the variance reduction for distributed slip on each geometry tested for each stage of the earthquake cycle.

The results of a synthetic test for the joint coseismic-postseismic inversion can be found in Figures B.15 and B.16 along with accompanying details in Text S4. Figure B.17 shows the coseismic and postseismic residuals for the joint coseismic-postseismic inversion for each geometry. Figure B.18 shows the results of two inversions on the planar geometry, one where the GNSS are strongly down-weighted and one using the normal combination of GNSS and InSAR.

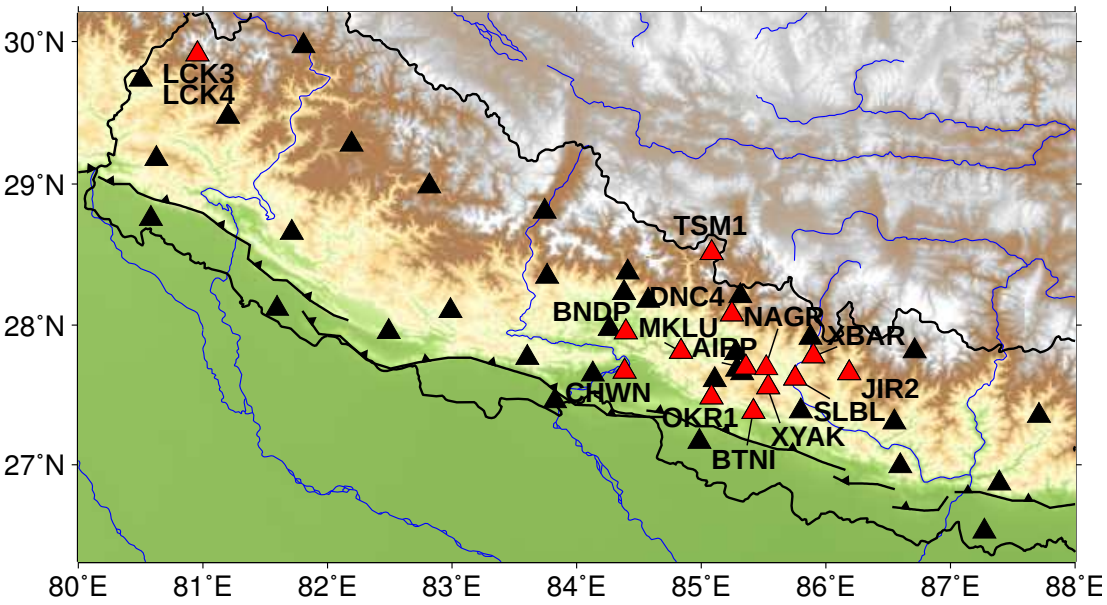

Figure B.1: Map of GNSS stations. Black triangles show locations of stations recording for at least one year before the earthquake. Red triangles with station names are stations which do not have enough preseismic data to detrend the time series and therefore required interpolation of the fitting coefficients from those stations shown in black.

Text S1: Atmospheric Variability

We used time series of ERA-I weather model nodes and delay measured by GNSS stations to examine the temporal and spatial variability of the troposphere over Nepal. The ERA-I model produces estimates of pressure, temperature and water vapour at a number of pressure levels on nodes spaced 0.75 degrees apart on the Earth's surface. These measurements can be converted to an InSAR LOS delay in order to investigate the possible atmospheric delays in the area. We modified TRAIN (*Bekaert et al.*, 2015a) in order to obtain LOS delays every 6 hours at each ERA-I node in the study area over a period of a year.

GNSS signals traverse the atmosphere between the satellite and receiver and are delayed through the troposphere in much the same way as InSAR signals. Regional GNSS data from western Nepal and the surrounding areas were retrieved from the UNAVCO datacenter [http://www.unavco.org/], and processed using the GAMIT software package (*Herring et al.*, 2013) to produce separate daily position estimates, using 30-second phase observations. Total zenith tropospheric delays, along with tropospheric gradients in north and east directions, were calculated for all stations in 2-hour increments across the UTC day using a piecewise-linear approach. Comparing our results with those provided by the Nevada Geodetic Laboratory demonstrates an excellent agreement, despite slightly different processing approaches (see Figure B.2). We then down-sampled our tropospheric time series to 6-hour increments for comparison with the ERA-I model predictions. Figure B.3 shows the time series of atmospheric delay

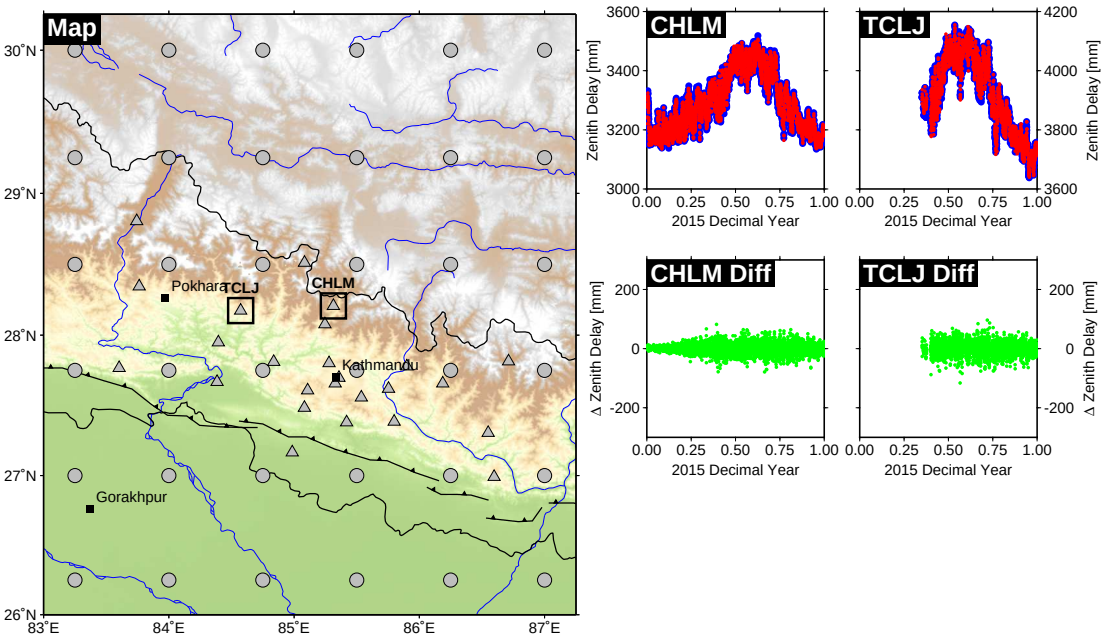

Figure B.2: Comparison between GNSS zenith delays obtained from the Nevada Geodetic Laboratory (http://geodesy.unr.edu/) and from our own processing. Map shows the locations of all ERA-I nodes (circles) and GNSS stations (triangles). GNSS stations with time series plotted are highlighted. Right hand panels show the zenith delay time series over 2015 obtained from our own processing (blue) and from the Nevada Geodetic Laboratory (red) for two example stations at different heights. Below this is the difference between the two estimates.

at each ERA node or GNSS station. There is a strong seasonal signal with amplitudes of 100s of millimetres with a more random atmospheric signal which can be 10s - 100s of mm in size superimposed.

We attempt to remove the atmospheric signal using a variety of techniques. Firstly, we use an empirical method based on an assumed linear relationship between InSAR phase and topography (e.g. *Elliott et al.*, 2008). This significantly reduces the apparent signal associated with the Himalayas. However, deformation signals correlated with topography may also be removed and this approach cannot handle spatial variations in atmospheric delay which are not associated with topographic variation. Secondly, we try a weather model based correction using ERA-I data. This produces similar results to the empirical correction discussed above but allows some spatial variability not associated with topography. This model can only capture spatial variability over length scales greater than 0.75 degrees in longitude/latitude, meaning that short length scale variations cannot be reproduced. Sometimes the ERA-I model can incorrectly estimate the atmospheric delay in an interferogram and increase atmospheric noise rather than decrease it (*Bekaert et al.*, 2015a). Neither of these approaches provided an adequate correction, particularly for InSAR data at lower heights. We therefore cut our InSAR data as described in the main article.

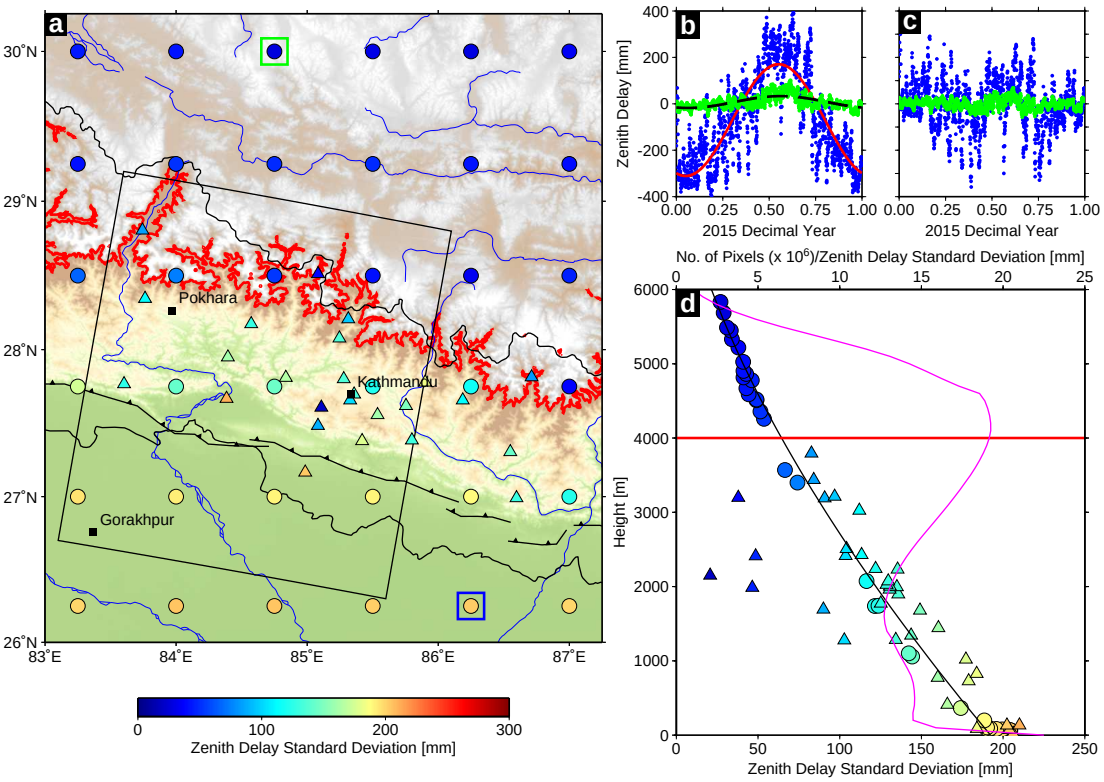

Figure B.3: Atmospheric delay variation over Nepal. a) Map view of ERA-I nodes (circles) and GNSS stations (triangles). Colours indicate the standard deviation of zenith delay at each node/station over a one year period. Black box shows Sentinel-1 swath. Green and blue boxes show nodes plotted as time series in panels (b) and (c). Red contour is at 4000m. b) Typical zenith delay time series for two ERA-I nodes over 2015. Blue and green dots correspond to nodes in the Ganges basin and the Tibetan plateau respectively. Red and black lines are seasonal fits. c) Same ERA-I zenith delay time series with the estimated seasonal component subtracted. d) Relationship between zenith delay variability and elevation. Triangles, circles and colour scale are the same as in a). Black curve is a power-law fit to the atmospheric variability with height (*Bekaert et al.*, 2015b). Magenta curve shows the ratio of the number of InSAR pixels over the expected zenith delay variation at different heights. Red line shows the 4000 m elevation cut-off used to cut the InSAR data.

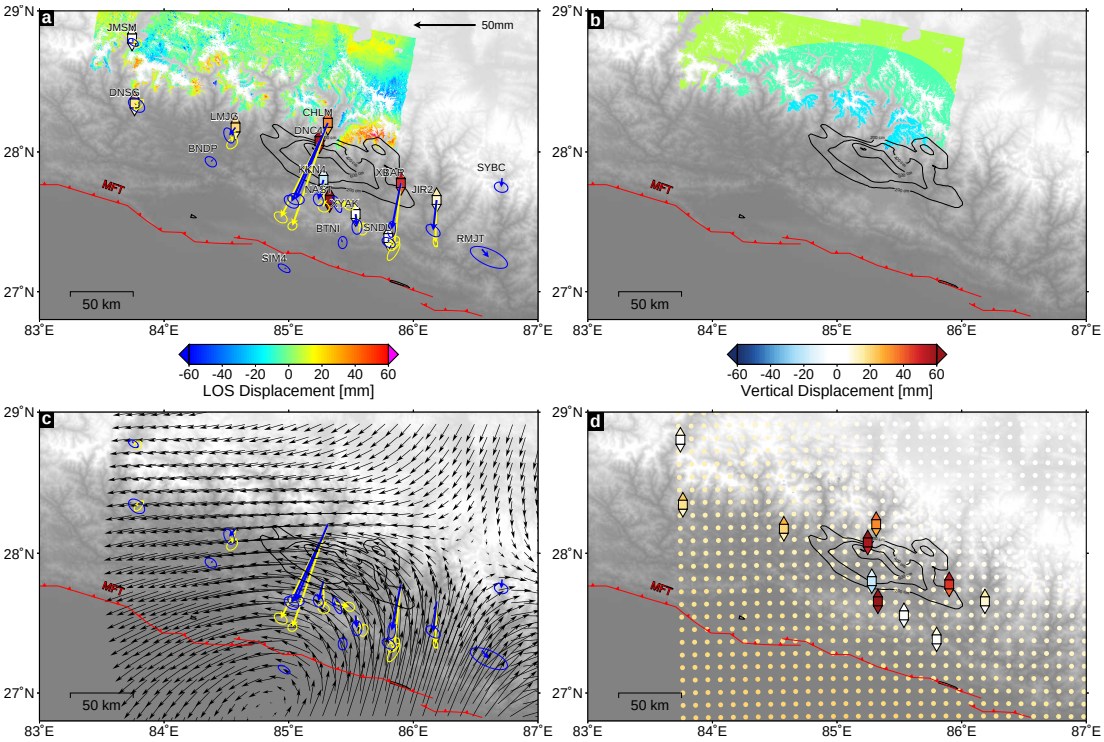

Figure B.4: Results of viscoelastic modelling using VISCO-1D. a) Observed postseismic deformation, showing GNSS displacements 1 year (blue) and 2 years (yellow) after the Gorkha earthquake. Colour map shows a Sentinel-1 interferogram spanning 29 April 2015 - 15 August 2015. Vertical GNSS displacements are represented as squares with triangles showing the 1-sigma range of values. Black lines show coseismic slip contoured every 2 metres from *Elliott et al.* (2016). b) Predicted LOS displacements covering the same period as the InSAR. c) Predicted horizontal displacements (black arrows) after 2 years of postseismic deformation. d) Predicted vertical displacements after 2 years of postseismic deformation.

Text S2: Viscoelastic Relaxation Model

We compared the postseismic deformation recorded by GNSS and InSAR with the predictions of a simple viscoelastic model. We used VISCO-1D (*Pollitz*, 1997) to generate surface displacements at the InSAR and GNSS observation times. We used a simple fault model to represent the Gorkha earthquake (see Table B.1) and tested various viscosity values. No single viscosity model can reproduce the necessary surface deformation field. The results of a model with a viscosity of 10^{18} Pa s are shown in Figure B.4 and show a clear discrepancy between the predicted surface displacements and those observed using GNSS and InSAR.

Text S3: Additional Geometric Inversions

Plane

We found that using the data errors alone as weights strongly favoured fitting the coseismic deformation and thus gave an optimal geometry almost identical to that inferred using coseismic data alone (black polygon in Figure B.5). The fit to the postseismic and interseismic deformation using this geometry was very poor. We then weighted the different data sets as explained in section 3.3 of the main article and performed the same inversion. The range of acceptable geometries from this inversion (green polygon in Figure B.5) have a much shallower dip, similar to the majority of best-fitting faults in section 3.2.2 of the main article. The fit to the coseismic data from this model is shown in Figure B.5.

In addition to these inversions, we also inverted for the best planar geometry using coseismic data from the west (profile A) and interseismic and postseismic deformation from profile E. We found that using the data errors alone again favoured fitting the coseismic data, but that in this case the fit to the coseismic and postseismic data was also good. Figure B.5 shows the best fitting geometries from this inversion as a black dot-dash polygon. Using the weighted inversion gave the range of model geometries shown in Figure B.5 as grey-scale squares with darker shades representing the most likely geometry. The range of acceptable models overlaps with the best-fit models inferred using the data errors alone and agrees with the geometry used by *Avouac et al.* (2015).

We then fixed the geometry and split it into multiple down-dip patches. The fixed geometry is within the range of acceptable models according to data from profile E. However, we choose a model with shallower dip than the most likely model for profile E since this is in greater agreement with geodetic data from western Nepal. We solved for slip in each stage of the earthquake cycle in a Bayesian sense. We use a Laplacian operator to smooth slip and solve for the optimal smoothing parameter for each earthquake cycle stage in the inversion. We use the data errors alone as weights in our distributed slip inversions since the fit to each stage of the earthquake cycle is independent of all others when the geometry is fixed. The results of this inversion are shown in Figure B.6. All three stages of the earthquake cycle can be explained relatively well using this model. Unsurprisingly, the western data are also well fit by this distributed slip model. Eastern coseismic slip reaches further north than western coseismic slip, as seen in a number of 3D distributed slip inversions on planar faults for this earthquake (e.g. *Wang and Fialko*, 2015, *Galetzka et al.*, 2015, *Avouac et al.*, 2015). Postseismic deformation is less well fit by smooth, distributed slip than the sharp-edged uniform dislocation model. Sharp edges to postseismic slip may be caused by steep stress change gradients from the earthquake.

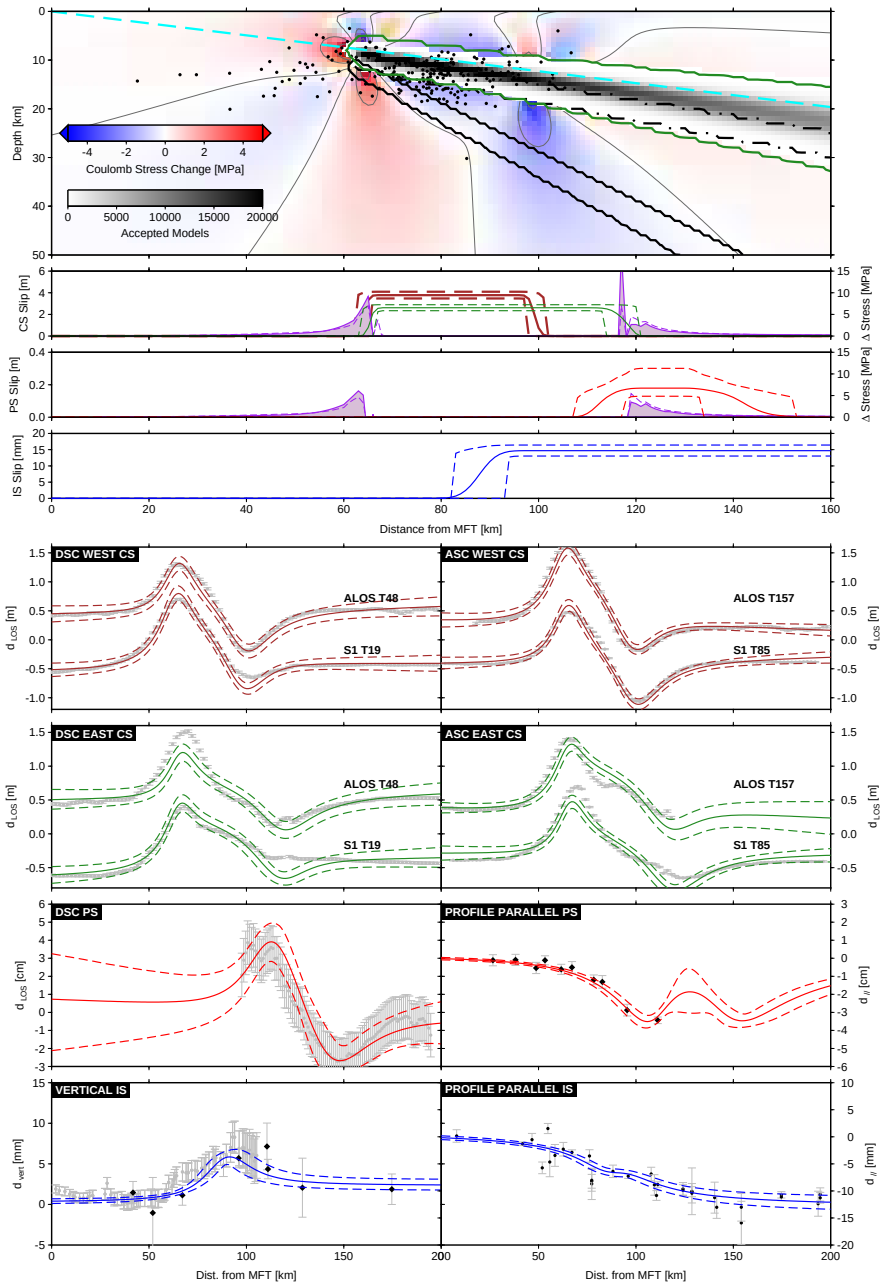

Figure B.5: Results for the best single planar geometry. Top panel: cross section with inferred geometries. Solid black polygon is the region of best-fit geometries for joint inversion of data from profile E using data weights only. Green solid polygon is for the same data, but with equal weight for each earthquake cycle stage. Dot-dash black polygon is for joint inversion of coseismic data from profile A and postseismic and interseismic data from profile E. Grayscale squares show joint inversion for the same data, but with equal weights for each earthquake cycle stage. Dashed cyan line is planar geometry from *Avouac et al.* (2015). Black dots are aftershocks from (*Bai et al.*, 2016). Coulomb stress change is calculated assuming friction coefficient, μ is 0.6. Below this are panels showing coseismic (top), postseismic (middle) and interseismic (bottom) slip on the proposed geometry. Solid lines show the mean and dashed lines show the 95% confidence interval. Purple lines show areas of Coulomb stress increase for $\mu = 0.6$ (solid) and $\mu = 0.01$ (dashed). Lower panels show predicted displacements from the slip distributions above, compared to each data set. Solid is the mean fit and dashed lines show the 95% confidence interval for model fits.

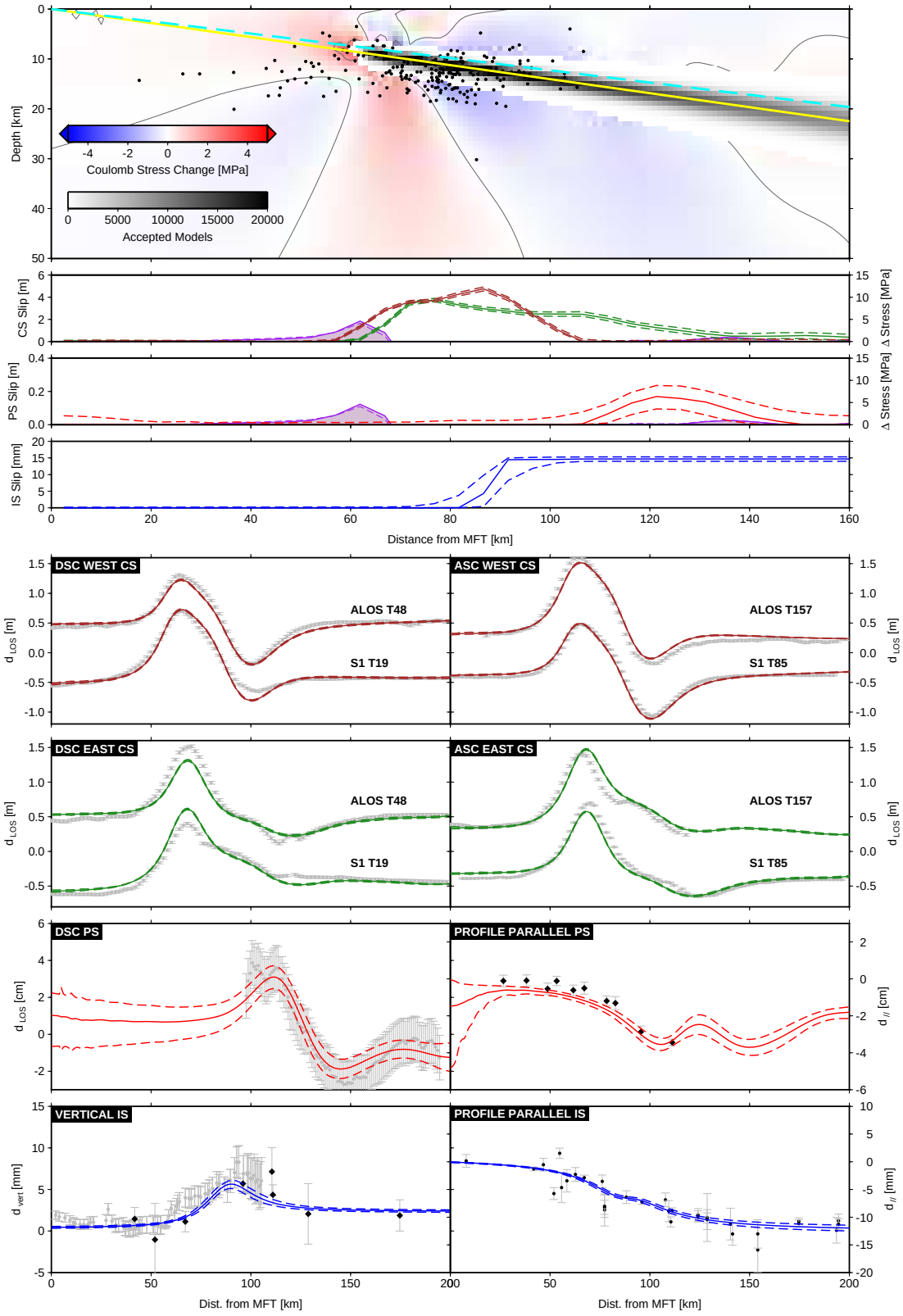

Figure B.6: Results for distributed slip on the best single plane geometry dipping at 8 degrees. Layout is similar to Figure B.5. Slip is shown as the mode (solid line) and 95% confidence interval (dashed lines). Solid yellow line shows fixed geometry use for distributed slip.

FRF

We again use both approaches to data weighting and compare the results. Using the data weights alone favours fitting the coseismic over the other data sets and produces a geometry similar to *Elliott et al.* (2016), shown as the black polygon in Figure B.7. This is likely because (*Elliott et al.*, 2016) primarily used coseismic geodetic data in their determination of the ramp location. Giving equal weight to each earthquake cycle stage improves the fit to the postseismic data with little degradation in overall fit for coseismic and interseismic data. Figure B.7 shows the range of acceptable models and the fit to the data.

We then fix the fault geometry, split into a number of patches (as discussed above) and solve for distributed slip both in the east and west. Results of this inversion are shown in Figure B.8. Whilst the geometry of the fault system is solved for using data from the easternmost profile, this fault geometry is also capable of matching data from the westernmost profile. This is because the upper flat section of this geometry closely resembles the planar geometry of the best fitting plane in the west. Coseismic slip in the west rapidly decreases north of the transition to the ramp in the structure and therefore doesn't degrade the fit. As previously, the best improvement in fit is seen in the coseismic data, whilst postseismic slip is more poorly fit by the smoothed, distributed slip than the sharp-edged uniform slip patch model.

FRF Splay

Once again, we use both approaches to data weighting and compare the results. Using the data weights alone suggests a narrower range of possible geometries and favours a deeper and more southerly ramp (black polygon in Figure B.9) whose position is dominated by fitting the coseismic data. Giving equal weight to each earthquake cycle stage gives a broader range of possible geometries, encompassing those suggested by data weights alone and by *Whipple et al.* (2016). We then fix the fault geometry and solve for distributed slip, taking into account the additional constraints required by the splay (see section 3.3.3 of the main article). As in previous inversions, an improvement of the fit in the coseismic data is seen whilst a degradation of fit is observed in the postseismic data.

Summary

Figure B.11 shows the variance reduction for each model geometry in the different inversion schemes for data from profile E. The lowest variance reductions (poorest data fits) are seen in the interseismic and postseismic data for the planar geometry when using data weights alone. In this inversion, the coseismic data dominate and prefer a steeply dipping fault plane which provides a poor fit to the interseismic and postseismic data. When using equal weights for each stage of the earthquake cycle, the optimal

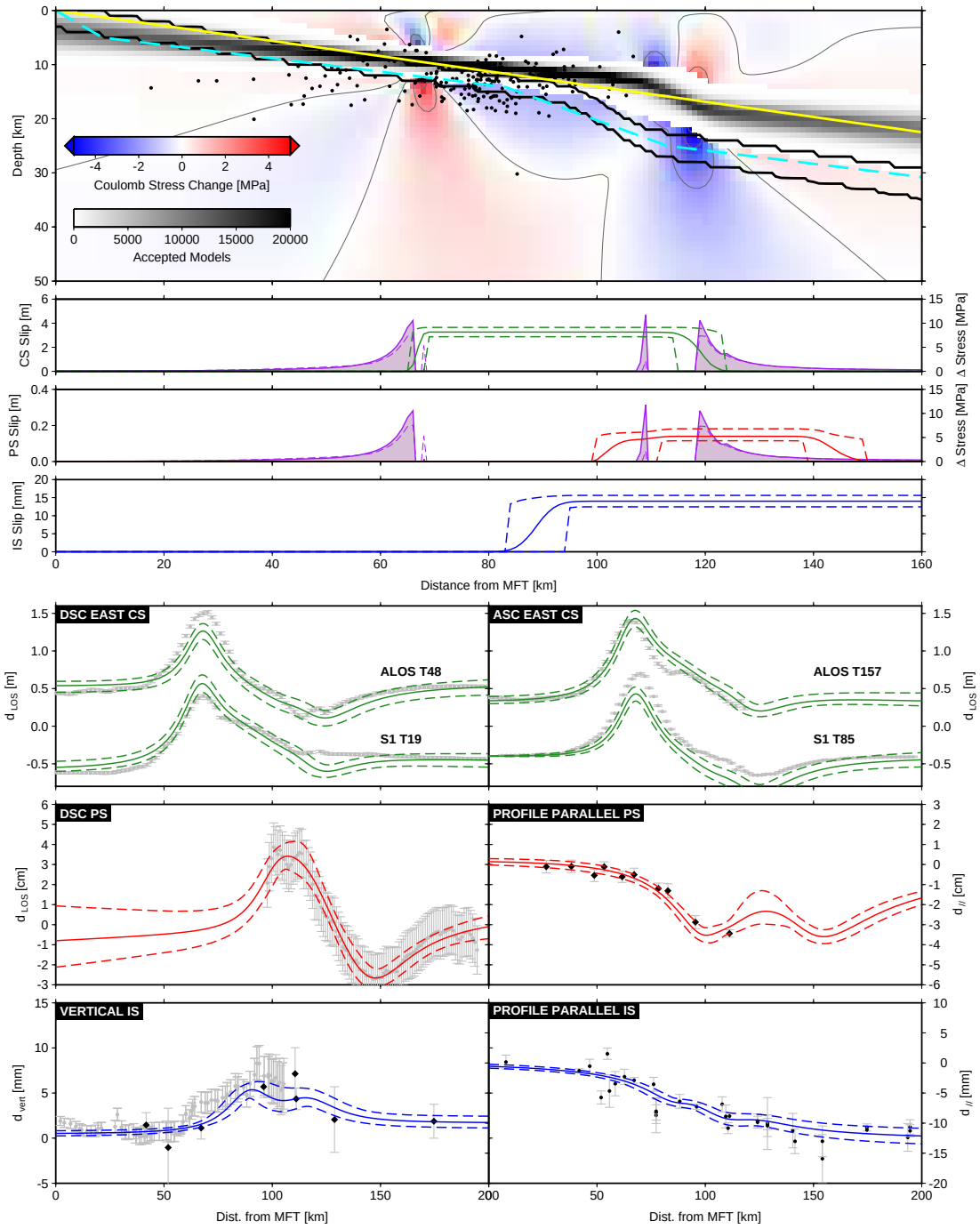

Figure B.7: Results for slip on three dislocations arranged in a flat-ramp-flat geometry. Note that only data from profile E is used when solving for the geometry. Black polygon shows region of acceptable geometries when using data weights alone. Grayscale squares show the acceptable flat-ramp-flat geometries when all earthquake cycle stages are given equal weight. Dashed cyan line is the flat-ramp-flat geometry inferred by *Elliott et al.* (2016). Yellow solid line is the best single plane geometry inferred in this study. See caption of Figure B.5 for more detailed explanation of various aspects of the figure.

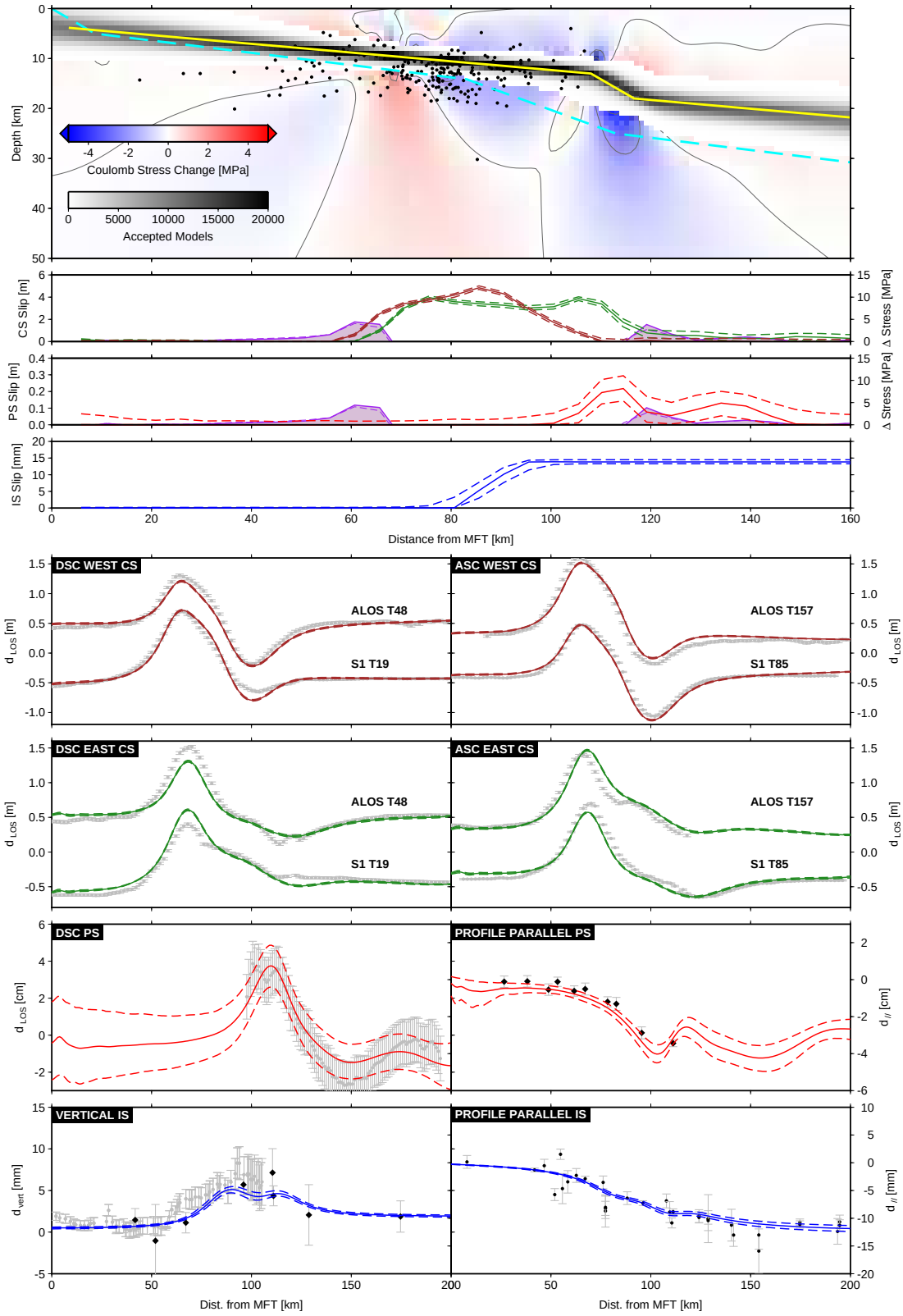

Figure B.8: Results for distributed slip on the best flat-ramp-flat geometry inferred in this study. Dashed cyan line is the flat-ramp-flat geometry inferred by *Elliott et al.* (2016). Yellow solid line is the fixed geometry used for the distributed slip modelling. See caption of Figure B.6 for more detailed explanation of various aspects of the figure.

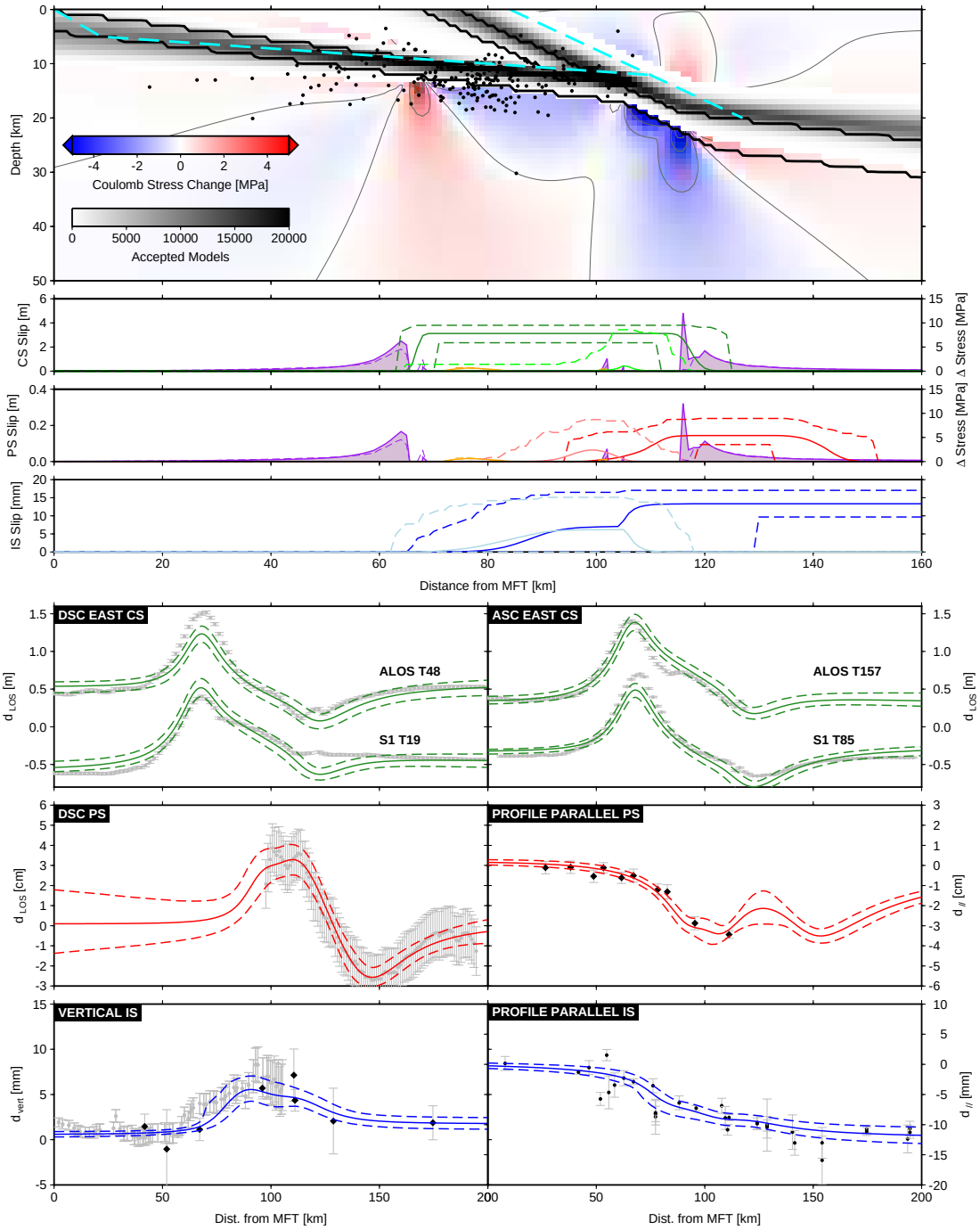

Figure B.9: Results for slip on three dislocations arranged in a flat-ramp-flat geometry with an additional dislocation projecting up from the ramp as a splay. Dashed cyan line is the geometry from *Whipple et al.* (2016). Details of the figure are similar to previous examples (see Figure B.5). In addition, lighter colours in the fault slip panels refer to slip on the splay.

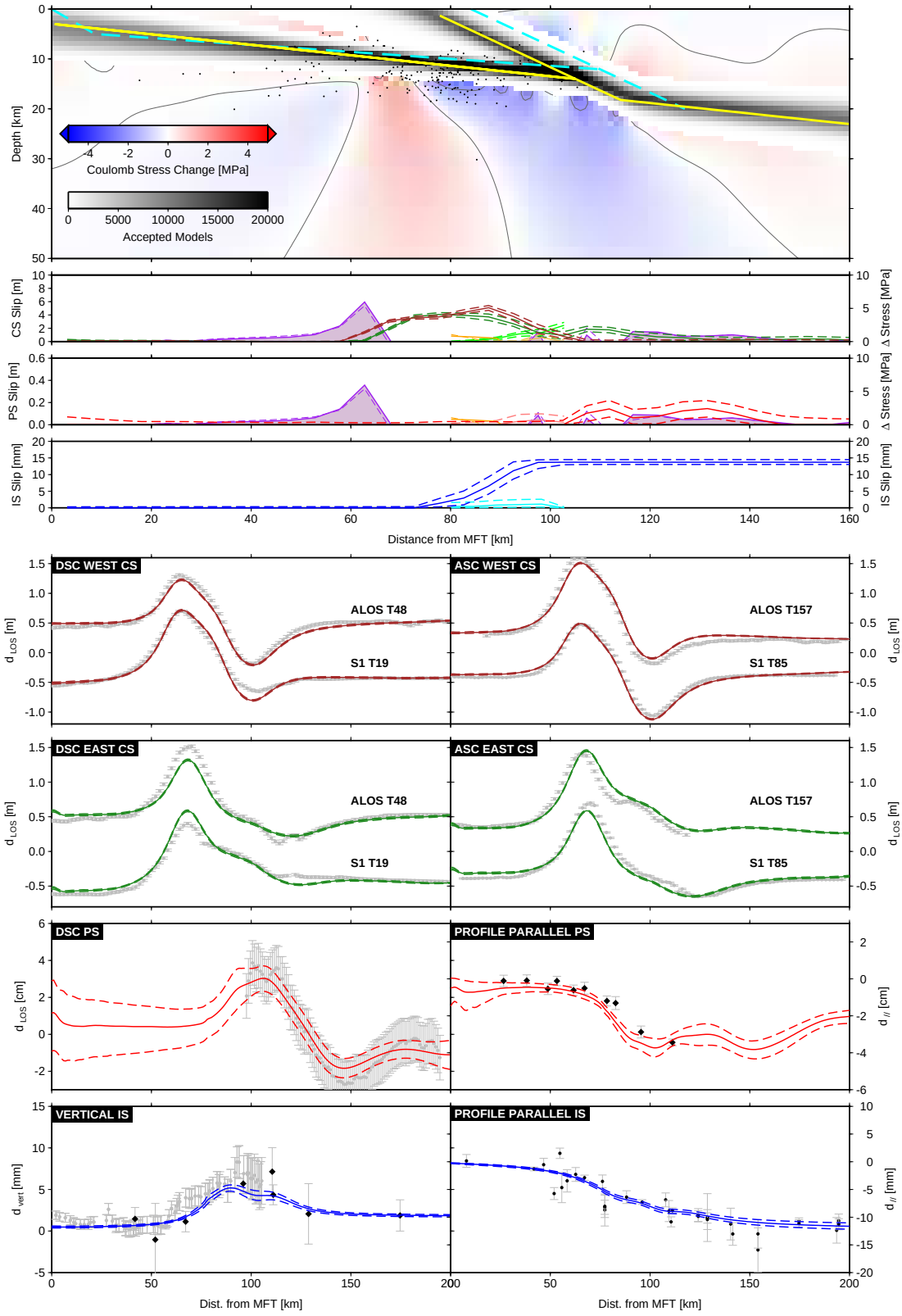

Figure B.10: Results for distributed slip on the best splay geometry inferred in this study. Details of the figure are similar to previous examples (see Figure B.6). In addition, lighter colours in the fault slip panels refer to slip on the splay.

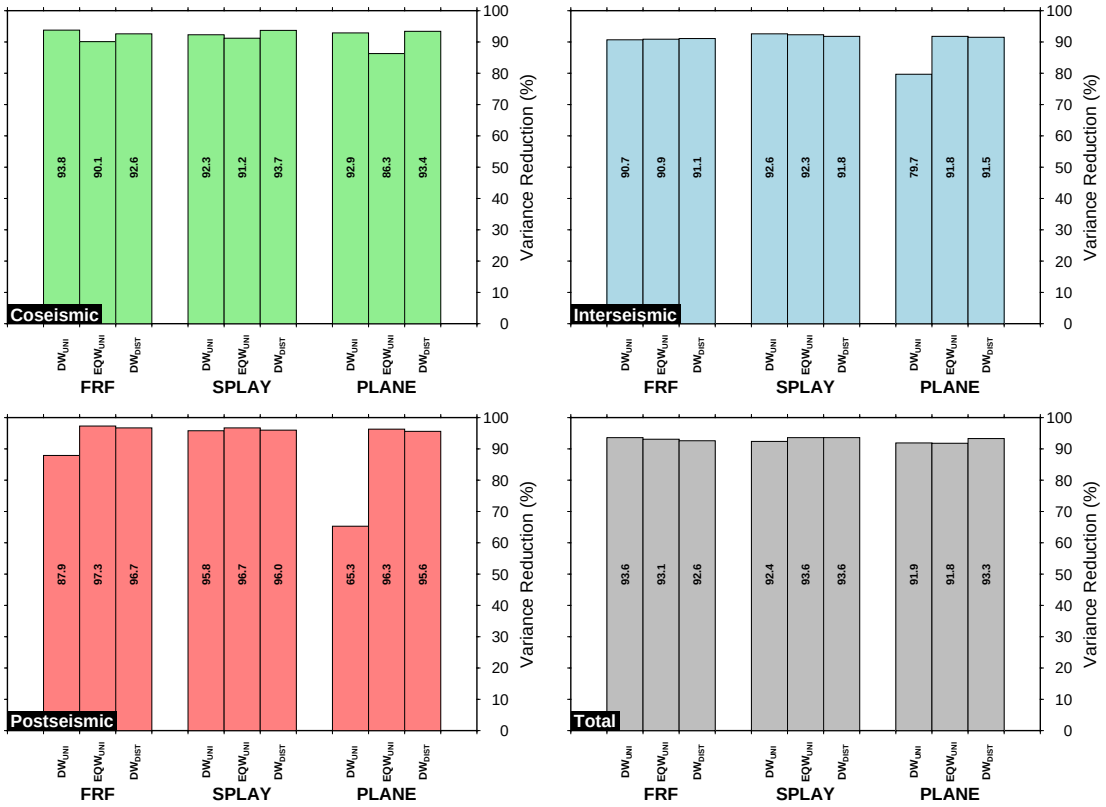

Figure B.11: Bar charts comparing the variance reduction for each geometry in the different inversion schemes. Numbers in bars give the variance reduction for each model. FRF: flat-ramp-flat. DW: data-weights only inversion. EQW: equal weights for each stage of the earthquake cycle. UNI: uniform slip dislocation model. DIST: distributed slip model on fixed geometry obtained using the equal weights uniform slip model.

plane is shallower but has a poorer fit to the coseismic data. In order for the planar geometry to match coseismic data, a distributed slip model is necessary.

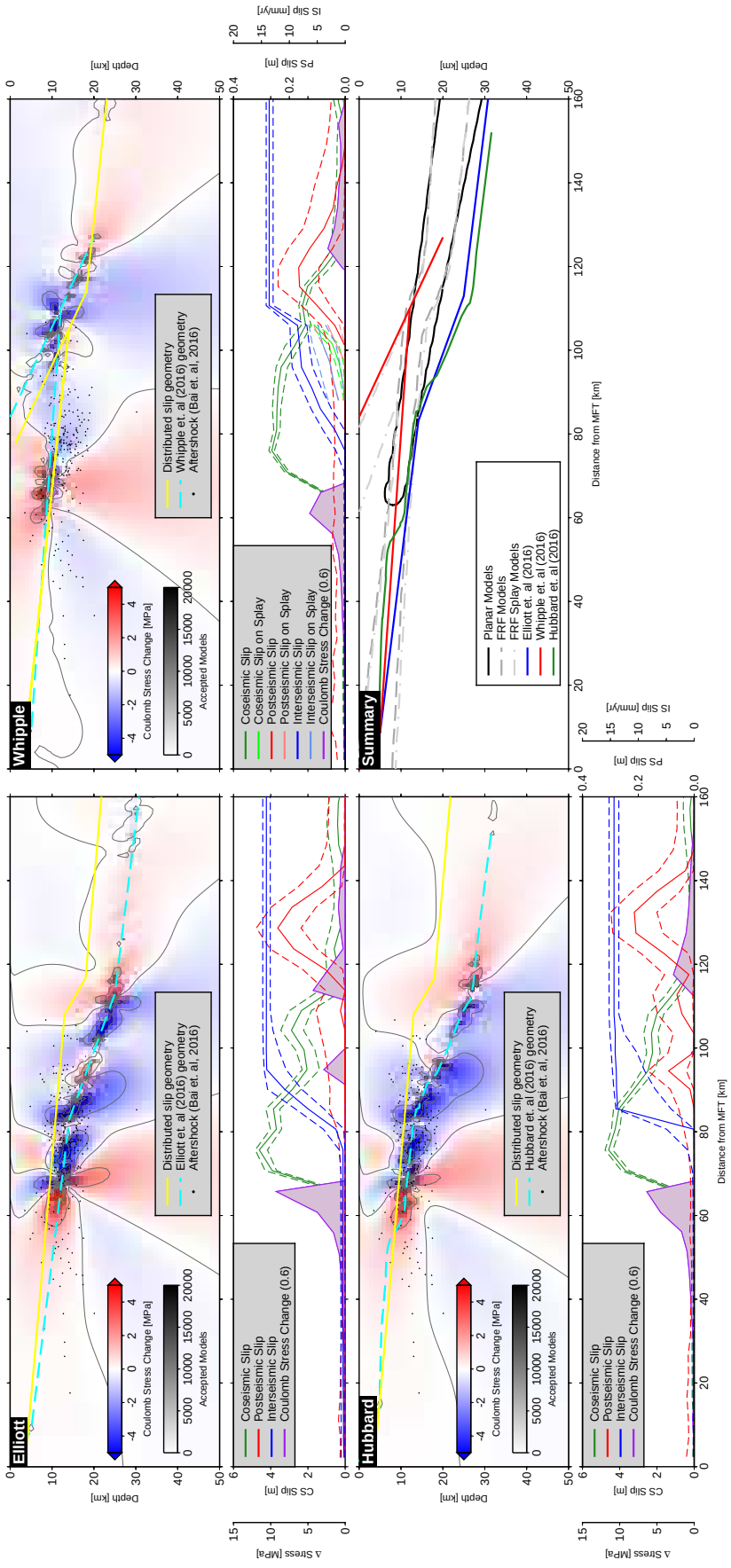

Figure B.12: Summary of different fixed geometries. For each geometry, the top panel shows a cross section beneath Nepal and the lower panel shows slip and stress changes on the faults. Cyan lines show the fixed geometries used for distributed slip modelling. Yellow lines show the similar fixed geometries obtained from our own inversions for geometry. Slip in each stage of the earthquake cycle is shown by the mode (solid line) and the 95% confidence interval (dashed lines) in the lower panels. The summary figure shows the region with > 1000 accepted models for each geometry from our inversions in grey/black compared with the fixed geometries suggested by *Elliott et al.* (2016), *Whipple et al.* (2016) and *Hubbard et al.* (2016).

Text S4: Synthetic test of the joint coseismic/postseismic inversion

Model Set-up

In order to validate the model, we perform a synthetic test using a simulated earthquake. The data setup is identical to that used for modelling real data. We use the down-dip geometries determined in our earlier profile inversions and extend these along strike. The fault is split into 10 km square patches and we simulate an earthquake with a slip distribution which is very similar to the Gorkha event. In order to examine trade-offs between parameters and the effect of assuming an incorrect geometry, our synthetic earthquake is generated on the FRF-splay model with slip on the splay. We use the synthetic coseismic slip to generate synthetic postseismic displacements using the rate-strengthening law used in our inversion and assigning values for a, V_0, z_0 and k. Coseismic and postseismic slip is used to generate surface displacements recorded by GNSS and InSAR before adding noise to the simulated measurements. GNSS noise is added by adding random values drawn from a normal distribution with a standard deviation equal to the standard deviation of the data point. We add spatially-correlated noise to the InSAR by using the covariance matrix of the InSAR measurements (*Lohman and Simons*, 2005).

We then run our inversion on the synthetic data, using the same approach as used on the real data (see section 4.1 of the main text). We invert the surface deformation data generated by slip on the FRF-splay model and solve for slip and frictional properties on the planar, FRF and FRF-splay geometries. After the simulated annealing stages, the Bayesian inversion algorithm keeps a record of model samples. After completion of the inversion and removal of any burn-in, we can use the kept models to obtain probability distributions for each model parameter.

Results

Figure B.15 shows a comparison between the input coseismic, aftershock and postseismic slip distributions and the mode of the recovered slip distributions on each geometry. A comparison between the input FRF-splay slip and the recovered FRF-splay slip shows excellent agreement, suggesting that the model can reliably recover slip. When the planar and FRF models are used, slip which would have been mapped on to the splay is instead mapped onto deeper sections of the main fault. The presence or absence of a splay therefore has an effect on both the coseismic and postseismic slip distributions inferred from the same data.

Figure B.16 shows the recovery of the frictional properties, a and V_0, for each of the geometries. The cyan lines and star all lie within the PDFs for the FRF-splay geometry, indicating that the various frictional parameters can be recovered reliably if the correct geometry is used. There is a positive correlation between estimates of a and V_0 for all of the geometries tested, which is to be expected given their relationship in the rate-

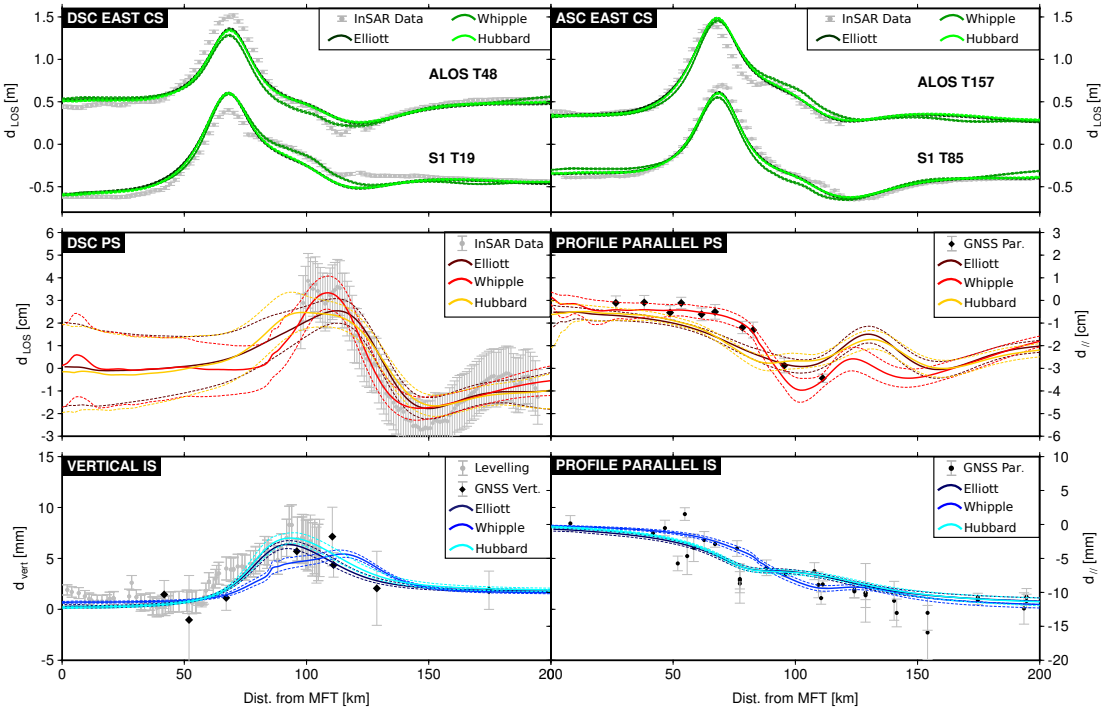

Figure B.13: Summary of model fits to coseismic(CS), postseismic (PS) and interseismic (IS) data profiles. Thick, solid lines show the mean model fit and similarly coloured thin dashed lines show the corresponding 95% confidence interval.

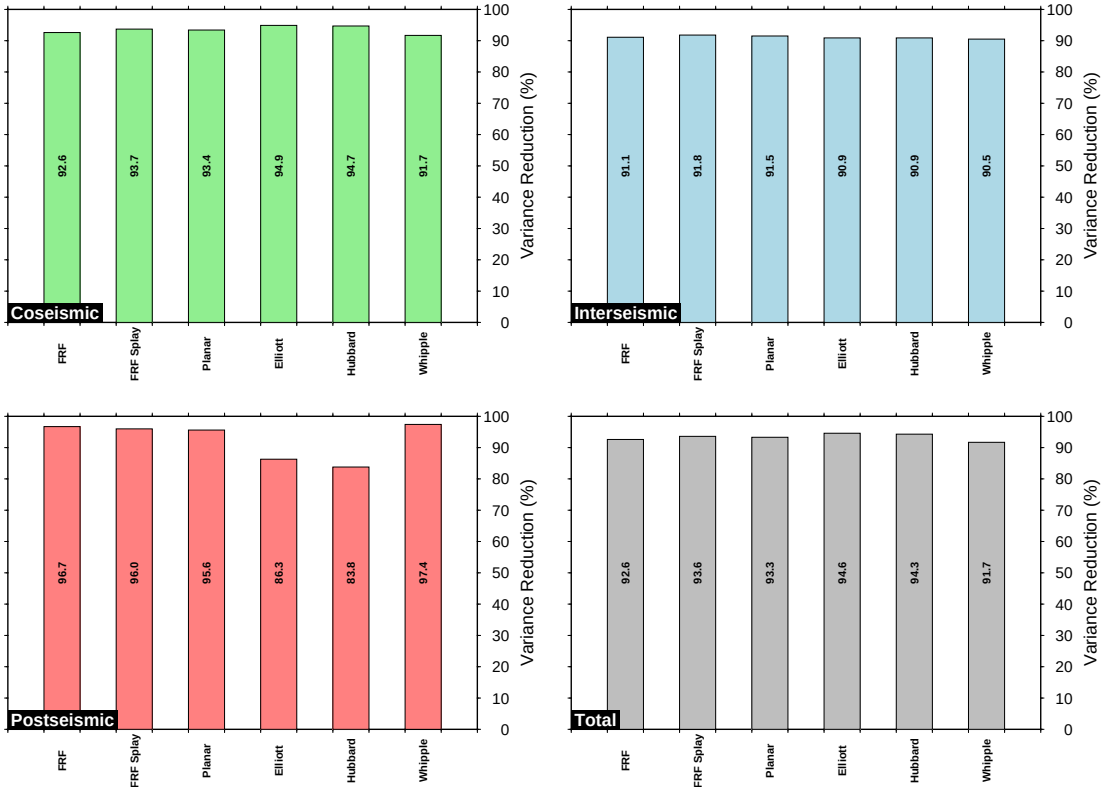

Figure B.14: Bar charts comparing the variance reduction for distributed slip on each geometry. Numbers in bars give the variance reduction for each model. FRF: flat-ramp-flat.

strengthening friction law (see equation 6 in the main text). As the value of a increases, a given stress change has less effect, therefore requiring higher V_0 values to produce the same postseismic slip. There is also a trade off between the depth of transition from velocity-weakening to velocity-strengthening behaviour and the value of the rate-strengthening parameter, a. Deeper transitions require lower values of a, as these deeper transitions may be further from high coseismic stress changes, therefore reducing the amount of afterslip. Furthermore, a deeper onset of postseismic slip produces less surface deformation and therefore requires more slip to produce the same effects at the surface. This trade-off is seen within the individual geometries, but also between geometries: the deeper V_0 sigmoid for the planar geometry in Figure B.16c corresponds to the lower a values in Figure B.16d.

The variation between each geometry is down to a combination of linked factors. The different geometries require different coseismic slip distributions to fit the coseismic data. These coseismic distributions produce different stress distributions and therefore require different transition depths and frictional properties. Furthermore, the postseismic slip distribution required on each geometry to match the data will be different. Despite these complexities, the slip distributions for each geometry appear relatively similar, and the inferred friction properties agree within error.

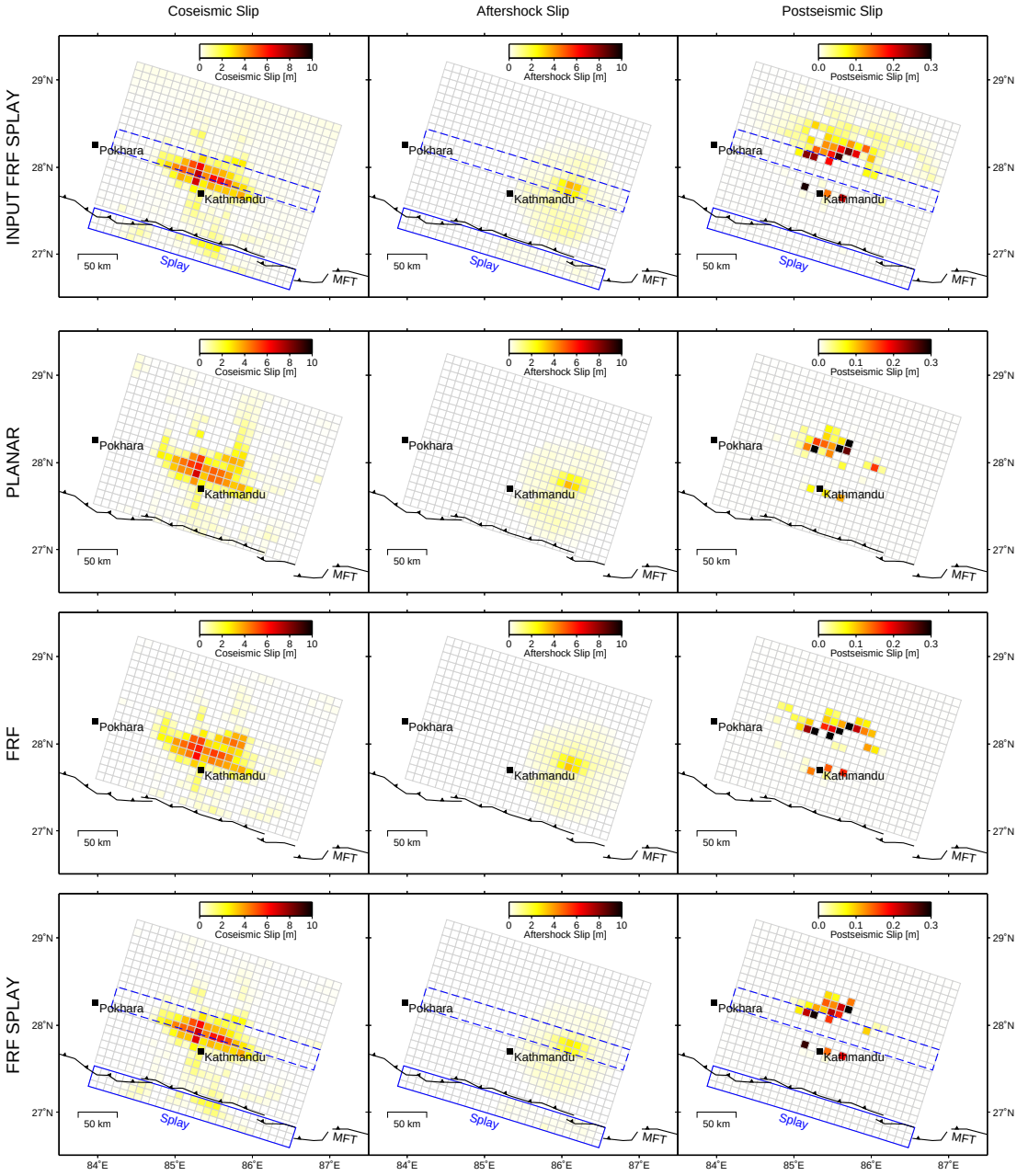

Figure B.15: Comparison of input and recovered slip for the synthetic test of the joint coseismic-postseismic inversion. Top row shows input coseismic, aftershock and postseismic slip on the FRF-splay geometry. Blue dashed rectangle shows location of splay and blue solid rectangle outlines the splay patches which have been shifted from their true location for the sake of clarity. Subsequent rows show the recovered slip on each geometry.

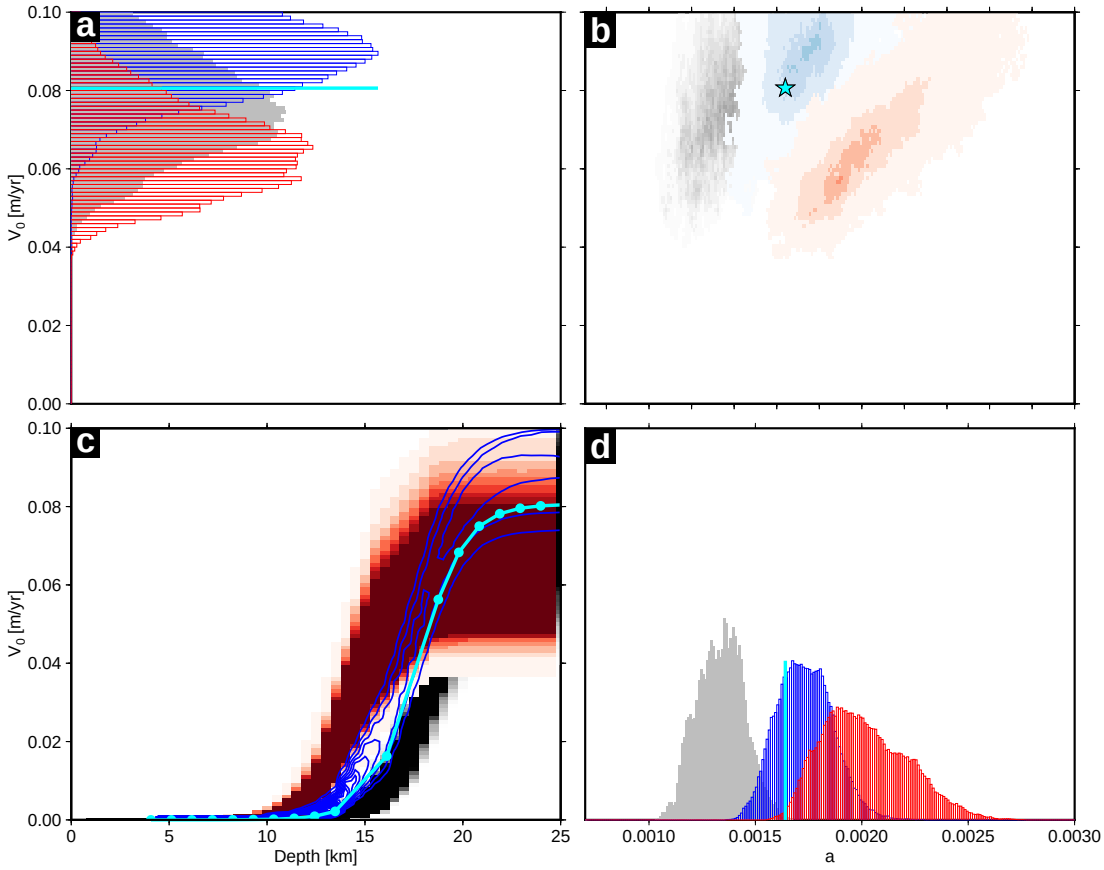

Figure B.16: Inferred distributions of frictional properties from the synthetic tests. a) Probability density function (PDF) of V_0 for each geometry. Blue = FRF-splay, red = FRF, gray = planar. Cyan bar shows the true value. b) Joint PDF for V_0 and a, showing a positive correlation between the two parameters for each geometry. Cyan star shows the true values. c) Variation of V_0 with depth for each geometry and the cyan dotted line shows the true values of V_0 at each slip patch depth. d) PDF of a for each geometry, with the cyan bar showing the true value.

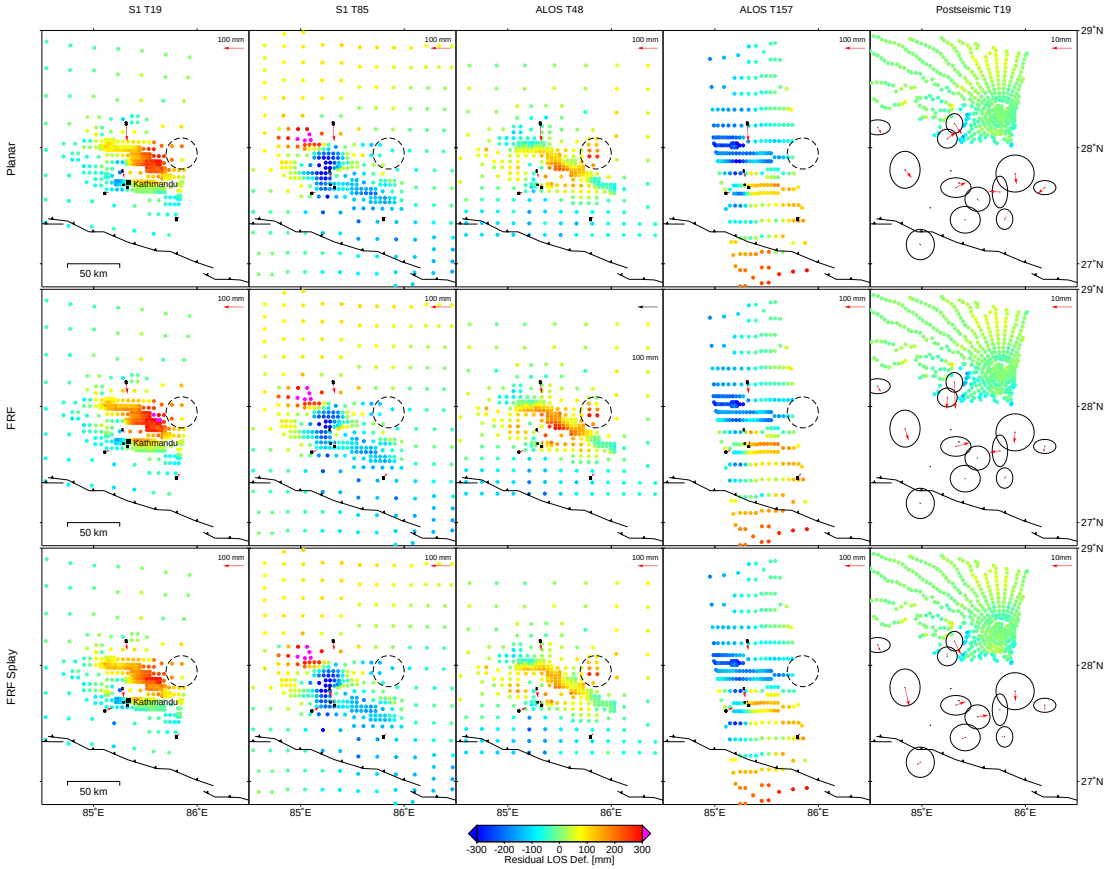

Figure B.17: Coseismic and postseismic residuals for each of the geometries used in the joint coseismic-postseismic inversion. Each row corresponds to a different geometry, and each column to a different data set. The black, dashed circle corresponds to the area where an uplift anomaly was identified by *Whipple et al.* (2016).

Table B.1: Fault parameters used for VISCO-1D model

Parameter	Value
Top Depth	10 km
Bottom Depth	20 km
Dip	8
Strike	288
Length	150
Rake	90
Slip	5 m

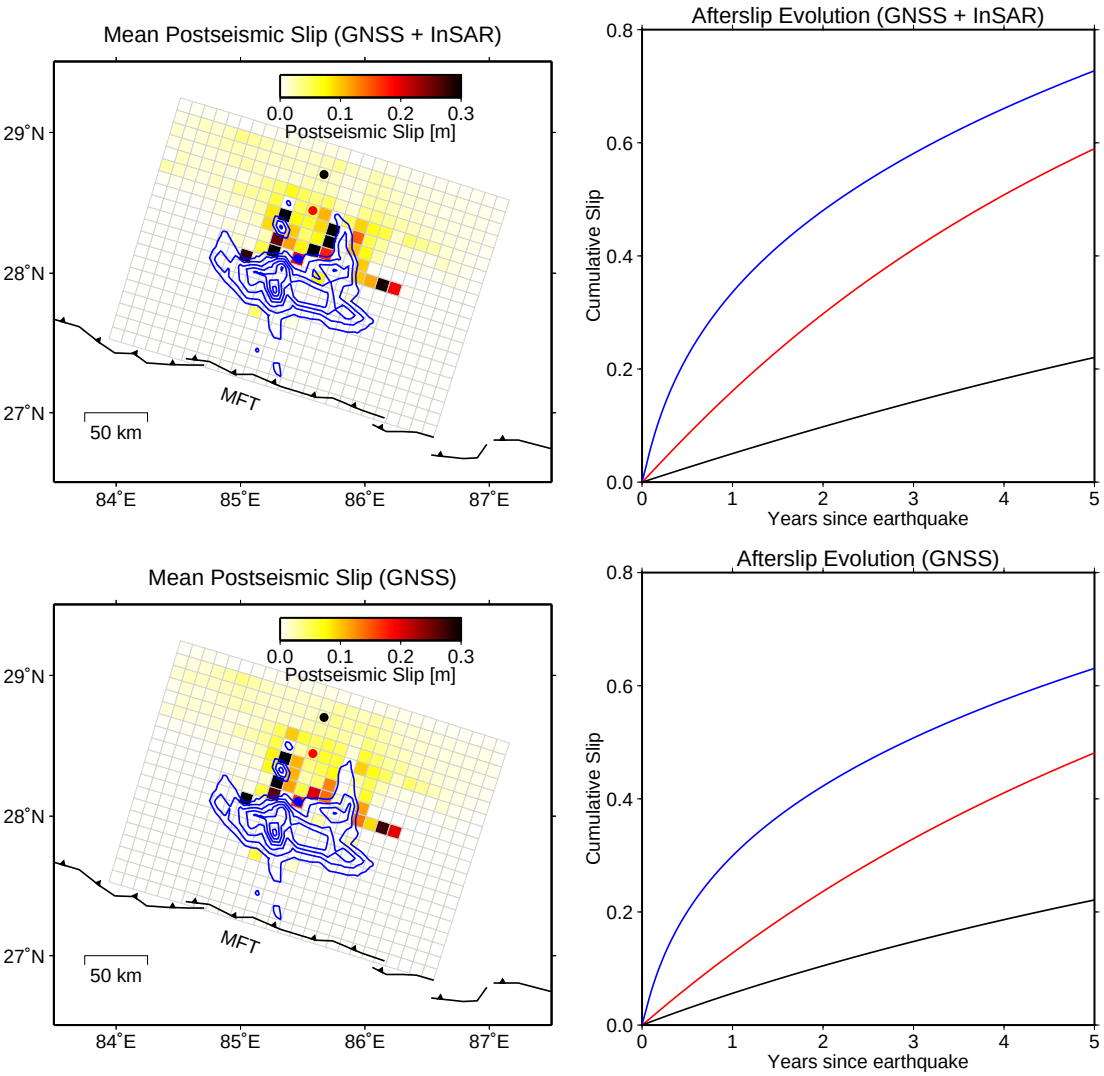

Figure B.18: Comparison between results of the joint coseismic-postseismic inversion using postseismic GNSS only or postseismic GNSS and InSAR. Blue contour lines show the mean coseismic slip distribution at 1 m intervals. Blue, red and black circles are the patches who have their temporal evolution plotted in the figures to the right.

References

Avouac, J.-P., L. Meng, S. Wei, T. Wang, and J.-P. Ampuero (2015), Lower edge of locked Main Himalayan Thrust unzipped by the 2015 Gorkha earthquake, *Nature Geoscience*, *8*(9), 708–711, doi:10.1038/ngeo2518. B.1, B.5

Bai, L., H. Liu, J. Ritsema, J. Mori, T. Zhang, Y. Ishikawa, and G. Li (2016), Faulting structure above the Main Himalayan Thrust as shown by relocated aftershocks of the 2015 M_w 7.8 Gorkha, Nepal, earthquake, *Geophysical Research Letters*, *43*(2), 637–642, doi:10.1002/2015GL066473. B.5

Bekaert, D., R. Walters, T. Wright, A. Hooper, and D. Parker (2015a), Statistical comparison of InSAR tropospheric correction techniques, *Remote Sensing of Environment*, *170*, 40–47, doi:10.1016/j.rse.2015.08.035. B.1, B.1

Bekaert, D. P. S., A. Hooper, and T. J. Wright (2015b), A spatially-variable power-law tropospheric correction technique for InSAR data, *Journal of Geophysical Research: Solid Earth*, pp. n/a–n/a, doi:10.1002/2014JB011558. B.3

Elliott, J., R. Jolivet, P. J. González, J.-P. Avouac, J. Hollingsworth, M. P. Searle, and V. Stevens (2016), Himalayan megathrust geometry and relation to topography revealed by the Gorkha earthquake, *Nature Geoscience*, *9*(2), 174–180, doi:10.1038/ngeo2623. B.1, B.4, B.1, B.7, B.8, B.12

Elliott, J. R., J. Biggs, B. Parsons, and T. J. Wright (2008), InSAR slip rate determination on the Altyn Tagh Fault, northern Tibet, in the presence of topographically correlated atmospheric delays, *Geophysical Research Letters*, *35*(12), n/a–n/a, doi:10.1029/2008GL033659. B.1

Galetzka, J., D. Melgar, J. F. Genrich, J. Geng, S. Owen, E. O. Lindsey, X. Xu, Y. Bock, J.-P. Avouac, L. B. Adhikari, B. N. Upreti, B. Pratt-Sitaula, T. N. Bhattarai, B. P. Sitaula, A. Moore, K. W. Hudnut, W. Szeliga, J. Normandeau, M. Fend, M. Flouzat, L. Bollinger, P. Shrestha, B. Koirala, U. Gautam, M. Bhatterai, R. Gupta, T. Kandel, C. Timsina, S. N. Sapkota, S. Rajaure, and N. Maharjan (2015), Slip pulse and resonance of the Kathmandu basin during the 2015 Gorkha earthquake, Nepal, *Science*, *349*(6252). B.1

Herring, T. A., R. W. King, and S. C. McClusky (2013), Introduction to GAMIT-GLOBK Release 10.5, *Tech. rep.* B.1

Hubbard, J., R. Almeida, A. Foster, S. N. Sapkota, P. Bürgi, and P. Tapponnier (2016), Structural segmentation controlled the 2015 M_w 7.8 Gorkha earthquake rupture in Nepal, *Geology*, *44*(8), 639–642, doi:10.1130/G38077.1. B.1, B.12

Lohman, R. B., and M. Simons (2005), Some thoughts on the use of InSAR data to constrain models of surface deformation: Noise structure and data downsampling, *Geochemistry, Geophysics, Geosystems*, *6*(1), n/a–n/a, doi:10.1029/2004GC000841. B.1

Pollitz, F. F. (1997), Gravitational viscoelastic postseismic relaxation on a layered spherical Earth, *Journal of Geophysical Research: Solid Earth*, *102*(B8), 17,921–17,941, doi:10.1029/97JB01277. B.1

Wang, K., and Y. Fialko (2015), Slip model of the 2015 M w 7.8 Gorkha (Nepal) earthquake from inversions of ALOS-2 and GPS data, *Geophysical Research Letters*, *42*(18), 7452–7458, doi:10.1002/2015GL065201. B.1

Whipple, K. X., M. Shirzaei, K. V. Hodges, and J. R. Arrowsmith (2016), Active shortening within the Himalayan orogenic wedge implied by the 2015 Gorkha earthquake, *Nature Geoscience*, *9*, 711–716. B.1, B.1, B.9, B.12, B.17

Appendix C

Supplementary material for Chapter 4

C.1 Introduction

The supporting information contains Figures C.1-C.6. Figure C.1 shows the errors for each LOS velocity map. Figure C.2 shows the results of an elastic dislocation model fit to the ERS interferogram and highlights the residuals. Figure C.3 shows the model set up when determining the postseismic fault geometry. Figure C.4 shows the results for the earthquake cycle inversion, assuming there is little difference between the look vectors for each satellite. Figure C.5 shows the difference between the ERS interferogram covering the 1997 earthquake and the estimated LOS offset predicted from the LOS earthquake cycle inversion shown in Figure C.4. Figure C.6 shows how the postseismic time constant is chosen.

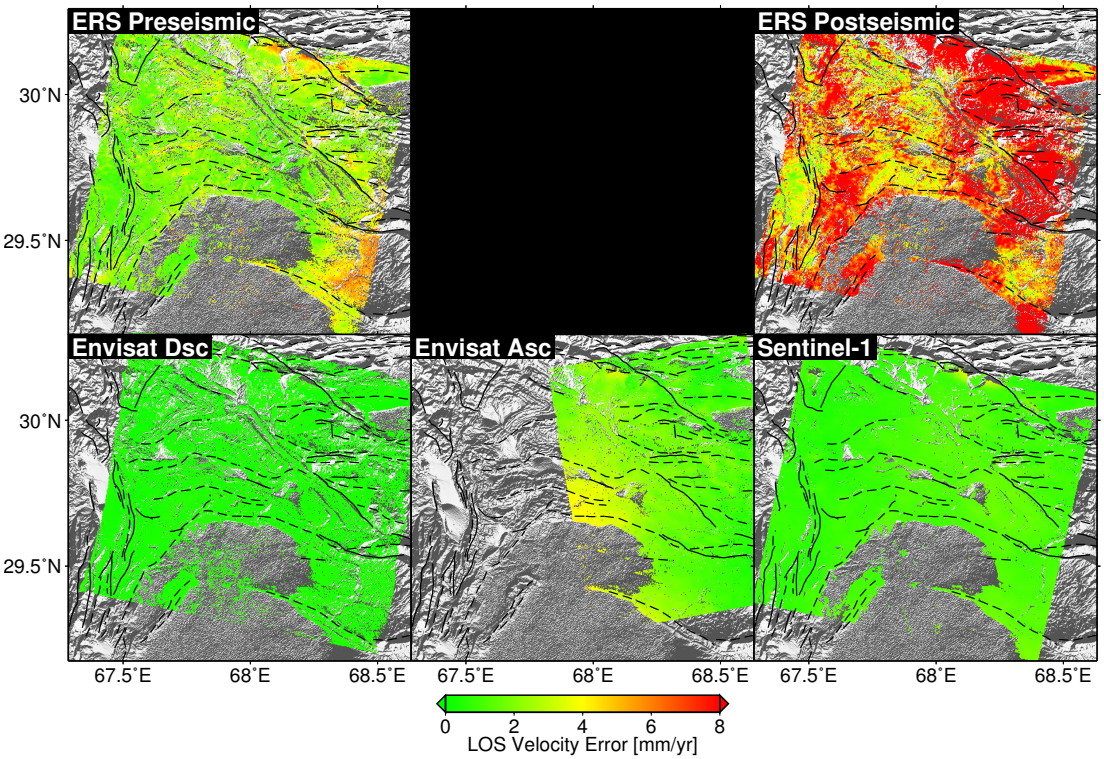

Figure C.1: Maps of LOS velocity error for each of the satellite velocity maps. Each map has been calculated on a pixel-by-pixel basis using bootstrapping. All maps are plotted using the same colour scale. Note there is no velocity error map for the ERS coseismic interferogram. Fold axes and fault traces from *Nissen et al.* (2016).

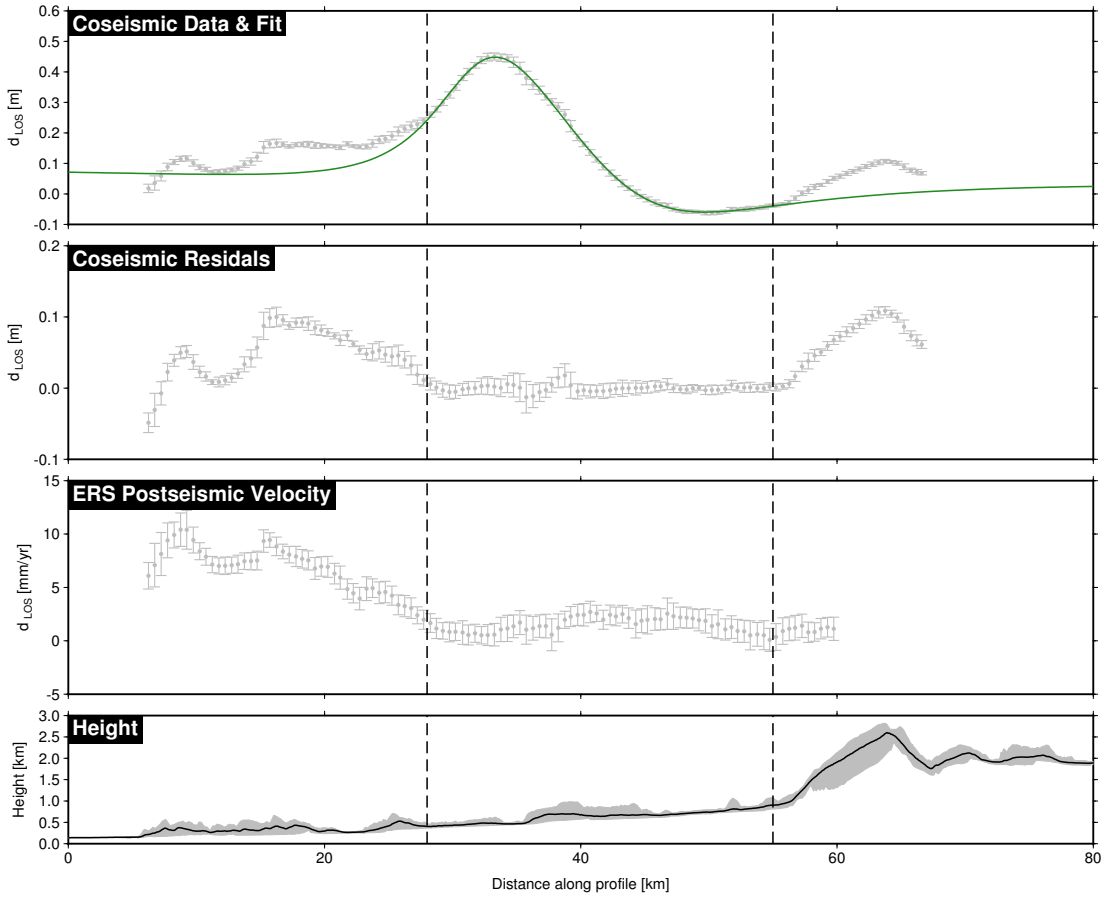

Figure C.2: Elastic dislocation model fit to data taken from a profile through the ERS interferogram. The coseismic data between the two dashed lines were used in the inversion. Residuals to the model fit closely resemble either postseismic deformation seen in later interferograms or topography.

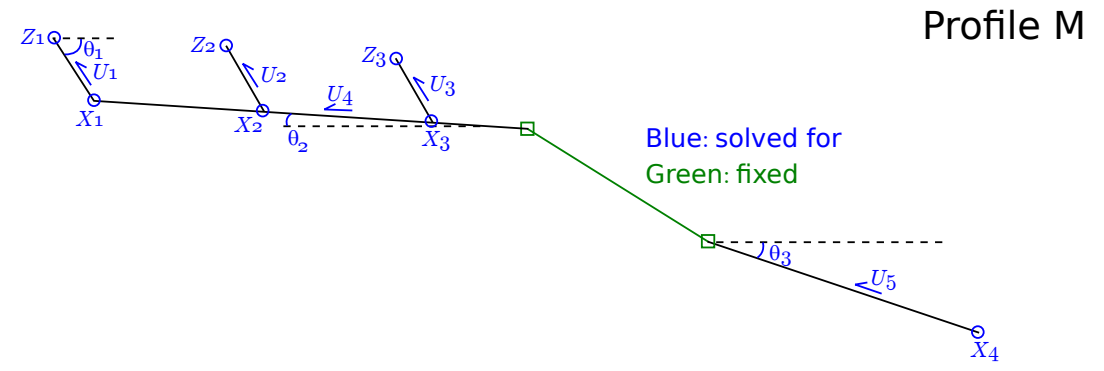

Figure C.3: Model set up for profiles taken through the postseismic deformation field. Green lines represent the location of coseismic slip found from previous modelling. Black lines represent the fault system which is solved for using postseismic deformation data. Blue shapes and associated labels represent parameters used to define the fault system and solved for in the inversion.

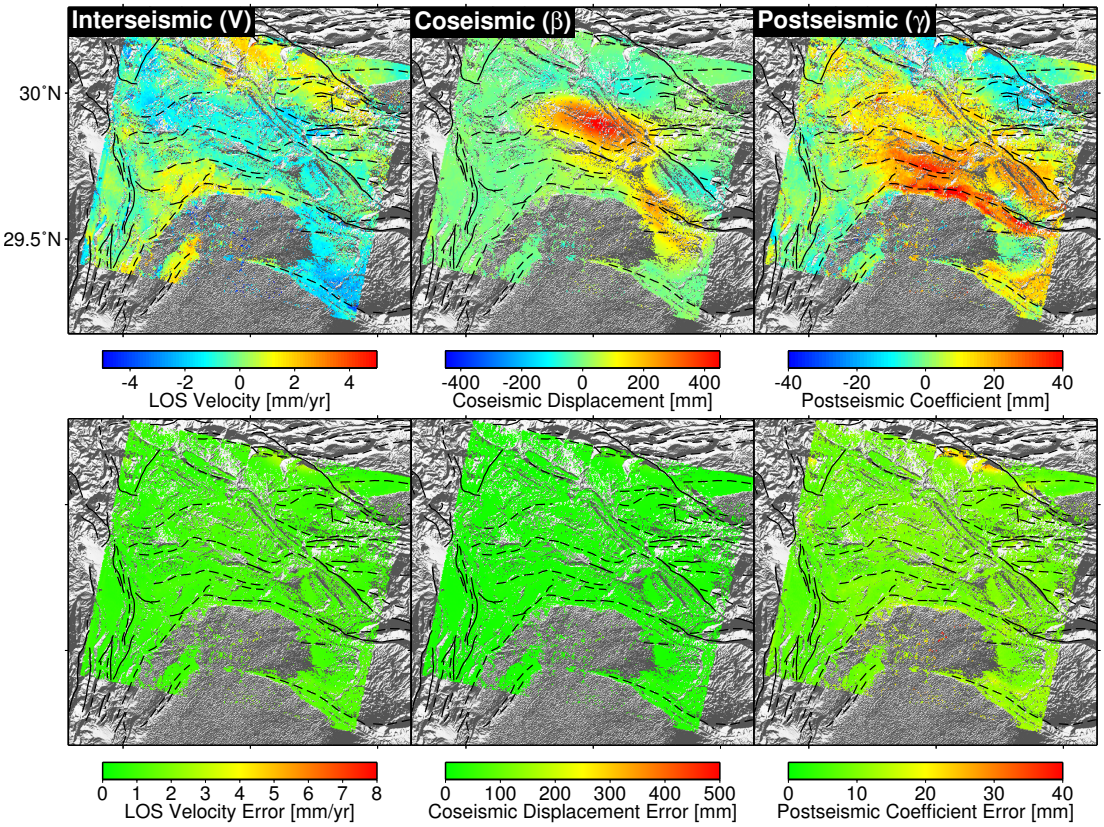

Figure C.4: Maps of earthquake cycle deformation without correcting for the variation of the look vector between different satellites.

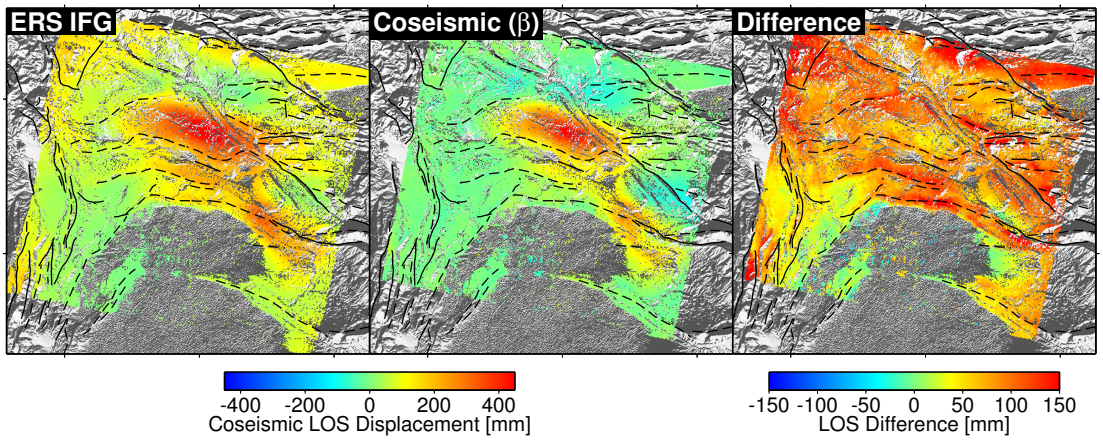

Figure C.5: Comparison between the original ERS interferogram and the coseismic deformation estimated in the earthquake cycle inversion. The difference is shown in the right-hand panel on a different colour scale. The largest differences are seen in areas associated with postseismic deformation or regions which may be affected by topographically correlated atmosphere.

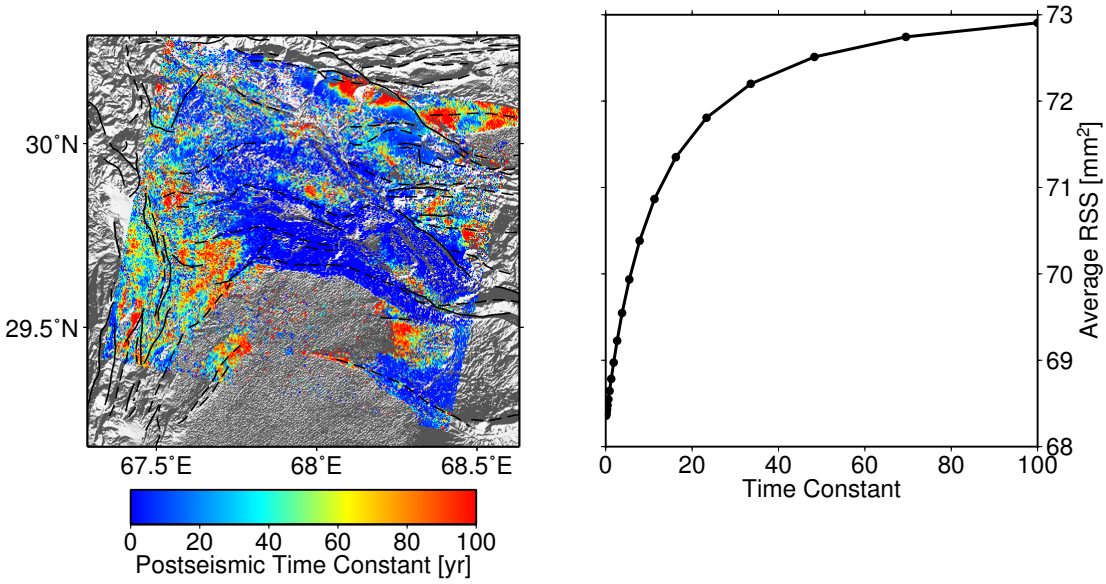

Figure C.6: Comparison of postseismic time constants used when tying the various InSAR data sets together. Left: map of the minimum misfit time constant for each pixel. Areas with a clear postseismic deformation signal tend to have low time constants. Right: average residual sum of squares (RSS) plotted against postseismic time constant for all pixels with a velocity greater than 7 mm/yr in the ERS postseismic velocity map.

References

Nissen, E., J. R. Elliott, R. A. Sloan, T. J. Craig, G. J. Funning, A. Hutko, B. E. Parsons, and T. J. Wright (2016), Limitations of rupture forecasting exposed by instantaneously triggered earthquake doublet, *Nature Geoscience 2016 9:4*, *9*(4), 330, doi:10.1038/ngeo2653. C.1